8-3-2006

Modeling the Power Evolution of Classical Double Radio Galaxies over Cosmological Scales

Paramita Barai

Modeling the Power Evolution of Classical Double Radio Galaxies over Cosmological Scales

by

Paramita Barai

Under the Direction of Paul J. Wiita

Abstract

During the quasar era (redshifts between 1 and 3) Radio Galaxies (RGs) have been claimed to have substantially influenced the growth and evolution of large scale structures in the universe. In this dissertation I test the robustness of these exciting claims. In order to probe the impacts in more detail, good theoretical models for such RG systems are required. With this motivation, I seek to develop an essentially analytical model for the evolution of Fanaroff-Riley Class II radio galaxies both as they age individually and as their numbers vary with cosmological epoch.

To do so, I first compare three sophisticated semi-analytical models for the dynamical and radio lobe power evolution of FR II galaxies, those given by Kaiser, Dennett-Thorpe & Alexander (1997, KDA), Blundell, Rawlings, & Willott (1999, BRW) and Manolakou & Kirk (2002, MK). I perform multi-dimensional Monte Carlo simulations leading to virtual radio surveys. The predictions of each model for redshift, radio power (at 151 MHz), linear size and spectral index are then compared with data. The observational samples are the low frequency radio surveys, 3CRR, 6CE and 7CRS, which are flux-limited and redshift complete. I next perform extensive statistical tests to compare the distributions of model radio source parameters and those of the observational samples. The statistics used are the 1-Dimensional and 2-Dimensional Kolmogorov-Smirnov (K-S) tests and the 4-variable Spearman partial rank correlation coefficient. I search for and describe the "best" parameters for each model. I then produced modifications to each of the three original models, and extensively compare the original and the modified model performances in fitting the data.

The key result of my dissertation is that using the Radio Luminosity Function of Willott et al. (2001) as the redshift birth function of radio sources, the KDA and MK models perform better than the BRW models in fitting the 3CRR, 6CE and 7CRS survey data when using K-S based statistical tests, and the KDA model provides the best fits to the correlation coefficients. However, no pre-existing or modified model can provide adequate fits for the spectral indices.

I also calculate the volume fraction of the relevant universe filled by the generations of radio galaxies over the quasar era. This volume filling factor is not as large as estimated earlier. Nonetheless, the allowed ranges of various model parameters produce a rather wide range of astrophysically interesting relevant volume fraction values. I conclude that the expanding RGs born during the quasar era may still play significant roles in the cosmological history of the universe.

Index Words: Radio Galaxies, FR II, Radio Luminosity Function, Quasar Era, AGN, IGM, WHIM, K-S Statistical Test, Cosmological Evolution, Redshift.

Modeling the Power Evolution of Classical Double Radio Galaxies over Cosmological Scales

by

Paramita Barai

A Dissertation
Presented in Partial Fulfillment of Requirements for the Degree of
Doctor of Philosophy
in the College of Arts and Sciences
Georgia State University

2006

Modeling the Power Evolution of Classical Double Radio Galaxies over Cosmological Scales

by

Paramita Barai

Major Professor: Paul J. Wiita
Committee: Vadym Apalkov
D. Michael Crenshaw
Douglas R. Gies
H. Richard Miller

Electronic Version Approved:

Office of Graduate Studies
College of Arts & Sciences
Georgia State University
August 2006

Dedication

I dedicate my dissertation, and the nights & days that went into it,

to my mother, Jharna Barai, & my father, Parimal K. Barai,

who taught me to dream & aim for the stars,

who helped me to pursue my goals & become what I am today,

and,

to my brother, Pallab Barai.

Paramita Barai
July 27, 2006

Acknowledgments

I would like to thank a multitude of people whose cumulative contribution made it possible for me to complete this dissertation work. First my family: my father, mother and brother, who have always been by my side, and who play a significant role behind everything I do today.

Then my mentor, Paul Wiita, under whose supervision and care I have taken my first steps toward becoming an astrophysicist. Looking back over the last four years, I see that he has continuously helped me in so many ways, starting from giving academic advice, to checking almost every form of official document I produced. He always had time for me for whichever silly question(s) I had, even multiple times during a day. His encouragement motivated me greatly to work on unraveling the mysteries of radio galaxies. Thank you Paul, for all your advice, and for being so friendly and approachable.

I thank Steve Rawlings (the referee of our submitted manuscript) for several useful suggestions which substantially improved the dissertation work, and for providing us with the source size data for 7C-I & II surveys, and Katherine Blundell for a helpful conversation. Thanks to Chris Willott for sending us the 6C and 7C-III data, Konstantina Manolakou for providing us with a version of her Fortran code implementing the MK model, Christian Kaiser for conversations, and to all of the above for clarifying correspondence. I also thank Jim Loudin and Hannu Miettinen for correspondence and for sending us a version of their multivariate statistics (multidimensional K-S test) code. I acknowledge useful conversations with our collaborators, Gopal-Krishna and Zeljko Ivezić, who gave me valuable research advice.

I am grateful to all the other faculty members in my dissertation committee: Vadym Apalkov, Mike Crenshaw, Doug Gies, Steve Manson and Dick Miller. I highly appreciate their spending time reading my thesis and giving their valuable comments. I would like to take this opportunity to again thank my advisor Paul Wiita, as well as Doug Gies, Gopal-Krishna, Mike Crenshaw and Dick Miller, for writing the letters of recommendation for the post-doctoral jobs I applied for. I thank all the professors of Physics and Astronomy at Georgia State University, all of whom have contributed in revealing to me, through courses, seminars and general discussions, the wonders of the physical universe around us and how we probe them.

I am most grateful to my colleague Angela Osterman for her efforts on initial versions of some codes to implement the models. That gave me the base to start working on the radio galaxy evolution models.

Since my dissertation involved heavy computational work, I needed substantial computer resources. I thank the astronomy system managers, John McFarland (initially), and Rajesh Deo (lately) for taking care of my requests promptly. Also thanks to Raj for helping me with several programming issues involving shell scripts. I thank all the astronomy graduate students who have their offices in 1 Park Place - Rm 730, as I was constantly running my simulations on their computers. (The machine where I sit is good for nothing!) They were interrupted at times and several of them (Alvin, Deepak and Eunwoo) came to ask me to stop the process; I am sorry if I have bothered them too much.

I am grateful to some of my colleagues who helped me in writing this thesis. Many thanks to Alvin Das who let me use his dissertation template, and to Wei-Chun Jao and Wenjin Huang, who helped me to grasp some intricate LaTeX details (with respect to long tables and figures).

Finally, thanks to all of the graduate students of Astronomy and Physics at Georgia State University, for making my stay here a fun-filled, lively experience, which I will forever cherish in the future.

Table of Contents

List of Tables

List of Figures

Abbreviations

1-D	1-dimensional
2-D	2-dimensional
AGN	Active Galactic Nuclei
BRW	Blundell, Rawlings, & Willott (1999)
CMB	Cosmic Microwave Background
CMBR	Cosmic Microwave Background Radiation
FR I	Fanaroff-Riley Class I
FR II	Fanaroff-Riley Class II
GKW01	Gopal-Krishna & Wiita (2001)
HST	Hubble Space Telescope
IR	infrared
ISM	interstellar medium
IGM	intergalactic medium
ICM	intracluster medium
IDL	Interactive Data Language
IC	Inverse Compton
KDA	Kaiser, Dennett-Thorpe, & Alexander (1997)
K-S	Kolmogorov-Smirnov
MK	Manolakou & Kirk (2002)
QE	Quasar Era
QSOs	Quasi Stellar Objects
SMBH	Supermassive Black Hole
RG	Radio Galaxy
RGs	Radio Galaxies
RLF	Radio Luminosity Function
UV	ultraviolet
WHIM	Warm/Hot Intergalactic Medium

– 1 –

Introduction

Many galaxies have been observed emitting significant amounts of energy at the radio wavelengths (1 mm - 100 m) of the electromagnetic spectrum, and have been given the name Radio Galaxies. The first observation of cosmic (extra-terrestrial) radio emission was made by Karl G. Jansky in 1932 working at Bell Labs, when he discovered radio emission (at 20.5 MHz or 14.6 m) from the center of our Galaxy, the Milky Way. The first definite detection of extragalactic radio emission occured in 1950 when radiation from M31, the big spiral galaxy in Andromeda, was detected at the Jodrell Bank Observatory by Brown & Hazard (1951). The first powerful radio galaxy was discovered in Cygnus; Cygnus A showed two radio lobes on opposite sides of an optical galaxy (Jennison & Das Gupta 1953). This marked the dawn of the age of Radio Astronomy, after which many more radio sources (galactic and extragalactic, diffuse, extended and compact) are continually being discovered, with ever-improving technology providing better resolution and sensitivity. Radio wavelengths feature several advantages over other wavebands: e.g., radio astronomy can be done from Earth without being too much affected by weather; radio telescopes can operate day and night; radio photons are not obscured by Galactic dust as are optical, ultraviolet (UV) and low energy X-ray photons.

In parallel, theoretical studies are in progress worldwide to explain the radio observations in order to understand the true nature of the emitters: their origin, formation, structure and evolution. Investigating the physical mechanisms going on in the radio sources will not only help us to better understand these discrete emitters, but will also shed light on the cosmic evolution of the universe at large. Study of the interactions of the radio galaxies with their environments, the interstellar medium (ISM), the intergalactic medium (IGM) and the intracluster medium (ICM), and how they affect each other's evolution, holds a key to comprehending the formation of structure in the universe. Hence, radio wavelengths provide us with a unique window to study the universe as a whole as well as its component galaxies and clusters.

It has been found that most of the galaxies emitting in the radio from their cores, also radiate significant amount of energies at other wavebands of the electromagnetic spectrum: infrared (IR), optical, UV, X-ray and gamma rays. A majority of these galaxies are classified as active, with most of the energy coming from the central

Active Galactic Nuclei (AGN).

The active galaxies are powered by a compact region in the galactic center, and this central engine (the fundamental source of energy) is most popularly believed to involve a Supermassive Black Hole (SMBH) of between 10^6 and 10^9 solar masses. The amount of radiation emitted by the central compact source is enormous; it ranges from being comparable to the total power emitted by all stars in the host galaxy (i.e., $\sim 10^{11}$ times the solar luminosity) and can go up by a factor of 100 or more (depending on the type of AGN) (Peterson 1997). The standard theoretical model assumes that the enormous energy is generated by matter falling onto the SMBH. As matter falls in, angular momentum causes the infalling material to flatten into an accretion disk, and frictional heating causes it to radiate energy strongly at optical and higher wavebands. Frequently, large-scale jets of matter are observed to emanate from the central region. These jets can then form the surrounding extended structures of diffuse radio emission called the radio lobes, and thus make the active galaxy a radio galaxy or a radio-loud quasar.

Radio Galaxies (RGs) with extended lobes (often hundreds of kpc apart) on opposite sides of their nuclei, are called the *classical double* sources; they constitute a small but important population of AGNs. Fanaroff & Riley (1974) classified these objects as Class II sources: those which have their radio luminosities higher than a critical transition, L_R^*, which corresponds to a monochromatic power of $P_{178\ \mathrm{MHz}} > 10^{25}$ W Hz^{-1} sr^{-1}. These are the "edge-brightened" population of radio sources, i.e., their brightness peak occurs near the outer edges of the two radio lobes, and these regions of most intense emission (towards the edges) are called the hotspots. The Fanaroff-Riley Class II (FR II) galaxies constitute the more powerful population of RGs, and they show less bending.

The radio map of the canonical FR II source, Cygnus A, a nearby powerful radio galaxy, is shown in Figure 1.1. This vividly illustrates one of the most striking feature of these radio sources, the transport of energy over stupendous length scales (100's of kpc) from the central nucleus, through the elongated jets, into the hotspots and lobes. The classical double radio galaxies are perhaps the largest known single entities in the universe.

Most RGs weaker than the critical radio luminosity, L_R^*, exhibit the Fanaroff-Riley Class I (FR I) type morphology. These are the "edge-dimmed" radio sources, whose structures are distinguished by diffuse radio lobes having their brightest regions

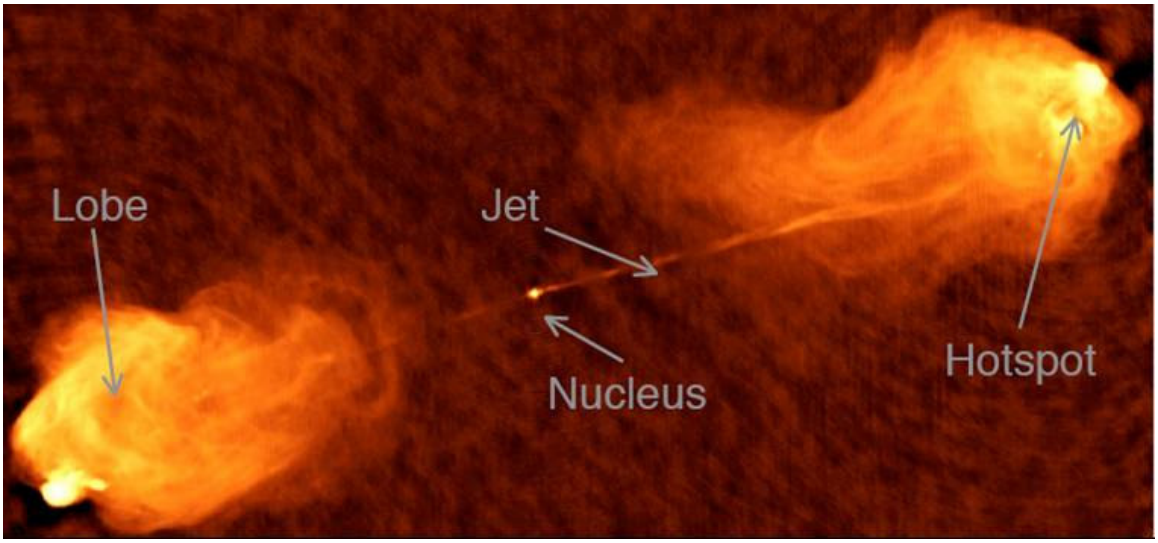

Figure 1.1: Radio Map of FR II galaxy Cygnus A, generated by Chris Carilli, from the Very Large Array observations at wavelength of 6 cm, with 0.5 arcsec resolution (Perley, Dreher, & Cowan 1984). In this powerful radio galaxy the relativistic jets beamed from the compact nuclear radio core, feeds the large double radio lobes which span over 200 kpc. [1]

within the inner half of the source. A typical FR I galaxy is shown in Figure 1.2. This map of the radio galaxy 3C31 clearly shows the typical FR I characteristics: intensity greatest in the central regions, and prominent jets launched from the compact nuclear radio core.

Investigations by Owen & White (1991) suggested that the FR I and FR II sources are not only separated by a radio power division, but the FR I/FR II break is also a function of the optical luminosity of the host galaxy (or, the optical galaxy identified with the radio core). More detailed studies based on improved radio maps established that the radio luminosity separating FR I from FR II sources is actually a rising function of the optical luminosity from the parent elliptical galaxy, $L_R^* \propto L_{opt}^{1.7}$ (e.g., Ledlow & Owen 1996).

An unification paradigm exists for AGN. This tries to explain the different types of AGN as the same underlying active galactic phenomenon, but different types arise because they are viewed differently by us (due to different angles to our line of sight and/or the presence of some obscuring source often called the dusty torus). The unification scheme considering radio-loud AGN unifies Fanaroff-Riley class II radio

[1] http://rocinante.colorado.edu/~pja/astr3830/lecture29.pdf

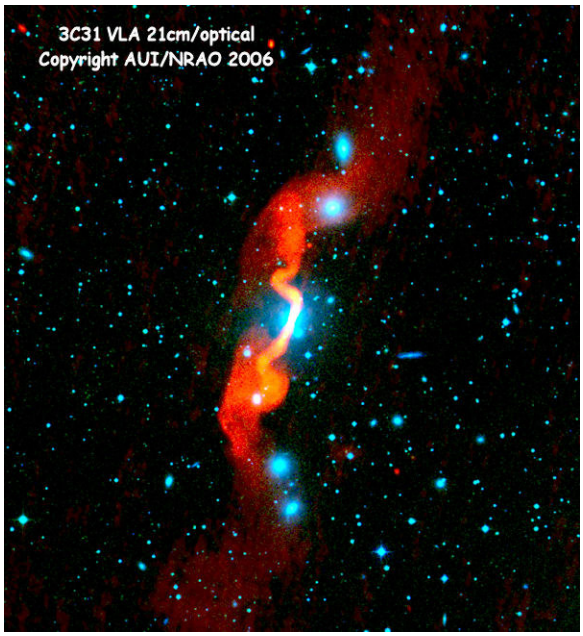

Figure 1.2: FR I (plumed) radio galaxy 3C31 at $z = 0.0169$, also showing the host galaxy [2]. *Red*: VLA radio map at 21 cm wavelength (1.4 GHz) with 5.5 arcsec resolution. *Blue*: optical image from the Palomar Sky Survey. The typical FR I characteristics are seen: prominent jets beamed from the compact nuclear radio core, and weaker diffuse extended emission.

galaxies with the radio-loud quasars. The key elements which form the basis of this unification scheme are the powerful radio jets (and/or core region) radiating anisotropically via the synchrotron mechanism, and our viewing angle to the jet's direction.

According to the unified model, the FR II RGs are the "parent population" (i.e., the more numerous unbeamed equivalent) of radio-loud quasars. The difference between them is due to the relativistic beaming of the radio jet, caused by the different viewing angle the jet emission makes with our line of sight. When viewed close to "face-on" (or, "end-on", i.e., parallel to the radio source/jet axis), RGs look like radio-loud quasars because the approaching radio jets become more prominent due to relativistic Doppler boosting, the lobe separation is reduced due to foreshortening by projection, the optical core dominates the host galaxy, and we can see deeply into the core. So quasars are "face-on" versions of the luminous RGs, where the radio jet axis makes a smaller angle to our line of sight. The FR II sources are those where

[2]From Alan Bridle's image gallery: http://www.cv.nrao.edu/∼abridle/images/3c31ldss.jpg

the jets lie at a larger angle to our line of sight; i.e., these are RGs viewed more "edge-on".

The basic concept of simple radio-loud unification models is as follows. There is the central black hole of the AGN, matter spiralling into the black hole in an accretion disk, and the elongated oppositely directed jets which feed the radio lobes. If our line of sight is nearly along the jet (seeing directly into the core) we observe a quasar with its bright Doppler boosted core/jet emission and both broad and narrow emission lines. If our line of sight makes a larger angle then we see a FR II radio galaxy.

The idea that blazars (being viewed "end-on" along their radio axis) are relativisticlly beamed versions of otherwise "normal" AGN, was first proposed by Blandford & Rees (1978), Scheuer & Readhead (1979) and Blandford & Konigl (1979). Several studies followed prescribing similar unification scenarios for other AGN. Orr & Browne (1982) discussed that flat spectrum radio quasars (or, core-dominated radio Quasi Stellar Objects (QSOs)) are more well aligned versions of steep-spectrum radio quasars (or, lobe-dominated radio QSOs). Further investigations indicated that the radio-loud QSOs which have their radio axis near the sky plane are seen as RGs (e.g., Bridle & Perley 1984; Scheuer 1987; Barthel 1987; Peacock 1987). Such ideas finally led to the FR II Radio Galaxy (RG)/quasar unification (e.g., Barthel 1989; Padovani & Urry 1992; Gopal-Krishna, Kulkarni, & Wiita 1996).

From similar arguments applied to the lower luminosity RG population, BL Lac objects are believed to be the beamed cores of FR I RGs (e.g, Browne 1983; Antonucci & Ulvestad 1985; Padovani & Urry 1991). Such unification ideas have been extensively discussed in many reviews and books (e.g., Antonucci 1993; Barthel 1994; Urry & Padovani 1995; Peterson 1997). While these scanarios may not explain everything about AGN, the basic idea that orientation is very important is now well accepted.

1.1 Motivation: Cosmological Impact of Radio Galaxies

Multi-frequency observations (McCarthy et al. 1987; Chambers et al. 1988a; Dunlop & Peacock 1990; Best et al. 1996; Dey et al. 1997; Blain et al. 1999; Jackson & Wall 1999; Steidel et al. 1999; Bicknell et al. 2000; Archibald et al. 2001) indicate that the RGs can have substantial impacts on the formation, distribution and evolution of galaxies and large scale structures of the universe (e.g., Gopal-Krishna & Wiita 2001,

hereafter GKW01; Rawlings & Jarvis 2004).

Flux limited samples indicate that the comoving densities of observed RGs were higher during the *quasar era* (i.e., between redshifts $\simeq 1.5$ and 3) by $100 - 1000$ times, as compared to the present epoch (Dunlop & Peacock 1990; Jackson & Wall 1999; Willott et al. 2001; Grimes et al. 2004). Optical and hard X-ray observations of powerful AGN also reveal a similar trend for the quasar era (Ueda et al. 2003). In a very recent work, Hopkins, Richards, & Hernquist (2006) combined a large set of quasar luminosity functions from several wavelength bands (rest-frame optical, soft and hard X-ray, near- and mid-infrared) and determined that the bolometric quasar luminosity function in the redshift interval $z = 0 - 6$ peaked at $z = 2.15$.

The star and galaxy formation rates were also considerably higher in the quasar era, as indicated by the following studies. Lilly et al. (1996) inferred that the observed luminosity density (and hence the star formation rate) of the universe in the UV, optical and near-infrared increases markedly with redshift over $0 < z < 1$ (from Canada-France Redshift Survey faint galaxy samples). Similarly, from Hubble Deep Field studies Connolly et al. (1997) and Madau, Pozzetti, & Dickinson (1998) found a sharp rise in the comoving luminosity density and global star formation rate with redshift, finding that it peaked at $z \simeq 1.5$, and decreased monotonically at higher z out to $z \simeq 3 - 4$. More recently, Bouwens & Illingworth (2006) found an apparent decrease in the rest-frame UV luminosity function and the cosmic star formation rate density from the peak redshift of $z \simeq 3$ up to $z \sim 6 - 10$. Studies made with the Spitzer Space Telescope (e.g., Pérez-González et al. 2005) also indicate that the infrared luminosity function and the cosmic star formation rate increase with redshift until the quasar era.

A peak in the UV luminosity density and overall star-formation rate during the quasar era is also evident from recent Keck deep field studies of Sawicki & Thompson (2006a,b). There is a gradual rise in luminosity density starting at $z \sim 4$ or earlier, followed by a shallow peak or a plateau within $z \simeq 3 - 1$, and then the steep decrease at lower redshifts. Submillimeter surveys show that the comoving luminosity density has a peak at $z \simeq 2 - 5$ (Blain et al. 1999; Archibald et al. 2001). This redshift range is somewhat higher than what optical surveys (possibly affected by dust obscuration) infer. At the same time, a more recent sub-mm study (Rawlings et al. 2004) indicates no compelling evidence that the far infrared luminosity of radio sources rises with redshift.

The combination of the above observations have prompted investigations of the effects of the RGs on the cosmological evolution and distribution of large scale structures in the universe. Preliminary work on this question indicates that these RGs can have substantial impacts on the formation, distribution and evolution of galaxies, and perhaps even on the large scale structures of the universe (e.g., GKW01; Kronberg et al. 2001; Gopal-Krishna & Wiita 2003b, hereafter GKW03b; Gopal-Krishna, Wiita, & Osterman 2003, hereafter GKWO; Gopal-Krishna, Wiita, & Barai 2004, hereafter GKWB; Rawlings & Jarvis 2004; Levine & Gnedin 2005; Silk 2005).

1.1.1 Star Formation: Radio-Optical Alignment

One important aspect of this process is the role played by the huge expanding RG lobes, particularly those of the FR II type, in triggering extensive star formation in a multi-phase intergalactic medium. This idea has been discussed by several authors in order to explain the alignment between large scale optical emission and radio source direction (e.g., Begelman & Cioffi 1989; De Young 1989; Rees 1989). Chokshi (1997) proposed that RG expansion could trigger much star formation in their host galaxies. Gopal-Krishna & Wiita (2001) stressed that RGs could impact a large fraction of the filamentary structures in which galaxies form, thus hastening their birth. Similar conclusions were drawn from different lines of argument by Kronberg et al. (2001) and Furlanetto & Loeb (2001). Recently, Silk (2005) argued that more efficient ultraluminous starburts can occur by positive feedback triggered by AGN jets. More recent studies by Nesvadba et al. (2006) suggest that feedback by AGN winds might have a similar (or even larger) cosmological impact in star formation in massive galaxies, than starburst-driven winds.

A very significant fraction of the volume of the universe in which star formation has occured was impinged upon by the growing radio lobes during the quasar era (GKW01, Kronberg et al. 2001). The radio lobes propagating through the protogalactic medium mainly encounter the hot ($T > 10^6$ K), volume-filling, lower density gas. But, when they envelop cooler clumps of gas ($T \sim 10^4$ K; Fall & Rees 1985) embedded within the hotter gas, the initial bow shock compression can trigger large-scale star formation, which is sustained by the persistent overpressure from the engulfing radio cocoon. The cocoon pressure is likely to be well above the equipartition estimate (Blundell & Rawlings 2000). This basic scenario is supported by many works, including analytical models (e.g., Begelman & Cioffi 1989; Rees 1989; Daly 1990), and

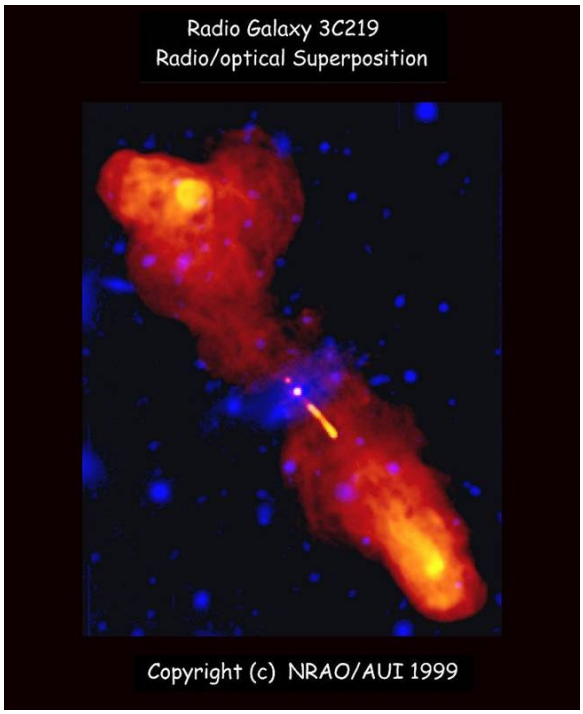

Figure 1.3: Radio-Optical Alignment in FR II radio galaxy 3C219, at $z = 0.1745$. The filamentary lobe structure extends several hundred kpc on both sides with bright, extended hot spots in each. *Red/yellow*: VLA 1.4+1.6 GHz combined image at 1.4 arcsec resolution. *Blue*: Optical V band image from Baum et al. (1988). [3]

hydrodynamical (e.g., De Young 1989; Cioffi & Blondin 1992; Mellema et al. 2002; Fragile et al. 2004; Saxton et al. 2005), and magnetohydrodynamical (e.g., Fragile et al. 2005) simulations. Recent hydrodynamical studies (e.g., Vernaleo & Reynolds 2006) show that the RGs are important in preventing strong cooling flows in galaxy clusters, but their elongation must be taken into account in this regard.

The triggered star formation provides an explanation for much of the remarkable radio-optical alignment effect exhibited by high-z RGs (e.g., McCarthy et al. 1987; Chambers et al. 1988a,b). In these sources optical emission extending over many tens of kpc is frequently found close to the radio axis, and hardly ever seen in directions far from them. Some of this emission is probably produced by ionizing photons from the AGN, which will also be concentrated along the radio axis in the unified schemes. As an example, Figure 1.3 illustrates the clear radio-optical alignment in the RG 3C219. The yellow and red colored features comprise of the radio image (showing the AGN,

[3] http://www.cv.nrao.edu/∼abridle/images/3c219lonopt_large.jpg

jet, hotspots and lobes); the optical emission is shown in blue. The optical galaxy (the central blue region) coincides with the radio AGN.

Additional support for jet or lobe-induced star formation comes from the Hubble Space Telescope (HST) images of $z \sim 1$ radio galaxies (Best, Longair, & Röttgering 1996) and of some radio sources at even higher z (e.g., Miley et al. 1992; Bicknell et al. 2000). Keck observations (Dey et al. 1997) and sub-mm observations (Greve, Ivison, & Stevens 2006) of high-z RGs also give evidence for this phenomenon. Clustered Lyman-α emitters have been found at high redshifts ($z \sim 2-5$) close to RGs (Venemans et al. 2004, 2005; Overzier et al. 2006), indicating that RGs form in high density regions of the universe and could have significant impact by accelerating star formation and the growth of galaxy clustering.

Venemans et al. (2002) (using Very Large Telescope imaging and spectroscopy) and Miley et al. (2004) (using HST observations) found mass density enhancements around a luminous radio galaxy at $z = 4.1$. From deep optical HST imaging Zirm et al. (2005) found evidence of star formation and a starburst driven superwind induced by AGN jet activity in the same RG at $z = 4.1$. Recently Zheng et al. (2006) found evidence for an overdensity of galaxies around the most distant known radio-loud quasar at $z = 5.8$, in whose field Ajiki et al. (2006) detected Lyman-α emitters.

1.1.2 Magnetization

In addition to their possible importance for galaxy formation, the expanding RG lobes could easily have infused magnetic fields of the significant strengths ($\sim 10^{-8}$ Gauss, e.g., Ryu, Kang, & Biermann 1998) apparently present in the cosmic web portion of the IGM (GKW01, GKWO, GKWB). Two entirely independent groups, approaching the problem from different directions, also concluded that QSOs were energetically capable of penetrating much of the IGM and were likely to be responsible for magnetizing the universe (Furlanetto & Loeb 2001; Kronberg et al. 2001).

An alternative route to magnetizing the IGM comes from the superwinds driven by outflows from stars and galaxies (Kronberg et al. 1999). However, this situation would not naturally lead to preferential alignment between radio lobes and newly forming galaxies as has been observed (e.g. Best et al. 1996; Bicknell et al. 2000). Also, the radio loud AGNs outside clusters offer a potentially more energetic route for magnetization of the wider IGM (Kronberg et al. 2001). From semi-analytic calculations coupled to N-body simulations, Bertone et al. (2006) claimed that galactic

winds, or outflows emerging from star-forming galaxies, are an efficient mechanism to provide intense and widespread "seed" magnetization.

1.1.3 Metalization

There is evidence of substantial metallicity in underdense regions of the IGM at $z \simeq 4-5$ (e.g., Schaye et al. 2003; Aguirre et al. 2004; Schaye & Aguirre 2005, and references therein), and metallicities higher than solar in quasar nuclei at similarly high-z (e.g., Dietrich et al. 2003). Massive star-forming galaxies of solar metallicity at $z > 2$ have been found by Shapley et al. (2004). Such observations require an efficient mechanism for spreading metals widely ("metalization") at early cosmic epochs.

Recent studies of metal distribution in the IGM (e.g., Pieri, Schaye, & Aguirre 2006b) indicate that metal enrichment is much more widespread than the immediate surroundings of Lyman-break galaxies. Using Monte-Carlo investigations, Pieri, Martel, & Grenon (2006a) showed that anisotropic galactic outflows can significantly enrich the low-density IGM, and also deposit metals in other, unrelated cosmological structures.

From HST (STIS) spectra, Aracil et al. (2006) detected cool ($T < 10^5$ K) intergalactic gas clouds distributed within large-scale filamentary structures of the universe, which have relatively high metallicity (> 0.9 solar). Tripp et al. (2006) found evidence that some regions of the cosmic web filaments are highly metal enriched, and suggested that the enrichment might have occurred long ago (at high-z). Yet, in both these recent studies, the nearest luminous galaxies which might pollute the IGM were observed to be far away. Other recent spectroscopic studies of absorber-galaxy connections (e.g., Tumlinson et al. 2005; Prochaska et al. 2006; Aracil et al. 2006) also find high-metallicity, highly ionized gas in large-scale structures, but with no nearby luminous galaxies.

Searching for the origin of the enrichment, observational studies by Adelberger et al. (2005) provide no clear evidence for superwinds at $2 < z < 3$ as a cause of the metal enhancement of the IGM. Along similar lines, Porciani & Madau (2005) conclude that the observed IGM metallicities are not necessarily generated by late "superwinds" from Lyman-break galaxies.

Such observations show that the IGM was been polluted with metals, presumably produced by early star formation; but the possible mechanism(s) to disperse the metals into widespread regions of the IGM is(are) still controvertial.

A viable possibility is that the radio sources born through the quasar era could have contributed toward metal enhancement of their environments. The huge radio lobes could have swept out the metal-rich ISM of young galaxies they encounter (including that of the active host) while they were expanding, thereby contributing substantially to the widespread metal pollution of the IGM (Gopal-Krishna & Wiita 2003b; GKWB). This enriched gas could then be compressed in subsequent phases of nuclear activity, in either the original active galaxy or in one of the newer galaxies triggered by that RG.

While the obvious sources for the production of metals detected in quasars are starbursts in the host galaxies, the possibility of nucleosynthesis in the accretion disks feeding the central black holes (e.g., Mukhopadhyay & Chakrabarti 2000; Kundt 2002) also should be considered. It is possible that the superwind outflow model (Kronberg et al. 1999) would also contribute to the metalization of IGM, though that aspect of this scenario has not yet been investigated.

1.2 Relevant Volume Fraction of Radio Galaxies

A key step toward ascertaining the importance of these processes of star formation, magnetization and metalization via RGs is addressing the question of what fraction of the relevant volume of the universe did the radio lobes occupy during the quasar era. By saying "relevant universe", we are referring to the volume containing the warm/hot intergalactic gas where most of the baryons in the universe at the present epoch apparently reside. This repository of cosmic baryons is popularly called the Warm/Hot Intergalactic Medium (WHIM) and has temperatures $10^5 < T < 10^7$ K (e.g., Cen & Ostriker 1999, 2006; Davé et al. 2001). These warm/hot baryons permeate the universe as extended large-scale filamentary structures, the junctions of which are the main sites of formation of galaxies and clusters.

So, for the radio lobes to have an important role in impacting star formation and spreading magnetic fields and metals, they need to penetrate a significant portion of this relevant volume of the warm/hot baryonic filaments only. Our "relevant universe", or the WHIM, occupied only $\sim 3\%$ of the total volume of cosmic baryons during most of the quasar epoch (i.e., between $2 \leq z \leq 3$); and pervades $\sim 10\%$ of the volume today. The mass of the WHIM as a fraction of the total baryonic mass in the universe was $\sim 15\%$ during the quasar era, and has grown dramatically since

then to reach $\sim 50\%$ today (Cen & Ostriker 1999, 2006). A very recent observational study by Soltan (2006) indicates good agreement between observed emission in the X-ray band and numerical (hydrodynamical) simulations for the spatial distribution, temperature and density of the WHIM.

During the early epochs of the quasar era, the cosmic web of filaments was accreting gas vigorously. The warm/hot gas is likely to have been more uniformly distributed within the filaments, but was in the process of becoming increasingly non-uniform due to gravitational accretion onto the dark matter halos and galaxies existing or forming within the filaments (e.g., Cen et al. 2001; Viel et al. 2003).

From arguments which provided approximate bounds, Gopal-Krishna & Wiita (2001) showed that during the 'quasar era' ($z \sim 2 - 3$), much of the denser (proto-galactic) warm/hot material in the universe (which was concentrated within the cosmic sheets and filaments) was probably impacted by the expanding lobes of the generations of RGs born during that era. Their most impressive claim is that this relevant volume filling fraction can be as high as 0.5 when integrated over the volumes occupied by all the generations of radio sources produced during the entire quasar era (taken as 2 Gyr long). Denser, cooler clumps of gas scattered across those cosmic filaments could thus be compressed, yielding global starbursts. The pervading overpressured radio lobes could trigger, or at least, accelerate, the formation of entire new galaxies (also, Gopal-Krishna & Wiita 2003a, hereafter GKW03a; cf. Daly 1990). GKW01 argued that this picture of a radio lobe-filled early universe can explain the much higher star formation rate found at high redshifts (Section 1.1.1); it also can readily account for the presence of magnetic fields in distant galaxies (Section 1.1.2), and the widespread distribution of metals in the proto-galaxies seen at these high redshifts (Section 1.1.3).

A comprehensive and robust study of the impact of radio galaxies on various events in the cosmological history of the universe seeks a reliable quantitative estimation of the relevant volume filling fraction of radio galaxies and their active lifetimes. A prerequisite for a more accurate computation of this volume impacted by radio lobes is a good model of the evolution of radio sources, for both individual sources and as a function of redshift. And here lies the essence of my thesis research, the contents of which are discussed in Section 1.4.

In a noteworthy recent work Rawlings & Jarvis (2004) agreed that RG lobes will penetrate much of the relevant universe, but they argued that this may often shut off

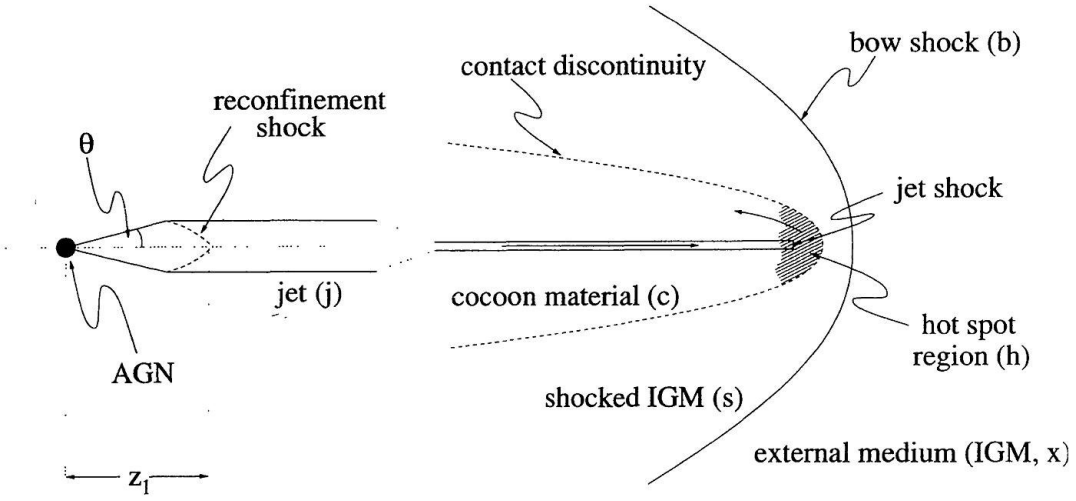

Figure 1.4: Schematic of the basic components of a radio galaxy. Copied from Figure 1 of Kaiser & Alexander (1997), the KDA model (described in Section 2.4 of this thesis).

star formation by expelling gas from protoclusters. However, unlike our picture (also, that of Rees 1989), they assume a single phase medium, so this negative conclusion is not surprising.

1.3 Brief Review of Radio Galaxy Evolution Models

The radio continuum observed from the classical double, or FR II, RGs is understood to be synchrotron radiation from relativistic particles (mostly electrons, maybe positrons) spiralling in the magnetic field in these sources. The accepted model can be summarized as: a jet (or beam) containing relativistic particles propagates from the central AGN (and is powered by the AGN); these particles encounter a shock near where the jet impacts the ambient ISM/IGM/ICM, forming the terminal hotspot; and the plasma leaving the hotspot continuously feeds the coccon (or lobe) around the jet with radio-emitting plasma (Longair et al. 1973; Scheuer 1974; Blandford & Rees 1974; Begelman et al. 1984). Figure 1.4 gives the basic schematic of a radio galaxy and its typical components, a structure which is used in all the models of RG evolution.

The jet in a FR II RG is believed to remain relativistic all the way from the

central engine to the terminal Mach disk shock (Wardle & Aaron 1997), and consists of particles distributed less densely than the surrounding IGM. The synchrotron nature of the radiation from FR II sources implies the presence of ultra-relativistic electrons in the radio cocoon (Rees 1971), though the nature of the charge balancing particles (positrons or protons) is still debated (e.g., Leahy 1991).

These observational and theoretical investigations paved the way for numerical studies of extragalactic radio sources (e.g., Norman et al. 1982; Burns et al. 1991; Wiita & Norman 1992; Hooda & Wiita 1998). Cioffi & Blondin (1992), following the model of Begelman & Cioffi (1989), performed simulations to show that the radio jets likely are confined via pressure balance with the lobe. Simulations by, e.g., Lind et al. (1989) indicate that at the terminal Mach disk shock the jet thrust is applied (even instantaneously) over an area (effective working surface) significantly larger than the jet cross section, and this spatial region is identified with the observed "hotspot" by most authors (e.g., Blundell et al. 1999).

Many analytical and semi-analytical models have been published, including more or less detailed and realistic physics, which attempt to characterize radio sources in terms of their dynamics and power evolution. In considering some of the more recent ones we note that Falle (1991) claimed that the jet size would grow self-similarly in external atmospheres where the density drops off more slowly than $1/r^2$ from the central AGN. Later, Kaiser & Alexander (1997, hereafter KA) showed that the cocoons can also have a self-similar growth. Although the most extensive numerical hydrodynamical studies (e.g., Carvalho & O'Dea 2002) indicate that radio source sizes and shapes grow in a more complex way than predicted by these self-similar analytical models, they are still reasonable approximations overall.

The radio power evolution in these models is based on energy losses that the relativistic particles undergo in the hotspot, where they are energized after being transported down the jets, and in the lobe into which they expand. The most significant effects on the energies of the radiating particles are "adiabatic" energy losses as the lobe expands, synchrotron radiation losses in the lobe magnetic field and Inverse Compton (IC) losses off the Cosmic Microwave Background (CMB) photons.

Goodlet (2006) presents a recent dissertation work on the environments of RGs and models of their power evolution. Using sub-samples of sources from the 3CRR, 6CE and 7C-III surveys, and models of KA and Kaiser, Dennett-Thorpe, & Alexander (1997), she found that the radio source environment is a strong function of the radio-

luminosity but is relatively unaffected by changes in cosmic epoch. This study also indicates that depolarisation and rotation measure variations are not ambient density indicators, but rather provide evidence for changes in the magnetic field disorder as a function of redshift.

1.4 What is Done in This Thesis and Why it is Important

Our ultimate aim in this thesis work is to develop an improved but essentially analytical model for the evolution of Fanaroff-Riley Class II radio galaxies as they age individually and as their numbers vary with cosmological epoch. Such modeling is essential in order to probe in more detail the cosmological impact of radio galaxies on the growth of structures and evolution history of the universe, effects which appear likely to have been quite significant during the quasar era (Sections 1.1 and 1.2).

As our first step toward the goal, we examined in detail and compared three fairly sophisticated analytical models for the evolution of linear size and lobe power of FR II radio galaxies with time, those given by Kaiser, Dennett-Thorpe, & Alexander (1997, hereafter KDA), Blundell, Rawlings, & Willott (1999, hereafter BRW) and Manolakou & Kirk (2002, hereafter MK). The source linear-size evolution in the BRW and MK models essentially follow the KDA prescription. However they differ in the way the relativistic particles are injected from the jet to the lobe, and in treatments of loss terms and particle transport. So there are some significant differences in their predictions for observed powers (P) as functions of source size (D) and redshift (z).

The simplest method to study the power evolution of RGs is to examine their radio power – linear size, or [P–D], diagram, introduced by Shklovskii (1963). Baldwin (1982), using Scheuer (1974)'s model of FR II RGs, calculated theoretical [P–D] evolutionary tracks, and compared them to the [P–D] diagram of the Third Cambridge Radio (3CR) sources (Jenkins et al. 1977). More recently, the [P–D] tracks have been used in KDA, MK, and in Machalski et al. (2004a,b) as the main way to look for consistency between observational data and radio galaxy evolution models. These papers compare theoretical model tracks with [P–D] diagrams of observed radio sources to evaluate the qualitative success of the models.

The innovative radio sky simulation prescription in Blundell, Rawlings, & Willott (1999, BRW) adds new dimensions to the observed parameter space. Deriving a RG

redshift distribution function from the work of Willott et al. (2001) on the Radio Luminosity Function (RLF), BRW prescribed a pseudo (or virtual) radio galaxy survey technique using cosmological arguments. This involves generation of a huge initial population of sources over cosmic epoch according to pre-defined distribution functions in redshift, jet power and source age. The simulation then makes these large number of sources evolve through their individual lives where they interact with the environment and undergo energy losses (Section 1.3). It finally allows only a few simulated sources to be detected in the virtual surveys when mathematical flux limits, corresponding to observational samples, are imposed. This multi-dimensional Monte Carlo simulation methodology leading to the virtual surveys is discussed in detail in Chapter 3.

Using the simulation technique for the virtual surveys mentioned in the previous paragraph, and any radio lobe power evolution model (here KDA, BRW or MK), one can get P, D, z, and spectral index, α (taking the convention $P_\nu \propto \nu^{-\alpha}$), values for the simulated model radio sources detected in the pseudo-surveys. The distributions of the characteristics of these simulated RGs can then be compared to observational data, to test the success of a model. In BRW, slices through the [P, D, z, α]-space generated by their model are qualitatively compared with observations for two data sets (3CRR and 7CRS); those authors claim good results, except for plots involving α.

In order to strongly claim success for a theoretical model a quantifiable test must be done. Here in the case of modeling the radio galaxy evolution, some statistical test between the model results and observational data can quantify the fit of the model. In this thesis we perform several statistical tests in this regard, and present the quantified results for the various model fits.

To our knowledge, no such comprehensive quantitative results for a range of radio source evolution models considering fits to multiple flux-limited surveys have been published heretofore. We note that, Kaiser & Alexander (1999a) performed a quantitative comparison of a cosmological radio source evolution model (KDA) predictions with a single observational data sample (the 3C data from Laing et al. 1983). They used χ^2 statistical tests to quantify the model fits.

Our fundamental conclusion from the studies of the models is that none of the heretofore published models provides an adequate description of the data. As our next major step towards the goal of isolating good RG models, we have varied the

radio lobe power evolution models. We performed analogous simulation-based virtual surveys on the modified models, and present the corresponding statistical results.

We compare the quantitative results of all the models investigated during the course of the thesis, and finally give our conclusions. We have also performed calculations of the relevant volume filling fractions of the radio lobes based on the resulting best-fit models.

1.5 Synopsis of the Thesis

In *Chapter 2*, we describe the main published detailed semi-analytical models of radio galaxy dynamics and lobe power evolution which we first investigated. These are the models of of Kaiser, Dennett-Thorpe, & Alexander (1997), or KDA, Blundell, Rawlings, & Willott (1999), or BRW, and Manolakou & Kirk (2002), or MK.

In *Chapter 3*, we elaborate the methodology for the initial population generation to do the virtual surveys, and describe the observational samples (3CRR, 6CE, 7CRS) to which we compare the model distributions. We then summarize the multi-dimensional Monte Carlo simulation prescription for the virtual radio surveys (following BRW). We perform extensive statistical tests between the distributions of radio source parameters predicted by each model and those of observational samples. The details of how the 1-dimensional (1-D) and 2-dimensional (2-D) Kolmogorov-Smirnov (K-S) tests and the correlation coefficient analyses are done are also described in this chapter.

In this way we can quantify in a few different ways the goodness-of-fit of the models to these three radio surveys. We vary the parameters of the models, aiming to find the parameters which give the best statistical fit for each model to all three surveys simultaneously. We examine how robust these fits are when the model parameters are changed.

Our results on detailed investigations of the three original models (KDA, BRW and MK) are given in *Chapter 4*. These include the $[P-D]$ tracks, the comprehensive quantitative 1-D and 2-D K-S statistics, and the correlation coefficient analyses results. Here we also discuss the slices through the $[P,\, D,\, z,\, \alpha]$-space for the simulated surveys arising from the various models, as these give a more qualitative comparison between the models and data.

In *Chapter 5*, we give the details on new modifications to the models we have

investigated so far. We present the relevant results following a format similar to that of the original models in Chapter 4.

Chapter 6 discusses some other models which we explored briefly. This work includes investigation of some alternative radio luminosity functions (RLFs), or different redshift birth functions for the sources in the initial ensemble.

In *Chapter 7*, we calculate the the volume fraction of the relevant universe, or the WHIM, occupied by the generations of radio galaxies during the quasar era. We give the results for this "relevant volume filling fraction" for the different models explored so far.

In *Chapter 8*, we give our conclusions from the studies done in this thesis work. We discuss the significance of our radio galaxy evolution model simulation work, along with the shortcomings and limitations of the models. We also suggest avenues for future exploration.

Appendices A and *B*, give the detailed 1-D K-S statistic results for the the simulation runs of original and modified models (whose results are described in Chapters 4 and 5).

– 2 –

Models of Dynamical and Power Evolution of Classical Double Radio Galaxies

2.1 Radio Galaxy Basics

A standard basic model of FR II extragalactic radio sources (e.g., Scheuer 1974; Blandford & Rees 1974; Begelman et al. 1984) has become widely accepted today. A powerful radio galaxy consists of the central active nucleus, and two jets emerging from opposite sides of it. After traveling substantial distances, the plasma in these jets collides with a tenuous environment. There the jets terminate in a Mach disk shock where relativistic electrons are accelerated and hotspots are formed; the plasma passing through the terminal shocks inflate the huge lobes of energetic particles on both sides. A bow shock propagates into the surrounding gas ahead of the jets.

The three models we compare are those of Kaiser et al. (1997), or KDA, Blundell et al. (1999), or BRW, and Manolakou & Kirk (2002), or MK. In brief, the physics of these models differ mainly in the ways in which particles are assumed to be transported from the jet through the hotspot and into the lobe. KDA assume a constant injection power law index, p, for the energy number distribution, $N(E)$, so $N(E) \propto E^{-p}$, for the radiating relativistic particles while the particles are injected from the hotspots into the lobes. BRW assume that the injection index varies between the different energy regimes, as governed by the break frequencies discussed in Section 2.5. MK assume a constant injection index but also argue that the particles are re-accelerated by some turbulent process in the head, an extended region of turbulent acceleration near the hotspot, during transport to the lobes. Several key points of each model and additional differences are noted below in Sections 2.4, 2.5 and 2.6, although the reader should refer to the original papers for a thorough understanding of each model's details. Table 2.1 lists the default values of the major model parameters (those that were used by the authors). We varied these parameters around their default values in our extensive simulations described in Section 3.3. The only parameter whose variation was not considered is the adiabatic index of the external environment, which was adopted as $\Gamma_x = 5/3$ in all our simulations; this

value is expected for all the monoatomic gases and plasmas through which the jets will propagate.

2.2 Dynamical Expansion

In all of the models we consider here the ambient gas around the double radio sources, into which the lobes propagate, is taken to have a power-law radial density distribution scaling with distance $r > a_0$ from the center of the host galaxy,

$$\rho(r) = \rho_0 \left(\frac{r}{a_0} \right)^{-\beta}, \tag{2.1}$$

where the central density ρ_0, scale length a_0, and radial density index β are given by the particular model as described in the subsequent sections. Baldwin (1982) first considered such a more realistic, power-law density profile of the ambient medium for the propagation of the radio jets, following the discovery of X-ray emitting hot gaseous halos around massive elliptical galaxies. Note that $\rho(r) = \rho_0$ for $r < a_0$ is assumed.

For this thesis work, we follow BRW and assume that the external density profile is invariant with redshift. While such a typical radial density distribution is almost certainly appropriate on the average for small redshifts, this may not to be a good approximation at the redshifts corresponding to the quasar era, which witnessed a $10^2 - 10^3$ times higher co-moving density of powerful radio-loud ellipticals (e.g., Jackson & Wall 1999). We note that for very large sources the density eventually will depart from a single power-law with radius and then approach a constant value appropriate to the intergalactic medium at that redshift (e.g., Gopal-Krishna & Wiita 1987; Furlanetto & Loeb 2001). Extending the models to include such environment density variation will be an important step forward (as discussed in the scopes of future work in Section 8.5). During the early epochs of the quasar era, the cosmic filaments were accreting gas vigorously. The hot gas is likely to have been close to uniformly distributed within the filaments, but was in the process of becoming increasingly non-uniform due to gravitational accretion onto the dark matter halos and onto the galaxies existing or forming within the filaments (e.g., Cen et al. 2001; Viel et al. 2003).

We plan to extend this work by allowing redshift variations in the environmental

density profile (in particular variations of ρ_0, a_0 and β with cosmic epoch), and seeing if such modified models perform substantially better in fitting the observations, but we have not completed such extensive modifications of the basic models. Barai et al. (2004) give the results of preliminary work on the implications of the volumes attained by radio sources considering cosmological evolution of the ambient gas density. Only modest differences were found for the assumptions made there.

From dimensional arguments (Kaiser & Alexander 1997, or KA; Komissarov & Falle 1998) the total linear size (from one hotspot to the other) of a radio source at an age t can be expressed as

$$D(t) = 2c_1 a_0 \left(\frac{t^3 Q_0}{a_0^5\ \rho_0}\right)^{1/(5-\beta)}; \tag{2.2}$$

here, $c_1 \sim 1$, is a model dependent, but only weakly varying, constant, which is discussed for each model in the subsequent sections. The jump conditions at the external bow shock and the expression for linear size gives the pressure of the head plasma immediately downstream of the bow shock as (KA Equation 12)

$$p_h(t) = \frac{18 c_1^{2-\beta}}{(\Gamma_x + 1)\,(5-\beta)^2} \left(\frac{\rho_0^3 a_0^{3\beta} Q_0^{2-\beta}}{t^{4+\beta}}\right)^{1/(5-\beta)}, \tag{2.3}$$

with Γ_x the adiabatic index for the external environment, and Q_0 the (assumed) constant bulk kinetic power of the jet. Though the same expressions have been used in all the models considered, there are significant differences in their underlying assumptions, as given in the following sections.

2.3 Power Evolution

An ensemble of a number density, $n(\gamma)$, of relativistic electrons with Lorentz factor γ in a volume V with magnetic field B emits synchrotron power per unit frequency, per unit solid angle given by (KDA Equation 2)

$$P_\nu = \frac{\sigma_T c}{6\pi} \frac{B^2}{2\mu_0} \frac{\gamma^3}{\nu} n\,(\gamma)\, V \tag{2.4}$$

Table 2.1: Default Values of the Model Parameters [a]

Parameter	KDA	BRW	MK
β	1.9	1.5	1.5
a_0 (kpc)	2	10	10
ρ_0 (kg m^{-3})	7.2×10^{-22}	1.67×10^{-23}	1.7×10^{-23}
Γ_x	5/3	5/3	5/3
Γ_c	4/3	4/3	
Γ_B	4/3		
R_T	1.3		
γ_{min}	1	1	10
γ_{max}	∞	10^{14}	10^7
p	2.14	2.14	2.23
r_{hs} (kpc)		2.5	2.5
t_{bs} (yr)		10^5	
t_{bf} (yr)		1	
η			0.4
ϵ			1.0
τ			2×10^{-3}

[a] Values of the model parameters used by the respective authors Kaiser et al. (1997) or KDA, Blundell et al. (1999) or BRW, and Manolakou & Kirk (2002) or MK. See text for parameter definitions.

in units of W Hz^{-1} sr^{-1}, with σ_T the Thomson cross-section, c the velocity of light and μ_0 the permeability of free space. These relativistic electrons are assumed to be injected into the lobe from the hotspot and through the head.

2.4 The Kaiser, Dennett-Thorpe, & Alexander (1997), KDA Model

For the density profile of the external atmosphere this model uses $\rho_0 = 7.2 \times 10^{-22}$ kg m^{-3}, $a_0 = 2$ kpc and $\beta = 1.9$. These values are argued to be typical for an elliptical galaxy out to ~ 100 kpc from its center (Forman et al. 1985; Canizares et al. 1987).

The factor c_1 in $D(t)$ is given by (Equation 32 of Kaiser & Alexander 1997),

$$c_1 = \left[\frac{c_2}{c_3 \theta^2} \frac{(\Gamma_x + 1)(\Gamma_c - 1)(5-\beta)^3}{18\left[9\left\{\Gamma_c + (\Gamma_c - 1)\frac{c_2}{4\theta^2}\right\} - 4 - \beta\right]} \right]^{1/(5-\beta)}. \tag{2.5}$$

Here Γ_c is the particle adiabatic index in the cocoon (or lobe), c_2 (kinetic) and c_3 (geometrical) are constants discussed shortly, and θ is the opening angle of the jet (a small value). By Kaiser & Alexander (1997)'s Equations (37) and (38),

$$c_3 = \frac{\pi}{4R_T^2}, \tag{2.6}$$

$$\frac{p_h}{p_c} = \frac{c_2}{\theta^2} \simeq 4R_T^2, \tag{2.7}$$

so c_1 depends weakly on R_T, the axial ratio, defined as the ratio of the total length (hotspot to hotspot) of the radio galaxy to its total width (lobe diameter) halfway down the jet. For $R_T = 1.3$, the value adopted by the authors, and usually by us, $c_1 = 1.23$. Here p_h is the pressure in the head of the source (Equation 2.3) and p_c is the pressure in the cocoon, whose value is originally taken by KDA from Equation (2.7). We follow this prescription while considering the original models of KDA.

We are concerned with the total power emitted by the source (rather than its spectral details); therefore we follow the authors and make the standard approximation that electrons with Lorentz factor γ, are emitting only at their critical frequency $\nu = \gamma^2 \nu_L$, where

$$\nu_L = \frac{eB}{2\pi m_e}, \tag{2.8}$$

is the Larmor frequency (in Hz), e and m_e are electron charge and mass respectively, and B is the magnetic field in the dominant emitting region, which is the lobe. Hence the Lorentz factor of electrons radiating energy at frequency ν at time t can be formulated as

$$\gamma = \left(\frac{m_e}{eB} 2\pi\nu\right)^{1/2}. \tag{2.9}$$

The electrons are assumed to be accelerated initially in the hotspot at time t_i, with corresponding initial Lorentz factor γ_i. The energy distribution of the electrons injected into the lobe is a power law function of γ_i, with γ_{min} and γ_{max} the low- and high-energy cut-offs, respectively, and the energy index p (first mentioned in

Section 2.1) is taken to be constant so,

$$n(\gamma_i, t_i)d\gamma_i = n_0\gamma_i^{-p}d\gamma_i \quad (\gamma_{min} \leq \gamma_i \leq \gamma_{max}). \tag{2.10}$$

Here n_0 is a normalizing factor. The particle energies are expected to be distributed according to such a power-law function of the initial Lorentz factor if they are initially accelerated via a first-order Fermi mechanism at the Mach disk shock (e.g., Heavens & Drury 1988).

The electrons injected into the lobe undergo energy losses first via "adiabatic expansion", with the volume V expanding as $V \propto t^{a_1}$, with $a_1 = (4+\beta)\,/\,[\Gamma_c\,(5-\beta)]$ (following KDA). The radiative losses are IC scattering off the CMB photons and direct synchrotron losses. The magnetic field (assumed to be completely tangled) with energy density u_B and adiabatic index, $\Gamma_B = 4/3$, satisfies $u_B \propto B^2(t) \propto t^{-\Gamma_B a_1}$. The equivalent energy density of the CMB, u_{CMB}, is taken to be constant for an individual radio source as each source evolves for only a few times 10^8 years (negligible compared to the age of the universe) during which period u_{CMB} changes little as long as $z < 5$. These energy losses can be mathematically expressed in the following equation giving the rate of change of Lorentz factor,

$$\frac{d\gamma}{dt} = -\frac{a_1\gamma}{3t} - \frac{4\sigma_T}{3m_ec}\gamma^2\left(u_B + u_{CMB}\right), \tag{2.11}$$

where the first term on right-hand side gives the adiabatic losses and the second term the radiative losses.

Integration of Equation (2.11) from the injection time (t_i) to the emission time (t) expresses the injection Lorentz factor as (KDA Equation 10),

$$\gamma_i = \frac{\gamma t_i^{-a_1/3}}{t^{-a_1/3} - a_2\left(t, t_i\right)\gamma}, \tag{2.12}$$

where,

$$a_2\left(t, t_i\right) = \frac{4\sigma_T}{3m_ec}\left[\frac{u_B\left(t_i\right)}{a_3}t_i^{a_1\Gamma_B}\left(t^{a_3} - t_i^{a_3}\right) + \frac{u_{CMB}}{a_4}\left(t^{a_4} - t_i^{a_4}\right)\right], \tag{2.13}$$

with $a_3 = 1 - a_1\left(\Gamma_B + \frac{1}{3}\right)$, and $a_4 = 1 - \frac{a_1}{3}$. Also, the normalizing factor n_0 in

Equation (2.10) can be formulated as

$$n_0 = \frac{u_e\left(t_i\right)}{m_e c^2}\left(\frac{\gamma_{min}^{2-p}-\gamma_{max}^{2-p}}{p-2}-\frac{\gamma_{min}^{1-p}-\gamma_{max}^{1-p}}{p-1}\right)^{-1}, \tag{2.14}$$

where $u_e(t_i)$ is the energy density of relativistic electrons at time t_i. The electrons are assumed to be uniformly distributed over the volume V, which expands adiabatically, and so,

$$t^{a_1} n\left(\gamma, t\right) d\gamma = t_i^{a_1} n\left(\gamma_i, t_i\right) d\gamma_i. \tag{2.15}$$

Hence the energy distribution of the electrons injected from the hotspots at time t is obtained as (KDA Equation 9)

$$n(\gamma, t) d\gamma = n_0 \frac{\gamma_i^{2-p}}{\gamma^2}\left(\frac{t}{t_i}\right)^{-4a_1/3} d\gamma. \tag{2.16}$$

Apart from the electrons (and perhaps positrons) injected from the hotspot having energy density u_e (discussed in the previous paragraph), the cocoon pressure includes contributions from two other kinds of fluids. These are the magnetic "fluid" with energy density u_B and thermal particles with energy density u_T and adiabatic index, Γ_T. So the total cocoon pressure is

$$p_c = \left(\Gamma_c - 1\right)\left(u_e + u_B + u_T\right), \tag{2.17}$$

where the adiabatic index of the cocoon as a whole, Γ_c, depends on the relative pressures of each component. The ratio of the magnetic field energy u_B, to the sum of the particle energies $u_e + u_T$ is taken as (from minimum energy arguments, Burbidge 1956),

$$\mathcal{R} = \frac{u_B}{u_e + u_T} = \frac{1+p}{4}. \tag{2.18}$$

The contribution of thermal particles to the total emitted radio power is absolutely negligible as compared to the emissivity of the relativistic particles, although they may actually contribute substantially to the total energy. Nonetheless, here and in all the other models of radio lobe power evolution we consider $u_T = 0$, as is common in the majority of papers on RGs.

The KDA model does not distinguish between the head and the hotspot, and considers a self-similar expansion of the head, where the jet terminates. The cocoon

is split into many small volume elements, each of which is allowed to evolve by slowly expanding, whereby the pressure changes from the head pressure $p_h(t_i)$ to the cocoon pressure $p_c(t_i)$, and the particles undergo the various energy loss processes mentioned previously. The energy of each volume element in the lobe is equated to the energy it had while in the head, minus the work done by that volume in adiabatically expanding from the head to the lobe. The radio emission from such a volume element is calculated, using the expressions of cocoon pressure and the energy distribution function. The total emission at a frequency ν is then obtained by summing over the contributions from all such small elements in the lobe. The expression of P_ν is a complicated integration over injection time t_i (KDA Equation 16),

$$P_\nu = \int_0^t \frac{\sigma_T c r Q_0 n_0}{6\pi\nu\,(r+1)} \left(4R_T^2\right)^{(1-\Gamma_c)/\Gamma_c} \frac{\gamma^{3-p} t_i^{a_1/(3p-6)}}{\left[t^{-a_1/3} - a_2\,(t,t_i)\,\gamma\right]^{2-p}} \left(\frac{t}{t_i}\right)^{-a_1(1/3+\Gamma_B)} dt_i. \tag{2.19}$$

This integration being analytically intractable, we used numerical techniques to get P_ν.

Relativistic particles injected at sufficiently early times into the radio cocoon undergo severe energy losses (via the mechanisms discussed before) so that $\gamma_i \to \infty$ in Equation (2.12). Such particles can no longer contribute to the radiation emitted at frequency ν at time t. Therefore a minimum time, t_{min}, can be defined when the injected particles are still radiating at ν (mathematically, t_{min} is the time after which the denominator of Equation (2.12) becomes positive). Then the integration in Equation (2.19) is from t_{min} to t.

Most of the notation in the subsequent models is adopted from the KDA model.

2.5 The Blundell, Rawlings, & Willott (1999), BRW Model

The ambient gas density parameters adopted by BRW are $\rho_0 = 1.67 \times 10^{-23}$ kg m^{-3}, $a_0 = 10$ kpc and $\beta = 1.5$. These are based on the polarization measurements of the lobe synchrotron emission (Garrington & Conway 1991), and X-ray images of nearby massive ellipticals in groups (e.g., Sarazin 1988; Mulchaey & Zabludoff 1998). A value of $c_1 = 1.8$ is adopted for the factor governing the source size in Equation 2.2, as BRW found it to give the best fit when models and data were compared.

These authors explicitly utilize the hotspot, unlike KDA, and define it to be

an unique small region inside the larger head, distinguished by the extremely high magnetic field region within and just beyond the Mach disk shock. A very large fraction of the bulk kinetic energy from the jet is thermalized and particle acceleration occurs in the hotspot. In other words, the hotspot is the compact region (the "working surface" most likely moving around according to Scheuer's (1982) "dentist's drill model") within the whole head region. The hotspots are assumed to not grow as the source ages and are taken by BRW to have a constant radius, $r_{hs} = 2.5$ kpc. Considering the expansion of the head and its bow shock (also Begelman & Cioffi 1989), the environmental ram pressure is related to the average internal pressure in the head, $p_h(t)$, which is given by Equation (2.3). The pressure in the lobe or cocoon, $p_c(t)$, is taken by BRW to be a constant fraction (1/6) of the head pressure,

$$p_c(t) = \frac{p_h(t)}{6}. \tag{2.20}$$

The jet, of constant bulk power Q_0, terminates at the hotspot. The pressure in the hotspot, p_{hs}, is given by the stagnation pressure in the post-jet shock,

$$p_{hs} = \frac{Q_0}{cA_{hs}}. \tag{2.21}$$

Here A_{hs} $(= \pi r_{hs}^2)$ is the area normal to the jet over which the jet thrust operates. The hotspot magnetic field, assumed to be tangled, is given by (BRW Equation 11)

$$B_{hs}^2 = \frac{3\mu_0 Q_0}{cA_{hs}}, \tag{2.22}$$

where the equipartition assumption has been made. The break frequency for synchrotron radiation in the hotspot is (BRW Equation 12)

$$\nu_{bh} = \frac{9c_7 B_{hs}}{4\left(B_{hs}^2 + B_{CMB}^2\right)^2 t_s^2}, \tag{2.23}$$

where $c_7 = 1.12 \times 10^3$ nT^3 Myr^2 GHz (Leahy 1991), and the equivalent magnetic field due to the CMB is $B_{CMB} = 0.318(1+z)^2$ nT. The synchrotron age, t_s, of the electron population is determined by the duration of the stay of the particles in the hotspot (and hence the length of their exposure to the hotspot magnetic field), before they reach the lobe.

In Section 8.4.2 of Blundell et al. (1999) it is shown that this model basically follows the KDA prescription of lobe luminosity, but with two main differences. First, while the particles are injected from the hotspot to the lobe, the injection index is governed by the breaks in the energy distribution of particles (unlike the constant injection index of KDA). Second, the constant hotspot pressure (Equation 2.21) governs the adiabatic expansion losses out of the hotspot (for particles injected into the lobe), while in KDA the head pressure (Equation 2.3, which evolves with time) drove the adiabatic losses. In BRW the head pressure only drives the source expansion.

The particles stay in the hotspot for different amounts of time before being injected into the lobe, and hence have different break frequencies. A break in the synchrotron frequency spectrum (Equation 2.23) is adopted as arising from the break in the energy spectrum of particles injected from hotspot to lobe. The default value of the longest dwell time in the hotspot is taken as $t_{bs} = 10^5$ yr, which, when used in Equation (2.23), gives the slow break frequency, ν_{bs}. Similarly the fast break frequency, ν_{bf}, is obtained assuming the shortest dwell time to be $t_{bf} = 1$ yr. These break frequencies (ν_{bs} and ν_{bf}), can be translated to the corresponding Lorentz factors (γ_{bs} and γ_{bf}) of energy emission by the particles via

$$\gamma_{bl}\left[t_i\right] = \left(\frac{\nu_{bh}}{\nu_L}\right)^{1/2} \left(\frac{B_{hs}^2}{2\mu_0 u_B\left[t_i\right]}\right)^{-2/(3\Gamma_c)}, \tag{2.24}$$

with the nonrelativistic gyrofrequency, $\nu_L = eB\left[t_i\right]/\left(2\pi m_e\right)$, (first given in Equation 2.8) and u_B is again the energy density of magnetic field in the lobe.

Assuming particles are accelerated by the first-order Fermi process (e.g. Bell 1978) in the hotspot, the power law exponent of the energy distribution, p, (the slope of $\log n(\gamma)$ vs. $\log \gamma$) in the low-γ domain (with upper cut-off γ_{bs}) is taken as 2 (corresponding to frequency spectral index α of 0.5, as $p = 2\alpha + 1$). In the high-γ end (with lower cut-off γ_{bf}), assuming the hotspot to be injecting particles continuously into the lobe (Carilli et al. 1991), the exponent is taken as 3 (corresponding to α of 1). The shape of the spectrum between γ_{bs} and γ_{bf} is taken as a straight line (for simplicity; a curve is more realistic) with slope p. In mathematical terms, the energy

distribution follows the multiple power laws,

$$\begin{aligned} n(\gamma) &= n_b \left(\frac{\gamma}{\gamma_{bs}}\right)^{-2} \quad , \quad \gamma \leq \gamma_{bs} \\ &= n_b \left(\frac{\gamma}{\gamma_{bs}}\right)^{-p} \quad , \quad \gamma_{bs} < \gamma \leq \gamma_{bf} \\ &= f n_b \left(\frac{\gamma}{\gamma_{bf}}\right)^{-3} \quad , \quad \gamma > \gamma_{bf}, \end{aligned} \tag{2.25}$$

with, $f = (\gamma_{bs}/\gamma_{bf})^p$. The details of the energy distribution are shown in Figure 11 of Blundell et al. (1999). The normalization factor n_b is given by,

$$n_b\left[t_i\right] = \frac{u_e\left[t_i\right]}{m_e c^2}\left[\gamma_{bs}^2\left(\ln\frac{\gamma_{bs}}{\gamma_{min}}\right) + \frac{\gamma_{bs}^p}{p-2}\left(\frac{1}{\gamma_{bs}^{p-2}} - \frac{1}{\gamma_{bf}^{p-2}}\right) + f\gamma_{bf}^3\left(\frac{1}{\gamma_{bf}} - \frac{1}{\gamma_{max}}\right)\right]^{-1}. \tag{2.26}$$

Here $u_e\left[t_i\right]$ is the relativistic particle energy density in the cocoon at time t_i (with the same notation as the KDA model) and its formulation is adopted from Kaiser et al. (1997), as follows:

$$u_B\left(t_i\right) = \frac{\mathcal{R}\, p_c\left(t_i\right)}{\left(\Gamma_c - 1\right)\left(\mathcal{R}+1\right)}, \tag{2.27}$$

$$u_e\left(t_i\right) = \frac{u_B\left(t_i\right)}{\mathcal{R}}. \tag{2.28}$$

Our calculations usually are done assuming the minimum and maximum values of the particle Lorentz factors in the hotspot quoted by BRW: $\gamma_{min} = 1$ and $\gamma_{max} = 10^{14}$.

A population in the lobe which emits at a time t_{obs} (or t) (the cosmic epoch when it intercepts our light cone), consists of particles injected from the hotspot between a time t_{min} (those with the largest Lorentz factors) and t (smallest Lorentz factors). The time t_{min} (found following the prescription in KDA given in the last paragraph of Section 2.4) is the minimum time of injection (found for every t), when particles contribute to the radiation at t at same frequency. Any particles injected before t_{min} do not contribute to the radiation at t, due to the severe energy losses they have already suffered.

The time evolution of the slope of the energy distribution of particles between t_{min} and t, dictates the exact form of the energy distribution (Equation 2.25) applicable for that population. The Lorentz factors of particles injected at t_{min}, t, and at intermediate times can be related to the time evolution of γ_{bs} and γ_{bf} in six possible

ways, as shown in Figure 12 of Blundell et al. (1999). If the Lorentz factors of the injected electrons at all times are either less than γ_{bs}, or greater than γ_{bf}, or in between γ_{bs} and γ_{bf} (cases 1, 6, and 2, respectively, of Figure 12 of BRW) then there is only one domain to consider, with the energy distribution taken either from the top, bottom or middle γ region of Equation (2.25). If the evolution of the Lorentz factor at injection overlaps with two regions (cases 3 and 4 of Figure 12 of BRW), then two distinct domains of energy distribution (where the overlap occurred) must be considered. If the Lorentz factor change overlaps with all three parts of the spectrum (i.e., γ_i was greater than γ_{bf} to start with, came in between γ_{bf} and γ_{bs} at intermediate times, and finally was less then γ_{bs}, corresponding to case 5 of Figure 12 in BRW), then all possible γ domains of the energy distribution are involved.

The final expression for the power emitted (P_ν) by a radio source at a frequnecy ν is given by the complicated Equation (21) of BRW, reproduced below,

$$
\begin{aligned}
P_\nu\left[t\right] = {} & \frac{\sigma_T c}{6\pi\nu} Q_0^{1/\Gamma_c} \left(cA_{hs}\right)^{\frac{\Gamma_c-1}{\Gamma_c}} \times \\
& \left[\int_{t_{\gamma bs}}^{t} \frac{u_B\left[t_i\right]}{p_c^{1/\Gamma_c}} \gamma_i^3\left[t_i\right] n_b \left(\frac{\gamma_i\left[t_i\right]}{\gamma_{bs}} \right)^{-2} \left(\frac{t}{t_i} \right)^{-a_1\left(\Gamma_c+\frac{1}{3}\right)} dt_i + \right. \\
& \int_{t_{\gamma bf}}^{t_{\gamma bs}} \frac{u_B\left[t_i\right]}{p_c^{1/\Gamma_c}} \gamma_i^3\left[t_i\right] n_b \left(\frac{\gamma_i\left[t_i\right]}{\gamma_{bs}} \right)^{-p} \left(\frac{t}{t_i} \right)^{-a_1\left(\Gamma_c+\frac{1}{3}\right)} dt_i + \\
& \left. \int_{t_{min}}^{t_{\gamma bf}} \frac{u_B\left[t_i\right]}{p_c^{1/\Gamma_c}} \gamma_i^3\left[t_i\right] f n_b \left(\frac{\gamma_i\left[t_i\right]}{\gamma_{bf}} \right)^{-3} \left(\frac{t}{t_i} \right)^{-a_1\left(\Gamma_c+\frac{1}{3}\right)} dt_i \right] . \qquad (2.29)
\end{aligned}
$$

Here $\gamma_i\left[t_i\right]$ is same as in KDA model, Equation (2.12). We independently solved this equation numerically.

2.6 The Manolakou & Kirk (2002), MK Model

The Manolakou & Kirk (2002) paper employs the same external density profile and source linear size expansion as does BRW.

The MK model essentially follows the common prescriptions of KDA (and BRW) for lobe luminosity evolution, with the key difference involving the particle transport mechanism. Two cases are considered for the propagation of particles from the termination shock through the hotspot and into the cocoon. In MK's Case A, the whole adiabatic loss between the hotspot and lobe (due to the pressure difference) is

computed. However, the authors found that this produced [P–D] tracks (discussed in Section 4.1) which conflicted with the observational data. So they considered a Case B, which involves some re-acceleration process (which is unspecified in detail in their paper) in the turbulent head region, whereby the adiabatic losses are partially compensated; MK found such a model is a qualitatively better fit to the data. Thus we consider only the case B (with re-acceleration) of the MK model in this thesis work.

Following the previous two models, MK assumes that electrons are accelerated by the first-order Fermi mechanism at the jet termination shock and are injected into the plasma behind the shock following a power-law energy distribution with a constant injection index p

$$\begin{aligned} Q_s(\gamma) &= q_0\gamma^{-p} \quad , \quad \gamma_{min} \leq \gamma \leq \gamma_{max} \\ &= 0 \qquad\quad , \quad \text{otherwise.} \end{aligned} \tag{2.30}$$

Assuming that a fraction η of the jet power Q_0 is transferred into the accelerated particles at the termination shock, this gives (MK Equation 8)

$$q_0 = \frac{\eta Q_0}{m_e c^2}(p-2)\left(\gamma_{min}^{2-p} - \gamma_{max}^{2-p}\right)^{-1}. \tag{2.31}$$

If the bulk Lorentz factor of the jet is modest, $\gamma_{jet} \sim 10$, then $2 < p < 2.3$ (Kirk et al. 2000; Achterberg et al. 2001). The upper and lower limits of particle Lorentz factors γ_{min} and γ_{max} are not obvious from theory. The MK model adopts $\gamma_{min} = \gamma_{jet}$, the constant bulk Lorentz factor of the jet. The authors say the results are not sensitive to γ_{max}; however, our different conclusions on this question are given in Chapters 4 and 8.

The magnetic energy density of the particles in the lobe u_{lobe} (denoted by u_c in the previous two models) is given by,

$$u_{lobe}(t) = u_{hs}\left(\frac{t}{t_0}\right)^{-a}. \tag{2.32}$$

Here $a = (4+\beta)/(5-\beta)$, and t_0 is the time when the size of the head was comparable

to the hotspot size, (MK Equation 6)

$$t_0 = \left[\frac{3c_1^{2-\beta} c A_{hs}}{(\Gamma_x + 1)(5-\beta)^2}\right]^{1/a} \left(\frac{\rho_0 a_0^{\beta}}{Q_0}\right)^{3/(4+\beta)} . \tag{2.33}$$

The lobe pressure $p_{lobe}(t) = p_h(t)/6$, where the head pressure $p_h(t)$ given by Equation (2.3). Mathematically, t_0 is the time when $p_{lobe}(t)$ equals the hotspot pressure p_{hs} given by Equation (2.21).

After being dumped in the primary hotspot by the jet, the electrons encounter turbulent motions of the plasma in transit through the head and finally reach the lobe. In this transition through the head the electrons are subject to synchrotron losses (in the strong magnetic field behind the termination shock) and IC losses off the CMBR. The effects of the losses depend on the distribution of the "escape times", i.e., the probability distribution of how many particles escape after a certain time interval. A generalized transport process is considered, with ϵ (denoted as α in Manolakou & Kirk (2002)) being the transport parameter (or the diffusion index). The mean square distance travelled by a particle $\langle \Delta r^2 \rangle \propto t^{\epsilon}$, with $0 < \epsilon < 2$. In the standard diffusive case, $\epsilon = 1$, with sub- (supra-) diffusive cases being $\epsilon < 1$ (> 1).

The energy loss rate during transport of an electron (with energy $\gamma(t) m_e c^2$) is given by

$$\frac{d\gamma}{dt} = -\frac{4\sigma_T}{3 m_e c}\left(u_{hs} + u_{CMB}\right)\gamma^2. \tag{2.34}$$

Here $u_{hs} = B_{hs}^2/(2\mu_0)$ is the magnetic energy density in the hotspot, $u_{CMB} = B_{CMB}^2/(2\mu_0)$ is the equivalent magnetic energy density of CMB, and B_{hs} and B_{CMB} are of same form as in the BRW model.

The expression for the total number of particles in a sphere of radius R (in the head), $N_R(\gamma)$, is given in Equations (13) and (15) of Manolakou & Kirk (2002); $N_R(\gamma)$ also satisfies the kinetic Equation (16) of Manolakou & Kirk (2002). The steady state solution of this for $Q_h(\gamma)$, the rate at which particles leave the sphere of radius R and enter the lobe, is given as

$$Q_h(\gamma) = q_0 \gamma^{-p} M(\hat{\gamma}, \rho_d, p, \tau) . \tag{2.35}$$

Here $M(\hat{\gamma}, \rho_d, p, \tau)$ is a modulation function which embodies the effects of cooling on

the incident distribution $Q_s(\gamma)$, and is given by (MK Equations 18 and 19).

$$\begin{aligned} M\left(\hat{\gamma},\rho_d,p,\tau\right) &= 0 \quad , \quad \hat{\gamma} > 1/\rho_d \\ &= \int_{x_1}^{\infty} \Theta_M\left(x\right) dx \ , \quad 1 < \hat{\gamma} < 1/\rho_d \\ &= \int_{x_1}^{x_2} \Theta_M\left(x\right) dx \ , \quad \hat{\gamma} < 1 \end{aligned} \tag{2.36}$$

where,

$$\begin{aligned} \Theta_M\left(x\right) &= \frac{2}{\sqrt{\pi}}\sqrt{x}e^{-x}\left[1-\frac{\tau\hat{\gamma}}{x^{(2-\epsilon)/\epsilon}}\right]^{p-2} , \\ x_1 &= \left[\frac{\hat{\gamma}\tau}{1-\rho_d\hat{\gamma}}\right]^{\epsilon/(2-\epsilon)} , \quad \text{and} \\ x_2 &= \left[\frac{\hat{\gamma}\tau}{1-\hat{\gamma}}\right]^{\epsilon/(2-\epsilon)} . \end{aligned} \tag{2.37}$$

The new notations introduced here are the normalized Lorentz factor, $\hat{\gamma} = \gamma/\gamma_{min}$, the reciprocal of the dynamic range of incident energy distribution, $\rho_d = \gamma_{min}/\gamma_{max}$, and a new parameter describing the ratio of the transport time and cooling time of a particle at γ_{min}, $\tau = t_{diff}/t_{cool}$. The default values of various parameters used by the authors for case B (with re-acceleration) are $\tau = 2\times10^{-3}, \gamma_{min} = 10, \gamma_{max} = 10^7, p = 2.23, \eta = 0.4$ (Table 2.1). While studying the original MK model, we did not vary the values of η since it is a characteristic for MK model case B, and we also held τ fixed, as according to MK the results are insensitive to its value as long as $\tau \ll 1$.

The adiabatic expansion of the volume brings a reduction in each particle's energy by a factor given by the ratio of the pressures before and after the expansion (Scheuer & Williams 1968). For the expansion while transporting particles from hotspot to lobe, the Lorentz factor of particles transform as $\gamma_{lobe} = \left(u_{lobe}/u_{hs}\right)^{1/4}\gamma_{hs}$. From particle number conservation (and assuming a constant injection index at the termination shock), the injection of particles into the lobe from the hotspot can be expressed by the function

$$Q_{lobe}\left(\gamma,t\right) = kQ_h\left(k\gamma,t\right) \quad , \quad k\left(t\right) = \left[\frac{u_{hs}}{u_{lobe}(t)}\right]^{1/4} . \tag{2.38}$$

During the transport of particles from hotspot to lobes, the details of re-acceleration by various processes have been considered by many previous authors (e.g. Spruit

1988; Begelman & Kirk 1990; Anastasiadis & Vlahos 1993; Manolakou et al. 1999; Marcowith & Kirk 1999; Gieseler & Jones 2000). Here MK simply assume that in the presence of reacceleration, the distribution of electrons entering the lobe is described by a power law above a lower cut-off energy, and at higher energies the distribution is modified by synchrotron and IC losses. This can be implemented by modifying the parameter $k(t)$ in Equation (2.38), which describes the effectiveness of adiabatic losses. If there is re-acceleration (case B, as we assume here), then $k(t) \equiv 1$ is used in Equation (2.38).

Once the electrons have reached the lobe, they undergo adiabatic, IC and synchrotron losses, similarly to the other models, and their energy evolution is given by

$$\frac{d\gamma}{dt} = -b\frac{\gamma}{t} - b_{ic}\gamma^2 - b_s\frac{\gamma^2}{t^a}. \tag{2.39}$$

The first term on right hand side of Equation (2.39) corresponds to adiabatic losses, with $b = a/4$. The second term represents inverse Compton scattering loss, with $b_{ic} = (4/3)(\sigma_T/m_e c)u_{CMB}$, which is constant with time. The last term is the synchrotron loss, with $b_s = (4/3)(\sigma_T/m_e c)u_{hs}t_0^a$.

The authors have used the method of characteristics and introduced a parameter χ, describing the evolution of individual particles as (MK Equation 23),

$$\chi(\gamma, t) = \frac{1}{t^b}\left(\frac{1}{\gamma} - \frac{b_{ic}t}{1-b} - \frac{b_s t^{1-a}}{1-b-a}\right). \tag{2.40}$$

The kinetic partial differential equation for the spatially integrated distribution $N(\gamma, t)$ of particles in the lobe is transformed, in order to compute the derivative of N along these family of curves $\chi(\gamma, t)$, so that $N(\chi, t)$ satisfies the ordinary differential equation,

$$\frac{dN}{dt} - \left[\frac{b}{t} + 2\gamma\left(b_{ic} + b_s t^{-a}\right)\right] N = Q_{lobe}(\gamma, t). \tag{2.41}$$

Here γ is an implicit function of χ and t according to Equation (2.40), and Q_{lobe} is given by Equation (2.38).

In a way analogous to that in the KDA model, for every time t of radio power emission, when radiating particles have Lorentz factor γ, there is an earliest time, $t_i(\gamma, t)$, at which particles injected into the lobe contribute to the radiation at t. We integrate Equation (2.41) numerically between the lower limit t_i, and the upper limit t, using the initial condition $N(\chi, t_i) = 0$.

The injection time, t_i, lies in the range $t_{start} < t_i < t$ if $\gamma_i > \gamma_{max}/k(t_{start})$, and $t_i = t_{start}$ if $\gamma_i < \gamma_{max}/k(t_{start})$, according to the following detailed prescription. If particles injected into the lobe at (some fiducial) time t_{start} with $\gamma_i < \gamma_{max}/k(t_{start})$ can cool to γ at time t, i.e., when

$$\frac{1}{\gamma_i} = t_{start}\left(\frac{b_{ic}}{1-b} + \frac{b_s t_{start}^{-a}}{1-b-a}\right) + t_{start}^{b}\chi\left(\gamma, t\right) < \frac{k\left(t_{start}\right)}{\gamma_{max}}, \tag{2.42}$$

then $t_i = t_{start}$ is set. On the other hand, if $\gamma_i > \gamma_{max}/k(t_{start})$, then t_i is found by iteratively solving the following equation:

$$\frac{k\left(t\right)}{\gamma_{max}} = t_i\left(\frac{b_{ic}}{1-b} + \frac{b_s t_i^{-a}}{1-b-a}\right) + t_i^{b}\chi\left(\gamma, t\right). \tag{2.43}$$

The specific power emitted at a frequency ν, $P_\nu(t)$ (power per unit frequency) is finally obtained by integrating the product of $N(\gamma, t)$ and the emissivity of a single electron,

$$P_\nu\left(t\right) = \frac{1}{4\pi}\int_1^\infty a_0 \frac{\gamma^3}{\nu} B_{lobe}^2\left(t\right)\delta\left(\nu - a_1 B_{lobe}\left(t\right)\gamma^2\right) N\left(\gamma, t\right) d\gamma. \tag{2.44}$$

This is MK Equation (27), except that its right-hand-side has been multiplied by a correction factor of (γ/ν). Here $B_{lobe}\left(t\right) = \left(2\mu_0 u_{lobe}\right)^{1/2}$, is the magnetic field in the lobe at time t, and the constants determining the radio lobe specific power found from a delta-function approximation of the frequency, $a_0 = 1.6 \times 10^{-14}$ W T^{-2} and $a_1 = 1.3 \times 10^{10}$ Hz T^{-1}, are adopted from MK.

We now demonstrate that P_ν is independent of an assumed constant hotspot size in the MK model. The authors specified $r_{hs} = 2.5$ kpc as the hotspot radius, following BRW. However, we find that the MK model is actually independent of the hotspot area A_{hs}. From

$$u_{hs} = \frac{3Q_0}{2cA_{hs}}, \tag{2.45}$$

which is Equation (2) in Manolakou & Kirk (2002), we have the proportionality

$$u_{hs} \propto 1/A_{hs}. \tag{2.46}$$

From their Equation (6) (our Equation 2.33),

$$t_0 \propto A_{hs}^{1/a}. \tag{2.47}$$

Now both

$$u_{lobe} \ , \text{ and } b_s \propto u_{hs} t_0^a \propto \frac{1}{A_{hs}} \left(A_{hs}^{1/a} \right)^a \propto A_{hs}^0, \tag{2.48}$$

from MK Equation (5), our Equation (2.32), for u_{lobe}, and from MK Equation (22), our Equation (2.39), for b_s. Thus these quantities, and everything else (at least all the analytic variables which have been defined in terms of A_{hs}, t, etc. and are used to calculate the lobe power in MK), including P_ν itself, are independent of A_{hs} in the Manolakou & Kirk (2002) model.

– 3 –

Multi-dimensional Monte Carlo Simulations and Observational Samples

3.1 Initial Population Generation

We follow the prescription given in detail in BRW to generate the initial radio source population. Here we summarize the initial distributions of source ages, redshifts and beam powers; these produce the redshift, beam power and the age at which each model RG will be intercepted by our light cone. This summary and update of the BRW prescription is necessary to define the parameters that go into the models.

One key difference from BRW is that we assume a consensus cosmology, i.e., a spatially flat universe with the present value of the Hubble constant $H_0 = 71$ km s^{-1} Mpc^{-1}, matter density parameter $\Omega_M = 0.3$, and vacuum energy density parameter $\Omega_\Lambda = 0.7$ (from WMAP results, Spergel et al. 2003). The cosmological equations are taken from Carroll, Press, & Turner (1992) and Peacock (1999).

3.1.1 Birth Time

From some initial high redshift, z_{start}, well above the peak of the RLF, sources are assumed to be born at an interval ΔT_{start} which is short compared to their lifetimes. The redshifts are translated to cosmic times (epochs) and vice versa according to the cosmology assumed (Eq. 5.4 of Weinberg 1989). In particular, the present age of an object that formed at a redshift z is given by,

$$t(z) = \frac{2}{3H_0}\left[1+\frac{\Omega_M}{\Omega_\Lambda}\right]^{1/2}\left[\sinh^{-1}\left(\frac{\Omega_\Lambda}{\Omega_M}\right)^{1/2} - \sinh^{-1}\left\{\left(\frac{\Omega_\Lambda}{\Omega_M}\right)^{1/2}(1+z)^{-3/2}\right\}\right]. \tag{3.1}$$

We use $z_{start} = 10$ and take $\Delta T_{start} = 10^6$ years, but the results should be insensitive to values of $z_{start} > 6$ and $\Delta T_{start} < 10^7$ years.

After a source is born at a redshift z_{birth}, its active lifetime is denoted as T_{MaxAge}. A default value of $T_{MaxAge} = 5 \times 10^8$ years is taken. This value is used by BRW, and more recent investigations involving X-ray activity in AGN (Barger et al. 2001), SDSS

optical studies of active galaxies (Miller et al. 2003) and black hole demographics arguments (e.g., Marconi et al. 2004) all support an AGN activity lifetime of over 10^8 yr (also, McLure & Dunlop 2004). In order to observe a radio galaxy when its nucleus is still actively feeding its jet, it must be intercepted by our light cone at some epoch between the cosmic time of its birth and the time when its beam is switched off, i.e., within an interval of T_{MaxAge} after its birth. For this interception to occur the source must lie inside a certain cosmic volume shell, the "Relevant Comoving Volume Element" (BRW).

The "Relevant Comoving Volume Element" at a particular redshift z_{birth}, is the volume of space-time where a source (born at z_{birth}) should lie for it to be intercepted by our light cone within a maximum age of T_{MaxAge}. This volume element can be estimated from the following cosmological considerations. A RG observed at its birth redshift z_{birth} lies at a cosmic distance along our light cone corresponding to that redshift. If we observe it (i.e., the source intercepts our light cone) at a time T_{MaxAge} after z_{birth}, then it lies at a smaller distance along our light cone to this later redshift (corresponding to the epoch $t(z_{birth})+T_{MaxAge}$). Together these define a cosmic radial shell at epoch z_{birth}, whose radii are the maximum and minimum distances within which a source (born at z_{birth} and with a lifetime T_{MaxAge}) must lie so that we may observe it today (i.e., so that it intercepts our light cone). The volume of this shell is the Relevant Comoving Volume.

For a spatially flat, zero curvature ($k = 0$) universe, if r is the radial comoving coordinate, the "Relevant Comoving Volume Element", V_C, can be expressed as

$$V_C = \frac{4\pi}{3} R^3(t) \left(r_2^3 - r_1^3\right), \tag{3.2}$$

where $R(t)$ is the scale factor of the universe at cosmic time t and is given later via Equation (3.14). Here the cosmic time is denoted such that $t = 0$ at the Big Bang, and at present t is the current age of the Universe.

The geodesic of a light ray traveling radially from some cosmological distance, and reaching us now, is

$$r = c \int_{t_0}^{t_{now}} \frac{dt}{R(t)}, \tag{3.3}$$

where t_0 is the cosmic time when the light started traveling and t_{now} is the present epoch, and r gives the comoving cosmic distance traveled by light. The photons we

are interested in travel from within the comoving volume shell to reach us at t_{now}. Hence the outer (r_2) and inner (r_1) radial coordinates of the volume shell at z_{birth} (or t_{birth}, the cosmic birth time for a population of sources) are respectively given by

$$r_2 = c \int_{t_{birth}}^{t_{now}} \frac{dt}{R(t)} \quad , \qquad r_1 = c \int_{t_{birth}+T_{MaxAge}}^{t_{now}} \frac{dt}{R(t)} \quad . \tag{3.4}$$

Due to the expansion of the universe, the value V_C in Equation (3.2) is the relevant volume at the epoch z_{birth} (or t_{birth}). The corresponding proper volume at the present epoch is

$$V_C(z=0) = (1+z_{birth})^3 \; V_C(z_{birth}). \tag{3.5}$$

3.1.2 Redshift Distribution

The sources are assumed to be distributed in redshift according to a gaussian RLF with

$$\rho(z) \propto \exp\left[-\frac{1}{2}\left(\frac{z-z_0}{\sigma_z}\right)^2\right], \tag{3.6}$$

a distribution that peaks at z_0 and has standard deviation of σ_z. According to the RLF of Willott et al. (2001), $z_0 = 2.2$, $\sigma_z = 0.6$, and we use these values in our simulations. Grimes et al. (2004) have given a more recent computation of the RLF where the values are $z_0 = 1.7, \sigma_z = 0.45$ (for details see their Table 5). We have briefly explored the Grimes et al. (2004) RLF and some results are given in Section 6.2.

This function, $\rho(z)$, parameterizes the number of sources born at some cosmic time (t), per unit cosmic time, per unit comoving volume element at redshift zero, through the relation $\rho(t)dt = \rho(z)dz$. For a homogeneous and isotropic universe, this relation is valid at all epochs and throughout the space. At a particular redshift z_{birth}, the comoving volume (V_C) is found from Equations (3.2) and (3.4), which is then converted to the volume at present epoch using Equation (3.5). Then, multiplying $V_C(z=0)$ by $\rho(z_{birth})$ gives the number of sources born at z_{birth} (per solid angle born in the chosen interval in cosmic time) which are intercepted by our light cone:

$$N_{born} \propto V_C(z=0) \; \rho(z_{birth}). \tag{3.7}$$

The total number, N_{born}, is obtained by using a normalization factor (Section 7.3.2) in the above proportionality which takes into account the sky area of the observed

data sample.

3.1.3 Source Age Distribution

From the homogeneity of the universe, the sources are taken to be randomly distributed within the comoving volume shell. The age of a source, T_{age}, is the time after t_{birth} it is intercepted by our light cone. Following BRW, in our computations T_{age} is drawn randomly from 0 to T_{MaxAge}, but weighted so that sources are distributed uniformly in volume within the relevant comoving volume shell. Each source's radial coordinate (r) is then derived by inverting the equation for comoving volume. After getting the radial coordinate (r) for a source, the cosmic time when we observe it (T_{obs}) can be found (iteratively) from

$$r = c \int_{T_{obs}}^{t_{now}} \frac{dt}{R(t)} \quad . \tag{3.8}$$

Hence the age of a source (or the time for which it will evolve) is $T_{age} = T_{obs} - t_{birth}$.

In each simulation (run) we have generated a very large number of sources, typically a few 10^6 to somewhat over 10^7, over a very wide range of cosmic time ($z \leq 10$). We find the number of sources born at some z_{birth} which will intercept our light cone, the age T_{age} (denoted by t henceforth in the thesis) of each source, and the redshift at which we observe it (z_{obs} actually, but for simplicity, denoted by z henceforth). The observed redshift, or z, is derived from T_{obs}, the cosmic time at which the light we see was emitted from the source by inverting Equation (3.1).

3.1.4 Jet Power Distribution

As very powerful sources are much rarer than weaker ones, each of the sources generated is assigned a jet power Q_0 (which is assumed to remain constant throughout its age) according to the probability distribution,

$$\begin{aligned} p(Q_0)dQ_0 &\propto Q_0^{-x}\, dQ_0 \quad && \text{if } Q_{min} < Q_0 < Q_{max}, \\ &= 0 && \text{if } Q_0 > Q_{max} \text{ or } Q_0 < Q_{min}. \end{aligned} \tag{3.9}$$

Here the power index x is positive, and we initially adopted the values used by BRW: $x = 2.6, Q_{min} = 5 \times 10^{37}$ W, and $Q_{max} = 5 \times 10^{42}$ W. Our best fit values of x are higher and are discussed in Section 4.4.

An initial Monte Carlo population generation is completed when t (the age), z (the redshift at which it is observed) and Q_0 (the beam or jet power) are randomly assigned to each source of the population according to the above prescriptions. Each source in that population is then allowed to evolve according to a model described in Chapter 2, so as to derive the observable quantities other than z: P, D and α. The details of the simulation procedures are described in Section 3.3.

3.2 Observational Samples

3.2.1 Selection Criteria

These models predict the emission from the radio lobes, which are taken to (and usually do) dominate the emission from extended FR II RGs. As is well known and is discussed in detail in BRW, at relatively low frequencies ($\sim$ 151 MHz) the radio flux observed is predominantly the emission from the cocoon or the lobe (with negligible contribution from the hotspots, jets or nucleus), and so these evolutionary models should fit the data best at such frequencies. At GHz frequencies, substantial contributions from Doppler boosted core or jet emission would often be present, especially for old quasars, but the slowly advancing lobes will still emit nearly isotropically. In addition, at these higher frequencies the effects of synchrotron, adiabatic and IC losses are more severe. At very low frequencies ($<$ 100 MHz), there are extra complications affecting the emission from synchrotron self-absorption, free-free absorption, and the poorly known low energy cut-off to the relativistic synchrotron emitting particles. Therefore samples such as those produced by the Cambridge group over the past decades, which were observed at between 151 and 178 MHz, some of which cover much of the northern sky, are most appropriate for this work.

We adopt observational samples from complete radio surveys (Table 3.1), each of which contains all the radio sources within each survey's flux limits but which are found inside smaller sky areas for deeper surveys. Redshifts have been obtained for the great majority of these radio sources. Selecting the sources from different flux limited surveys bring in a P–z correlation, as the flux decreases with a source's redshift. To decouple this P–z correlation one must use multiple complete samples at increasingly fainter flux limits.

3.2.2 Observed Characteristics

For an individual source in each survey, the following characteristics were considered:

- its redshift (z),
- the specific power at 151 MHz (P_{151} or P for simplicity) in W Hz^{-1} sr^{-1}, emitted in the rest frame of the source,
- the projected linear size (D in kpc) as observed,
- the spectral index at 151 MHz (α_{151} or α) in the rest frame of the source.

The redshifts in the samples are spectroscopically determined for the vast majority of the sources. For the 3CRR catalog the redshift completeness is 100%, for 6CE it is 98% and it is $\approx$ 92% for 7CRS. The 6CE and 7CRS catalogs consist of sources with the observed flux densities (in Jy) taken at 151 MHz; details and references are in Section 3.2.3. The rest frame spectral indices (α) were directly adopted from the values given in the literature. Using the source's redshifts (i.e., their distances from us), the observed flux densities were converted to P_{151}, and the angular sizes were converted to projected linear source sizes (D), as discussed below.

The sample flux densities, $S_\nu(\nu_0)$ in Jy, observed at frequency $\nu_0 = 151$ MHz, were converted to the specific power emitted at $([1+z]\nu_0)$, $P_\nu([1+z]\nu_0)$ in W Hz^{-1} sr^{-1}, using Equation (3.87) of Peacock (1999),

$$P_\nu([1+z]\nu_0) = S_\nu(\nu_0)\,(R_0 r)^2\,(1+z), \tag{3.10}$$

where R_0 is the current scale factor of the Universe, r is the comoving coordinate, and $(R_0 r)$ is the distance to the source at the present epoch, mathematically formulated by integrating Equation (3.14) below. These were then converted to the specific power emitted at rest frame ν_0 ($P_\nu(\nu_0)$ or $P_{151} \equiv P$) using the respective source rest frame spectral indices α,

$$P = P_\nu(\nu_0) = P_\nu([1+z]\nu_0)\;(1+z)^\alpha. \tag{3.11}$$

The observational angular sizes (θ) (accepted from the literature) were converted to the projected linear sizes, D_{proj} or D as following,

$$D = D_{proj} = \theta(\text{radians})\;D_A, \tag{3.12}$$

where D_A is the angular diameter distance, which for a flat universe can be written as (Peacock 1999, Equations 3.76, 3.91),

$$D_A = \frac{R_0 r}{(1+z)}, \tag{3.13}$$

where

$$R_0 dr = \frac{c}{H_0}\left[(1-\Omega)(1+z)^2 + \Omega_\Lambda + \Omega_M (1+z)^3 + \Omega_r (1+z)^4\right]^{-1/2} dz. \tag{3.14}$$

Here the cosmological parameters are assumed to have consensus values (as mentioned in Section 3.1) for a standard flat universe: Hubble constant, $H_0 = 71$ km s^{-1} Mpc^{-1}, matter density parameter, $\Omega_M = 0.3$, vacuum density or dark energy parameter, $\Omega_\Lambda = 0.7$, radiation density parameter, $\Omega_r = 0$, and the total density parameter of the universe, $\Omega = \Omega_M + \Omega_\Lambda + \Omega_r = 1$, which is equivalent to a flat geometry.

3.2.3 Sample Details

Brief details of the surveys (flux limits, number of sources, sky areas covered) are given in Table 3.1. Henceforth, for brevity, 3C, 6C, and 7C refer to the refined surveys 3CRR, 6CE and 7CRS, respectively, as described below. We excluded the FR I RGs from the following catalogs and considered only FR II sources (including quasars, weak quasars, high-excitation FR II RGs and low-excitation FR II RGs. The [P–D–z–α] planes for the observational samples 3C, 6C and 7C are given in Figure 3.1.

3.2.3.1 3CRR:

This is the Third Cambridge Revised Revised sample of extragalactic radio sources (Laing, Riley, & Longair 1983). We adopted the data (including only the FR II sources) from the online compilation of the list by Willott[1]. In 3CRR the observations were done at a frequency of 178 MHz, so for each 3CRR source P_{178} (specific power at 178 MHz) was obtained and then converted to P_{151} using a standard average spectral index of 0.8. Given the closeness of these two frequencies, any reasonable variations in α would make for only small differences in the derived P_{151} values.

[1] http://www-astro.physics.ox.ac.uk/∼cjw/3crr/3crr.html

Table 3.1: Observational samples [a]

Survey	Flux Limit (Jy)	No. of Sources [a]	Sky Area (sr)
3CRR	$S^b_{178} > 10.9$ $S_{151} > 12.4$	145	4.23
6CE	$2 \leq S_{151} \leq 3.93$	56	0.102
7CRS	$S_{151} > 0.5$	126	0.022
7C-I	$S_{151} \geq 0.51$	37	0.0061
7C-II	$S_{151} \geq 0.48$	37	0.0069
7C-III	$S_{151} > 0.5$	52	0.009

[a] Only FR II RGs considered.

[b] Flux at 178 MHz, the frequency at which the 3CRR survey was performed. S_{178} for these sources were converted to flux at 151 MHz, S_{151}, using a constant spectral index of 0.8.

3.2.3.2 6CE:

The Sixth Cambridge radio survey by Eales (1985) is the original 6C survey. We adopt the sample from the reselected and updated version in Rawlings, Eales, & Lacy (2001), along with the most recent redshifts, which have been updated online by Rawlings[2].

3.2.3.3 7CRS:

The Seventh Cambridge Redshift Survey is a combination of parts I, II and III of the original 7C survey (McGilchrist et al. 1990). For 7C-I and II we adopt P_{151} and z from Willott et al. (2003) (their Tables 2 and 3), which uses the present consensus cosmology. The values of D (the projected linear size data) were obtained from a web-site maintained by Steve Rawlings[3]. However, the α_{151} values for 7C-I and II are not available in a collated form in the literature, and only a few individual sources have these values published. Thus we used α_{151} for 7C-III only. For 7C-III, the key observed and reduced data, including redshift, flux density in Jy, angular size in

[2]http://www-astro.physics.ox.ac.uk/∼sr/6ce.html

[3]http://www-astro.physics.ox.ac.uk/∼sr/grimestable.ascii

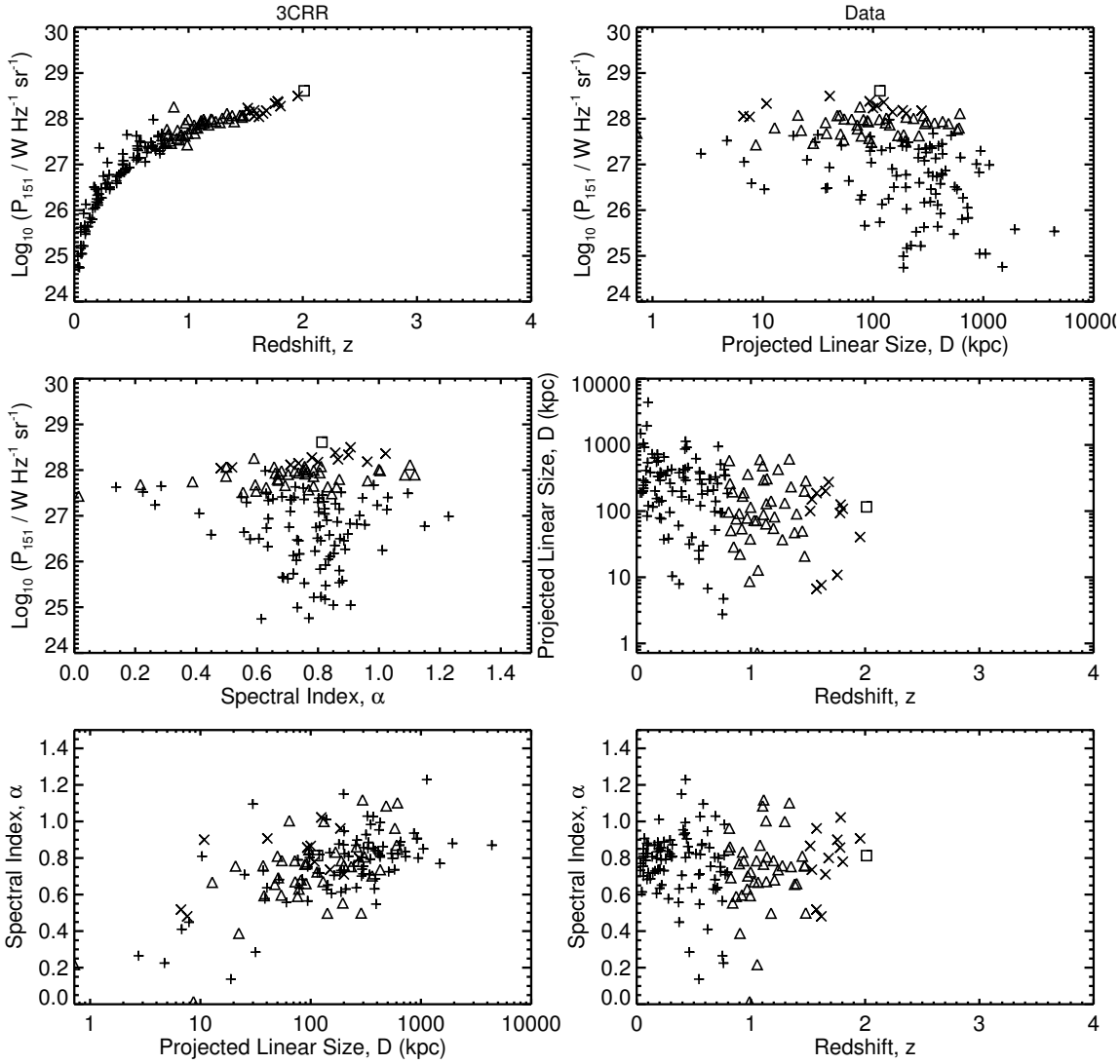

Figure 3.1a: The $[P$–D–z–$\alpha]$ planes for the observational 3CRR sample. In all the panels of this figure and all subsequent $[P$–D–z–$\alpha]$ slice figures the symbols distinguish the sources in different redshift bands as, *plus*: $z < 0.8$, *triangle*: $0.8 \leq z < 1.5$, *cross*: $1.5 \leq z < 2.0$, *square*: $z \geq 2.0$.

arcsec and spectral index between 38 and 151 MHz were kindly provided to us by Chris Willott; from these we computed the relevant observational parameters in the cosmology we use. The observed spectral index between 38 and 151 MHz was taken as the rest-frame 151 MHz spectral index (a fairly good estimate, at least for the higher z sources). The relevant sample can also be found in Lacy et al. (1999) (their Table 9, containing both the 7C-III and NEC samples); or online from the website of

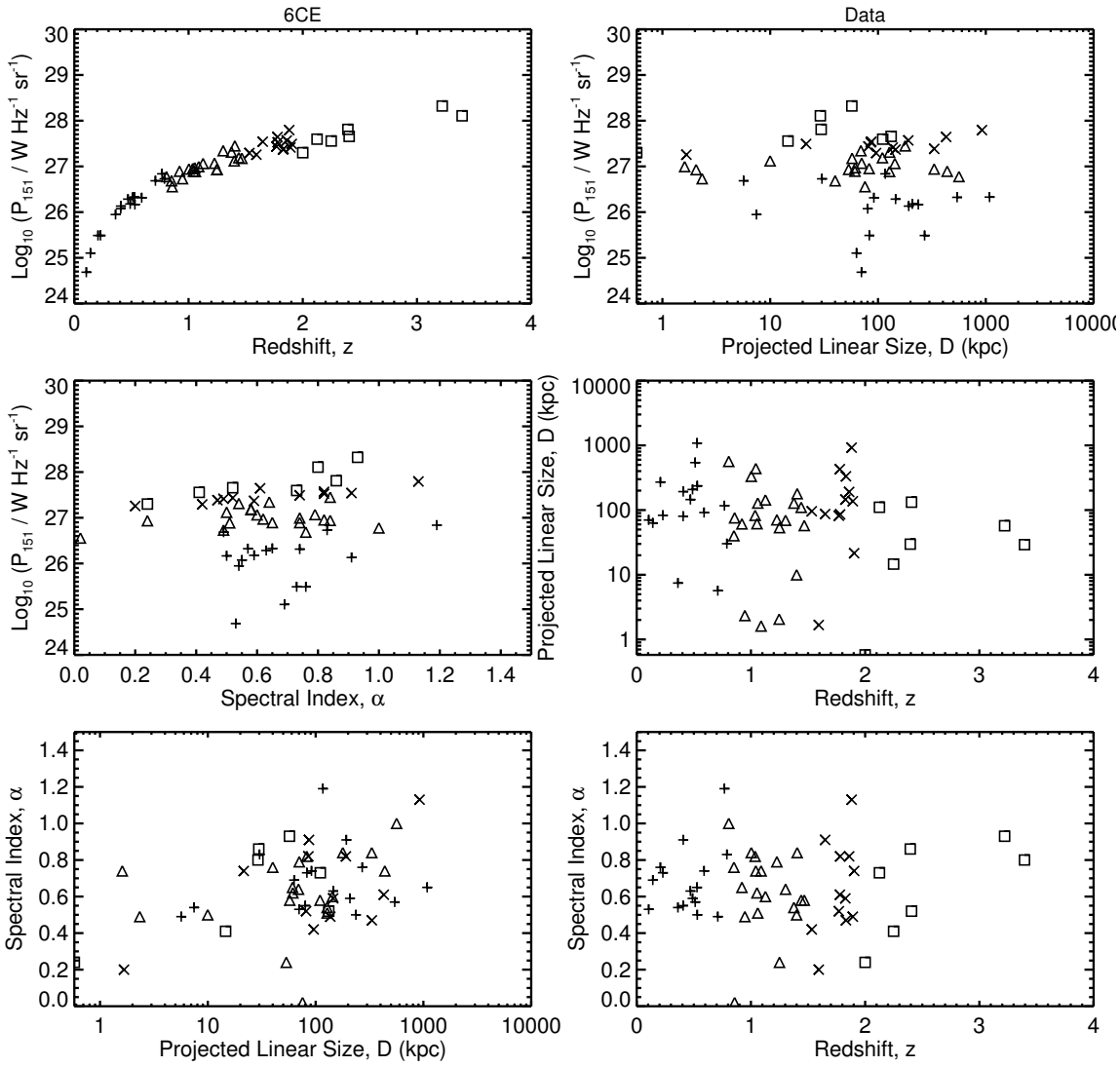

Figure 3.1b: The [P–D–z–α] planes for the observational 6CE sample. The plotting symbols are the same as in Figure 3.1a.

Oxford University[4] (but with a different cosmology).

3.3 The Simulated Surveys

Large radio source populations are randomly generated, according to the source age, redshift and beam power distributions as given in Section 3.1, for each choice of model parameters. Each simulated source, in a population, is then allowed to evolve

[4]http://www-astro.physics.ox.ac.uk/∼cjw/7crs/7crs.html

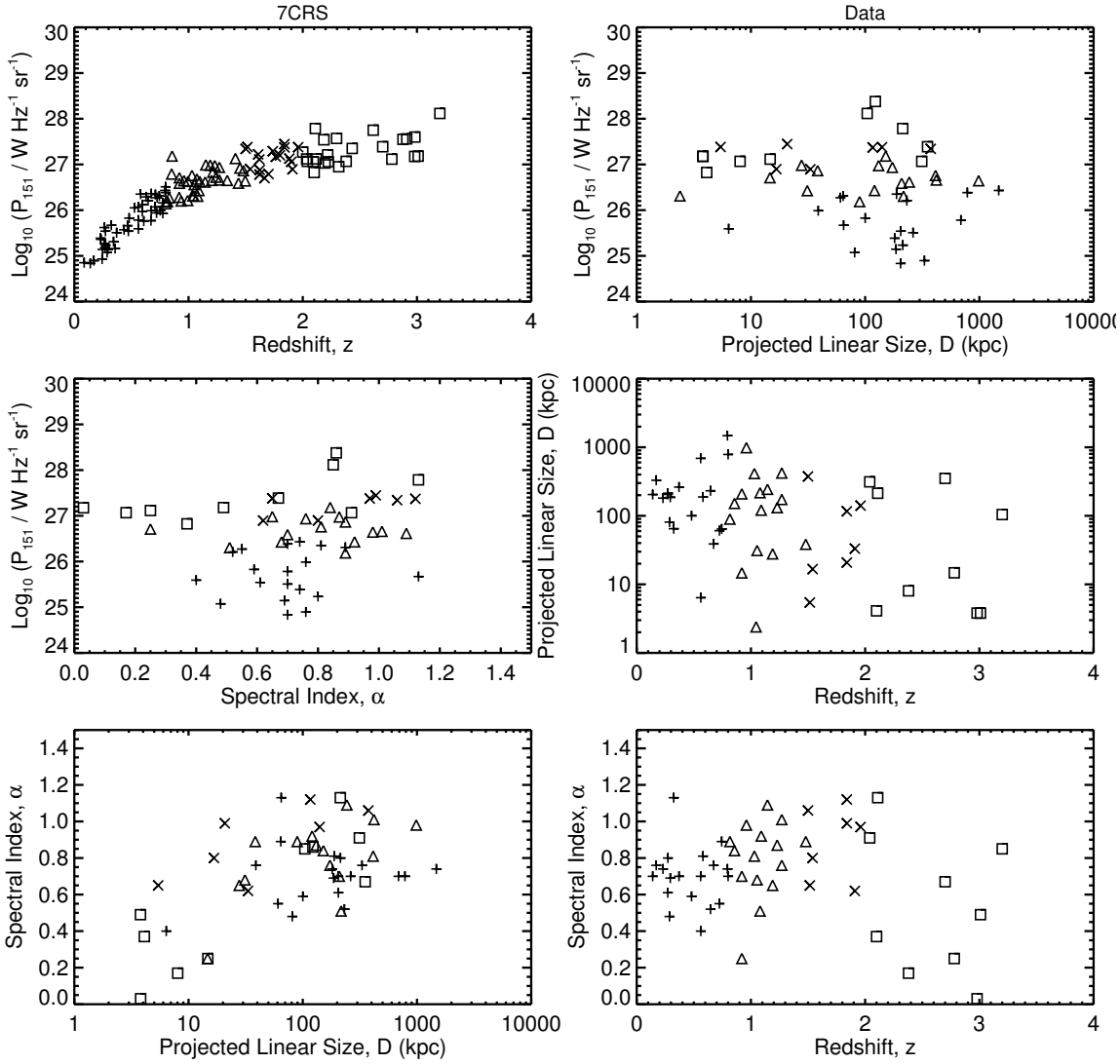

Figure 3.1c: The [P–D–z–α] planes for the observational 7CRS sample. The plotting symbols are the same as in Figure 3.1a.

in age according to one of the power evolution models discussed in Chapter 2. The temporal evolution must be done at a rest frame frequency of the source, which is related to the observational frequency by the source redshift. Due to the expansion of the universe radiation at a frequency ν_{rest} emitted by a RG at redshift z, actually reaches us at an observed frequency $\nu_{obs} = \nu_{rest}/(1+z)$. In this thesis work the frequency of observation is $\nu_{obs} = 151$ MHz. So a source observed at a redshift z, is evolved according to the models at a frequency $\nu_{rest} = 151 \times (1+z)$ MHz.

The monochromatic power (P_{151} in W Hz^{-1} sr^{-1}) each source would emit at the

observed time T_{obs} corresponding to it (Section 3.1.3) is calculated; this depends on the corresponding model as described in Chapter 2. At this cosmic time (T_{obs}), its redshift, and hence its distance from us, is found. The flux (in units of Jy = 10^{-26} W Hz^{-1} m^{-2}) of this source is then obtained (using Peacock (1999): Equations 3.10, 3.76 and 3.87 for a flat universe), given that it emitted P_{151} from the cosmic distance calculated. If the flux for a source is greater than a (lower) survey flux limit (or between two flux limits in the case of 6C) then that source is considered to be detected in the corresponding simulated survey, and counted for the later comparisons with real data.

It is assumed in our simulations that the central AGN, or the radio jets feeding the lobes, stay "on" only for the time t (or T_{age}) corresponding to each source (Section 3.1.3), which is also taken as the lifetime of a source. After the time t, the relativistic plasma in the lobes continue to radiate but the flux drops very rapidly once the central engine has stopped feeding the lobes. So the sources can be considered to be turned "off" instantaneously after t. The validity of this assumption is supported by the fact that the radio powers (P_{151}) drop substantially while the jets are still on (i.e., within the time t after birth), as shown by the P–D tracks in Section 4.1.

To perform our simulations we initially generate an ensemble containing a huge number ($\sim$ few 10^6) of pseudo-radio sources. After evolving each source by the above prescription, the ensemble is examined to see how many of them would actually be detected in a simulated complete survey. If the number of sources in this pseudo-survey is significantly different from the number in the actual survey, then we do the following: in another simulation run with the same parameter set, the initial population size is increased or decreased so as to obtain similar numbers of sources detected in the virtual surveys as are found in the real surveys. To achieve this, we usually had to generate such "standard" initial ensembles containing $\sim 10^6$ to 10^7 radio sources. Assuming the observed regions are fair samples of the universe, the population size is proportional to the sky area of a survey. The populations needed in order to simulate the 6C and 7C surveys are generated from that of 3C by reducing the total 3C population size according to the corresponding sky area ratio. Given a 3C initial ensemble of size S_{3C}, the populations for 6C and 7C are created by plucking sources randomly from that initial ensemble, and producing populations of sizes S_{6C}

and S_{7C} where,

$$S_{6C} = S_{3C} \times \frac{\text{Sky Area of 6C in sr}}{\text{Sky Area of 3C in sr}} = S_{3C} \times \frac{0.102}{4.23} = \frac{S_{3C}}{41.5};$$
$$S_{7C} = S_{3C} \times \frac{\text{Sky Area of 7C in sr}}{\text{Sky Area of 3C in sr}} = S_{3C} \times \frac{0.022}{4.23} = \frac{S_{3C}}{192.3}. \quad (3.15)$$

The initial populations generated for comparison with the 6C and 7C data following the above procedure detected more or less comparable numbers of sources in the simulations as compared to the actual surveys. We compute the over (-under) detection factors, defined as the ratios of the number of sources detected in the simulated 6C and 7C surveys to the numbers in the actual surveys as proportionate to the same ratio for the 3C survey; explicitly,

$$\text{Ratio}_{6C} = \text{Number of sources detected in } \left[\frac{\text{6C (simulation / data)}}{\text{3C (simulation / data)}}\right];$$
$$\text{Ratio}_{7C} = \text{Number of sources detected in } \left[\frac{\text{7C (simulation / data)}}{\text{3C (simulation / data)}}\right]. \quad (3.16)$$

The deviation of these ratios from 1.0 (see discussion in Section 4.9.1) may be considered a measurement of the statistical (sample) variance if they are not skewed in multiple realizations of our simulations. Although we tabulate these values in our result tables (in Chapters 4, 5 and Appendices A, B), we do not rely upon the closeness of these factors to unity as good quantitative tests for agreement between models and data. These ratios can be made closer to 1 by varying the redshift birth function or the RLF (Equation 3.6). So the ratios are not good tests of the radio lobe power evolution models (KDA, BRW and MK, discussed in Chapter 2) per se.

The simulation procedures were implemented using a combination of IDL and C codes. The initial population of sources was generated and each lobe power evolution model was implemented in C, and the other supporting codes were written in IDL. Numerical Recipes in C (Press et al. 1992) were used to speed up the calculations of lobe powers for the huge ensembles of sources.

Each simulation run required the generation and evolution of a few 10^6 to over 10^7 radio sources and hence substantial amounts of computing power, memory and time.

3.3.1 Computation of Projected Size

Each model gives the total linear size of a radio source; but we observe each one as projected on the plane of the sky. The projection effect of the sources in the radio surveys is incorporated into the simulations as follows. Sources are considered to be randomly oriented in the sky, so the angle to the line of sight (θ_{LOS}) of each source is drawn from a distribution uniform in $(1 - \cos\theta_{LOS})$. The projected length of each simulated source is then found from,

$$D_{proj} = D(t) \times \sin\theta_{LOS} = D(t) \times \sqrt{r_N(2 - r_N)}, \tag{3.17}$$

where r_N is an uniform random number between 0 and 1, and $D(t)$ is the total linear size of the source (Equation 2.2). For compactness, we denote the projected size D_{proj} as just D.

3.3.2 Computation of Spectral Index, α

The spectral index (α) in the rest frame of a source at 151 MHz was estimated as follows. For each source in the simulated surveys, log [ν (MHz)] was considered as the independent variable and log(P_ν) as the dependent variable. The specific powers (P_ν in W Hz^{-1} sr^{-1}) at the age t corresponding to the source, were calculated (Section 3.3) at three frequencies, namely, 151, 151/(1 + z) and 151(1 + z) MHz. A quadratic polynomial was fitted to the log(P_ν) vs. log [ν (MHz)] data. The fit coefficients a_1 and a_2, where $\log P_\nu = a_0 + a_1 \log\nu + a_2(\log\nu)^2$, were obtained. These were used to find the spectral index as $\alpha = -a_1 - 2a_2 \log[151/(1.0 + z)]$.

3.4 Statistical Tests

The sources detected in the simulated surveys were compared with those in the actual survey samples. Extensive statistical tests were performed to test the model fits, and to quantitatively compare them with each other in search of a best fit. For our first attempt to quantitatively compare the simulated radio surveys to the actual data, we used 1-D K-S statistical tests, for which the prescription is given in Section 3.4.1. Based on the results of such 1-D K-S tests we chose some parameter variations for the models on which two more statistical tests were done. These are 2-dimensional Kolmogorov-Smirnov tests (as described in Section 3.4.2), and Correlation Coefficient analyses (Section 3.4.3). Finally, we discuss merits of the models.

In doing the statistical tests (described specifically in the following subsections) we compared the model predictions with the observational samples as follows. In a single run a random initial population of millions of sources was generated such that (by constraining the ensemble size) after evolution of each source in the ensemble and after comparing each to the flux limits, the ensemble produced simulated samples (for the 3C, 6C and 7C catalogs) which were of sizes very comparable to or somewhat larger than the real surveys. The simulated samples (generally of larger size than the real surveys) were then reduced in size, if necessary, by uniformly selecting sources from them. In particular, this was done by selecting every (N_{sim}/N_{samp})'th source from a simulated survey, where N_{samp} is the number of sources in one of the real surveys 3C, 6C or 7C and N_{sim} (usually $> N_{samp}$), is the number of sources in the corresponding simulated survey. Finally statistical tests (whose results are tabulated) were done on the $[P, D, z, \alpha]$ data from the real surveys and a similar sized simulated sample generated from a single random seed.

Each of the [P–D–z–α] plane figures (in Chapters 4 and 5), show the final simulated sample (after reduction to the actual data sample sizes) of the random run done using specific parameters for each semi-analytical model. The plotted cases are the simulation results for the default models and the best overall fits for each model as determined by the 1-D K-S tests.

3.4.1 1-Dimensional Kolmogorov-Smirnov Combination Statistic

We use 1-D K-S tests to compare the simulated radio surveys to the actual data. Each of the distribution's key characteristics $[P, D, z, \alpha]$ of the radio sources detected in the simulated surveys were compared to those of the sources in the real radio surveys 3C, 6C and 7C, according to procedures given in the second and third paragraphs of Section 3.4. The 1-D K-S probabilities, $\mathcal{P}$, that the two data sets being compared are drawn from the same distribution function were taken to be a figure of merit of each model used in the simulation. High values of $\mathcal{P}$ (close to 1.0) indicate very good fits, while very small $\mathcal{P}$ values imply that the model and data distributions are significantly different. We consider twelve 1-D test statistics in total, the twelve probabilities found from the 1-D K-S statistics for comparisons of each of $[P, D, z, \alpha]$ for each of the three radio surveys; these quantify the closeness of the model fits to the datasets.

In order to quantify the overall success of a model we would prefer to have a single figure-of-merit instead of twelve indivdual ones, but there is no obvious way to produce such a statistic, particularly since the three surveys have significantly different numbers of objects. The number of sources in the catalogs 3C, 6C and 7C are $N_{3C} = 145$, $N_{6C} = 56$ and $N_{7C} = 126$, respectively. Here we have combined the 1-D K-S probabilities in the two following ways.

First, we add the 1-D K-S probability statistic for comparisons of P, D, z and α (i.e. $[\mathcal{P}(P) + \mathcal{P}(D) + \mathcal{P}(z) + \mathcal{P}(\alpha)]$) for the three surveys, weighting the statistic of a survey by the square-root of the number of simulated sources detected in that survey. So the first overall figure of merit of a model, which we denote as $\mathcal{P}_{[P,D,z,\alpha]}$, is given by:

$$\mathcal{P}_{[P,D,z,\alpha]} = [\mathcal{P}(P) + \mathcal{P}(D) + \mathcal{P}(z) + \mathcal{P}(\alpha)]_{Total} = [\mathcal{P}(P) + \mathcal{P}(D) + \mathcal{P}(z) + \mathcal{P}(\alpha)]_{3C} + \sqrt{\frac{N_{6C}}{N_{3C}}}\,[\mathcal{P}(P) + \mathcal{P}(D) + \mathcal{P}(z) + \mathcal{P}(\alpha)]_{6C} + \sqrt{\frac{N_{7C}}{N_{3C}}}\,[\mathcal{P}(P) + \mathcal{P}(D) + \mathcal{P}(z) + \mathcal{P}(\alpha)]_{7C} \quad (3.18)$$

Here N_{3C}, N_{6C} and N_{7C} are, respectively, the number of sources detected in each of the simulated surveys 3C, 6C and 7C, for a simulation run with a particular parameter set used in the model. If the simulations "detect" too many sources as compared to the data, then each of the resulting simulation survey samples for 3C, 6C and 7C are reduced by randomly removing sources to make the final simulation sample sizes equal to that of the data samples. This reduction of the simulated sample size was done primarily to get a more accurate realization of the number of FR II sources which existed over the quasar era (the radio galaxies in the initial ensemble), which is essential to calculate the relevant volume fraction in Chapter 7. Another reason for performing this reduction is that if the two samples being compared are of same sizes then K-S statistical test gives more accurate results.

The second figure of merit we employ adds the 1-D K-S statistic probability for P, z and α to twice the statistic for D, i.e., $[\mathcal{P}(P) + 2\mathcal{P}(D) + \mathcal{P}(z) + \mathcal{P}(\alpha)]$ for the three surveys, using the same weighting method. We denote this as $\mathcal{P}_{[P,2D,z,\alpha]}$. This second choice was considered because results for P and z usually correlate (due to flux-limit arguments); thus double weighting the probability for D added to the combined probability for P and z is a reasonable alternative approach, which dilutes the impact of the $[\mathcal{P}(P), \mathcal{P}(z)]$ correlation. Unsurprisingly, in most of the runs we have performed the combined test statistics $\mathcal{P}_{[P,D,z,\alpha]}$ and $\mathcal{P}_{[P,2D,z,\alpha]}$ (or $[\mathcal{P}(P) + \mathcal{P}(D) + \mathcal{P}(z) + \mathcal{P}(\alpha)]$

and $[\mathcal{P}(P) + 2\mathcal{P}(D) + \mathcal{P}(z) + \mathcal{P}(\alpha)]$) behaved in a similar fashion; i.e., if the $\mathcal{P}_{[P,D,z,\alpha]}$ for one model was better than that for a second, then in most cases $\mathcal{P}_{[P,2D,z,\alpha]}$ was also better for the first model.

A likelihood-type statistical test would involve the product instead of the sum of the K-S probabilities, but given the extremely small values of these products (mainly because of the tiny value of $\mathcal{P}(\alpha)$ for nearly all simulations) we rejected this figure of merit as not providing a useful discrimination between the models.

3.4.2 2-Dimensional Kolmogorov-Smirnov Tests

We used the 2-D K-S test procedure ("ks2d2s.c") from Numerical Recipes in C (Press et al. 1992), which is based on the work of Fasano & Franceschini (1987), which in turn is a variant of an earlier idea due to Peacock (1983). The relevant 2-dimensional 2-sample K-S probabilities (or the significance level indicating that the two populations are drawn from the same distribution), $\mathcal{P}$, give a quantitative measure of the model fits. High values of $\mathcal{P}$(K-S) (close to 1.0) indicate good fit, and very small $\mathcal{P}$(K-S) imply that the model and data distributions are significantly different. The comparisons of the model simulated samples to the real data samples are done in a way analogous to that for the 1-D K-S tests (Section 3.4.1).

3.4.3 Correlation Coefficient Analysis

We also considered the Spearman partial rank correlation coefficients between the four relevant source characteristics P, D, z and α. Following Macklin (1982), we calculated the partial rank correlation coefficients with four variables, e.g.,

$$r_{PD,z\alpha} = \frac{r_{PD,z} - r_{P\alpha,z} r_{D\alpha,z}}{\left[\left(1 - r_{P\alpha,z}^2\right)\left(r_{D\alpha,z}^2\right)\right]^{1/2}}, \tag{3.19}$$

for the correlation between P and D independent of z and α. Here the three-variable partial correlation coefficient is

$$r_{PD,z} = \frac{r_{PD} - r_{Dz} r_{Pz}}{\left(1 - r_{Dz}\right)^2 \left(1 - r_{Pz}\right)^2}, \tag{3.20}$$

with r_{PD} being the usual Spearman correlation coefficient between two variables P and D.

The significance level associated with the 4-variable correlation is

$$\Sigma_{PD,z\alpha} = \frac{(N_{samp} - 5)^{1/2}}{2} \ln\left(\frac{1 + r_{PD,z\alpha}}{1 - r_{PD,z\alpha}}\right), \tag{3.21}$$

where N_{samp} is the size of the sample considered. One can get some feeling for how well a simulation compares to actual data by examining their respective $r_{XY,ab}$ values, where $[X, Y, a, b]$ correspond to different permutations of $[P, D, z, \alpha]$.

3.4.4 Exploration of Multi-Dimensional K-S Tests

Unfortunately, for the complicated problem of radio source cosmological evolution, which involves many parameters and several dimensions, any figure of merit based upon 1-D and/or 2-D K-S tests is a crude approach in comparing models with observations.

We attempted to use multi-dimensional statistical tests (e.g., Holmström et al. 1995; Loudin 2003) which, in principle, could yield a more robust single figure of merit for the fit of our distributions to the data in $[P, D, z, \alpha]$ space. Unfortunately, the limited sizes of the observational samples (< 150) preclude obtaining reliable results from such generalizations of the K-S test. Here we are trying to fit four variables, namely $[P, D, z, \alpha]$; so in practice the minimum useful sample size required will be $\sim 10^4$ for a four-dimensional test. Thus any attempt to use such a multi-dimensional test for our problem will be beset by very large uncertainities and errors. In future work we plan to expand our method to include simulations of large scale radio surveys containing many thousands of sources, such as FIRST (Becker et al. 1995), WENSS (Rengelink et al. 1997) and NVSS (Condon et al. 1998), which can be made adequately complete in z through optical identifications (Ivezić et al. 2004) from SDSS (York et al. 2000). Then we might successfully incorporate a multi-dimensional test, and achieve a single figure of merit.

– 4 –

Results From the Published Models

4.1 [P–D] Tracks

As a radio source gets older, its power (P) vs. linear-size (D) track becomes steeper. While this is true for all models, the rate of steepening is different in the three original models (KDA, BRW and MK), as seen from Figure 4.1. These P–D tracks have been generated using the default parameters of each model (given in Table 2.1), by allowing each source (with beam powers and redshifts given in the plot) to evolve at frequency $\nu = 151$ MHz. For this Figure (alone) the total linear sizes were converted to the projected sizes assuming an average viewing angle to the line of sight of 39.5° (following KDA), i.e.

$$D_{proj} = D(t) \times \sin 39.5^{\circ}. \tag{4.1}$$

Our computed tracks are in agreement with the conclusion drawn by Manolakou & Kirk (2002) that their P–D tracks are more akin to those presented by Kaiser et al. (1997) than to those of Blundell et al. (1999). The differences between different models and between results obtained for different values of parameters for the models allow us to separate satisfactory from unsatisfactory models. Crude evaluations of the quality of different models and the allowable ranges of parameters for them can be found by comparing the regions in the P–D diagram that are actually populated with those that are accessible to models with those parameters (e.g., KDA, MK). All of the default models (original ones, discussed in Chapter 2), are in rough accord with the data in this regard.

Several studies attempt to explain the linear size evolution of RGs with redshift, an important feature of the P–D tracks. In considering the observed source sizes in radio surveys, steady decreases of the physical size with redshift, for both radio luminous quasars and double-lobed FR II sources were noted, with the parameterization $D \propto (1+z)^{-n}$, and $n \sim 1-2$ was found (Legg 1970; Miley 1971; Kapahi 1975, 1985; Oort et al. 1987). This cosmological evolution of linear size was first interpreted in terms of a systematic decrease in the ambient density due to the expansion of the universe ($\rho \propto (1+z)^3$) (e.g., Wardle & Miley 1974), and was analyzed in detail by

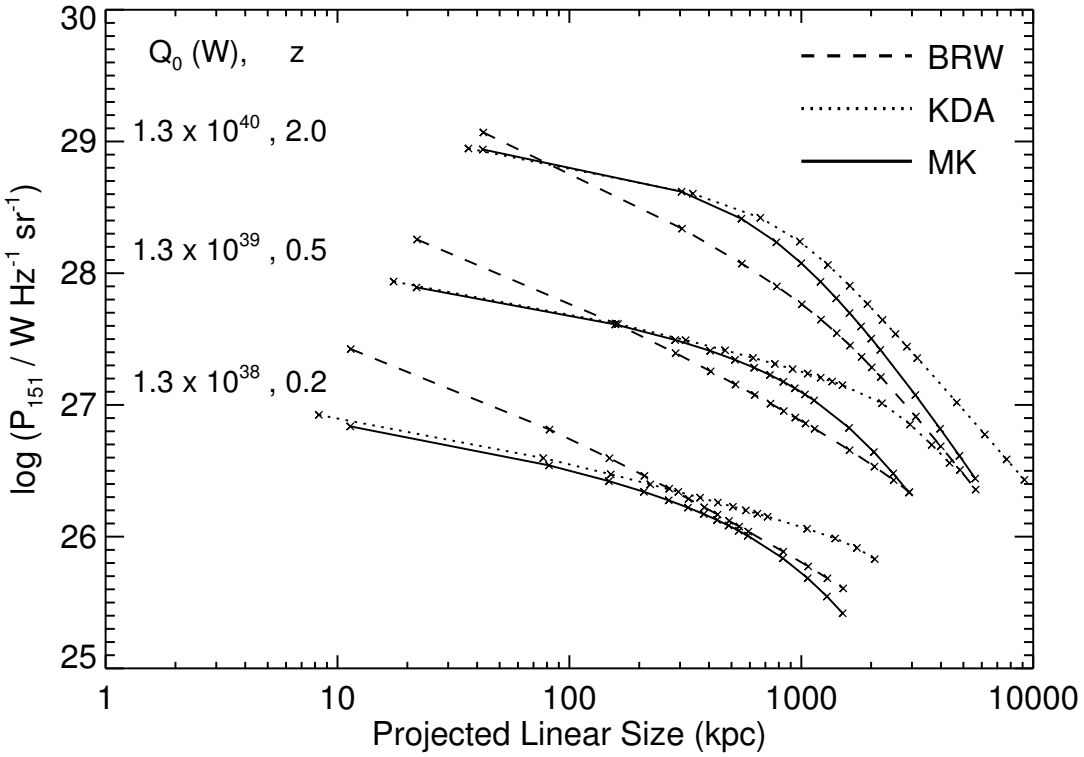

Figure 4.1: $[P$–$D]$ tracks of three sources with jet powers (Q_0) in Watts and redshifts (z) of $[1.3 \times 10^{40}, 2.0]$, $[1.3 \times 10^{39}, 0.5]$, $[1.3 \times 10^{38}, 0.2]$ (from top to bottom). Each of the *dashed*, *dotted* and *solid* curves correspond to the tracks predicted by the default versions of the BRW, KDA and MK models respectively. The crosses on the tracks denote source lifetimes of 1, 10, 20, 30, ..., 90, 100, 150, 200, 250, 300 Myr.

Gopal-Krishna & Wiita (1987); Rosen & Wiita (1988) within this interpretation.

In a radical departure from the approach, Blundell & Rawlings (1999), more recently argued that the observed linear size evolution may well be an artifact of the "youth–redshift degeneracy" of radio sources. This can be perceived by examining the different P–D tracks of Figure 4.1, where it is clearly found that the luminosity falls off faster for sources with high power and high redshift. So the observed intensity of an older, powerful source can fall below the flux limit of a survey before that of a younger one does. This gives rise to the observational consequence that, the higher the redshift of a radio source, the shorter the fraction of its life that can be detected by flux limited radio surveys. The youth–redshift degeneracy is imposed by the steeply rising IC losses against the cosmic microwave background at earlier epochs

(the importance of IC losses was first noted by Rees & Setti 1968), coupled with substantial adiabatic losses as the lobes expand. These points were earlier mentioned and discussed by Gopal-Krishna, Wiita, & Saripalli (1989) and Wiita et al. (1989). This means that in our flux limited radio surveys we will observe a high redshift source at an younger age, as compared to a low redshift source. The typical trend is, the higher the redshift of a source, the younger its age must be for it to be detected in our flux limited radio surveys.

4.2 Preliminary Statistical Tests as a Figure of Merit

We call the parameters governing the radio lobe power evolution as given in the papers KDA, BRW (including the parameters used for the initial radio source population generation for all models) and MK, to be the default ones. For KDA and MK, which discuss some alternate parameter sets, our defaults are their first, and favored, parameters.

We performed 1-D K-S statistical tests between the simulated radio surveys and the actual data, as a preliminary attempt to quantitatively compare the models. Based on the results of such tests we chose some parameter variations for the models as "better" (in providing higher combined probabilities from the 1-D K-S tests) than the others. For more robust comparison, further simulations and additional statistical tests (Section 4.8) were done on these nominally superior parameter sets.

The 1-D K-S results shown in this thesis comprise a large subset of all the simulation runs we have performed; however, the results of every single run done are not listed here, both to conserve paper and because those results provide little new information. To reach the final cases with some acceptable statistical fits, we had to simulate huge runs for a large number of cases with different parameter sets. Each simulation run required the generation of a few 10^6 to 10^7 radio sources in the initial ensemble, and hence substantial amounts of computing power, memory and time.

We present the 1-D K-S test results in tables grouped by radio source evolution model, with each entry illustrating a different parameter set. Tables 4.1, 4.4 and 4.7 give our results for the KDA model, Tables 4.2, 4.5 and 4.8 for the BRW model, and Tables 4.3, 4.6 and 4.9 for the MK model. The tables for each model follow the same format and pattern. Hence we describe only the table entries for the KDA model

(Tables 4.1, 4.4 and 4.7).

Each of the Tables 4.1, 4.2 and 4.3 give the individual 1-D K-S statistic probabilities $\mathcal{P}(P)$, $\mathcal{P}(D)$, $\mathcal{P}(z)$ and $\mathcal{P}(\alpha)$, along with the combined total probabilities, for some of the runs done by varying the initial ensemble generation parameters. The results for each model are given in three consecutive rows. The first column lists the values of the RG jet power distribution index x and T_{MaxAge} (in Myr) used for the initial population generation in that model run (these two parameters were expected to be the most important in governing the numbers of acceptable sources each Monte Carlo simulation would generate and are least constrained by other observations); it then gives the initial population (ensemble) size used to realize the 3C simulation in that model. The second column notes to which survey the 1-D K-S probabilities given in the next columns correspond. The first row in columns 3, 4, 5, 6, and 7 gives the 3C results, with the second and third rows giving the 6C and 7C results, respectively. The third column gives the ratio of number of sources detected in each survey over their actual number in the catalog, normalized to the 3C ratio. This normalized factor is naturally 1 for the first row (3C survey). In order to illustrate how many 3C sources are actually detected we give the 3C detection ratio (= number of sources in the 3C simulation divided by the number in 3C catalog) explicitly in parenthesis. The second and third rows of column three give Ratio_{6C} and Ratio_{7C}, as defined in Equation (3.16). The fourth, fifth, sixth and seventh columns show the $\mathcal{P}(P)$, $\mathcal{P}(D)$, $\mathcal{P}(z)$ and $\mathcal{P}(\alpha)$ respectively for each of the surveys 3C, 6C and 7C in 3 rows. The final, eighth, column lists the combined probabilities, $\mathcal{P}_{[P,D,z,\alpha]}$ and $\mathcal{P}_{[P,2D,z,\alpha]}$, in two consecutive rows, for each particular parameter set.

In a similar fashion, each of the Tables 4.4, 4.5 and 4.6 give the individual and total 1-D K-S statistic probabilities, for some of the initial runs. These tables follow a very similar format to the ones discussed in the last paragraph, except that the first column entries of these tables are different. Here (Tables 4.4, 4.5 and 4.6) the first column first lists the parameter(s) which has (have) been varied from the default case in the top row(s), and then the ensemble size used for the 3C simulation in that model.

Table 4.1: KDA Model 1-D K-S Results: Different Initial Ensemble Parameters [a]

x	Survey	Ratio_{3C}	$\mathcal{P}(K\text{–}S)$				$\mathcal{P}_{[P,D,z,\alpha]}$
T_{MaxAge} [b]		Ratio_{6C}	$\mathcal{P}(P)$	$\mathcal{P}(D)$	$\mathcal{P}(z)$	$\mathcal{P}(\alpha)$	$\mathcal{P}_{[P,2D,z,\alpha]}$
Ensemble Size		Ratio_{7C}					
2.6	3C	1 (2.18) [c]	9.56e-08	0.00366	7.65e-07	5.76e-08	0.881
500	6C	0.514	0.537	0.00387	0.729	3.66e-10	0.942
4397469	7C	0.652	0.0115	0.0907	0.00771	0.0416	
2.6	3C	1 (2.17)	9.07e-12	0.00379	1.38e-08	5.59e-14	0.591
150	6C	0.573	0.123	0.174	0.420	3.66e-10	0.837
1553389	7C	0.700	1.58e-04	0.216	0.00124	0.00144	
3.0	3C	1 (0.86)	6.06e-04	4.27e-04	0.0513	6.48e-10	1.17
50	6C	1.15	0.583	0.989	0.185	3.66e-10	1.80
999361	7C	1.75	8.62e-06	0.00986	1.53e-05	4.15e-04	
3.0	3C	1 (1.14)	0.0674	0.126	0.467	1.20e-11	1.88
100	6C	1.02	0.583	0.697	0.580	3.66e-10	2.48
1993745	7C	1.48	0.00543	0.0603	0.00323	5.02e-05	
3.0	3C	1 (1.16)	0.320	0.274	0.360	4.74e-12	1.84
150	6C	0.74	0.434	0.0141	0.585	3.66e-10	2.34
2652842	7C	1.20	0.00134	0.365	0.00498	9.72e-04	
3.0	3C	1 (0.92)	0.284	0.0943	0.222	1.51e-09	1.49
200	6C	0.96	0.527	0.120	0.0836	3.66e-10	2.07
2979285	7C	1.32	0.00815	0.668	0.0178	0.00551	
3.0	3C	1 (1.25)	0.132	0.0366	0.171	1.26e-13	0.864
300	6C	1.08	0.261	0.113	0.185	3.66e-10	1.11
4963343	7C	1.18	0.0257	0.233	0.00498	0.00148	
3.0	3C	1 (1.92)	0.122	9.76e-04	0.524	1.36e-08	1.77
500	6C	0.98	0.819	0.0428	0.308	3.66e-10	2.16
11236430	7C	1.20	0.0125	0.735	0.00766	0.00299	
3.0	3C	1 (1.08)	0.122	6.06e-04	0.130	4.55e-12	1.15
600	6C	1.01	0.527	0.0680	0.182	3.66e-10	1.38
6615831	7C	1.25	0.0773	0.319	0.143	0.0237	

[a] Runs done using different x and T_{MaxAge}, with other model parameters as in the default KDA case. The results do not exclude sources with $D < 1$ kpc; see discussion in Section 4.5.

[b] T_{MaxAge} in units of Myr.

[c] From its definition, $\text{Ratio}_{3C} = 1$. The number in parentheses gives the ratio of the number of sources detected in 3C simulation (with given ensemble size) as compared to the real 3C survey.

Table 4.2: BRW Model 1-D K-S Results: Different Initial Ensemble Parameters [a]

x	Survey	Ratio_{3C}	$\mathcal{P}(K\text{–}S)$				$\mathcal{P}_{[P,D,z,\alpha]}$
T_{MaxAge} [b]		Ratio_{6C}	$\mathcal{P}(P)$	$\mathcal{P}(D)$	$\mathcal{P}(z)$	$\mathcal{P}(\alpha)$	$\mathcal{P}_{[P,2D,z,\alpha]}$
Ensemble Size		Ratio_{7C}					
2.6	3C	1 (2.38) [c]	4.90e-11	1.24e-10	1.43e-08	0.0322	0.0172
500	6C	0.66	1.93e-05	0.0240	0.00120	3.66e-10	0.0336
2930490	7C	0.703	5.97e-08	0.00197	5.86e-08	0.00231	
2.6	3C	1 (2.12)	1.12e-10	7.31e-13	1.47e-09	0.0450	0.134
250	6C	0.70	0.00415	9.92e-04	0.189	3.66e-10	0.146
1466378	7C	0.66	1.27e-07	0.0191	2.78e-09	0.0237	
3.0	3C	1 (3.39)	1.55e-06	5.66e-23	1.81e-05	1.43e-04	0.0510
50	6C	1.08	5.00e-04	9.36e-05	0.0790	3.58e-10	0.0517
99936	7C	1.05	1.46e-08	0.00104	2.88e-08	0.00110	
3.0	3C	1 (6.03)	3.20e-05	2.00e-21	2.59e-04	6.80e-04	0.0643
150	6C	1.03	0.00879	4.74e-04	0.090	3.66e-10	0.0658
4861474	7C	1.09	5.70e-07	0.00197	2.64e-07	0.00431	
3.0	3C	1 (0.99)	9.63e-06	4.11e-17	8.84e-05	2.40e-04	0.0655
200	6C	1.12	0.0128	4.03e-05	0.0893	3.66e-10	0.0664
1019403	7C	0.94	2.73e-09	0.00136	3.07e-08	0.0127	
3.0	3C	1 (1.33)	8.84e-05	1.90e-19	0.00112	1.45e-04	0.202
250	6C	0.93	0.00789	2.13e-04	0.277	3.66e-10	0.223
1571349	7C	1.01	8.04e-06	0.0343	1.37e-05	0.0126	
3.0	3C	1 (1.49)	2.89e-06	6.82e-22	1.59e-04	6.43e-04	0.134
300	6C	0.88	0.00815	0.00401	0.193	3.66e-10	0.142
2107441	7C	1.03	5.70e-07	0.00781	1.27e-07	0.00231	
3.0	3C	1 (1.25)	1.34e-08	2.01e-20	5.45e-06	4.82e-05	0.0909
350	6C	1.02	0.00401	3.74e-05	0.0850	3.66e-10	0.125
2138676	7C	1.01	2.75e-05	0.0564	8.49e-05	0.0217	
3.0	3C	1 (1.21)	5.59e-08	1.99e-19	1.55e-04	8.59e-05	0.0115
500	6C	0.87	5.06e-04	9.50e-05	0.0162	3.66e-10	0.0123
2930490	7C	1.04	2.76e-08	0.00120	5.09e-07	0.00231	

[a] Runs done using different x and T_{MaxAge}, with other model parameters as in the default BRW case. The results do not exclude sources with $D < 10$ kpc; see Section 4.5.

[b] T_{MaxAge} in units of Myr.

[c] From its definition, $\text{Ratio}_{3C} = 1$. The number in parentheses gives the ratio of the number of sources detected in 3C simulation (with given ensemble size) as compared to the real 3C survey.

Table 4.3: MK Model 1-D K-S Results: Different Initial Ensemble Parameters [a]

x	Survey	Ratio_{3C}	$\mathcal{P}(K\text{–}S)$				$\mathcal{P}_{[P,D,z,\alpha]}$
T_{MaxAge} [b]		Ratio_{6C}	$\mathcal{P}(P)$	$\mathcal{P}(D)$	$\mathcal{P}(z)$	$\mathcal{P}(\alpha)$	$\mathcal{P}_{[P,2D,z,\alpha]}$
Ensemble Size		Ratio_{7C}					
2.6	3C	1 (1.37) [c]	3.77e-12	2.68e-05	3.99e-07	0	0.270
500	6C	0.391	0.0283	0.0685	0.308	1.80e-24	0.324
4397469	7C	0.458	2.84e-05	0.0175	0.00323	1.54e-15	
2.6	3C	1 (3.26)	4.05e-14	0.00375	4.97e-06	0	0.670
150	6C	0.42	0.0149	0.254	0.585	1.80e-24	0.961
3888492	7C	0.45	6.00e-09	0.207	4.00e-06	1.58e-15	
3.0	3C	1 (2.48)	0.0122	0.174	0.484	0	1.72
50	6C	0.83	0.161	0.664	0.437	1.80e-24	2.55
4452567	7C	1.16	2.64e-04	0.394	0.00768	2.49e-21	
3.0	3C	1 (1.2)	6.06e-04	0.216	0.346	0	1.87
100	6C	0.72	0.879	0.174	0.0823	1.80e-24	2.73
3508016	7C	0.96	0.00207	0.878	0.0546	6.51e-22	
3.0	3C	1 (1.2)	0.0277	0.420	0.633	0	1.95
150	6C	0.76	0.310	0.420	0.182	3.14e-23	2.92
4861474	7C	1.08	8.11e-04	0.461	0.0121	2.49e-21	
3.0	3C	1 (1.08)	0.413	0.00853	0.354	0	1.34
200	6C	0.91	0.667	0.00203	0.00223	1.80e-24	1.43
6129212	7C	1.14	7.530e-04	0.126	0.0717	2.49e-21	
3.0	3C	1 (1.02)	0.332	0.00247	0.171	0	1.25
300	6C	0.76	0.667	0.0417	0.0460	1.80e-24	1.43
7070784	7C	0.88	0.0258	0.240	0.103	1.15e-20	
3.0	3C	1 (1.06)	0.00819	0.0356	0.229	0	1.23
500	6C	0.57	0.0419	0.353	0.580	1.54e-18	1.83
11236430	7C	0.95	4.47e-04	0.555	0.00321	2.49e-21	

[a] These runs are done using different initial random ensembles with x and T_{MaxAge} as listed. In these MK simulations, the model parameters for dynamical and power evolution are the same as in the default MK case. The results do not exclude sources with $D < 1$ kpc; see discussion in the last two paragraphs of Section 4.5.

[b] T_{MaxAge} in units of Myr.

[c] From its definition, $\text{Ratio}_{3C} = 1$. The number in parentheses gives the ratio of the number of sources detected in 3C simulation (with given ensemble size) as compared to the real 3C survey.

4.3 Fits with Default Initial Population & Default Model Parameters

To begin with, an initial population, generated using the default parameters from BRW for the RG population generation, was evolved according to the three different default models discussed before. The default values (those used by the respective authors) of the corresponding model parameters are listed in Table 2.1. The simulated sources detected (according to the prescription in Section 3.3) were compared to the actual data in the 3C, 6C, and 7C catalogs. As shown by the 1-D K-S test statistics of the first parameter entry (the very first 3 rows) of Tables 4.1, 4.2 and 4.3 the model fits are all very poor. A major problem is that too many high-z and too few low-z sources were produced by the models as compared to the data.

4.4 Dependence on Beam Power Slope, x

To look for improved statistical agreement between simulations and data, we decided to steepen the beam power distribution function of the sources generated in the initial population. This modification was expected to produce fewer high P – high z sources.

The exponent in the power law distribution of the jet powers, x (in Equation 3.9), was increased from $x = 2.6$ (as used by BRW), in intervals of $\Delta x = 0.2$ or 0.3. For the KDA and MK models the overall statistics improved the most at $x = 3.0$, but were less good for $x = 3.3$ or 3.6. For the BRW model the P and z fits were best for $x = 3.6$, making the overall performance look fairly good, but the D fits were all very bad. As will be discussed further in Section 4.4.1, the former modifcation ($x = 3.0$) produced a clear overall improvement for the BRW model too.

4.4.1 Initial Population with Varied x, Default Model Parameters

The initial population generated with $x = 3$ (but otherwise using the BRW prescription), was evolved according to each of the KDA and MK power evolution models. The corresponding 1-D K-S statistics are given as the first entries in Tables 4.4 and 4.6. For the BRW model the big population generated using $x = 3.6$ often gave acceptable P and z fits, leading us to perform simulation runs using initial ensembles generated with $x = 3.6$. But these BRW simulations had a very strong P–D

Table 4.4: KDA Model Results: 1-D K-S Statistics for Parameter Variations with $x = 3$ [a]

Model Ensemble Size	Survey	Ratio_{3C} Ratio_{6C} Ratio_{7C}	$\mathcal{P}(K\text{–}S)$				$\mathcal{P}_{[P,D,z,\alpha]}$ $\mathcal{P}_{[P,2D,z,\alpha]}$
			$\mathcal{P}(P)$	$\mathcal{P}(D)$	$\mathcal{P}(z)$	$\mathcal{P}(\alpha)$	
Default [b]	3C	1 (1.92) [c]	0.122	9.76e-04	0.524	1.36e-08	1.77
11236430	6C	0.98	0.819	0.0428	0.308	3.66e-10	2.16
	7C	1.20	0.0125	0.735	0.00766	0.00299	
BRW Env. [d]	3C	1 (1.26)	0.143	1.18e-10	0.130	2.83e-08	0.707
β, a_0, ρ_0	6C	0.63	0.458	6.85e-07	0.129	5.33e-09	0.708
4886474	7C	0.89	0.0271	0.00222	0.0376	0.00951	
$\beta = 1.0$	3C	1 (1.52)	0.00206	1.47e-10	0.0108	0.0	0.0880
485979	6C	0.72	0.0325	1.10e-07	0.0857	1.80e-24	0.0882
	7C	0.63	1.93e-08	4.44e-04	4.10e-05	4.84e-16	
$\beta = 2.02$	3C	1 (1.05)	0.207	0.0523	0.459	1.31e-10	2.15
9772948	6C	0.92	0.979	0.509	0.529	2.20e-09	2.60
	7C	1.27	0.0140	0.121	0.0722	1.62e-04	
$a_0 = 1.5$ kpc	3C	1 (0.98)	0.174	0.00880	0.381	1.04e-14	2.05
9772948	6C	0.93	0.952	0.0286	0.344	3.86e-09	2.37
	7C	1.21	0.0769	0.477	0.300	1.44e-06	
$a_0 = 5$ kpc	3C	1 (3.28)	0.114	0.00379	0.287	3.78e-10	1.30
4886474	6C	0.91	0.434	0.0709	0.132	5.36e-18	1.84
	7C	1.06	4.73e-04	0.806	0.00319	8.17e-12	
$\rho_0 = \rho_1$ [e]	3C	1 (1.13)	0.0681	0.0175	0.351	1.03e-15	2.17
12703438	6C	0.76	0.641	0.452	0.792	6.97e-09	2.72
	7C	1.25	0.0769	0.405	0.233	1.91e-05	
$\rho_0 = \rho_2$ [f]	3C	1 (3.00)	0.229	0.00159	0.288	1.71e-08	1.75
4886474	6C	0.87	0.740	0.174	0.132	3.03e-17	2.42
	7C	1.03	7.65e-04	0.921	0.00502	1.02e-09	
$\Gamma_B = 5/3$	3C	1 (1.19)	0.264	9.70e-04	0.622	4.71e-17	2.07
7816964	6C	0.76	0.952	0.0394	0.581	4.68e-09	2.23
	7C	1.13	0.0275	0.212	0.0364	6.80e-05	
$\Gamma_C = 5/3$	3C	1 (0.97)	0.00704	0.0158	0.00177	1.37e-11	1.44
14659422	6C	0.80	0.482	0.718	0.426	6.73e-09	2.00
	7C	1.26	0.180	0.147	0.138	8.68e-05	

Continued on next page ...

Table 4.4: continued from previous page ...

Model Ensemble Size	Survey	Ratio_{3C} Ratio_{6C} Ratio_{7C}	$\mathcal{P}(K\text{–}S)$ $\mathcal{P}(P)$	$\mathcal{P}(D)$	$\mathcal{P}(z)$	$\mathcal{P}(\alpha)$	$\mathcal{P}_{[P,D,z,\alpha]}$ $\mathcal{P}_{[P,2D,z,\alpha]}$
$\Gamma_B = 5/3$	3C	1 (0.83)	0.0462	0.0180	0.0104	1.91e-15	1.51
$\Gamma_C = 5/3$	6C	0.80	0.307	0.676	0.542	1.08e-07	2.12
14659422	7C	1.28	0.235	0.262	0.102	8.51e-07	
$R_T = 2.0$	3C	1 (0.917)	0.0382	3.89e-04	0.0132	1.98e-18	1.04
18078888	6C	0.789	0.310	0.110	0.211	1.29e-09	1.24
	7C	1.38	0.317	0.212	0.178	7.19e-06	
$R_T = 2.5$	3C	1 (0.36)	0.0112	0.0586	0.0360	6.63e-13	0.587 [g]
11236430	6C	0					0.772 [g]
	7C	1.19	0.262	0.207	0.116	9.10e-07	
$R_T = 3.0$	3C	1 (0.241)	0.00654	6.55e-04	0.0100	2.98e-08	0.472 [g]
14659422	6C	0.786	0.440	0.00277	0.709	0.00397	0.483 [g]
	7C	1.65	0.0769	0.0161	0.153	3.25e-08	
$R_T = 4.0$	3C	1 (0.09)	0.117	0.184	0.147	4.68e-05	0.875 [g]
11236430	6C	0					1.29 [g]
	7C	1	0.0575	0.372	0.155	3.92e-04	
$\gamma_{min(hs)} = 10$	3C	1 (1.10)	0.0752	3.74e-4	0.680	8.12e-13	2.03
4886474	6C	1.1	0.915	0.0683	0.413	3.66e-10	2.42
	7C	1.25	0.0186	0.558	0.0366	0.00431	
$\gamma_{max(hs)} = 10^{14}$	3C	1 (1.09)	0.333	3.83e-4	0.435	8.07e-13	1.58
6056742	6C	0.94	0.524	0.00288	0.185	3.66e-10	1.88
	7C	1.10	0.0188	0.497	0.0377	0.00431	
$\gamma_{max(hs)} = 10^7$	3C	1 (1.03)	0.107	9.76e-04	0.680	8.12e-13	1.82
4886474	6C	0.99	0.511	0.0229	0.194	3.66e-10	2.32
	7C	1.17	0.0271	0.793	0.0688	0.00431	
$p = 2.05$	3C	1 (1.19)	0.0372	1.36e-04	0.0191	2.68e-18	1.16
12703438	6C	0.80	0.356	0.0150	0.185	2.73e-08	1.60
	7C	1.24	0.105	0.701	0.239	5.62e-07	
$p = 2.12$	3C	1 (1.32)	0.288	2.36e-04	0.433	7.77e-13	1.90
7816964	6C	0.92	0.819	0.0657	0.286	1.27e-09	2.34
	7C	1.17	0.00831	0.646	0.0383	0.00185	

Continued on next page ...

Table 4.4: continued from previous page ...

Model Ensemble Size	Survey	Ratio_{3C} Ratio_{6C} Ratio_{7C}	$\mathcal{P}(K\text{–}S)$ $\mathcal{P}(P)$	$\mathcal{P}(D)$	$\mathcal{P}(z)$	$\mathcal{P}(\alpha)$	$\mathcal{P}_{[P,D,z,\alpha]}$ $\mathcal{P}_{[P,2D,z,\alpha]}$
$p = 2.3$	3C	1 (1.16)	0.161	0.00370	0.282	1.44e-07	1.65
12703438	6C	0.72	0.293	0.416	0.648	9.41e-13	1.99
	7C	1.19	0.0551	0.121	0.233	1.95e-08	
$p = 2.12$	3C	1 (0.393)	0.111	5.44e-04	0.0570	3.75e-08	1.57 [g]
$\rho_0 = \rho_1$ [e]	6C	1.18	0.474	0.423	0.920	2.65e-06	1.95 [g]
6451283 [h]	7C	1.73	0.289	0.319	0.340	4.93e-05	

[a] These runs are done with initial ensembles of given sizes generated using $x = 3.0$, $T_{MaxAge} =$ 500 Myr. In these KDA simulations, the model parameter(s) for dynamical and power evolution listed in the first column is(are) varied; the rest are same as in the default KDA case. The results do not exclude sources with $D < 1$ kpc (unless otherwise noted); see discussion in the last two paragraphs of Section 4.5.

[b] Parameter values set equal to those given in the first KDA model (Kaiser, Dennett-Thorpe, & Alexander 1997); see Table 2.1.

[c] Always, $\text{Ratio}_{3C} = 1$, because of the way it is defined. The number in parentheses gives the ratio of the number of sources detected in 3C simulation (with given ensemble size) as compared to the real 3C survey.

[d] Parameters defining external environment density profile are set to those of the BRW model, namely, $\beta = 1.6, a_0 = 10$ kpc, $\rho_0 = 1.67 \times 10^{-23}$ kg m^{-3}.

[e] $\rho_1 = \rho_{0\ \text{(Default)}}/2 = 3.6 \times 10^{-22}$ kg m^{-3}.

[f] $\rho_2 = 5 \times \rho_{0\ \text{(Default)}} = 3.6 \times 10^{-21}$ kg m^{-3}.

[g] Number of sources detected in the simulated surveys is considerably smaller than in the real surveys, so the K-S statistic does not hold any significance.

[h] Linear size, $D(t)$ cut off of 1 kpc has been used in this simulation.

anticorrelation, producing too many small sources and too few large ones, in strong disagreement with the data. The combined 1-D K-S statistics were also much worse than those of the KDA and MK models. So, although we list the BRW model results with $x = 3.6$ in Table 4.5, we do not consider that parameter variation any further.

Some of the 12 1-D K-S probabilities for the KDA and MK models (albeit very few for BRW) provide acceptable fits to the data. The statistics for P and z correlate positively in most cases because they are related by cosmological arguments when we pick up radio sources by imposing a flux limit on them. In some cases the P and/or z fits are good and fits to D are bad; and vice versa in other cases. To search for

Table 4.5: BRW Model: 1-D K-S Statistics for Parameter Variations with $x = 3.6$ [a]

Model Ensemble Size	Survey	Ratio_{3C} Ratio_{6C} Ratio_{7C}	$\mathcal{P}(K\text{–}S)$ $\mathcal{P}(P)$	$\mathcal{P}(D)$	$\mathcal{P}(z)$	$\mathcal{P}(\alpha)$	$\mathcal{P}_{[P,D,z,\alpha]}$ $\mathcal{P}_{[P,2D,z,\alpha]}$
Default [b]	3C	1 (1.68) [c]	0.0531	2.10e-21	0.110	2.69e-06	0.307
6447729	6C	1.16	0.0157	3.21e-07	0.212	3.66e-10	0.307
	7C	1.45	8.04e-06	7.32e-05	2.57e-05	0.00231	
KDA Env. [d]	3C	1 (1.68)	3.25e-09	5.36e-36	1.65e-06	1.73e-18	7.74e-04
β, a_0, ρ_0	6C	0.96	7.68e-06	8.54e-11	0.00121	3.33e-15	7.74e-04
3517239	7C	0.98	2.63e-09	6.92e-07	5.06e-10	4.15e-04	
$\beta = 1.0$	3C	1 (1.58)	1.63e-04	0.0179	4.42e-04	7.11e-08	0.967
3517239	6C	1.27	0.140	0.253	0.308	2.94e-17	1.65
	7C	1.77	2.67e-04	0.793	7.62e-04	6.68e-09	
$\beta = 2.0$	3C	1 (1.20)	4.57e-12	3.43e-42	1.48e-09	4.08e-25	3.69e-04
3517239	6C	0.81	1.37e-05	1.44e-12	5.70e-04	3.42e-15	3.69e-04
	7C	0.75	8.69e-10	2.02e-10	2.03e-12	0.00208	
$a_0 = 7.5$ kpc	3C	1 (1.20)	0.0138	1.88e-22	0.145	1.63e-05	0.543
6447729	6C	1.18	0.173	2.13e-04	0.434	1.29e-09	0.544
	7C	1.40	4.95e-05	5.05e-05	7.25e-06	0.00582	
$a_0 = 20$ kpc	3C	1 (2.10)	0.220	1.08e-13	0.192	4.99e-06	0.522
3517239	6C	1.25	0.0146	8.41e-07	0.141	8.69e-14	0.534
	7C	1.48	1.38e-07	0.0199	1.06e-06	3.51e-08	
$\rho_0 = \rho_1$ [e]	3C	1 (1.09)	0.00240	6.36e-23	0.0978	3.94e-04	0.111
7034478	6C	0.96	5.00e-04	1.05e-09	0.0164	1.29e-09	0.111
	7C	1.56	2.84e-05	1.57e-06	2.60e-05	0.00502	
$\rho_0 = \rho_2$ [f]	3C	1 (1.60)	0.133	3.20e-16	0.189	2.85e-05	0.436
3517239	6C	1.19	0.0157	3.97e-05	0.140	3.83e-13	0.451
	7C	1.53	5.70e-07	0.0254	2.06e-06	1.94e-07	
$\Gamma_C = 5/3$	3C	1 (1.94)	2.03e-21	0.0	4.99e-17	1.11e-29	2.31e-04
7034478	6C	0.47	2.16e-06	1.19e-14	3.63e-04	1.19e-14	2.31e-04
	7C	0.47	8.90e-08	7.76e-13	3.00e-09	5.45e-04	
$\gamma_{min(hs)} = 10$	3C	1 (1.21)	0.00628	2.65e-23	0.0313	4.93e-06	0.0708
3517239	6C	1.16	0.00110	1.10e-07	0.0494	3.66e-10	0.0719
	7C	1.42	1.56e-04	0.00185	1.35e-05	0.00231	

Continued on next page ...

Table 4.5: continued from previous page ...

Model Ensemble Size	Survey	Ratio$_{3C}$ Ratio$_{6C}$ Ratio$_{7C}$	$\mathcal{P}(K$–$S)$				$\mathcal{P}_{[P,D,z,\alpha]}$ $\mathcal{P}_{[P,2D,z,\alpha]}$
			$\mathcal{P}(P)$	$\mathcal{P}(D)$	$\mathcal{P}(z)$	$\mathcal{P}(\alpha)$	
$\gamma_{max(hs)} = 10^{10}$	3C	1 (1.32)	0.0250	6.69e-21	0.0603	1.60e-05	0.237
4980859	6C	1.03	0.0277	8.87e-07	0.212	1.27e-09	0.238
	7C	1.48	8.79e-05	3.10e-04	2.73e-05	0.00231	
$p = 2.001$	3C	1 (1.12)	0.329	1.99e-19	0.661	1.43e-04	1.82
7911349	6C	1.20	0.879	9.36e-05	0.427	3.66e-10	1.82
	7C	1.67	2.72e-04	1.58e-04	4.69e-05	0.00651	
$p = 2.999$	3C	1 (2.70)	0.0222	4.55e-17	0.0437	1.61e-05	0.175
6447729	6C	1.14	0.00232	6.02e-06	0.127	3.58e-10	0.202
	7C	1.38	8.16e-06	0.0444	2.06e-06	0.00120	
$r_{hs} = 5$ kpc	3C	1 (1.83)	0.0198	2.12e-20	0.044	5.36e-05	0.130
3517239	6C	1.11	0.00232	9.02e-07	0.0803	3.83e-13	0.145
	7C	1.25	2.83e-07	0.0238	2.62e-07	1.11e-07	
$r_{hs} = 1$ kpc	3C	1 (0.99)	0.0505	1.49e-24	0.467	2.40e-04	0.607
8498098	6C	1.11	0.00772	3.52e-09	0.127	1.27e-09	0.607
	7C	1.83	2.64e-04	1.16e-05	5.04e-05	0.0149	
$t_{bs} = 10^3$ yr	3C	1 (1.19)	0.123	6.38e-21	0.382	1.60e-05	0.958
6447729	6C	1.28	0.282	2.45e-06	0.434	3.66e-10	0.958
	7C	1.56	1.50e-05	5.05e-05	2.57e-05	0.00329	
$t_{bs} = 10^7$ yr	3C	1 (1.19)	4.36e-04	1.27e-25	0.00711	1.96e-12	0.0187
3517239	6C	1.14	2.38e-04	1.08e-07	0.0164	3.07e-15	0.0194
	7C	1.24	4.58e-05	0.00104	1.35e-05	6.27e-08	
$t_{bf} = 0.01$ yr	3C	1 (1.22)	0.0491	4.11e-17	0.0819	1.43e-04	0.357
4980859	6C	1.06	0.0473	6.42e-06	0.310	3.66e-10	0.357
	7C	1.52	2.75e-05	4.25e-04	2.73e-05	0.00465	
$t_{bf} = 100$ yr	3C	1 (1.04)	0.0314	6.93e-20	0.0437	1.43e-04	0.110
3517239	6C	1.12	0.00449	3.27e-07	0.0494	1.27e-09	0.111
	7C	1.48	8.79e-05	0.00157	4.65e-05	0.00431	
$a_0 = 7.5$ kpc	3C	1 (1.03)	0.108	1.78e-12	0.247	3.70e-06	0.483
6451283 [g]	6C	1.03	0.0157	0.00203	0.0893	1.27e-09	0.545
	7C	1.74	2.75e-05	0.0991	7.58e-06	1.41e-04	

[a] These runs are done with initial ensembles of given sizes generated using $x = 3.6$, $T_{MaxAge} = 500$ Myr (unless otherwise noted). In these BRW simulations, the model parameter(s) for dynamical and power evolution listed in the first column is(are) varied, the rest are same as in default BRW (Blundell et al. 1999). The results do not exclude sources with total linear size, $D < 10$ kpc; see discussion in the last two paragraphs of Section 4.5.

[b] Parameter values set equal to those given in the BRW model (Blundell, Rawlings, & Willott 1999); see Table 2.1.

[c] Always, $\text{Ratio}_{3C} = 1$, because of the way it is defined. The number in parentheses gives the ratio of the number of sources detected in 3C simulation (with given ensemble size) as compared to the real 3C survey.

[d] Parameters defining external environment density profile are set to those of the KDA model, namely, $\beta = 1.9, a_0 = 2$ kpc, $\rho_0 = 7.2 \times 10^{-22}$ kg m^{-3}.

[e] $\rho_1 = \rho_{0\ \text{(Default)}}/2 = 8.35 \times 10^{-24}$ kg m^{-3}.

[f] $\rho_2 = 2 \times \rho_{0\ \text{(Default)}} = 3.34 \times 10^{-23}$ kg m^{-3}.

[g] The initial ensemble is generated using $x = 3$, $T_{MaxAge} = 500$ Myr. Linear size, $D(t)$ cut off of 10 kpc has been used in this simulation.

possible further improvements, we varied the other parameters prescribing the power evolution in the models as described below.

4.4.2 Dependences on Other Parameters for Better x Values

Accepting $x = 3.0$ as a tentative value for the exponent of the beam power distribution for the generated initial population, we then varied the parameters governing the lobe power evolution of the KDA and MK models. For BRW the exponent $x = 3.6$ was initially accepted, as it gave good fits for P and z, though the D fit was very poor. Simulations were done by setting the parameter values at the end points of physically reasonable ranges; for example we might perform two additional runs using the same random initial population but we would set a parameter to half or twice its default value.

Simulated surveys were constructed using the parameter listing given in Table 4.4 (each variation done one at a time) of KDA power evolution model, in addition to the default case. Simulations done with higher axial ratios, $[R_T = 2.0, 2.5, 3.0, 4.0, 5.0]$, which are favored by morphological data, all yielded severe underdetections in the virtual surveys when compared to the actual number of sources in the catalog (the underdetection factor rising dramatically as R_T was increased). Hence we adopted KDA's default value of the axial ratio, $R_T = 1.3$.

The initial simulation runs done with parameters variations in the BRW model, using an ensemble with $x = 3.6$, did not give acceptable D fits (discussed in Section 4.4.1). Also, the combined statistical results, as seen from Table 4.5, were much

Table 4.6: MK Model Results: 1-D K-S Statistics for Parameter Variations with $x = 3$ [a]

Model Ensemble Size	Survey	Ratio_{3C} Ratio_{6C} Ratio_{7C}	$\mathcal{P}(K\text{–}S)$ $\mathcal{P}(P)$	$\mathcal{P}(D)$	$\mathcal{P}(z)$	$\mathcal{P}(\alpha)$	$\mathcal{P}_{[P,D,z,\alpha]}$ $\mathcal{P}_{[P,2D,z,\alpha]}$
Default [b]	3C	1 (1.06) [c]	0.00819	0.0356	0.229	0.0	1.23
11236430	6C	0.57	0.0419	0.353	0.580	1.54e-18	1.83
	7C	0.95	4.47e-04	0.555	0.00321	2.49e-21	
KDA Env. [d]	3C	1 (1.14)	0.126	4.01e-04	0.353	0.0	0.842
β, a_0, ρ_0	6C	0.80	0.212	0.135	0.134	3.14e-23	0.935
14659422	7C	1.09	0.00197	0.0116	0.0517	2.28e-23	
$\beta = 1.0$	3C	1 (1.28)	0.0122	1.42e-06	0.280	0.0	0.858
4886474	6C	0.63	0.805	1.48e-06	0.0367	7.60e-22	0.859
	7C	0.69	0.0259	5.55e-04	0.00959	6.72e-20	
$\beta = 1.6$	3C	1 (1.12)	0.267	0.288	0.351	0.0	1.73
14659422	6C	0.66	0.150	0.311	0.169	7.86e-21	2.38
	7C	0.96	0.0271	0.279	0.239	2.49e-21	
$a_0 = 7.5$ kpc	3C	1 (0.98)	0.282	0.0741	0.106	0.0	1.76
14659422	6C	0.56	0.117	0.674	0.438	1.43e-17	2.61
	7C	0.90	0.0796	0.569	0.104	2.53e-17	
$a_0 = 20$ kpc	3C	1 (1.04)	0.00819	0.00853	0.441	0.0	1.33
5372453	6C	0.80	0.654	0.00957	0.0991	1.08e-23	1.63
	7C	0.82	0.00500	0.469	0.101	2.72e-25	
$\rho_0 = \rho_1$ [e]	3C	1 (1.0)	0.400	0.0913	0.130	0.0	1.63
14659422	6C	0.60	0.0770	0.205	0.335	1.54e-18	2.30
	7C	0.88	0.0796	0.736	0.104	2.53e-17	
$\rho_0 = \rho_2$ [f]	3C	1 (1.28)	0.0670	0.0176	0.283	0.00	0.978
7816964	6C	0.63	0.470	0.0428	0.338	1.24e-22	1.08
	7C	0.77	1.01e-04	0.0907	0.0173	3.33e-24	
$\gamma_{min(hs)} = 7$	3C	1 (0.74)	0.170	0.0961	0.147	1.12e-44	1.44
14659422	6C	0.65	0.361	0.624	0.376	3.54e-16	2.00
	7C	0.95	0.0197	0.109	0.0877	9.54e-21	
$\gamma_{min(hs)} = 100$	3C	1 (3.90)	0.0628	5.05e-08	0.312	2.60e-33	0.777
4886474	6C	0.76	0.310	9.07e-04	0.302	1.32e-23	0.785
	7C	0.74	8.04e-06	0.0127	0.00761	6.08e-15	

Continued on next page ...

Table 4.6: continued from previous page ...

Model Ensemble Size	Survey	Ratio_{3C} Ratio_{6C} Ratio_{7C}	$\mathcal{P}(K\text{–}S)$				$\mathcal{P}_{[P,D,z,\alpha]}$ $\mathcal{P}_{[P,2D,z,\alpha]}$
			$\mathcal{P}(P)$	$\mathcal{P}(D)$	$\mathcal{P}(z)$	$\mathcal{P}(\alpha)$	
$\gamma_{max(hs)} = 3 \times 10^8$	3C	1 (1.34)	0.290	0.0692	0.171	0.0	1.53
14659422	6C	0.66	0.404	0.0540	0.321	8.73e-23	1.98
	7C	0.89	0.0389	0.565	0.138	2.49e-21	
$p = 2.001$	3C	1 (1.59)	0.0917	3.68e-05	0.354	2.99e-27	1.35
9772948	6C	0.79	0.819	0.00394	0.183	2.60e-20	1.48
	7C	0.81	0.00341	0.215	0.138	8.17e-12	
$p = 2.3$	3C	1 (0.98)	0.174	0.0373	0.0570	0.0	1.20
14659422	6C	0.58	0.101	0.170	0.400	6.69e-18	1.69
	7C	0.93	0.0745	0.575	0.0858	1.01e-22	
$\epsilon = 0.675$	3C	1 (1.33)	0.0493	4.66e-05	0.0980	0.0	0.768
11236430	6C	0.65	0.538	0.00271	0.345	1.48e-22	0.817
	7C	0.88	0.00341	0.0768	0.0117	6.20e-23	
ϵ=1.5	3C	1 (0.97)	0.00323	0.211	0.702	0.0	1.96
11236430	6C	0.61	0.0468	0.258	0.618	3.19e-18	2.78
	7C	1.01	4.60e-04	0.741	0.00502	2.50e-18	

[a] These runs are done with initial ensembles of given sizes generated using $x = 3.0$, $T_{MaxAge} =$ 500 Myr. In these MK simulations, the model parameter(s) for dynamical and power evolution listed in the first column is(are) varied, the rest are same as in default MK (Manolakou & Kirk 2002). The results do not exclude sources with total linear size, $D < 1$ kpc; see discussion in the last two paragraphs of Section 4.5.

[b] Parameter values set equal to those given in the MK model (Manolakou & Kirk 2002); see Table 2.1.

[c] Always, $\text{Ratio}_{3C} = 1$, because of the way it is defined. The number in parentheses gives the ratio of the number of sources detected in 3C simulation (with given ensemble size) as compared to the real 3C survey.

[d] Parameters defining external environment density profile are set to those of the KDA model, namely, $\beta = 1.9, a_0 = 2$ kpc, $\rho_0 = 7.2 \times 10^{-22}$ kg m^{-3}.

[e] $\rho_1 = \rho_{0\ \text{(Default)}}/1.5 = 1.133 \times 10^{-23}$ kg m^{-3}.

[f] $\rho_2 = 2 \times \rho_{0\ \text{(Default)}} = 3.4 \times 10^{-23}$ kg m^{-3}.

worse than those of the KDA and MK models.

The changes of parameters done apart from the default case for the MK power evolution model are given in Table 4.6. The simulation results were found to be

invariant on changing the hotspot radius; as already noted at the end of Section 2.6, an analytic argument indicates that the radio lobe power in the MK model is independent of the hotspot size, as long as it is assumed to be a fixed parameter.

As seen from the tables, often several of the 12 1-D K-S probabilities for some cases give acceptable fits, but it is difficult to find a single model (or a parameter variation) where all are really good fits. In other words, *none* of the models discussed here simultaneously give good fits to the data from all of the three radio surveys considered, 3C, 6C and 7C. As noted above, P and z seem to correlate together in most cases because they are related when we pick up radio sources by imposing a flux limit on them. Once again, in some cases the P and/or z fits are good and those to D are bad; and vice versa in other cases. The 1-D K-S statistic for the model runs which gave any improvement over the "improved" default case ($x = 3$, otherwise Default model parameters) are examined from Tables 4.4, 4.5 and 4.6. Listed according to the performance rank (the best one first) the modified parameters (with all others set to their default values listed in Table 2.1), having combined 1-D K-S statistics better or as good as the default are as follows.

For the KDA model (Table 4.4): $\rho_0 = 3.6 \times 10^{-22}$ kg m^{-3}, $\beta = 2.02$, $\Gamma_B = 5/3$, $a_0 = 1.5$ kpc, $\gamma_{min(hs)} = 10$, $p = 2.12$, and $\gamma_{max(hs)} = 10^7$. The variation with $\rho_0 = 3.6 \times 10^{-21}$ kg m^{-3} performs essentially equally as the default model.

For the BRW model (Table 4.5): $p = 2.001$, $\beta = 1.0$, $t_{bs} = 10^3$ yr, $r_{hs} = 1$ kpc, $a_0 = 7.5$ kpc, $a_0 = 20.0$ kpc, $\rho_0 = 3.34 \times 10^{-23}$ kg m^{-3}, and $t_{bf} = 0.01$ yr.

For the MK model (Table 4.6): $\epsilon = 1.5$, $a_0 = 7.5$ kpc, $\beta = 1.6$, $\rho_0 = 1.133 \times 10^{-23}$ kg m^{-3}, $\gamma_{max(hs)} = 3 \times 10^8$, $\gamma_{min(hs)} = 7$, $p = 2.001$, and $a_0 = 20$ kpc.

Recall that the default values (those used by the respective authors) of the corresponding parameters are all in Table 2.1.

4.5 Dependence on Radio Galaxy Maximum Age

An important parameter for the generation of the initial population of radio sources according to the BRW prescription is the maximum age T_{MaxAge}. It defines the maximum active lifetime of the RG central engine and thus how long the radio lobes (being fed by jets powered by AGN activity) continue to expand. Hence it is one of the most important parameters to constrain if we are to estimate the fraction of the relevant volume of the universe occupied by radio galaxies during the quasar epoch

(Section 1.2 and Chapter 7). As our ultimate goal involves this relevant volume fraction, we aim to find the value of T_{MaxAge} which gives the best fit to the data for each of the RG evolution models. We performed simulation runs with default parameters for each of the models, using initial populations with $x = 3$ (which gives the least-bad overall 1-D K-S fits for P, D, z and α in all the models); we then set T_{MaxAge} to values in the range $50 - 600$ Myr (in intervals of 50 Myr), and obtained the following results.

For the KDA model, the combined 1-D K-S probabilities, $[\mathcal{P}(P) + \mathcal{P}(D) + \mathcal{P}(z) + \mathcal{P}(\alpha)]$ or $[\mathcal{P}(P) + 2\mathcal{P}(D) + \mathcal{P}(z) + \mathcal{P}(\alpha)]$ lacked a single maximum over the range in maximum age considered, and peaked at both 150 Myr and 500 Myr. However the higher peak was adopted and hence the best maximum age is $T_{MaxAge} = 150$ Myr. In the other two models, the combined 1-D K-S probabilities, $[\mathcal{P}(P)+\mathcal{P}(D)+\mathcal{P}(z)+\mathcal{P}(\alpha)]$ or $[\mathcal{P}(P) + 2\mathcal{P}(D) + \mathcal{P}(z) + \mathcal{P}(\alpha)]$, varied smoothly over the range in maximum age considered. In the BRW model the single peak was at $T_{MaxAge} = 250$ Myr, and in the MK model it was at $T_{MaxAge} = 150$ Myr; hence these were adopted for the subsequent runs.

Monte Carlo runs were done with the above best T_{MaxAge} for each model and with $x = 2.6$ (the default from BRW), to check if that was better. For BRW the best T_{MaxAge} when combined with $x = 3.0$, produced better statistics (in particular, less bad D fits), and was hence adopted for later runs. In all cases $x = 3.0$ was better than $x = 2.6$ by a very substantial amount. The supporting 1-D K-S statistics are given in the later parts of Tables 4.1, 4.2 and 4.3, for models KDA, BRW and MK respectively. Hence we used initial populations with $x = 3.0$ and the above "optimal" T_{MaxAge} values for each model in subsequent runs.

During the simulation runs we found that a few (for the KDA and MK models) and some more (for the BRW model) very small sources ($D < 1$ kpc) were being detected in the three modeled surveys (mostly in 3C). The actual survey data has a negligible number of such small sources, which would not normally be considered FR II types, though these compact steep-spectrum sources (e.g., Fanti et al. 1995) could well evolve into proper FR IIs. Of course, if the viewing angle is small enough the projected distance could be much smaller than the actual size. The 3C survey has 1 source with projected size $D < 1$ kpc, and 8 with sizes between 1 and 10 kpc. The 6C survey has 1 source with $D < 1$ kpc, and 6 between 1 and 10 kpc. The 7C-III survey has no source of < 1 kpc projected size, and 6 between 1 and 10 kpc.

As any such small source (with $D < 1$ kpc) will normally not be regarded as a FR II radio galaxy, we decided to put a linear size cut-off in our simulations. For the KDA and MK models a cut-off of 1 kpc was adopted. We ignored any source which had a total linear size less than 1 kpc, and removed any such source from the simulated surveys. For the BRW model we found that a cut off of 10 kpc gave much better fits than 1 kpc cut off. So in BRW we considered sources only with total linear sizes greater than 10 kpc. The KDA and MK simulations did not produce many sources with linear size < 10 kpc, hence it did not make much of a difference if we imposed a 10 kpc or a 1 kpc size cut off. Then for all the models, the projection was done (via the random number chosen to define the angle to the line of sight, which used Equation 3.17 in Section 3.3.1) such that the projected size always comes as $D > 1$ kpc. In the results presented henceforth, this D cut-off has been incorporated.

4.6 Dependences on Other Model Parameters

Using initial samples with $x = 3.0$ and $T_{MaxAge} = 150$ Myr for KDA and MK, and $x = 3.0$, $T_{MaxAge} = 250$ Myr for BRW (from the discussion in the previous section), Monte Carlo simulations were done using the same large population and varying the parameters around their default values (as in Section 4.4.2). Then only those cases that gave any improvement in statistics over the default case or were essentially as good as the default were considered further. In order to get a feel for the statistical variance involved in this methodology, three more runs (making a total of four runs) of these picked parameter sets were done using the same big population size but with different pseudo-random seeds. The means and standard deviations of the relevant 1-D K-S based statistics, $[\mathcal{P}(P) + \mathcal{P}(D) + \mathcal{P}(z) + \mathcal{P}(\alpha)]$ or $\mathcal{P}_{[P,D,z,\alpha]}$, and $[\mathcal{P}(P) + 2\mathcal{P}(D) + \mathcal{P}(z) + \mathcal{P}(\alpha)]$ or $\mathcal{P}_{[P,2D,z,\alpha]}$, for these "improved" parameter sets for each model were found.

The three cases involving variations of a single parameter which gave the best 1-D statistics (highest mean of the combined probability $\mathcal{P}_{[P,D,z,\alpha]}$) were then chosen, and models in which two of those "changes for the better" were simultaneously employed were computed. These "2-change" cases also were calculated four times (with the same large population size) as well. If these 2-change variations continued to give better performances, all three changes were incorporated together in a single run, to see if yet better fits were obtained.

Table 4.7: KDA Model Results: 1-D K-S Statistics for Best Fit Parameter Variations [a]

Model	$\mathcal{P}(K\text{–}S)$	Run 1	Run 2	Run 3	Run 4	Mean	S.D. (σ)	Rank [b]
Revised	$\mathcal{P}_{[P,D,z,\alpha]}$	1.774	1.227	1.950	1.621	1.643	0.3080	11
	$\mathcal{P}_{[P,2D,z,\alpha]}$	2.153	1.521	2.544	1.824	2.010	0.4396	10 – 11
1-Change [c]								
$\beta = 2.02$	$\mathcal{P}_{[P,D,z,\alpha]}$	1.852	1.347	1.283	1.955	1.609	0.3429	9
	$\mathcal{P}_{[P,2D,z,\alpha]}$	2.252	1.686	1.460	2.126	1.881	0.3711	10 – 11
$a_0 = 1.5$ kpc	$\mathcal{P}_{[P,D,z,\alpha]}$	1.890	1.440	1.916	1.916	1.791	0.2339	4
	$\mathcal{P}_{[P,2D,z,\alpha]}$	2.286	1.819	2.521	2.262	2.222	0.2932	5
$\rho_0 = \rho_1$ [d]	$\mathcal{P}_{[P,D,z,\alpha]}$	2.091	1.577	2.118	2.162	1.987	0.2747	1 – 2
	$\mathcal{P}_{[P,2D,z,\alpha]}$	2.288	1.856	2.520	2.717	2.345	0.3703	2
$\Gamma_B = 5/3$	$\mathcal{P}_{[P,D,z,\alpha]}$	2.283	1.239	1.825	1.355	1.675	0.4775	8
	$\mathcal{P}_{[P,2D,z,\alpha]}$	3.058	1.408	2.594	1.688	2.187	0.7703	6 – 7
$\gamma_{max(hs)} = 10^7$	$\mathcal{P}_{[P,D,z,\alpha]}$	2.013	1.383	1.250	1.681	1.582	0.3390	9 – 10
	$\mathcal{P}_{[P,2D,z,\alpha]}$	3.167	1.758	1.418	2.282	2.156	0.7616	4
$p = 2.12$	$\mathcal{P}_{[P,D,z,\alpha]}$	2.008	1.603	2.010	1.822	1.861	0.1930	3
	$\mathcal{P}_{[P,2D,z,\alpha]}$	2.565	2.199	2.787	2.381	2.483	0.2519	1
2-Changes [e]								
$\rho_0 = \rho_1$ [d]	$\mathcal{P}_{[P,D,z,\alpha]}$	2.333	1.488	2.304	1.751	1.969	0.4177	1 – 2
$p = 2.12$	$\mathcal{P}_{[P,2D,z,\alpha]}$	2.596	1.657	2.881	1.947	2.270	0.5657	3
$\rho_0 = \rho_1$ [d]	$\mathcal{P}_{[P,D,z,\alpha]}$	1.976	2.297	1.405	1.639	1.829	0.3903	6 – 7
$a_0 = 1.5$ kpc	$\mathcal{P}_{[P,2D,z,\alpha]}$	2.059	2.515	1.561	2.230	2.091	0.4006	8
$p = 2.12$	$\mathcal{P}_{[P,D,z,\alpha]}$	2.207	1.247	1.851	1.624	1.732	0.4025	6 – 7
$a_0 = 1.5$ kpc	$\mathcal{P}_{[P,2D,z,\alpha]}$	2.795	1.435	2.145	1.862	2.059	0.5706	9
3-Changes [f]								
ρ_0, p, a_0	$\mathcal{P}_{[P,D,z,\alpha]}$	2.205	2.487	1.578	1.274	1.886	0.5574	5
	$\mathcal{P}_{[P,2D,z,\alpha]}$	2.421	2.800	1.937	1.631	2.197	0.5172	6 – 7

[a] Each run is done using $x = 3.0$ and $T_{MaxAge} = 150$ Myr for the initial population of size 4861474; the 4 runs averaged here differ in the initial random seeds. The K-S statistics are calculated by excluding sources with total linear size $D < 1$ kpc.

[b] Overall rank (obtained by averaging separate ranks from the four runs) of each of the 11 KDA cases shown here; two values indicate a tie.

[c] Value of 1 parameter, as listed in the first column, is changed w.r.t. the default KDA model.

[d] $\rho_1 = \rho_{0\ (\text{Default})}/2 = 3.6 \times 10^{-22}$ kg m^{-3}.

[e] Values of 2 parameters, listed in the first column, are changed w.r.t. the default KDA model.

[f] Values of 3 parameters changed in the runs to $\rho_0 = \rho_1$, $p = 2.12$, $a_0 = 1.5$ kpc.

The 1-D K-S statistic results of these four runs (described in the previous two paragraphs) for the parameter variations of the three models are given in Appendix A. Tables A.1, A.2, A.3 and A.4 give the results for the KDA model; Tables A.6, A.7, A.8 and A.9 for the BRW model; Tables A.11, A.12, A.13 and A.14 for the MK model. The ranks of the combined statistics, $\mathcal{P}_{[P,D,z,\alpha]}$ and $\mathcal{P}_{[P,2D,z,\alpha]}$, from the four runs are shown in Tables A.5, A.10 and A.15 for the KDA, BRW and MK models, respectively.

Two sets of parameter variations are considered equivalent in performance if the difference between their means is smaller than their combined standard deviation (σ's added in quadrature). Each parameter case was assigned an overall performance rank, calculated by the average of their rank in the four runs, thereby providing a summary figure of merit.

The means and standard deviations of the combined 1-D K-S probabilities (or, $\mathcal{P}_{[P,D,z,\alpha]}$ and $\mathcal{P}_{[P,2D,z,\alpha]}$) are given in Tables 4.7, 4.8 and 4.9 for the KDA, BRW and MK models, respectively. The result for each model is given in two consecutive rows. The initial population generation parameters and the big ensemble size used are given in the table notes. The first column identifies the model by listing the parameter(s) which has (have) been varied from the default case. The second column gives which of $\mathcal{P}_{[P,D,z,\alpha]}$ or $\mathcal{P}_{[P,2D,z,\alpha]}$ the entries in the next seven columns correspond. The first row in columns 3 – 9 gives the results for $\mathcal{P}_{[P,D,z,\alpha]}$ and the second row gives results for $\mathcal{P}_{[P,2D,z,\alpha]}$. The third, fourth, fifth, and sixth columns list the combined 1-D K-S statistics, $\mathcal{P}_{[P,D,z,\alpha]}$ and $\mathcal{P}_{[P,2D,z,\alpha]}$, in consecutive rows, for runs 1, 2, 3 and 4 respectively (whose detailed results are in Appendix A as described in a paragraph before); these were done with the same ensemble size but different initial random seeds. The seventh and eighth columns give the mean and standard deviations of $\mathcal{P}_{[P,D,z,\alpha]}$ and $\mathcal{P}_{[P,2D,z,\alpha]}$ over the four runs. The final, ninth column lists the overall rank of each case (among the 11 or 14 parameter variations computed), obtained by averaging the ranks over the four runs.

4.6.1 KDA

Using the best fitting initial beam power population distribution with $x = 3.0$, and the preferred $T_{MaxAge} = 150$ Myr, the KDA models which produced combined 1-D K-S statistics within 1σ of each other consist of the parameter variations listed in Table 4.7. The cases better than the default, in order of their average rank, as

Table 4.8: BRW Model Results: 1-D K-S Statistics for Best Fit Parameter Variations [a]

Model	$\mathcal{P}(K$–$S)$	Run 1	Run 2	Run 3	Run 4	Mean	S.D. (σ)	Rank [b]
Revised	$\mathcal{P}_{[P,D,z,\alpha]}$	0.6548	0.8059	0.6011	0.6613	0.6808	0.08765	10
	$\mathcal{P}_{[P,2D,z,\alpha]}$	0.8667	0.9520	0.7376	0.9587	0.8788	0.1030	8
1-Change [c]								
$a_0 = 7.5$ kpc	$\mathcal{P}_{[P,D,z,\alpha]}$	0.6317	0.7358	1.631	1.014	1.003	0.4488	6
	$\mathcal{P}_{[P,2D,z,\alpha]}$	0.6942	0.7725	1.726	1.048	1.060	0.4693	7
$\gamma_{max(hs)} = 10^{10}$	$\mathcal{P}_{[P,D,z,\alpha]}$	0.6134	0.6908	0.7607	0.5527	0.6544	0.0907	11
	$\mathcal{P}_{[P,2D,z,\alpha]}$	0.7573	0.7033	1.058	0.7771	0.8239	0.1591	9
$p = 2.001$	$\mathcal{P}_{[P,D,z,\alpha]}$	1.369	1.390	0.8067	0.7299	1.074	0.3545	1 – 2
	$\mathcal{P}_{[P,2D,z,\alpha]}$	1.457	1.717	0.9151	0.8023	1.223	0.4362	1
$r_{hs} = 1$ kpc	$\mathcal{P}_{[P,D,z,\alpha]}$	1.212	1.387	0.8245	0.6659	1.022	0.3341	3 – 4
	$\mathcal{P}_{[P,2D,z,\alpha]}$	1.303	1.415	0.8280	0.6834	1.057	0.3562	4
$r_{hs} = 5$ kpc	$\mathcal{P}_{[P,D,z,\alpha]}$	0.7012	0.3872	0.3583	0.3670	0.4534	0.1656	14
	$\mathcal{P}_{[P,2D,z,\alpha]}$	1.233	0.6376	0.5813	0.5923	0.7611	0.3157	11 – 12
$t_{bs} = 10^3$ yr	$\mathcal{P}_{[P,D,z,\alpha]}$	1.416	0.9638	1.013	0.8713	1.066	0.2404	1 – 2
	$\mathcal{P}_{[P,2D,z,\alpha]}$	1.891	0.9928	1.043	0.9192	1.211	0.4557	2
$t_{bs} = 10^7$ yr	$\mathcal{P}_{[P,D,z,\alpha]}$	0.6819	0.8130	0.4401	0.5182	0.6133	0.1669	12
	$\mathcal{P}_{[P,2D,z,\alpha]}$	0.7482	0.8532	0.4769	0.5433	0.6554	0.1753	13 – 14
$t_{bf} = 0.01$ yr	$\mathcal{P}_{[P,D,z,\alpha]}$	1.015	0.9244	0.6702	0.6404	0.8125	0.1856	7 – 8
	$\mathcal{P}_{[P,2D,z,\alpha]}$	1.420	1.176	0.7446	0.6662	1.002	0.3576	6
$t_{bf} = 100$ yr	$\mathcal{P}_{[P,D,z,\alpha]}$	0.8296	0.5627	0.3598	0.3597	0.5279	0.2227	13
	$\mathcal{P}_{[P,2D,z,\alpha]}$	1.198	0.6649	0.4722	0.4827	0.7046	0.3410	13 – 14
2-Changes [d]								
$p = 2.001$	$\mathcal{P}_{[P,D,z,\alpha]}$	1.481	1.195	0.7595	0.7527	1.047	0.3556	3 – 4
$t_{bs} = 10^3$ yr	$\mathcal{P}_{[P,2D,z,\alpha]}$	1.680	1.309	0.8344	0.8747	1.175	0.3998	3
$t_{bs} = 10^3$ yr	$\mathcal{P}_{[P,D,z,\alpha]}$	1.017	1.325	0.4725	1.399	1.054	0.4212	5
$r_{hs} = 1$ kpc	$\mathcal{P}_{[P,2D,z,\alpha]}$	1.031	1.489	0.4865	1.586	1.148	0.5033	5
$p = 2.001$	$\mathcal{P}_{[P,D,z,\alpha]}$	1.095	1.108	0.6687	0.5204	0.8480	0.2990	7 – 8
$a_0 = 7.5$ kpc	$\mathcal{P}_{[P,2D,z,\alpha]}$	1.101	1.148	0.6913	0.5798	0.8800	0.2866	10
$t_{bs} = 10^3$ yr	$\mathcal{P}_{[P,D,z,\alpha]}$	0.8658	0.8252	0.7128	0.5312	0.7338	0.1498	9
$a_0 = 7.5$ kpc	$\mathcal{P}_{[P,2D,z,\alpha]}$	0.8997	0.8919	0.7357	0.5357	0.7657	0.1709	11 – 12

[a] Each run is done using $x = 3.0$ and $T_{MaxAge} = 250$ Myr for the initial population of size 3355926; the 4 runs averaged here differ in the initial random seeds. The K-S statistics are calculated by excluding sources with total linear size $D < 10$ kpc.

[b] Overall rank (obtained by averaging separate ranks from the four runs) of each of the 14 BRW cases shown here; two values indicate a tie.

[c] Value of only 1 parameter, as listed in the first column, is changed w.r.t. the default BRW model.

[d] Values of 2 parameters, as listed in the first column, are changed w.r.t. the default BRW model.

calculated by averaging the ranks of mean $\mathcal{P}_{[P,D,z,\alpha]}$ and mean $\mathcal{P}_{[P,2D,z,\alpha]}$ through all 11 cases for which the four large runs with equal ensemble size were done (with the other parameters set to their default values) are: $\rho_0 = 3.6 \times 10^{-22}$ kg m^{-3}; $\rho_0 = 3.6 \times 10^{-22}$ kg m^{-3} and $p = 2.12$ together; $p = 2.12$; $\rho_0 = 3.6 \times 10^{-22}$ kg m^{-3}, $p = 2.12$ and $a_0 = 1.5$ kpc together; $a_0 = 1.5$ kpc; $\rho_0 = 3.6 \times 10^{-22}$ kg m^{-3} and $a_0 = 1.5$ kpc together; $\Gamma_B = 5/3$; $p = 2.12$ and $a_0 = 1.5$ kpc together; $\gamma_{max(hs)} = 10^7$. The case $\beta = 2.02$ is worse then the default. However, none of these differences are statistically significant as even the "best" and "worst" cases of these models differ by only $\sim 1\sigma$. Note that this mean rank order is close, but not identical, to the rank which would be obtained by ordering the mean values of $\mathcal{P}_{[P,D,z,\alpha]}$ or $\mathcal{P}_{[P,2D,z,\alpha]}$.

4.6.2 BRW

For the BRW simulations (using the initial ensemble with $x = 3.0$ and $T_{MaxAge} = 250$ Myr) the models which produced combined 1-D K-S statistics within 1σ of each other consist of the parameter variations listed in Table 4.8. The cases better than the default (writing in order of average ranks, as for the KDA model) consist of the following changes (with the other parameters set to their default values): $p = 2.001$; $t_{bs} = 10^3$ yr; $p = 2.001$ and $t_{bs} = 10^3$ yr together; $t_{bs} = 10^3$ yr and $r_{hs} = 1$ kpc together; $a_0 = 7.5$ kpc; $r_{hs} = 1$ kpc; $t_{bf} = 0.01$ yr; $p = 2.001$ and $a_0 = 7.5$ kpc together. The ones with mean statistics worse than the default are: $t_{bs} = 10^3$ yr and $a_0 = 7.5$ kpc together; $\gamma_{max(hs)} = 10^{10}$; $t_{bs} = 10^7$ yr; $t_{bf} = 100$ yr; $r_{hs} = 5$ kpc. Here there are marginally statistically significant differences between the two or three "best" parameter sets and the two or three "worst" ones, at least as determined by $\mathcal{P}_{[P,D,z,\alpha]}$.

4.6.3 MK

For power evolution according to the MK prescription (after generating the initial ensemble using $x = 3.0$ and $T_{MaxAge} = 150$ Myr) the models which produced combined 1-D K-S statistics within 1σ of each other consist of the parameter variations as listed

Table 4.9: MK Model Results: 1-D K-S Statistics for Best Fit Parameter Variations [a]

Model	$\mathcal{P}(K\text{–}S)$	Run 1	Run 2	Run 3	Run 4	Mean	S.D. (σ)	Rank [b]
Revised	$\mathcal{P}_{[P,D,z,\alpha]}$	1.759	1.048	1.866	1.669	1.586	0.3673	8
	$\mathcal{P}_{[P,2D,z,\alpha]}$	2.199	1.313	2.439	2.079	2.008	0.4863	9
1-Change [c]								
$\beta = 1.6$	$\mathcal{P}_{[P,D,z,\alpha]}$	1.832	1.481	2.369	1.591	1.818	0.3953	2
	$\mathcal{P}_{[P,2D,z,\alpha]}$	2.296	2.196	3.399	2.149	2.510	0.5956	2
$a_0 = 7.5$ kpc	$\mathcal{P}_{[P,D,z,\alpha]}$	1.560	1.498	1.728	1.293	1.520	0.1796	11
	$\mathcal{P}_{[P,2D,z,\alpha]}$	1.646	2.112	2.149	1.917	1.956	0.2306	10
$a_0 = 20$ kpc	$\mathcal{P}_{[P,D,z,\alpha]}$	1.736	1.200	1.357	1.671	1.491	0.2550	10
	$\mathcal{P}_{[P,2D,z,\alpha]}$	2.531	1.732	2.005	2.415	2.171	0.3694	6 – 7
$\rho_0 = \rho_1$ [d]	$\mathcal{P}_{[P,D,z,\alpha]}$	1.974	1.323	1.607	1.815	1.680	0.2815	5
	$\mathcal{P}_{[P,2D,z,\alpha]}$	2.391	1.788	1.991	2.923	2.273	0.5003	4 – 5
$\rho_0 = \rho_2$ [e]	$\mathcal{P}_{[P,D,z,\alpha]}$	1.690	1.210	2.330	1.496	1.682	0.4749	7
	$\mathcal{P}_{[P,2D,z,\alpha]}$	2.388	1.635	3.654	2.009	2.421	0.8773	6 – 7
$\gamma_{min} = 7$	$\mathcal{P}_{[P,D,z,\alpha]}$	1.825	1.767	1.613	1.650	1.714	0.09868	3
	$\mathcal{P}_{[P,2D,z,\alpha]}$	2.110	2.286	1.995	2.582	2.243	0.2554	4 – 5
$\gamma_{max} = 3 \times 10^8$	$\mathcal{P}_{[P,D,z]}$	2.470	1.486	2.119	1.853	1.982	0.4159	1
	$\mathcal{P}_{[P,2D,z]}$	3.577	2.072	2.923	2.462	2.758	0.6473	1
2-Changes [f]								
$\gamma_{max(hs)} = 3 \times 10^8$	$\mathcal{P}_{[P,D,z,\alpha]}$	1.526	1.865	1.911	1.430	1.683	0.2406	6
$\beta = 1.6$	$\mathcal{P}_{[P,2D,z,\alpha]}$	1.742	2.917	2.511	1.973	2.286	0.5303	8
$\gamma_{max(hs)} = 3 \times 10^8$	$\mathcal{P}_{[P,D,z,\alpha]}$	2.117	1.693	1.882	1.202	1.723	0.3885	4
$\gamma_{min(hs)} = 7$	$\mathcal{P}_{[P,2D,z,\alpha]}$	2.679	2.171	2.604	1.781	2.309	0.4171	3
$\beta = 1.6$	$\mathcal{P}_{[P,D,z,\alpha]}$	1.784	1.572	1.274	1.380	1.503	0.2245	9
$\gamma_{min(hs)} = 7$	$\mathcal{P}_{[P,2D,z,\alpha]}$	2.224	1.718	1.625	1.781	1.837	0.2660	11

[a] Each run is done using $x = 3.0$ and $T_{MaxAge} = 150$ Myr for the initial population of size 4861474; the 4 runs averaged here differ in the initial random seeds. The K-S statistics are calculated by excluding sources with total linear size $D < 1$ kpc.

[b] Overall rank (obtained by averaging separate ranks from the four runs) of each of the 11 MK cases shown here; two values indicate a tie.

[c] Value of 1 parameter, as listed in the first column, is changed w.r.t. the default MK model.

[d] $\rho_1 = \rho_{0\ \text{(Default)}}/1.5 = 1.133 \times 10^{-23}$ kg m^{-3}.

[e] $\rho_2 = 2 \times \rho_{0\ \text{(Default)}} = 3.4 \times 10^{-23}$ kg m^{-3}.

[f] Values of 2 parameters, listed in the first column, are changed w.r.t. the default MK model.

in Table 4.9. The cases better than the default (writing in order of average ranks as for the KDA and BRW models) consist of the following changes (with the other parameters set to their default values): $\gamma_{max(hs)} = 3 \times 10^8$; $\beta = 1.6$; $\gamma_{max(hs)} = 3 \times 10^8$ and $\gamma_{min(hs)} = 7$ together; $\rho_0 = 3.4 \times 10^{-23}$ kg m^{-3}; $\gamma_{max(hs)} = 3 \times 10^8$ and $\beta = 1.6$ together; $\gamma_{min(hs)} = 7$; $\rho_0 = 1.133 \times 10^{-23}$ kg m^{-3}. The ones with test statistics worse than the default, but still within 1σ are: $a_0 = 7.5$ kpc; $a_0 = 20$ kpc; $\beta = 1.6$ and $\gamma_{min(hs)} = 7$ together.

4.7 Spectral Index (α) Behavior

The 1-D K-S results for the fits of the spectral index (α) calculated for all the surveys employing each model are uniformly bad, as clear from the $\mathcal{P}(\alpha)$ values enlisted in the tables. The poor qualitative fits to the α distribution were already noted by Blundell et al. (1999) for their models. Still, it is the BRW model which gives the least unsatisfactory 1-D K-S statistics for α fits.

Examining the real spectral index distribution in the 3C, 6C and 7C data (Figures 3.1a, 3.1b and 3.1c), we find that the α values of the observed sources range between $0 - 1.2$; however, a majority of the sources pile up between $\alpha \sim 0.5 - 1.0$. There is a weak positive correlation between α and D, with the spectra of larger sources steeper that the smaller ones. Also α correlates very (still more) weakly with the rest frame specific power P, where less powerful sources are only seen to have steep spectra, while the more powerful sources have both shallow and steep spectra. The correlation of α with z is negligible, with the sources more or less uniformly distributed in the $\alpha - z$ plane. The intrinsic P–z correlation in the observations (due to imposing flux limits, discussed in Section 3.2.1) makes it difficult to analyze if some trend is due to change in P or z.

The 1-D K-S statistics for α fits were extremely bad for the KDA model. Here, the spectral index distributions consist of a dense cluster at $\alpha \sim 0.58$, with no sources having smaller α and some having steeper spectral indices upto $\alpha \sim 1.0$. There is a weak $\alpha - D$ anti-correlation until $D \sim 10^3$ kpc, after which there is a trend for increasing α as D increases; but this involves only a few giant sources.

The BRW model produced mostly very poor α fits, but occasionally it gave quasi-acceptable 1-D K-S statistics, with $\mathcal{P}(\alpha) \sim 0.01$. Here, the spectral indices are almost uniformly distributed within $\alpha \sim 0.58 - 0.85$, with some sources at smaller α. There

is also a weak $\alpha - D$ anti-correlation in the BRW model; here it extends throughout the simulated results.

The MK model produced the worst 1-D K-S statistics for α. Here, the spectral indices came out very steep, with $\alpha > 0.9$ almost always found. The distribution includes a cluster at $\alpha \sim 0.9 - 1.0$, and it extends to very steep spectrum sources with $\alpha \sim 1.5$. Here there is a clear trend of α being higher as D increases in all of the 3C, 6C, and 7C simulations.

Thus, it is clear that all of the models considered to date require modifications if they are to produce adequate representations of the observed radio spectral indices. Making such modifications is an important long term goal of our future work (Section 8.5).

4.8 Additional Statistical Tests

In order to check the robustness of the quantitative tests based on 1-D K-S combined statistics, we performed some additional statistical analyses. We selected the cases of parameter variations that gave the highest combined probability, $\mathcal{P}_{[P,D,z,\alpha]}$, of each model, according to the amplified 1-D K-S test results (described in Section 4.6). We compared these nominally superior parameter sets for each model with the default versions (those with no parameter changes) by performing additional statistical tests on them.

4.8.1 2-Dimensional Kolmogorov-Smirnov Tests

The 2-D K-S probabilities for comparisons of the properties P, D, z and α, taken two at a time, for the data and the models, were computed. Table 4.10 shows results for both the default versions and the parameter sets giving the highest total 1-D K-S probability, denoted as "varied" in the table. The results are listed in a similar way as are the 1-D K-S statistics in previous tables. The first column gives the model and parameter variation (if any). The third, fourth, fifth, sixth, seventh and eighth columns list the K-S probabilities for comparisons of [P–z], [P–D], [z–D], [P–α], [z–α] and [D–α] respectively; in each case, the three rows give results for 3C, 6C and 7C, respectively.

It is non-trivial to compare the models as there are 18 values of $\mathcal{P}$ which must be considered. The general trends are discussed in Section 4.9.2.

Table 4.10: 2-D K-S Test Results for the Three Original Models [a]

Model Parameters	Survey	2-D K-S Probability, $\mathcal{P}(K–S)$					
		$\mathcal{P}(P–z)$	$\mathcal{P}(P–D)$	$\mathcal{P}(z–D)$	$\mathcal{P}(P–\alpha)$	$\mathcal{P}(z–\alpha)$	$\mathcal{P}(D–\alpha)$
KDA	3C	1.05e-06	4.27e-09	3.99e-07	4.79e-09	7.55e-08	1.45e-09
Default [b]	6C	0.816	0.0164	0.00741	3.38e-05	4.71e-05	2.17e-04
	7C	0.0108	0.0124	0.00876	0.0135	0.00763	0.00192
KDA	3C	0.531	0.0258	0.129	5.70e-15	4.86e-14	7.88e-23
Varied [c]	6C	0.445	0.370	0.244	9.88e-04	9.15e-04	0.00458
	7C	0.00832	0.251	0.226	8.73e-05	3.21e-05	5.51e-07
BRW	3C	1.47e-08	8.20e-10	1.06e-08	1.22e-08	2.05e-08	3.90e-14
Default [d]	6C	3.08e-04	0.00116	0.00944	2.81e-09	2.81e-08	5.87e-05
	7C	5.89e-08	7.40e-07	3.15e-06	2.04e-04	3.09e-05	4.30e-06
BRW	3C	0.432	1.34e-07	5.70e-07	3.68e-05	3.36e-05	2.71e-17
Varied [e]	6C	0.654	0.00918	0.0205	1.19e-05	2.92e-05	1.81e-05
	7C	2.30e-04	5.89e-04	1.60e-04	8.75e-04	1.29e-04	5.06e-05
MK	3C	5.05e-10	3.20e-13	3.40e-09	4.09e-35	1.55e-35	3.28e-31
Default [f]	6C	0.0843	0.0491	0.221	2.24e-16	3.88e-17	3.27e-13
	7C	1.98e-04	4.04e-04	4.81e-03	4.72e-10	2.36e-10	9.57e-09
MK	3C	0.0431	0.0117	0.0701	2.24e-35	2.73e-35	8.38e-34
Varied [g]	6C	0.177	0.510	0.244	2.75e-17	9.82e-18	1.50e-13
	7C	0.0247	0.0688	0.0885	3.72e-10	1.87e-10	1.05e-08

[a] 2-D K-S probabilities for different model runs, as written in the first column. The "Varied" model correspond to the parameter variation case that gave the highest combined 1-D K-S probability for that model.

[b] KDA simulations with the respective model parameters as used by the authors Kaiser et al. (1997). The initial population (of size 4397469) is generated using $x = 2.6$, $T_{MaxAge} = 500$ Myr. The 1-D K-S statistics for this case are in the first entry of Table 4.1.

[c] KDA model simulation using initial population with $x = 3.0$, $T_{MaxAge} = 150$ Myr. The power evolution is with parameter changes $\rho_0 = \rho_{0\ (\mathrm{Default})}/2 = 3.6 \times 10^{-22}$ kg m^{-3} and $p = 2.12$; the other parameters are set to their default values, for Run 1 with initial source population size = 4861474. The 1-D K-S statistics for this case are in Table A.1 (14th entry).

[d] BRW simulations with the respective model parameters as used by the authors Blundell et al. (1999). The initial population (of size 2930490) is generated using $x = 2.6$, $T_{MaxAge} = 500$ Myr. The 1-D K-S statistics for this case are in the first entry of Table 4.2.

[e] BRW model simulation using initial population with $x = 3.0$, $T_{MaxAge} = 250$ Myr. The power evolution is with parameter change $a_0 = 7.5$ kpc, with other parameters set to their default values, for Run 3 with initial source population size = 3355926. The 1-D K-S statistics for this case are in Table A.8 (2nd entry).

[f] MK simulations with the respective model parameters as used by the authors Manolakou & Kirk (2002). Initial population (of size 4397469) is generated using $x = 2.6$, $T_{MaxAge} = 500$ Myr. The 1-D K-S statistics for this case are in the first entry of Table 4.3.

[g] MK model simulation using initial population with $x = 3.0$, $T_{MaxAge} = 150$ Myr. The power evolution is with parameter change $\gamma_{max(hs)} = 3 \times 10^8$, other parameters set to their default values, for Run 1 with initial source population size = 4861474. The 1-D K-S statistics for this case are in Table A.11 (9th entry).

4.8.2 Correlation Coefficient Analyses

Spearman partial rank correlation coefficients between the observables $[P, D, z, \alpha]$ for the data and for the models were calculated for those cases for which the 2-D K-S tests were done. At first, we examined the 4-variable correlation coefficients by considering the sources of the data and model simulations in each survey separately. The correlation coefficient and the corresponding significance level results are listed in Tables 4.11, 4.12 and 4.13, for the 3C, 6C and 7C-III surveys, respectively. We could not efficiently use the data from 7C-I and 7C-II surveys, since the spectral index values for these sources are not available.

In a single flux-limited complete survey, there is a tight [P–z] correlation. This is clear from the results in Tables 4.11, 4.12 and 4.13. The coefficient between P and z ($r_{Pz,D\alpha}$) overwhelms most of the other correlations in the table. Among the others, a meaningful coefficient is found between D and α ($r_{D\alpha,Pz}$) in 3C and 7C-III (and some cases of 6C), P and α ($r_{P\alpha,Dz}$) in 7C-III, P and D ($r_{PD,z\alpha}$) in 6C. In order to dilute the [P–z] correlation and to detect correlations which exist between the other characteristics, we must combine multiple complete surveys with different flux limits (BRW).

So the full $[P, D, z, \alpha]$ datasets of the observed data or the model "simulated" data for all the relevant surveys, 3C, 6C and 7C-III, were combined together, and the four-variable Spearman partial rank correlation coefficients ($r_{PD,z\alpha}, r_{Pz,D\alpha}$, etc) were computed on the combined data. The results are presented in Table 4.14.

On the way toward computing the 4-variable coefficients, we examined the corresponding 2-variable and 3-variable correlations. The following noteworthy fact was found for the P–D correlation. The 2-variable correlation r_{PD}, was always negative, as obviously indicated by the trends in the [P–D] diagrams. However, in the 4-variable case, when correlation between P and D is found with the effects of z and α removed, a small positive correlation was seen between P and D (i.e., positive $r_{PD,z\alpha}$).

Table 4.11: 4-variable Spearman Partial Rank Correlation Analyses for 3C

Correlation Coefficient	Data	Model (3C Survey [a])					
		KDA		BRW		MK	
	3C [a]	Default [b]	Varied [b]	Default [b]	Varied [b]	Default [b]	Varied [b]
$r_{PD,z\alpha}$ [c]	-0.0305	0.0735	0.175	-0.196	-0.388	0.853	0.512
$\Sigma_{PD,z\alpha}$ [d]	-0.361	0.875	2.10	-2.36	-4.86	15.0	6.72
$r_{Pz,D\alpha}$	0.964	0.953	0.945	0.924	0.952	0.838	0.873
$\Sigma_{Pz,D\alpha}$	23.6	22.2	21.2	19.2	22.0	14.4	16.0
$r_{Dz,P\alpha}$	-0.0766	-0.134	-0.102	-0.183	-0.0178	0.111	0.184
$\Sigma_{Dz,P\alpha}$	-0.908	-1.60	-1.22	-2.19	-0.211	1.32	2.21
$r_{P\alpha,Dz}$	0.0290	0.121	0.174	0.300	0.142	-0.126	-0.102
$\Sigma_{P\alpha,Dz}$	0.343	1.45	2.09	3.68	1.70	-1.51	-1.22
$r_{D\alpha,Pz}$	0.533	-0.146	-0.782	-0.937	-0.907	0.916	0.923
$\Sigma_{D\alpha,Pz}$	7.03	-1.74	-12.5	-20.3	-18.0	18.6	19.1
$r_{z\alpha,PD}$	0.0130	-0.0274	-0.0220	-0.180	-0.0535	-0.339	-0.303
$\Sigma_{z\alpha,PD}$	0.154	-0.325	-0.261	-2.17	-0.636	-4.20	-3.71

[a] The four observables P, D, z and α for the sources from the 3C survey (whether real or simulated) only.

[b] The particular parameters used are the same as those in Table 4.10 for each of the "Default" and "Varied" cases of the KDA, BRW and MK models.

[c] Spearman partial rank correlation coefficient between two variables P and D, when the effects of the other two variables, z and α, are removed.

[d] Significance level associated with the correlation between P and D, independent of z and α.

We also found the three-variable correlation coefficients ($r_{PD,z}, r_{Pz,D}$ and $r_{Dz,P}$) for the $[P, D, z]$ data from all the surveys (3C, 6C and 7C I+II+III), which are listed in Table 4.15.

4.9 Discussion of the Results Obtained

During our multi-dimensional Monte Carlo simulation procedure we found that it is very difficult to get acceptable simultaneous fits to the radio properties P, D, z and α, for all three redshift complete subsamples of the 3C, 6C and 7C radio catalogs. This is true using either the default parameters suggested by each of these three leading models, or when considering simple variations upon them, involving changing

Table 4.12: 4-variable Spearman Partial Rank Correlation Analyses for 6C

Correlation Coefficient	Data	Model (6C Survey [a])					
		KDA		BRW		MK	
	6C [a]	Default [b]	Varied [b]	Default [b]	Varied [b]	Default [b]	Varied [b]
$r_{PD,z\alpha}$ [c]	0.314	-0.0467	0.172	-0.516	-0.573	0.510	0.496
$\Sigma_{PD,z\alpha}$ [d]	2.32	-0.343	1.28	-4.20	-4.80	4.14	4.00
$r_{Pz,D\alpha}$	0.981	0.972	0.982	0.967	0.976	0.979	0.970
$\Sigma_{Pz,D\alpha}$	16.7	15.7	17.3	15.0	16.2	16.7	15.4
$r_{Dz,P\alpha}$	-0.237	-0.0741	-0.178	-0.193	0.171	0.106	0.194
$\Sigma_{Dz,P\alpha}$	-1.72	-0.546	-1.32	-1.44	1.27	0.782	1.45
$r_{P\alpha,Dz}$	0.587	0.156	0.0791	0.370	-0.0841	0.132	0.277
$\Sigma_{P\alpha,Dz}$	4.81	1.16	0.582	2.85	-0.619	0.974	2.09
$r_{D\alpha,Pz}$	0.105	-0.00983	-0.548	-0.908	-0.880	0.911	0.832
$\Sigma_{D\alpha,Pz}$	0.751	-0.0722	-4.52	-11.1	-10.1	11.3	8.78
$r_{z\alpha,PD}$	-0.575	-0.141	-0.0558	-0.312	0.0996	-0.232	-0.429
$\Sigma_{z\alpha,PD}$	-4.67	-1.04	-0.410	-2.37	0.734	-1.73	-3.37

[a] The four observables P, D, z and α for the sources from the 6C survey (whether real or simulated) only.

[b] The particular parameters used are the same as those in Table 4.10 for each of the "Default" and "Varied" cases of the KDA, BRW and MK models.

[c] Spearman partial rank correlation coefficient between two variables P and D, when the effects of the other two variables, z and α, are removed.

[d] Significance level associated with the correlation between P and D, independent of z and α.

one or more of the parameters to plausible different values. Usually the P and z fits were correlated, due to flux limiting arguments discussed before. The fits to the 6C survey were generally better compared to those for 3C and 7C; however, we believe this is due to the smaller number of sources in the 6C catalog and the nature of the K-S test, which tends to give a higher probability value if there are smaller numbers of data points in the samples being compared. Our weighting of the "total 1-D K-S probability" by the square root of the number of sources in a survey helps to compensate for this. It was most difficult to get acceptable fits to the faintest sources, cataloged in 7C.

While varying the model parameters from their default values, the greatest improvement came from steepening the power law index for the beam power distribution

Table 4.13: 4-variable Spearman Partial Rank Correlation Analyses for 7C-III

Correlation Coefficient	Data	Model (7C-III Survey [a])					
		KDA		BRW		MK	
	7C-III [a]	Default [b]	Varied [b]	Default [b]	Varied [b]	Default [b]	Varied [b]
$r_{PD,z\alpha}$ [c]	0.166	-0.131	-0.179	-0.318	-0.236	0.112	0.482
$\Sigma_{PD,z\alpha}$ [d]	1.15	-0.910	-1.28	-2.33	-1.69	0.777	3.64
$r_{Pz,D\alpha}$	0.916	0.810	0.892	0.612	0.746	0.733	0.686
$\Sigma_{Pz,D\alpha}$	10.7	7.81	10.1	5.04	6.68	6.49	5.83
$r_{Dz,P\alpha}$	-0.189	-0.128	-0.0780	0.143	-0.0100	0.419	0.145
$\Sigma_{Dz,P\alpha}$	-1.31	-0.893	-0.553	1.02	-0.0696	3.09	1.01
$r_{P\alpha,Dz}$	0.334	-0.0132	0.355	0.265	0.258	-0.0569	-0.288
$\Sigma_{P\alpha,Dz}$	2.38	-0.0914	2.63	1.92	1.83	-0.395	-2.05
$r_{D\alpha,Pz}$	0.450	-0.0590	-0.351	-0.589	-0.809	0.951	0.935
$\Sigma_{D\alpha,Pz}$	3.32	-0.409	-2.59	-4.79	-7.78	12.8	11.7
$r_{z\alpha,PD}$	-0.210	0.175	-0.325	0.0426	-0.0170	-0.468	-0.283
$\Sigma_{z\alpha,PD}$	-1.46	1.22	-2.39	0.301	-0.118	-3.52	-2.01

[a] The four observables P, D, z and α for the sources from the 7C-III survey (whether real or simulated) only.

[b] The particular parameters used are the same as those in Table 4.10 for each of the "Default" and "Varied" cases of the KDA, BRW and MK models.

[c] Spearman partial rank correlation coefficient between two variables P and D, when the effects of the other two variables, z and α, are removed.

[d] Significance level associated with the correlation between P and D, independent of z and α.

to $x = 3$, from the $x = 2.6$ used by Blundell et al. (1999). This change improved the KDA and MK model performances greatly (Tables 4.1 and 4.3). The 1-D K-S statistics for any BRW model were never wonderful, especially the D fits (Tables 4.2, 4.5 and 4.8). Nonetheless, varying the maximum age assumed for the sources from 500 Myr to 150 Myr for the KDA and MK models and to 250 Myr for the BRW model also produced better fits (Tables 4.1, 4.2 and 4.3).

4.9.1 Comparison of Numbers of Sources Detected in the 3 Models

We found the following trends for the ratios of number of sources detected in the 6C and 7C simulations and the number in the actual catalogs, as compared to the

Table 4.14: 4-variable Spearman Partial Rank Correlation Analyses

Correlation Coefficient	Data	Model (combining all surveys [a])					
		KDA		BRW		MK	
	All [a]	Default [b]	Varied [b]	Default [b]	Varied [b]	Default [b]	Varied [b]
$r_{PD,z\alpha}$ [c]	0.0303	0.0528	0.198	0.102	0.0944	0.358	0.196
$\Sigma_{PD,z\alpha}$ [d]	0.478	0.844	3.20	1.63	1.51	5.96	3.16
$r_{Pz,D\alpha}$	0.716	0.668	0.648	0.415	0.576	0.569	0.495
$\Sigma_{Pz,D\alpha}$	14.2	12.9	12.3	7.04	10.4	10.3	8.63
$r_{Dz,P\alpha}$	-0.268	-0.274	-0.206	-0.106	-0.234	0.303	0.433
$\Sigma_{Dz,P\alpha}$	-4.33	-4.48	-3.33	-1.70	-3.78	4.97	7.37
$r_{P\alpha,Dz}$	0.147	0.0456	0.318	0.329	0.428	-0.167	-0.103
$\Sigma_{P\alpha,Dz}$	2.33	0.729	5.25	5.45	7.27	-2.68	-1.65
$r_{D\alpha,Pz}$	0.472	-0.0287	-0.640	-0.890	-0.881	0.922	0.888
$\Sigma_{D\alpha,Pz}$	8.08	-0.459	-12.1	-22.7	-22.0	25.5	22.5
$r_{z\alpha,PD}$	-0.0234	0.0970	-0.0935	-0.0237	-0.226	-0.465	-0.569
$\Sigma_{z\alpha,PD}$	-0.369	1.55	-1.50	-0.379	-3.65	-8.01	-10.3

[a] The four observables P, D, z and α for the 3C, 6C and 7C-III surveys (whether real or simulated), combined together in a single sample.

[b] The particular parameters used are the same as those in Table 4.10 for each of the "Default" and "Varied" cases of the KDA, BRW and MK models.

[c] Spearman partial rank correlation coefficient between two variables P and D, when the effects of the other two variables, z and α, are removed.

[d] Significance level associated with the correlation between P and D, independent of z and α.

3C simulations (Ratio_{6C} and Ratio_{7C}, defined in Equation 3.16). For the KDA and BRW models, the detection number ratio was more consistent for 6C than for 7C simulations; i.e., Ratio_{6C} was closer to 1.0 (which it should equal ideally) than was Ratio_{7C}. For the MK model, the detection number ratios for 6C and 7C were equally consistent, and were usually better than both the KDA and BRW predictions. Comparing the models by these detection number ratios, the MK model gives the best fit to the data, followed by KDA which gave some acceptable fits, whereas BRW gives the worst fits (almost never acceptable with respect to the Ratio_{7C}). The details of these results follow.

In most of the cases, the KDA models gave slight underdetections in 6C simulations and overdetection in 7C when compared to 3C. The Ratio_{6C} was mostly in the

Table 4.15: 3-variable Spearman Partial Rank Correlation Analyses

Correlation Coefficient	Data	Model (combining all surveys [a])					
		KDA		BRW		MK	
	All [a]	Default [b]	Varied [b]	Default [b]	Varied [b]	Default [b]	Varied [b]
$r_{PD,z}$ [c]	0.0731	0.0708	0.0281	-0.386	-0.520	0.222	0.143
$\Sigma_{PD,z}$ [d]	1.32	1.28	0.510	-7.38	-10.4	4.09	2.60
$r_{Pz,D}$	0.672	0.620	0.575	0.322	0.446	0.689	0.598
$\Sigma_{Pz,D}$	14.6	13.1	11.9	6.04	8.69	15.3	12.5
$r_{Dz,P}$	-0.322	-0.308	-0.181	-0.214	-0.0853	-0.365	-0.246
$\Sigma_{Dz,P}$	-5.99	-5.76	-3.32	-3.94	-1.55	-6.93	-4.56

[a] The three RG observables P, D and z for the 3C, 6C and 7C I+II+III surveys (whether real or simulated), combined together in a single sample.

[b] The particular parameters used are the same as those in Table 4.10 for each of the "Default" and "Varied" cases of the KDA, BRW and MK models.

[c] Spearman partial rank correlation coefficient between two variables P and D, when the other variable z is kept fixed. The null hypothesis is "correlation between P and D arises entirely from those of z with P and D separately".

[d] The significance level associated with the correlation between P and D, independent of z. $\Sigma_{PD,z}$ is normally distributed about 0 with variance = 1, if the null hypothesis is true.

range $(0.9 - 1.0)$, with few cases going up to 1.1. The Ratio_{7C} was usually between 1.3 and 1.6, and went up to 1.7 for a few cases of the simulation runs.

The BRW models gave overdetection in both 6C and 7C simulations when compared to 3C, with too many sources over-detected in 7C. The Ratio_{6C} was mostly in the range $(1.0 - 1.4)$, with a few results going to 2.0. The Ratio_{7C} usually ranged between $1.4 - 2.2$, but some cases went up to as high as 2.8. The main reason for such a high overdetection factor is the imposition of the linear size cut-off of 10 kpc in the BRW models. As a result, the 3C simulations lose more sources, since they had a greater numbers of smaller sources than do the 6C and 7C simulations (Section 4.5).

The detection number ratios were the best (closest to 1.0) for the MK models. In general, there was underdetection in 6C and overdetection in 7C when compared to 3C (as in the KDA model), but the factors were smaller than for KDA or BRW models. The Ratio_{6C} was always in the range $(0.7 - 1.0)$ and the Ratio_{7C} in between $(1.0 - 1.2)$ for the MK simulations.

Though we calculated and displayed the detection number ratios, and gave the preceeding discussion about the performances of the models in predicting these ratios,

we should not formally consider them in comparing the models. These ratios can be made closer to 1 by varying the redshift birth function or the RLF (Equation 3.6), so that the contribution of the initial radio source population at different redshifts are taken into account differently. Hence these ratios really are not good tests of the radio lobe power evolution models (KDA, BRW and MK, discussed in Chapter 2) per se.

4.9.2 Comparing Models Through Additional Statistical Tests

From the 2-D K-S test results we find that the $[P–z]$, $[P–D]$ and $[z–D]$ planes can be reasonably fitted by the "varied" models, particularly those for KDA and MK. Most of these 2-D probabilities are > 0.2 for the KDA and most exceed 0.05 for MK. Also, all of the 2-D $\mathcal{P}$'s of the "varied" BRW model not involving α are higher than those of the default BRW model. Improvements are also seen for all of the non-α MK 2-D $\mathcal{P}$'s using the "varied" model. This is also the case for only 7 of 9 $\mathcal{P}$'s of the KDA "varied" model. Still, these models cannot fit any plane involving α, with all the α-related 2-D K-S probabilities ≤ 0.01 for every model. These 2-D results provide support for the hypothesis that the "varied" models based on 1-D K-S tests are indeed better fits, as both the 1-D and 2-D statistics point to the same direction.

By comparing the values of 2-D K-S probabilities in the models of Table 4.10, we conclude that KDA model is the best (having the highest number of 2-D $\mathcal{P}$'s close to 1) in fitting the observational data, very closely followed by MK, and finally by BRW.

From the 3- and 4-variable correlation coefficient results on the combined data of the 3 surveys (Table 4.14 and 4.15) we see that the KDA model is able to match the survey data correlations very closely (at least for $[P, D, z]$). The matches to the data correlations are less good for the BRW and MK models. The parameter variation cases which were the best fits (i.e., gave highest combined $\mathcal{P}_{[P,D,z,\alpha]}$) when judged with respect to 1-D K-S tests, or the "varied" cases (Table 4.10, Section 4.8.1), are not necessarily the better cases according to the correlation analyses. The KDA default performs better than the KDA "varied" (1-D K-S best fit) case. For BRW and MK models, the default and the "varied" models perform comparably (i.e., sometimes the default verison is a better match to the data correlations and sometimes the "varied" fit is better).

Considering the signs of the four-variable correlation coefficients of the combined surveys, the MK model predicts a [P–α] anti-correlation and a [D–z] correlation which are trends opposite to those seen in the survey data and to those seen in the other models. The sign of the [D–α] correlation of the combined surveys is only predicted by MK, while the other models produce an anti-correlation; however, given the very poor α-distribution for the MK model this nominal advantage is meaningless.

From the correlation coefficient analyses (judging from the correlations obtained by combining data from all surveys together) we conclude that the KDA model fits the correlations in the data most closely, followed by BRW, and finally MK. Similar trends are also seen if we examine the coefficients obtained by considering each survey separately.

4.9.3 Discussion of [P–D–z–α] Planes

We now plot slices through the [P–D–z–α] volume (P vs z, P vs D, P vs α, D vs z, α vs D, and α vs z) for each of the simulated surveys, and examine their consistency by comparing them with the overall trends in the [P–D–z–α] planes of the actual data. We also plot the P vs. Q_0 (the jet power), and t (source age) vs. z diagrams for the simulated sources, in order to visualize the simulated source distributions in jet powers and ages. The actual data are shown in Figures 3.1a, 3.1b and 3.1c for the 3C, 6C and 7C surveys. The simulated data are shown in Figures 4.2, 4.3 and 4.4 for the default versions of KDA, BRW and MK models, respectively. Figures 4.5, 4.6 and 4.7 show the same things for the "best" parameter sets for each model, which were explored further by performing additional statistical tests on them (Section 4.8). The parameter sets of these figures are denoted as "varied" in Tables 4.10 and 4.14, and are the ones which give the highest total 1-D K-S probability within each model (as described in Section 4.8.1).

It is comforting that the plots for other "good" parameter values appear similar, while those for "worse" parameters (according to our 1-D K-S summary statistic) look less like the data. Sources are detected out to similar values of redshift, power and size in the 3C simulations as in the data. The KDA and MK models show very similar trends in P, D, and z. This is likely to be a consequence of the conclusion drawn by Manolakou & Kirk (2002) that their P–D tracks are more akin to those presented by Kaiser et al. (1997) than to those of Blundell et al. (1999). The unique features of the BRW model results are discussed below.

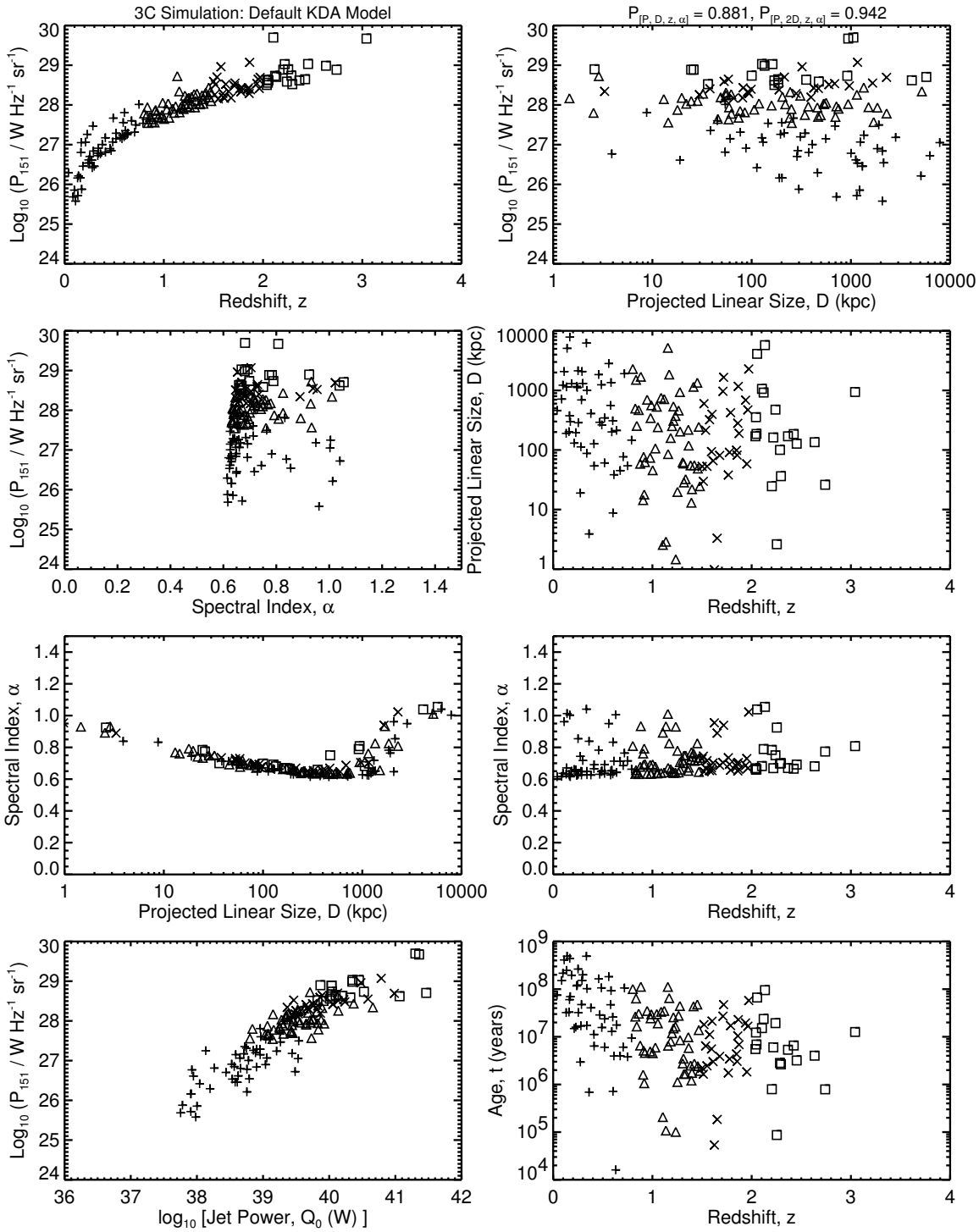

Figure 4.2a: The $[P$–D–z–$\alpha]$ planes for the 3C simulations of the default KDA model. The initial ensemble (of size 4397469) is formed using $x = 2.6$, $T_{MaxAge} = 500$ Myr; the power evolution is with the default parameter values used in KDA. The 1-D K-S statistics for this case are in the first entry of Table 4.1. Compare to Figure 3.1a.

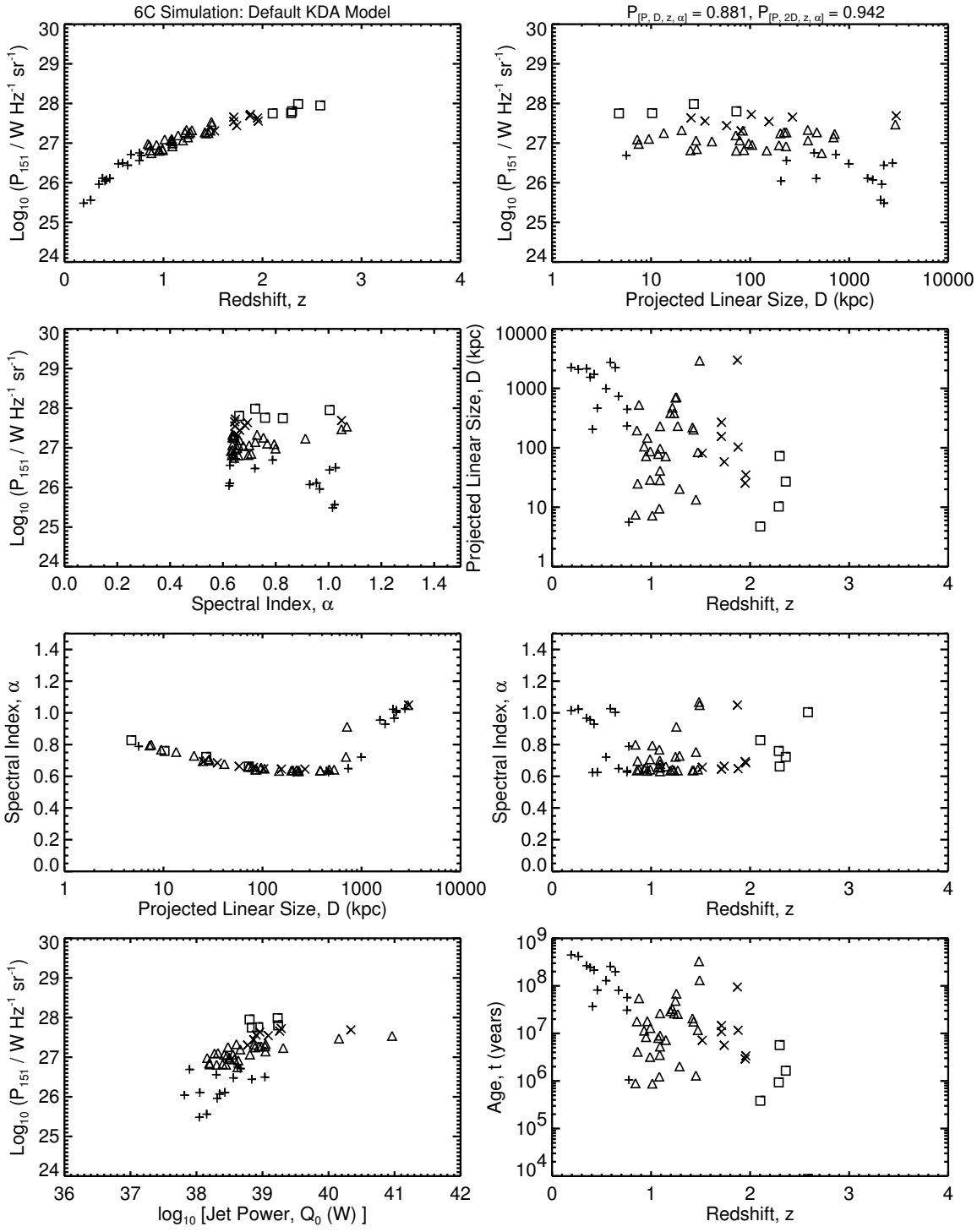

Figure 4.2b: The [P–D–z–α] planes for the 6C simulations of the default KDA. The model is the same as in Figure 4.2a. Compare to Figure 3.1b.

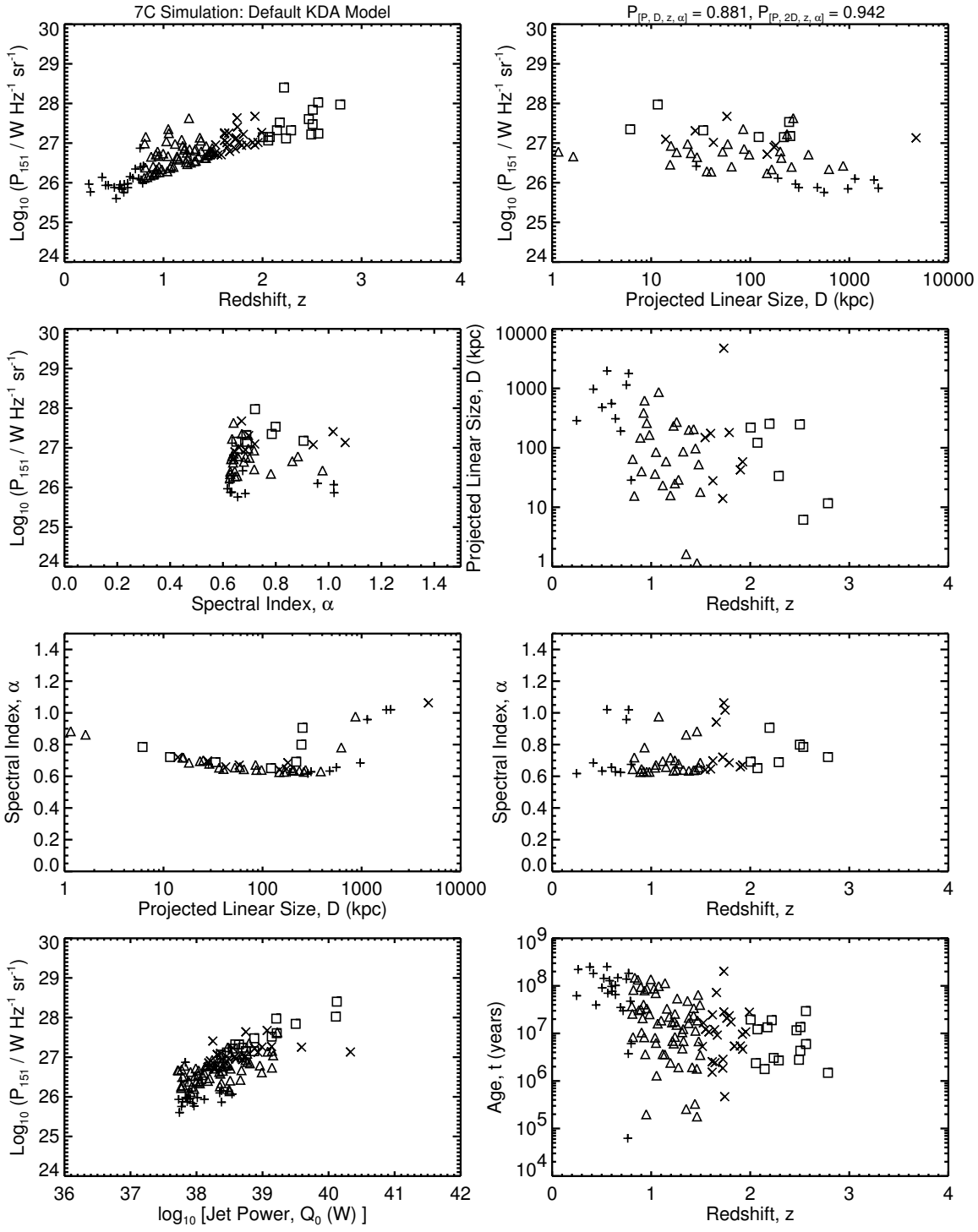

Figure 4.2c: The [P–D–z–α] planes for the 7C simulations of the default KDA. This model is the same as in Figure 4.2a. Compare to Figure 3.1c.

4.9.3.1 [P–z] Plane:

Unsurprisingly, the values of P and z exist in a cluster in the [P–z] plane, above a lower curve determined by the flux limit of the survey. Some notable features of these plots are as follows.

All of our simulated surveys of all models miss many of the low-z/low-P sources seen in the data. In particular, the simulated 7C surveys produce too few low-z sources. Very high-z sources ($z > 2.5$) are underproduced in all the 7C simulations and a similar, but less pronounced, trend is also present for 6C. All the 3C simulations present a greater scatter in P for high-P/high-z sources (at $z > 1$) when compared to the data. A few powerful, high-z sources are detected in the 3C simulations at $z > 2.0$ which are not present in the data. The scatter in P is naturally less in the 6C survey because of the imposed upper, as well as lower, flux limits.

4.9.3.2 [P–D] Plane:

Examining the [P–D] planes of the simulations, we find that the KDA and MK models overproduce small and large high power sources in 3C, and underproduce the large weaker sources. The underproduction of low-z sources is manifested in the [P–D] planes of the 6C and 7C simulations as the absence of less powerful sources (due to the P–z correlation).

There is a strong P–D evolution seen in the BRW model, which is most pronounced in the 3C and 6C simulations. The 3C simulation overproduces powerful smaller sources and misses several large powerful and weaker ones. The 6C and 7C simulations underproduce less powerful, smaller sources. Again, the KDA and MK models show a weaker P–D anti-correlation than does the data (at least for 3C), whereas the BRW model shows too strong an anti-correlation.

4.9.3.3 [D–z] Plane:

The 6C and 7C simulations show a paucity of low-z and high-z sources in the [D–z] planes of all the models. The KDA and MK models overproduce very small and very large 3C sources at all redshifts. The BRW simulation presents a stronger anti-correlation of linear size with redshift, specially for 3C, where there are no large sources at intermediate redshifts.

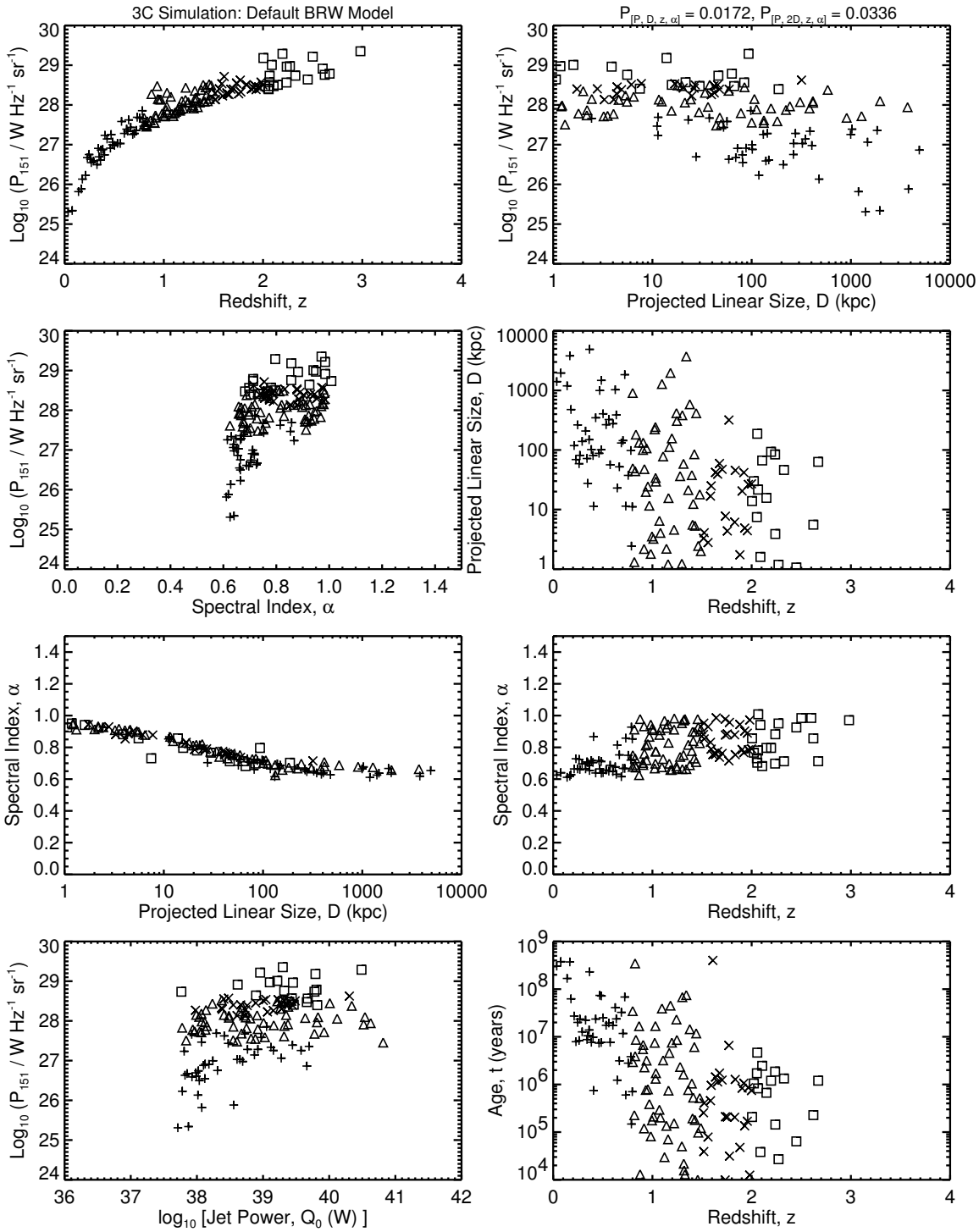

Figure 4.3a: The $[P$–D–z–$\alpha]$ planes for the 3C simulations of the default BRW model. The initial ensemble (of size 2930490) is formed using $x = 2.6$, $T_{MaxAge} = 500$ Myr; the power evolution is with the default parameter values used in BRW. The 1-D K-S statistics for this case are in the first entry of Table 4.2. Compare to Figure 3.1a.

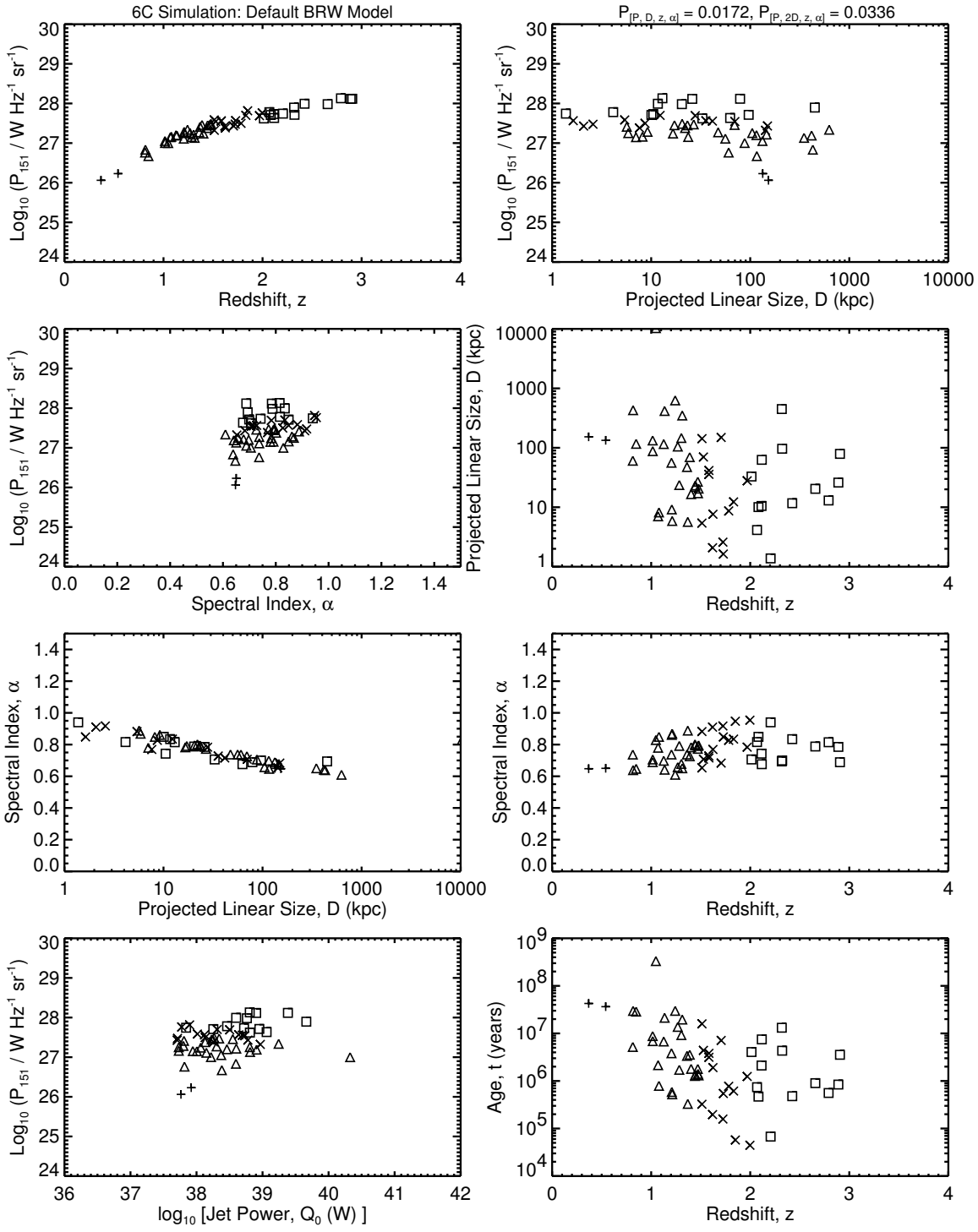

Figure 4.3b: The $[P$–D–z–$\alpha]$ planes for the 6C simulations of the default BRW model, which is the same as in Figure 4.3a. Compare to Figure 3.1b.

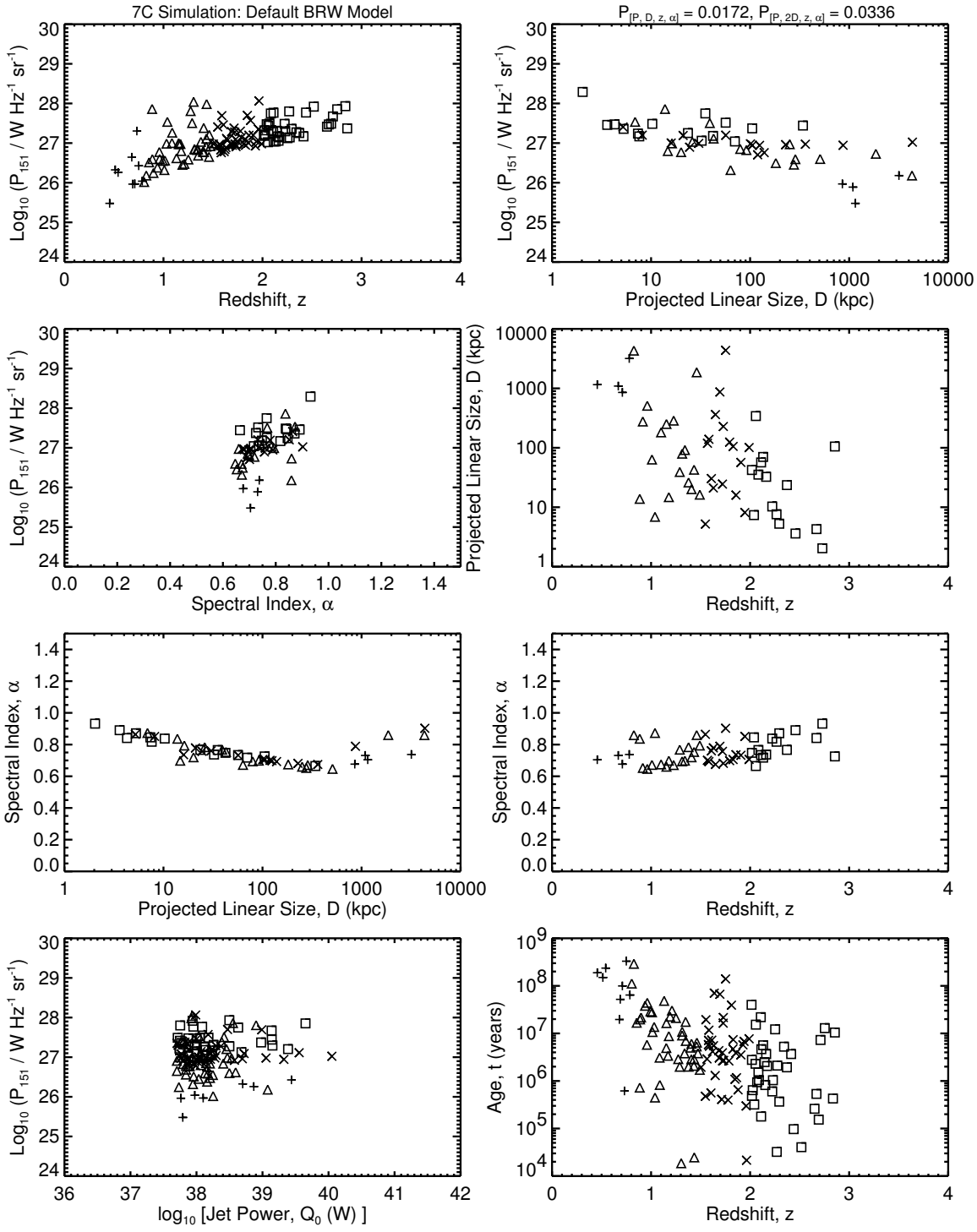

Figure 4.3c: The [P–D–z–α] planes for the 7C simulations of the default BRW model, which is the same as in Figure 4.3a. Compare to Figure 3.1c.

The D–z evolution (decrease of D as z increases) occurs due to imposing survey flux limits. This is a ramification of the "youth-redshift degeneracy" discussed in Section 4.1. The high redshift sources show a very steep decline of their luminosities with age (seen from the P–D tracks in Figure 4.1) and fall below the survey flux limits at early ages, as their radiating particles undergo severe inverse Compton losses off the cosmic microwave background and adiabatic expansion losses as they are transported from the constant high pressure hotspot to the lobes. Thus, we can only detect these high-z sources at an early age when they are still above the limiting survey flux. These younger high-z sources are naturally smaller and yield the weak "linear size evolution" (seen in the [D–z] plane). Both the KDA and MK simulations do not show this effect as clearly as does the actual data. On the other hand, the BRW simulations show stronger D–z anti-correlations than do the data.

4.9.3.4 [P–α] and [α–z] Planes:

Examining the trend of any characteristic with α shows a tight correlation with the spectral index.

The α distribution for the KDA model presents a very sharp spectral cutoff at $\alpha \approx 0.6$, with all sources having steeper spectra. Actually, a large subset of all the simulated sources pile up at α values just above 0.6, and their numbers decrease at higher spectral index values, with sources only existing until $\alpha \sim 1.0$. So the KDA model fails to produce any source flatter than $\alpha \sim 0.6$. It underproduces some of the less powerful and steep sources even in the $0.6 < \alpha < 1.0$ range.

In the BRW model, the spectral indices are almost uniformly distributed between $0.6 < \alpha < 0.85$, except for a greater number of weaker sources at $\alpha \approx 0.6$. So it does not produce any source with very flat or with very steep spectra.

The MK model always produces too many steep spectrum sources, with the spectral indices distributed between $0.9 < \alpha < 1.5$. There exists a dense collection of sources at $\alpha \sim 0.9 - 1.0$, and the number decreases at higher α. Some very steep, less powerful, sources show up (which are seen neither in the data, nor the KDA and BRW models), at the cost of less steep less powerful sources.

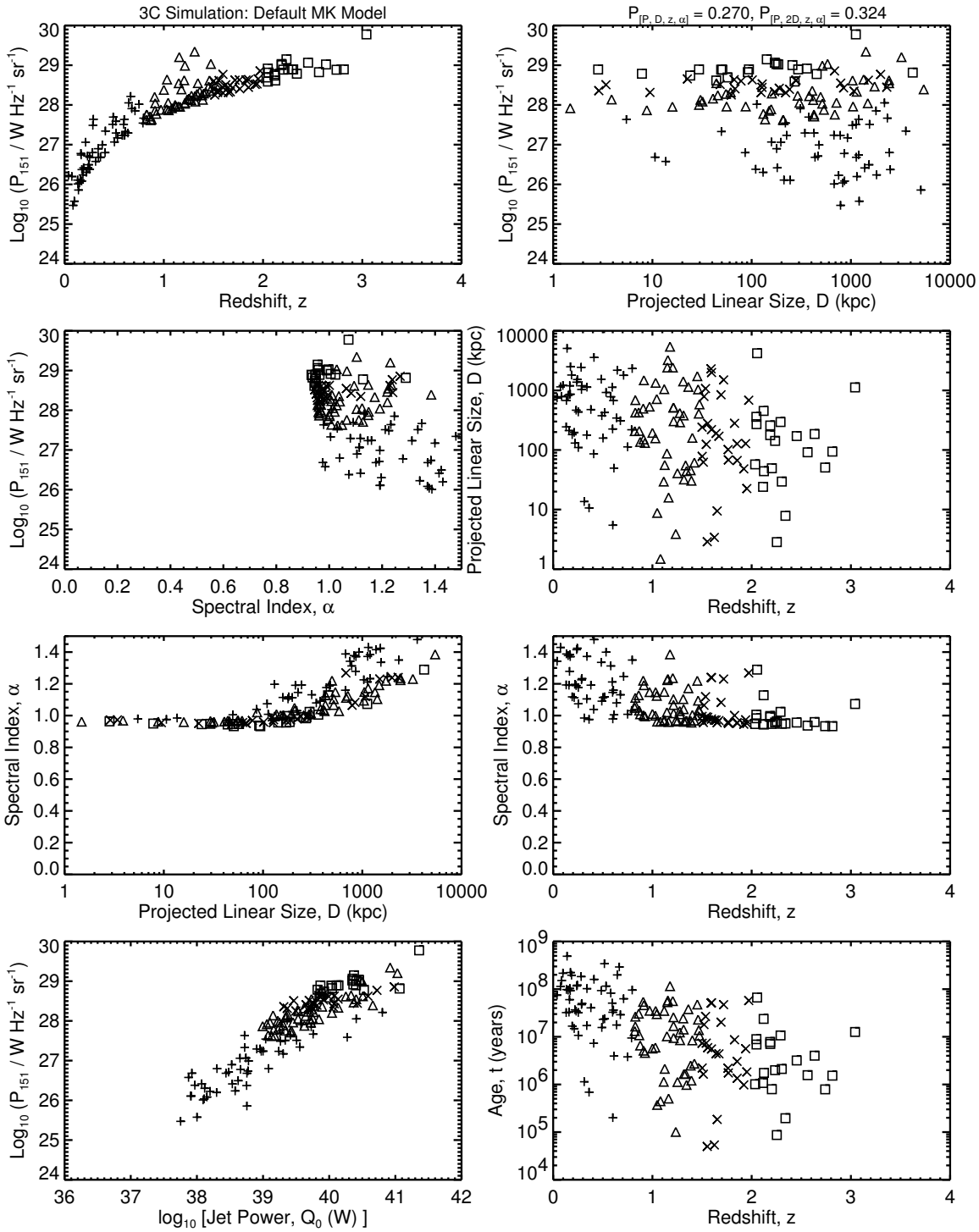

Figure 4.4a: The $[P$–D–z–$\alpha]$ planes for the 3C simulations of the default MK model. The initial ensemble (of size 4397469) is formed using $x = 2.6$, $T_{MaxAge} = 500$ Myr; the power evolution is with the default parameter values used in MK. The 1-D K-S statistics for this case are in the first entry of Table 4.3. Compare to Figure 3.1a.

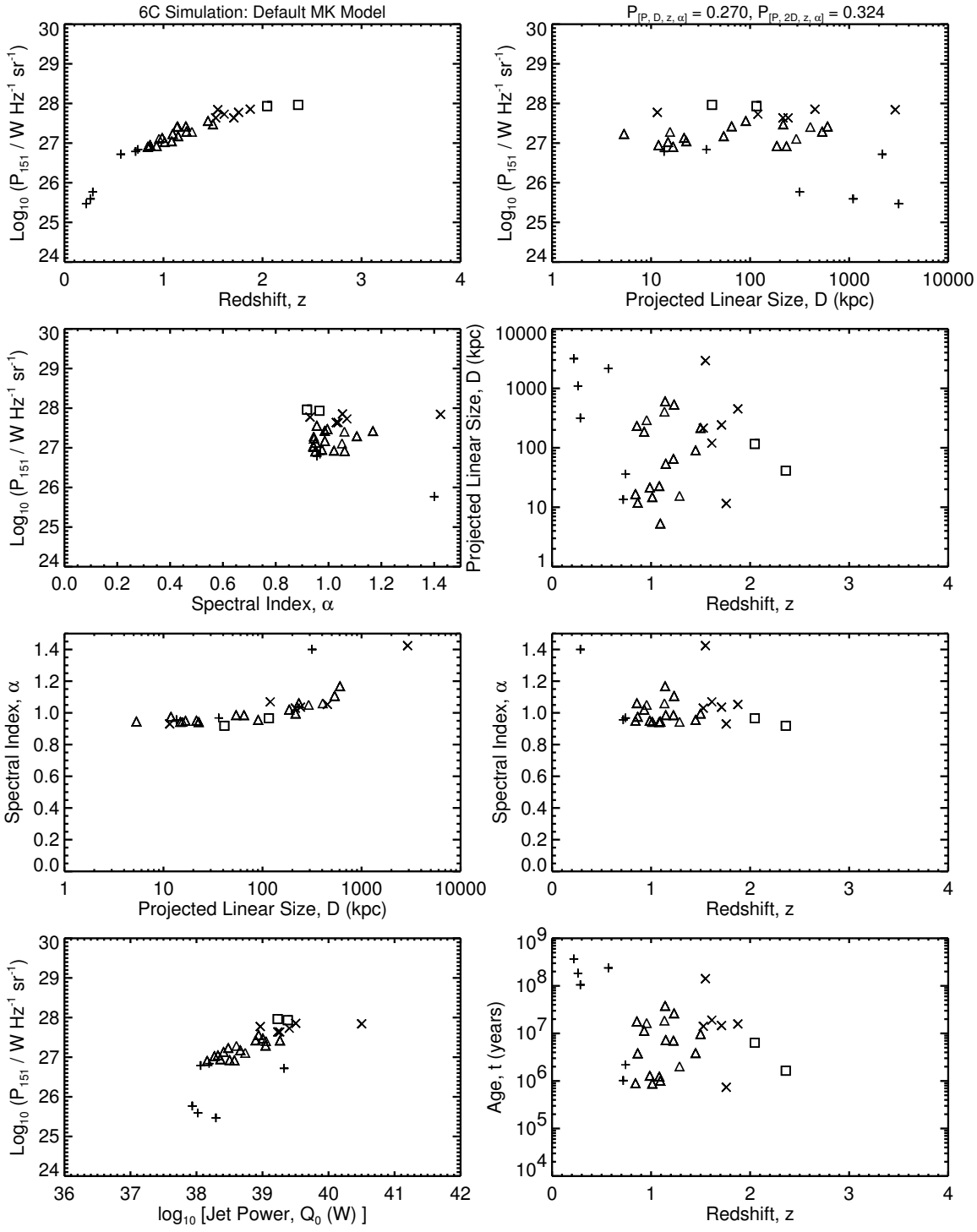

Figure 4.4b: The [P–D–z–α] planes for the 6C simulations of the default MK model, which is the same as in Figure 4.4a. Compare to Figure 3.1b.

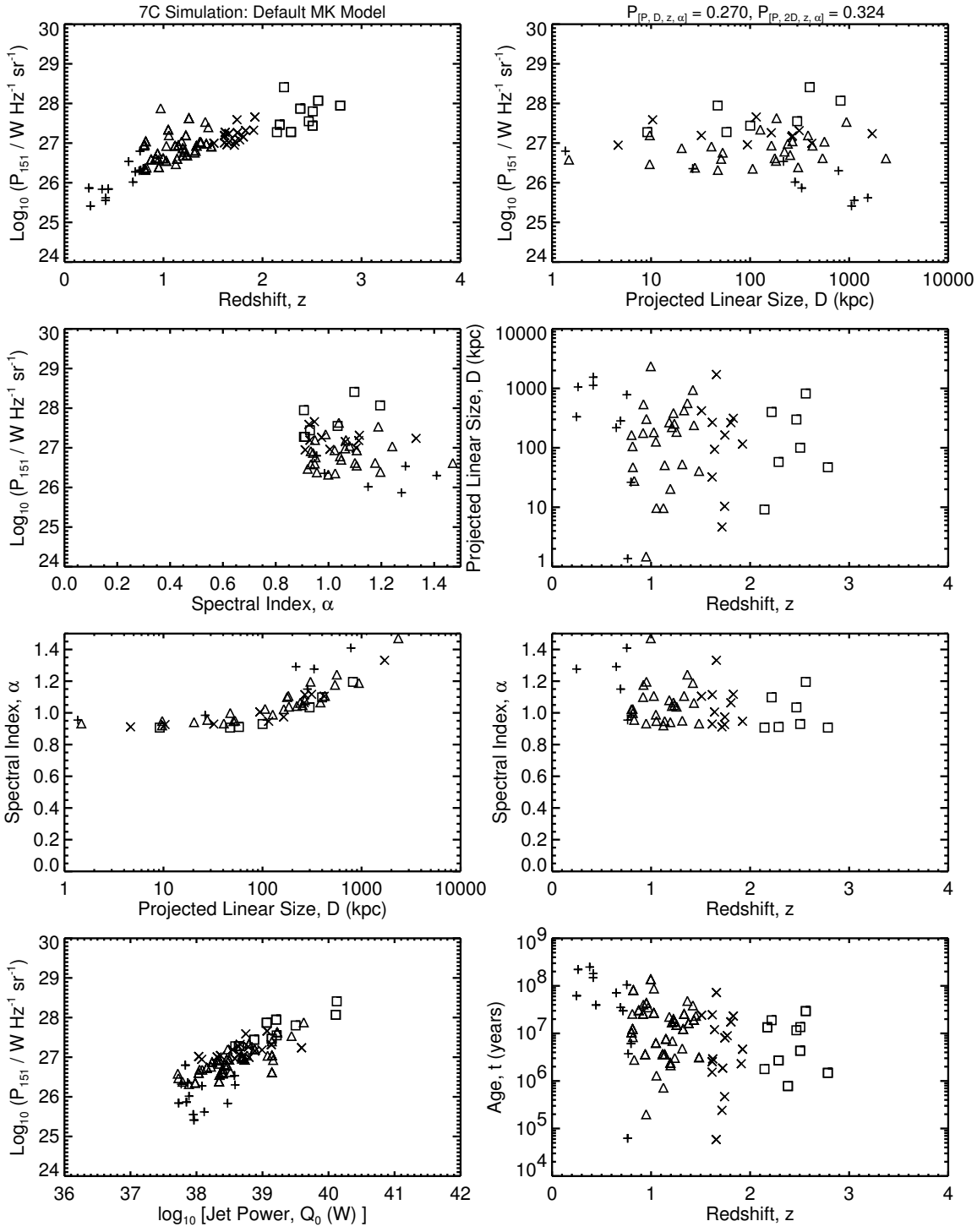

Figure 4.4c: The [P–D–z–α] planes for the 7C simulations of the default MK model, which is the same as in Figure 4.4a. Compare to Figure 3.1c.

4.9.3.5 [α–D] Plane:

The α–D plane of the KDA model shows a weak tendency of α decreasing as D increases most of the time, but the trend reverses, so that α increases with D, at linear sizes greater than $\sim$ 1000 kpc. In the BRW model, a trend of α decreasing as D increases can be seen, which continues for all D. This is opposite to that seen in data where α shows a weak trend of increasing with D. The MK model shows a trend of α increasing as D increases, and this is more pronounced at higher sizes. This trend is similar to that seen in the data, but the MK spectra are much too steep as compared to the data.

These plots confirm the conclusions from the K-S tests that none of these models gives an appropriate description of the actual spectral index distributions.

4.9.4 Best Fit Parameters of Each Model and Physical Implications

We now consider the parameter sets of each model which gave the best K-S statistical fit to the data, according to our amplified 1-D K-S test results (Section 4.6), and the additional 2-D K-S tests (Section 4.8.1). Below we discuss the physical implications of these parameters for the conditions prevailing in FR II RGs and their environments.

4.9.4.1 KDA:

The means and standard deviations of 1-D K-S performance statistics for the relevant parameter sets for the KDA models are given in Table 4.7. Considering all single-parameter, double-parameter and triple-parameter changes, the cases giving the three best fits (in order of their mean $\mathcal{P}_{[P,D,z,\alpha]}$) to the data samples are those with the following variations (with other parameters the same as default values): $\rho_0 = 3.6 \times 10^{-22}$ kg m^{-3}; $\rho_0 = 3.6 \times 10^{-22}$ kg m^{-3} and $p = 2.12$ together; $\rho_0 = 3.6 \times 10^{-22}$ kg m^{-3}, $p = 2.12$ and $a_0 = 1.5$ kpc together. The "preferred" value of the central density, ρ_0, is half of the default value and the slightly preferred scale length, a_0 (= 1.5 kpc), is somewhat smaller than the default of 2 kpc. This implies that a lower central density at a smaller scale length gives better fit to the observational data. Hence (according to the best fits here), the ambient medium around a typical RG out to $\approx$ 100 kpc from the center, would be less dense than that deduced by Forman et al. (1985). The preferred energy distribution exponent $p = 2.12$ is slightly lower

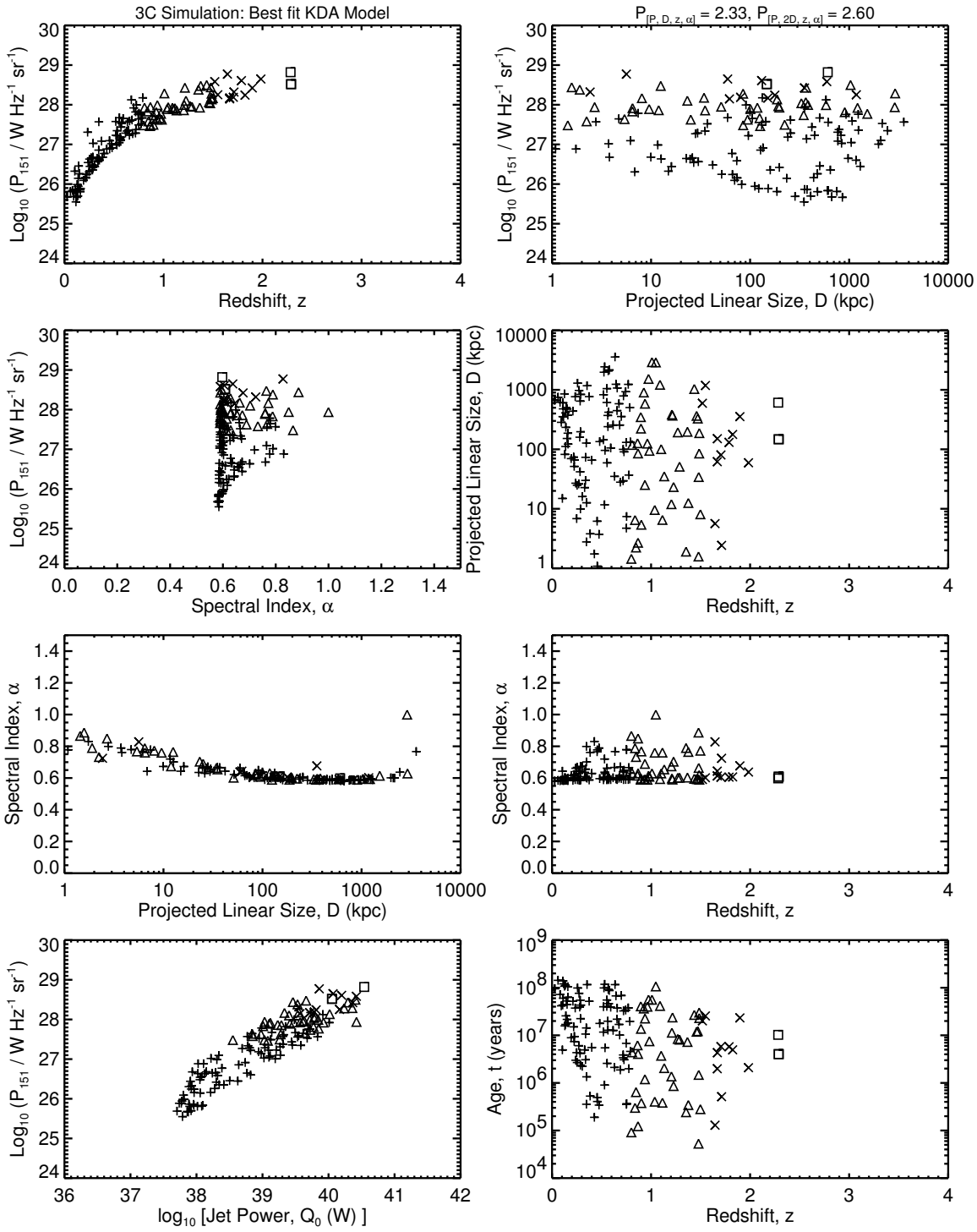

Figure 4.5a: The $[P$–D–z–$\alpha]$ planes for the 3C simulations of the best fit KDA model. The initial ensemble (of size 4861474 – Set 1) is formed using $x = 3.0$, $T_{MaxAge} = 150$ Myr; the power evolution is with parameter variations $\rho_0 = \rho_{0(\mathrm{Default})}/2$ and $p = 2.12$, the rest being their default values as in the KDA model. The 1-D K-S statistics for this case are in Table 4.7 (8th row, Run 1) and in Table A.1 (14th entry). Compare to Figure 3.1a.

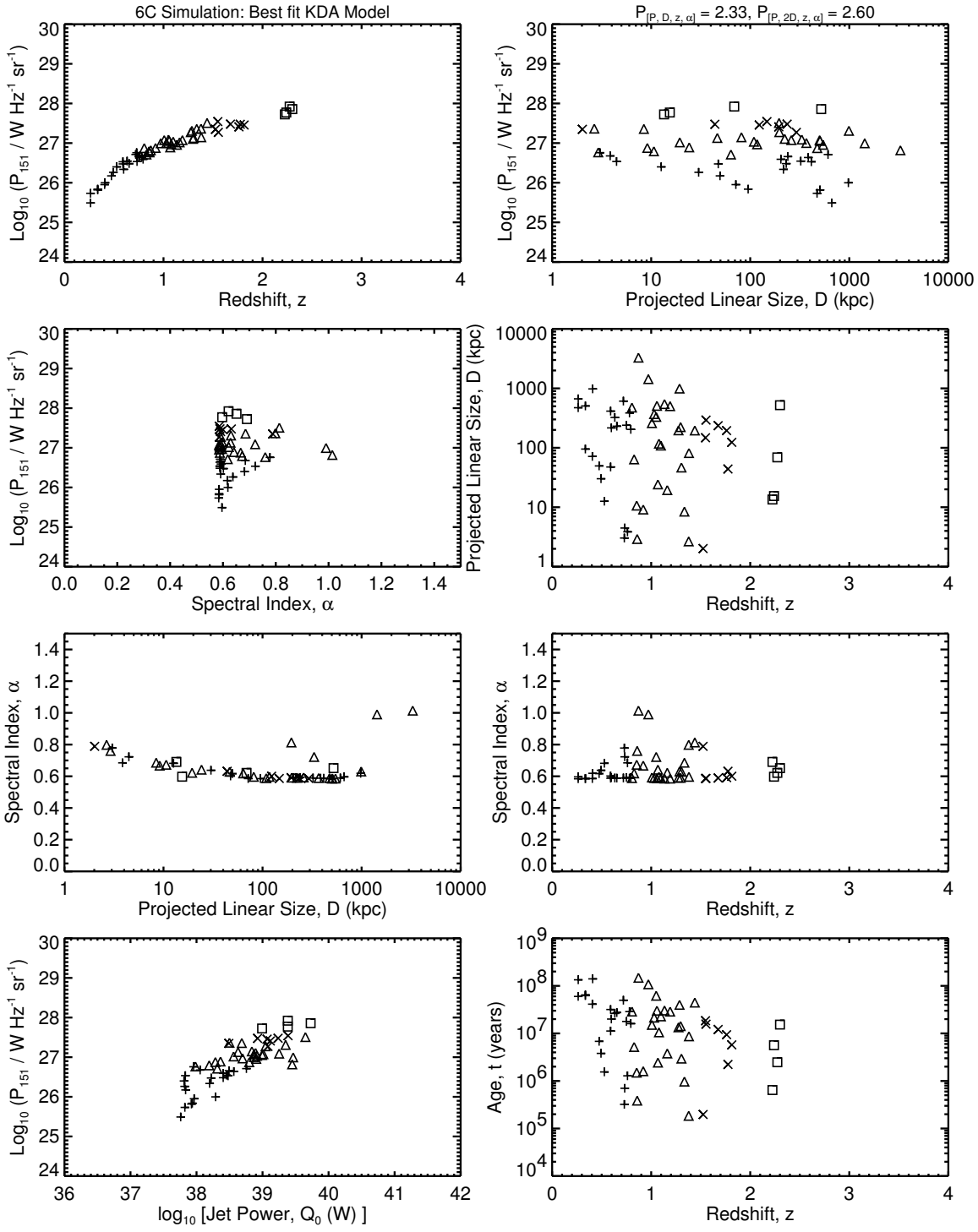

Figure 4.5b: The $[P$–D–z–$\alpha]$ planes for the 6C simulations of the best fit KDA model, which is the same as in Figure 4.5a. Compare to Figure 3.1b.

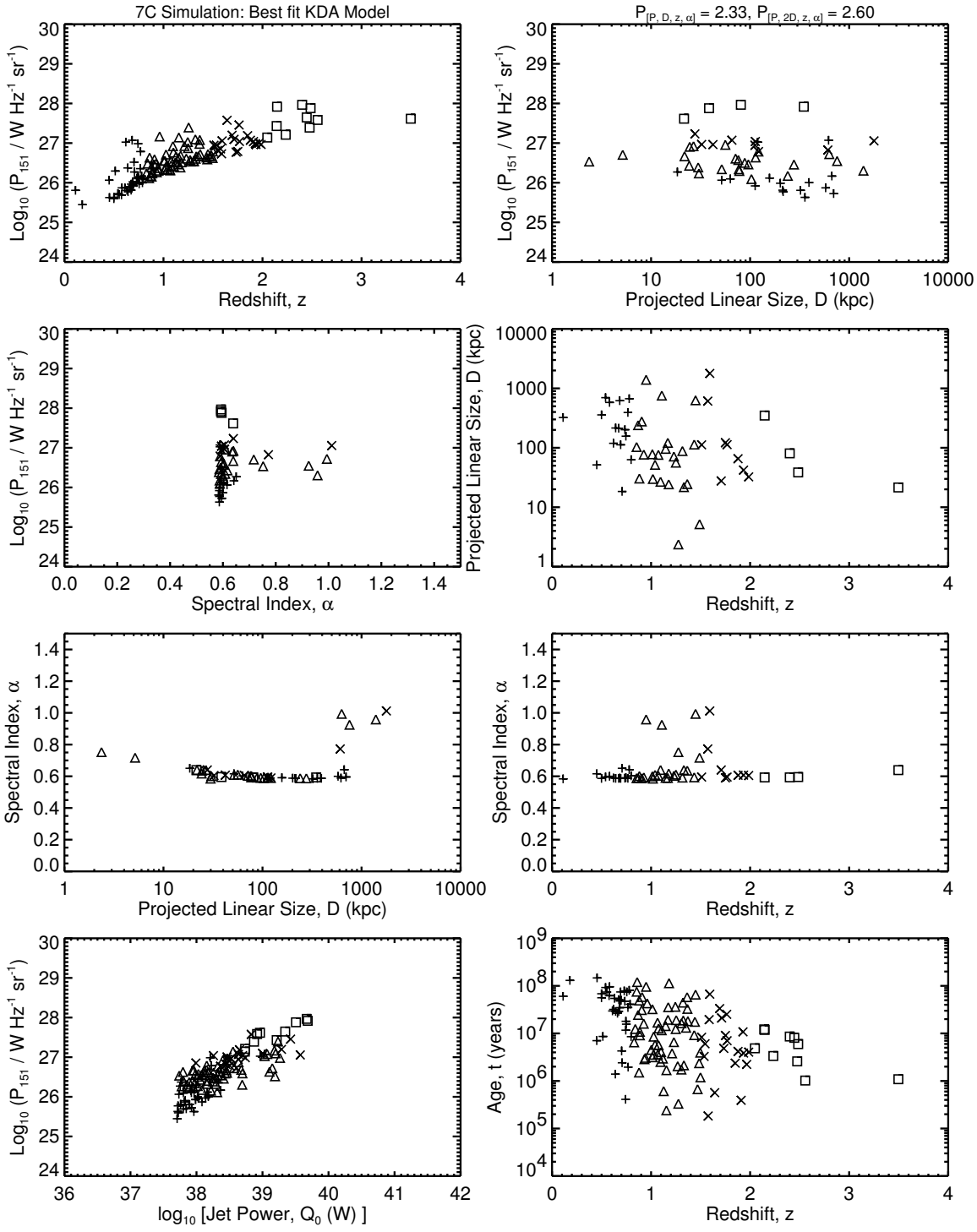

Figure 4.5c: The [P–D–z–α] planes for the 7C simulations of the best fit KDA model, which is the same as in Figure 4.5a. Compare to Figure 3.1c.

than the default value of 2.14, implying a marginally more efficient initial acceleration mechanism while the electrons are injected from the jet to the lobe. We found that while varying the exponent from 2.0 to 3.0 (essentially the range obtained from the observed spectral indices of extended radio sources), the resulting lobe power peaked at $p = 2.12$. So for the energy distribution of electrons in the cocoon, an exponent (slightly lower than the default value assumed by KDA) that maximizes the power emitted gives a better fit to the observations.

4.9.4.2 BRW:

Table 4.8 lists the means and standard deviations of relevant 1-D K-S statistics for the BRW simulations. Considering all single and double parameter changes, the cases giving the three best fits to the data samples involve the following variations: $p = 2.001$; $t_{bs} = 10^3$ yr; $t_{bs} = 10^3$ yr and $r_{hs} = 1$ kpc together. Following BRW's notation in their Figure 11, a "preferred" model is "very leaky", since $p = 2.001$ (compared to the default value of 2.14). The particles (with Lorentz factors between γ_{bs} and γ_{bf}, Section 2.5) are accelerated more efficiently at the hotspot before being injected into the lobe, thus making the hotspots more leaky. The "preferred" slow break time, $t_{bs} = 10^3$ yr, two orders of magnitude smaller than the default value of 10^5 yr, implies that the slowest radiating particles reside in the hotspots (and hence are affected by the magnetic field there) for smaller times than those adopted by BRW. This again speaks for a more efficient acceleration mechanism at the hotspot for the radiating particles. The "best-fit" hotspot radius, $r_{hs} = 1$ kpc, is lower than the default of 2.5 kpc used by BRW. This provides another way for the electrons to leak out of the hotspot more quickly.

4.9.4.3 MK:

The relevant means and standard deviations of 1-D K-S combined probabilities are given in Table 4.9 for the MK model simulations. Considering all single-parameter and double-parameter changes, the cases which give the three best fits to the data samples are: $\gamma_{max(hs)} = 3 \times 10^8$; $\beta = 1.6$; $\gamma_{max(hs)} = 3 \times 10^8$ and $\gamma_{min(hs)} = 7$ together. The preferred maximum Lorentz factor of radiating particles at the hotspots, $\gamma_{max(hs)} = 3 \times 10^8$, is higher than the default value of 10^7, and the minimum Lorentz factor $\gamma_{min(hs)} = 7$ is lower than the default of 10. The former indicates that some

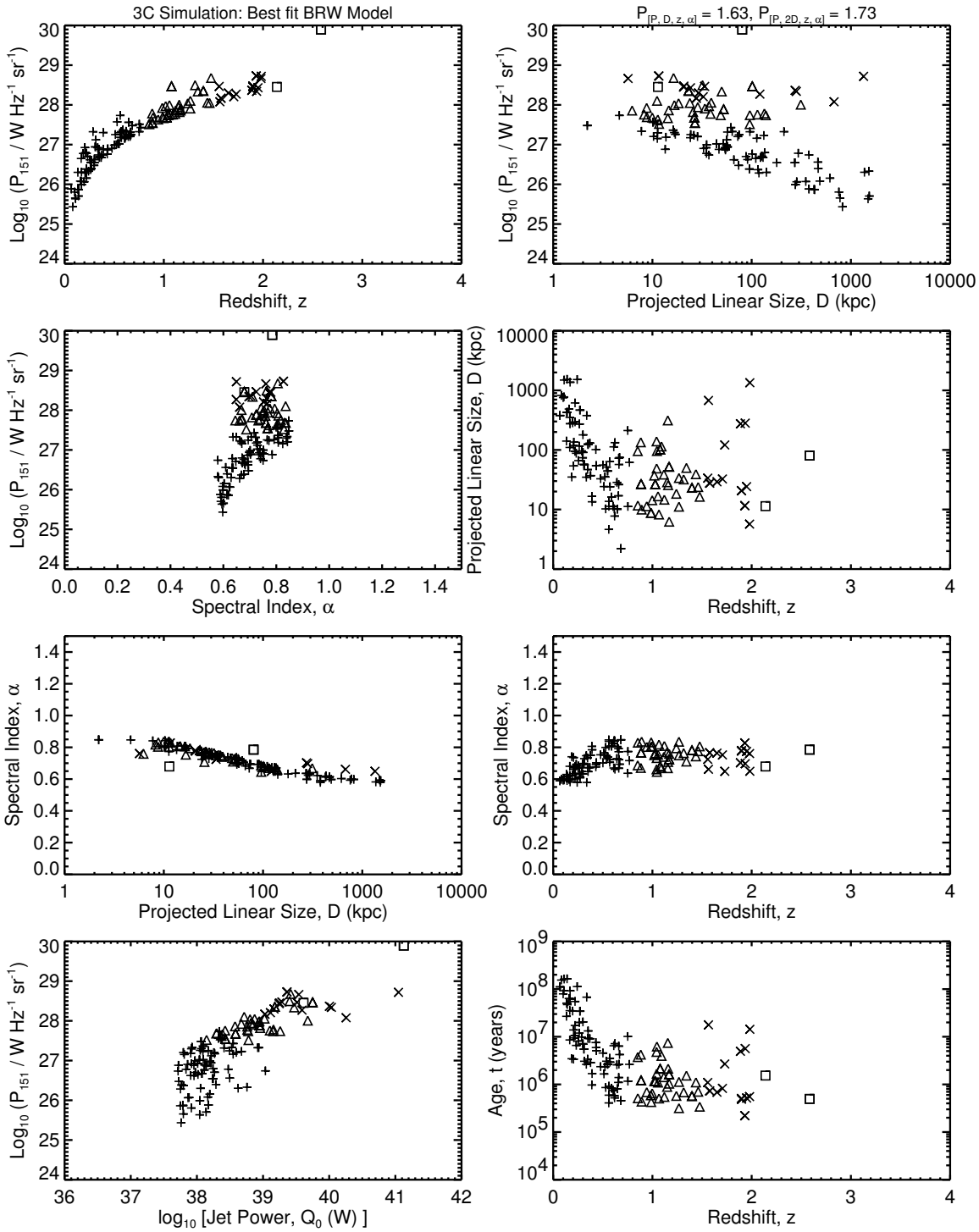

Figure 4.6a: The $[P$–D–z–$\alpha]$ planes for the 3C simulations of the best fit BRW Model. The initial ensemble (of size 3355926 – Set 3) is formed using $x = 3.0$, $T_{MaxAge} = 250$ Myr; the power evolution is with the parameter variation of $a_0 = 7.5$ kpc, with the rest being their default values as in the BRW model. The 1-D K-S statistics for this case are in Table 4.8 (2nd row, Run 3) and in Table A.8 (2nd entry). Compare to Figure 3.1a.

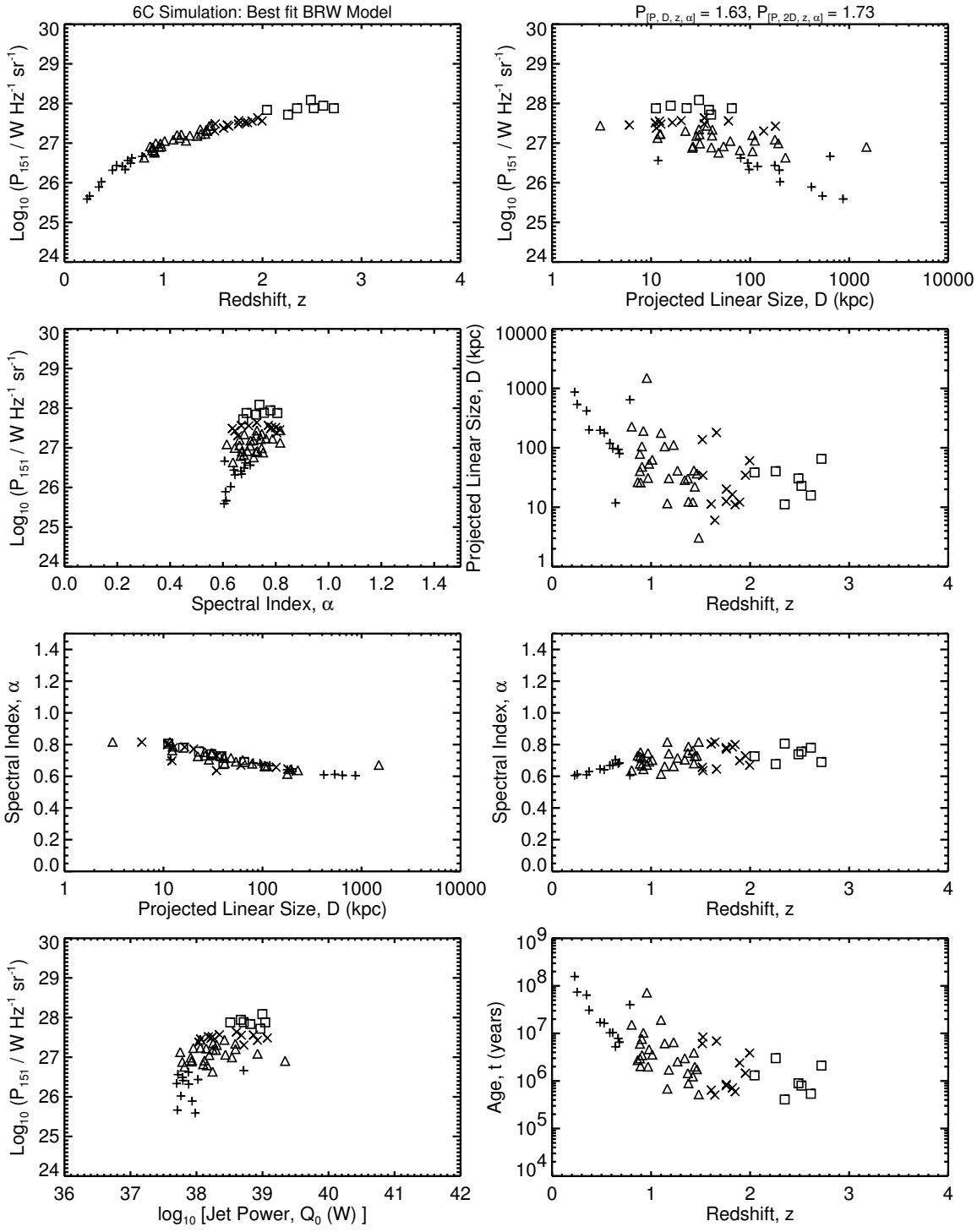

Figure 4.6b: The $[P$–D–z–$\alpha]$ planes for the 6C simulations of the best fit BRW model, which is the same as in Figure 4.6a. Compare to Figure 3.1b.

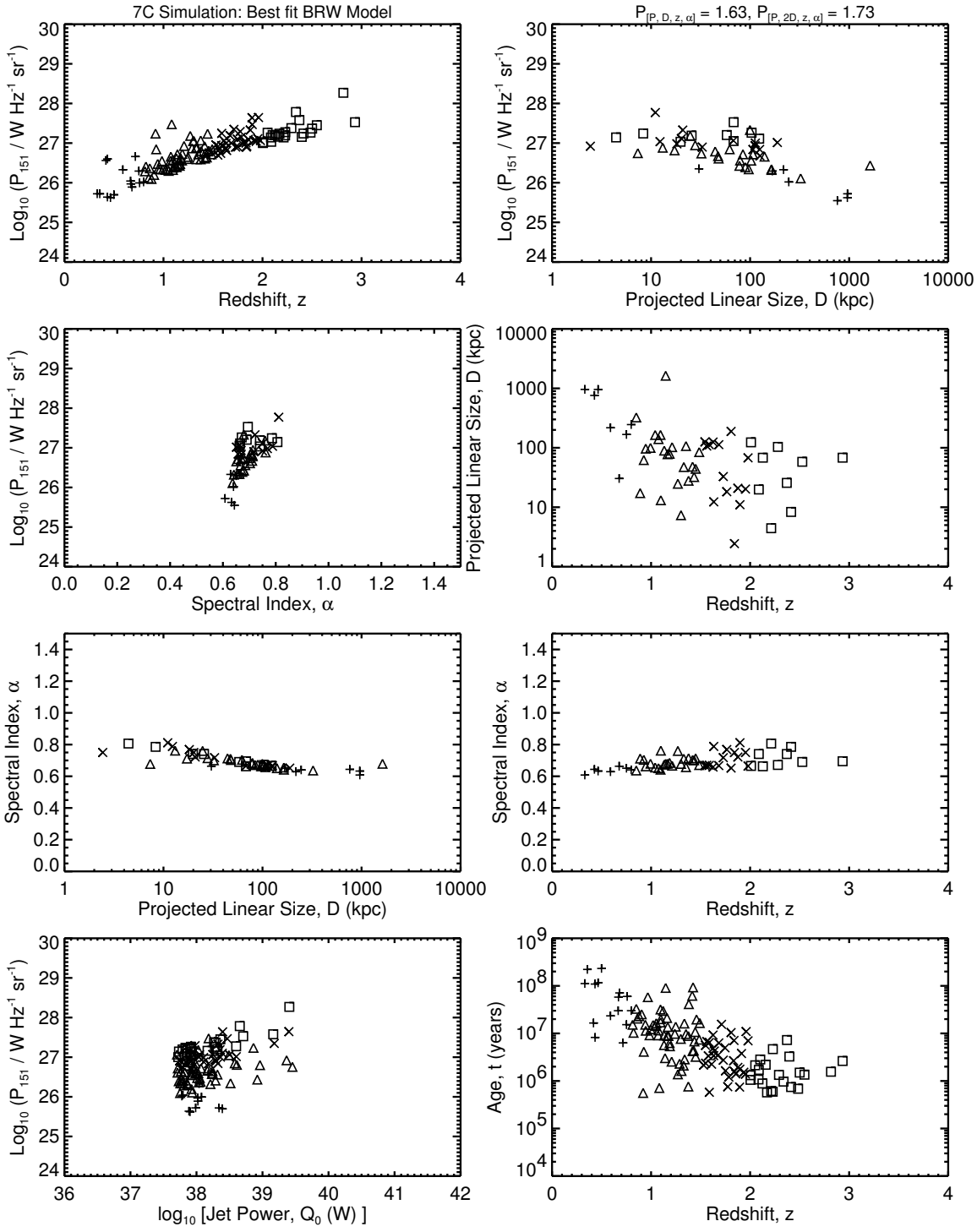

Figure 4.6c: The [P–D–z–α] planes for the 7C simulations of the best fit BRW model, which is the same as in Figure 4.6a. Compare to Figure 3.1c.

vigorous process accelerates the most energetic radiating particles to energies needed to produce microwaves from RG hotspots. The possible preference for $\gamma_{min(hs)} = 7$ implies there may be a significant contribution to the observed power from particles with low Lorentz factors. The "preferred" ambient medium density power law index of $\beta = 1.6$ is slightly higher than the default 1.5. This implies that the external environment density might fall a bit more more steeply than deduced by Mulchaey & Zabludoff (1998).

Examining the preferred parameter sets of all the models, the best fits found here weakly indicate the following: the ambient medium for RGs maybe less dense than that adopted in previous works; the acceleration mechanism in the hotspots and/or injection into the cocoon is perhaps more vigorous than usually assumed.

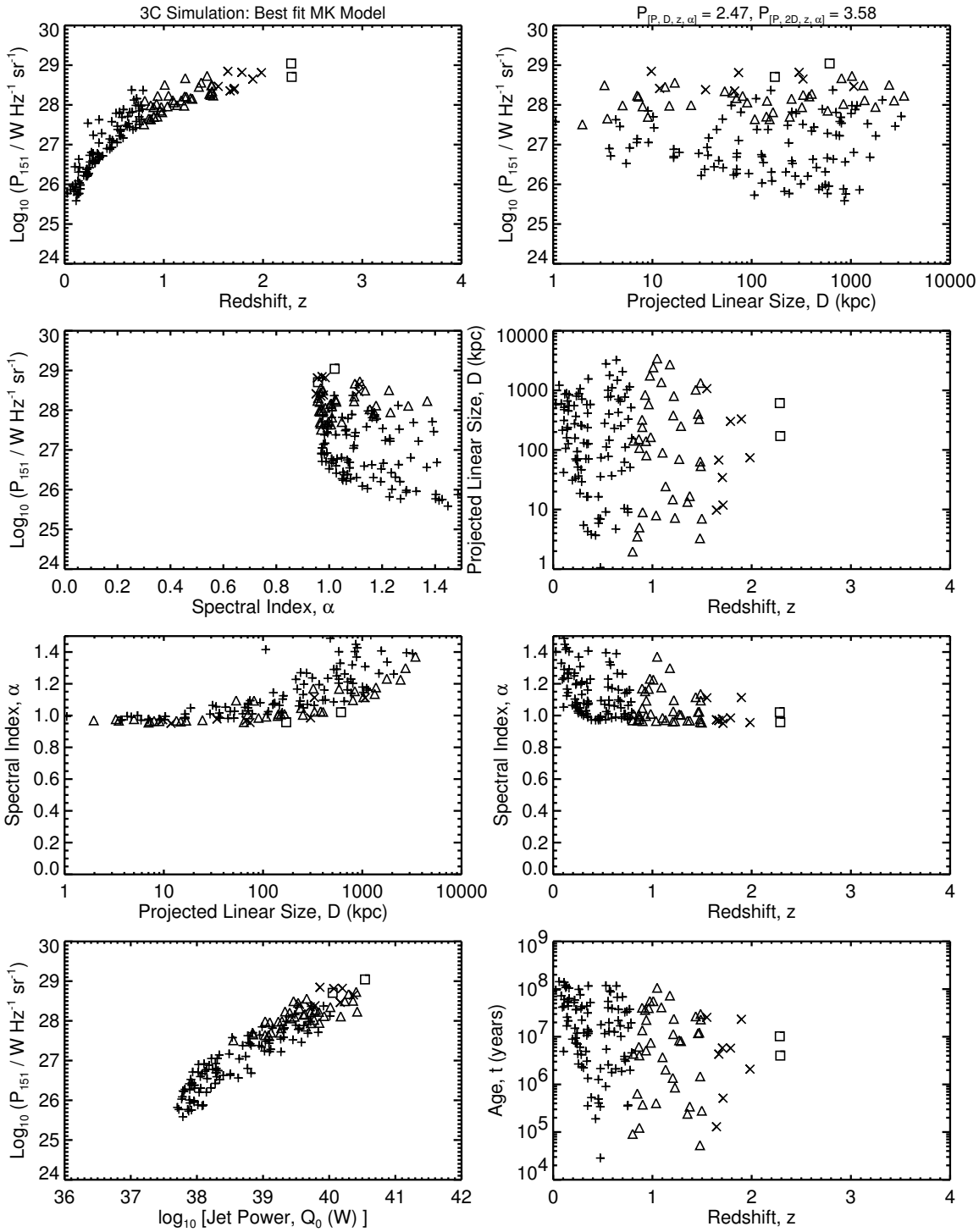

Figure 4.7a: The $[P$–D–z–$\alpha]$ planes for the 3C simulations of the best fit MK model. The initial ensemble (of size 4861474 – Set 1) is formed using $x = 3.0$, $T_{MaxAge} = 150$ Myr; the power evolution is with parameter variation $\gamma_{max} = 3 \times 10^8$, the rest of the parameters having their default values of the MK model. The 1-D K-S statistics for this case are in Table 4.9 (8th row, Run 1) and in Table A.11 (9th entry). Compare to Figure 3.1a.

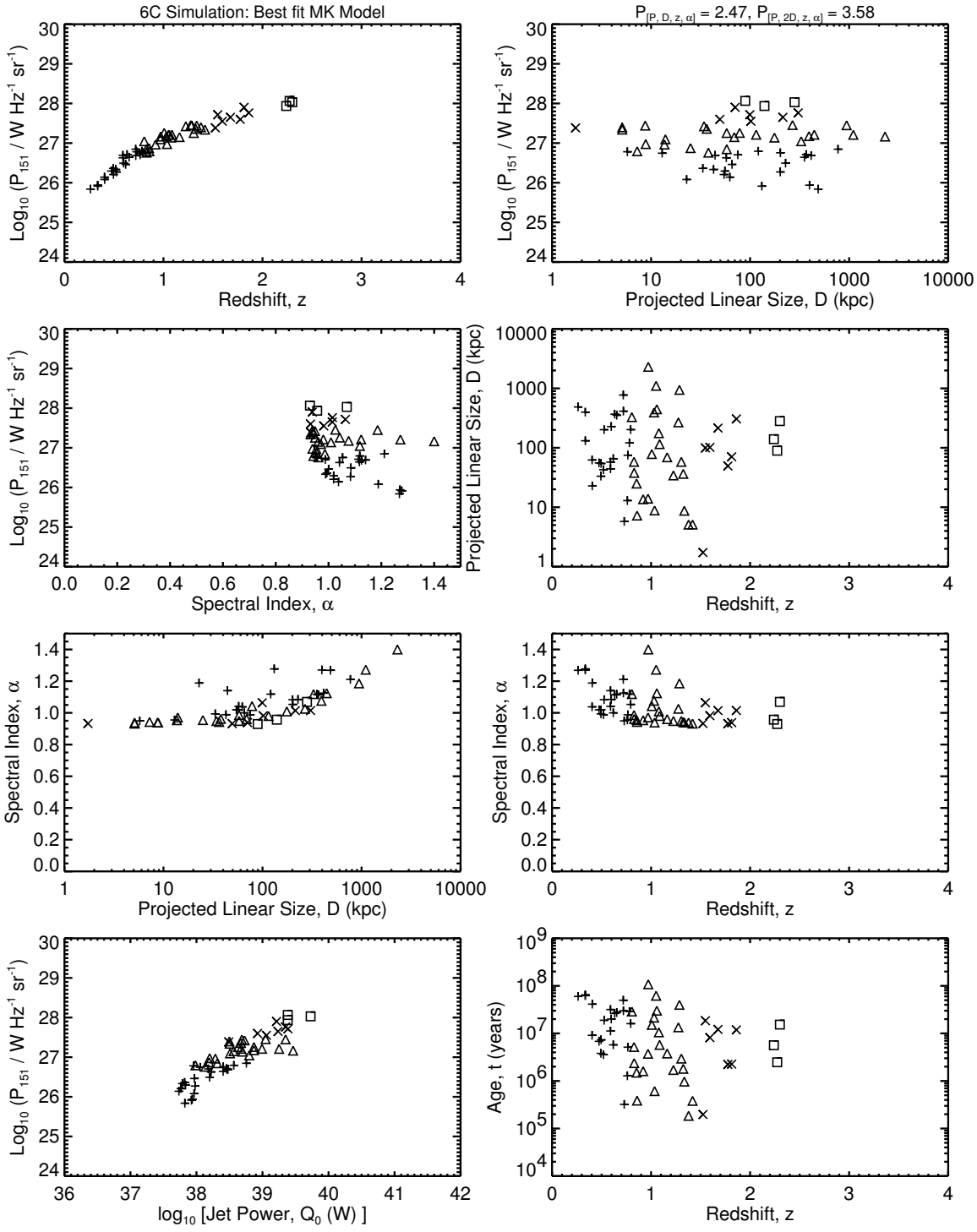

Figure 4.7b: The [P–D–z–α] planes for the 6C simulations of the best fit MK model, which is the same as in Figure 4.7a. Compare to Figure 3.1b.

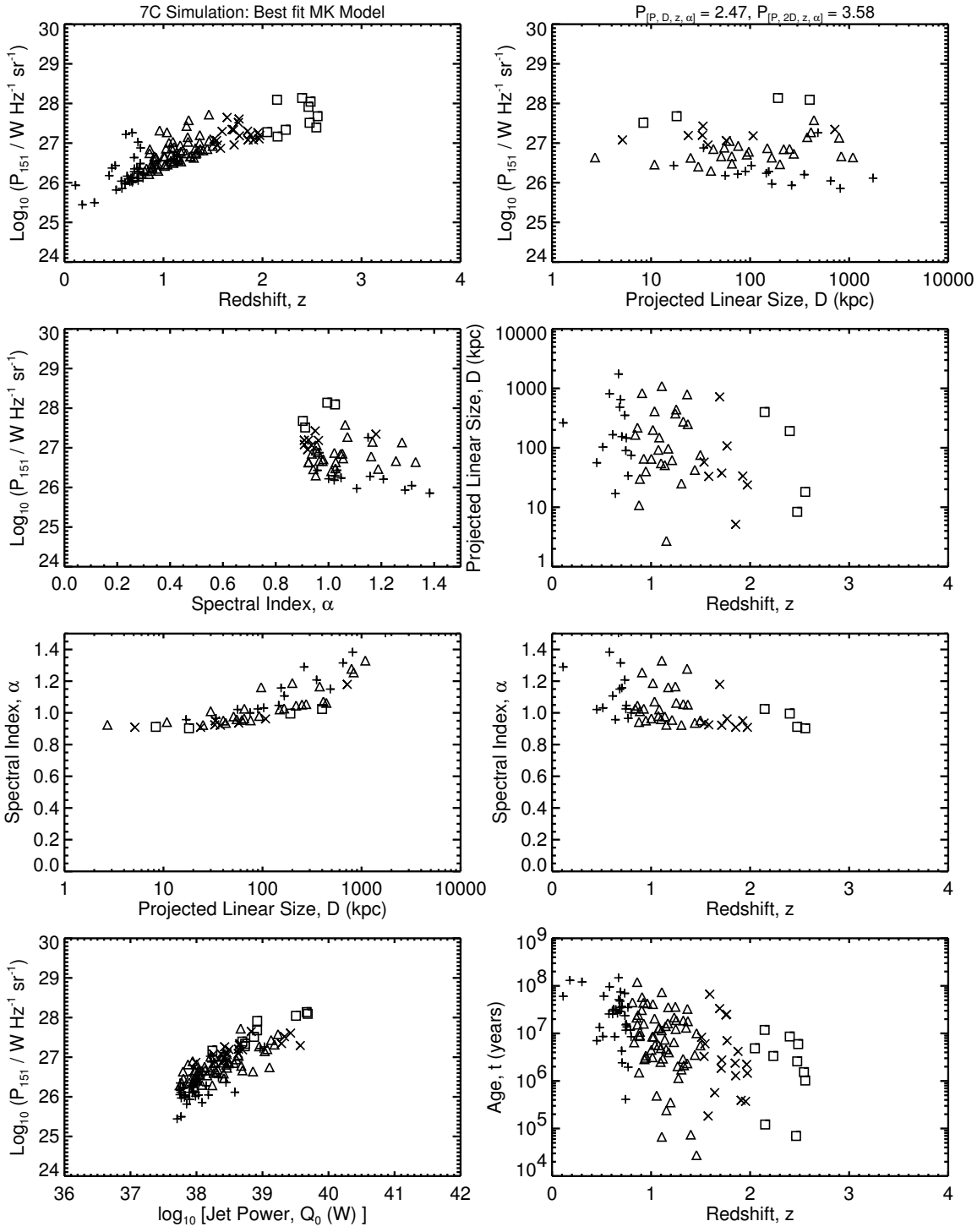

Figure 4.7c: The [P–D–z–α] planes for the 7C simulations of the best fit MK model, which is the same as in Figure 4.7a. Compare to Figure 3.1c.

– 5 –

Modified Models

I modified the original models of Blundell, Rawlings, & Willott (1999), Manolakou & Kirk (2002) and Kaiser, Dennett-Thorpe, & Alexander (1997). A variable hotspot size growing with the source age was incorporated in the BRW and MK models. The axial ratio in the KDA model was varied.

5.1 Growing Hotspot Size

The major modification to the BRW and MK models is done by allowing its hotspots to grow in size as a source ages. The data used to make a sensible modification are taken from Jeyakumar & Saikia (2000), who studied the dependence of sizes of hotspots on overall source sizes for a sample of FR II sources which included both compact steep spectrum and larger-sized sources spanning a projected source size range from about 50 pc to nearly 1 Mpc.

I parameterize the hotspot radius,

$$r_{hs} = r_{hs_0} + f(L), \tag{5.1}$$

where r_{hs_0} is some normalizing initial hotspot radius, and $f(L)$ is a power law expression of the total linear size L of the source. We choose r_{hs_0} such that the hotspot of a source grows to $r_{hs} = 2.5$ kpc when the total linear size is $L = 200$ kpc, since it is a reasonable average length and a rough average of the actual values. This is also the value which was assumed to be a constant by BRW.

The hotspot and source angular size data are adopted from Jeyakumar & Saikia (2000) as follows. We follow these authors and consider the average angular hotspot size for each source (δ_{hs}). This is the geometric mean of each hotspot (major and minor axes) sizes and, for those sources with hotspots detected on both sides, the arithmetic average of the sizes of two oppositely directed hotspots.

Each angular size is then converted to the linear hotspot diameter ($D_{hs} = 2r_{hs}$) as,

$$D_{hs} = \delta_{hs}(\text{radians}) \times D_A, \tag{5.2}$$

where D_A is the angular diameter distance. For a flat universe D_A can be found from

the following Equations (Peacock 1999, Equations 3.10, 3.76, 3.91).

$$S_k(r) = r \qquad \text{(for a flat, or } k = 0 \text{, universe)}, \tag{5.3}$$

$$R_0 dr = \frac{c}{H_0} \left[(1-\Omega)(1+z)^2 + \Omega_\Lambda + \Omega_M (1+z)^3 + \Omega_r (1+z)^4 \right]^{-1/2} dz, \tag{5.4}$$

$$D_A = \frac{R_0 S_k(r)}{(1+z)}. \tag{5.5}$$

The angular diameter distance and most of the associated symbols have been mentioned before in Section 3.2.2 (Equations 3.13 and 3.14).

The projected linear size (L_{proj}) of a source (from Jeyakumar & Saikia 2000) is analogously found from the maximum angular hotspot separation, using the angular diameter distance prescription discussed above. The total linear size (L) is obtained by assuming an average angle to the line of sight of 39.5° (as we did for the [*P*–*D*] tracks in Section 4.1 following KDA),

$$L = L_{proj} / \sin(39.5^\circ). \tag{5.6}$$

The hotspots are much smaller than the total source size and are assumed to be spherical, so the projection effects are negligible for them.

We performed least-squares fits to the $\log(r_{hs})$ vs. $\log(L)$ data, considering various types of curve (polynomial) fitting:

- Case 1 – a single straight line fit to all data,
- Case 2 – a single quadratic (second order polynomial) fit to all data,
- Case 3 – two straight line fits with a break at 20 kpc,
- Case 4 – two straight line fits with a break at 1 kpc.

The functional forms of the fit polynomials and the respective coefficients are listed in Table 5.1. The hotspot size vs. linear size data and the pictorial representation of the polynomial fits to them are shown in Figure 5.1.

Table 5.1: Hotspot Diameter, D_{hs} vs. Linear Size, L Fits (Jeyakumar & Saikia 2000) [a]

Fit Case	L (kpc) Range	$\log(D_{hs})$ Parametrization	Fit Coefficient Value c_{hs_1}	c_{hs_2} (y_1)	y_2	χ^2	Reduced χ^2
Case 1	All	$c_{hs_1} + c_{hs_2}(\log L)$	-3.227	0.8918		20.73	0.3094
Case 2	All	$c_{hs_1} + y_1(\log L) + y_2(\log L)^2$	-3.199	1.053	-0.0306	17.95	0.2720
Case 3	< 20	$c_{hs_1} + c_{hs_2}(\log L)$	-3.290	1.022		7.432	0.2859
	≥ 20	$c_{hs_1} + c_{hs_2}(\log L)$	-2.394	0.7325		10.63	0.2725
Case 4	< 1	$c_{hs_1} + c_{hs_2}(\log L)$	-2.903	1.306		3.328	0.3697
	≥ 1	$c_{hs_1} + c_{hs_2}(\log L)$	-2.926	0.8297		15.23	0.2719

[a] See text (Section 5.1) for parameter definitions and details.

A quadratic fit (Case 2) to the data gave the least reduced χ^2, although all these fits are satisfactory. So the hotspot size was taken to be growing with the source size as,

$$\log(D_{hs}) = c_{hs_1} + y_1 \log L + y_2 \left(\log L\right)^2 . \tag{5.7}$$

From this, the adopted functional form of $f(L)$ (Equation 5.1) is,

$$f(L) = \frac{D_{hs}}{2} = \frac{1}{2} \exp\left[c_{hs_1} + y_1 \log L + y_2 \left(\log L\right)^2\right] . \tag{5.8}$$

Finally, the hotspot radius was expressed as in Equation (5.1) using the above $f(L)$,

$$r_{hs} = r_{hs_0} + F_0 L^{y_1} \exp[y_2 \left(\log L\right)^2], \tag{5.9}$$

with $F_0 = \exp\left(c_{hs_1}\right)/2$. The value of r_{hs_0} to be used in the models was found by assuming $r_{hs} = 2.5$ kpc at a total linear size of $L = 200$ kpc.

5.2 BRW and MK Models Modified with Growing Hotspot Size

The hotspot radius r_{hs}, was allowed to grow with the source linear size (i.e., with source age) according to Equation (5.9) in both the BRW and MK models. Then the hotspot area, $A_{hs} = \pi r_{hs}^2$, increased with time, and other source characteristics which depend on r_{hs} (or A_{hs}) also varied as a source aged and evolved.

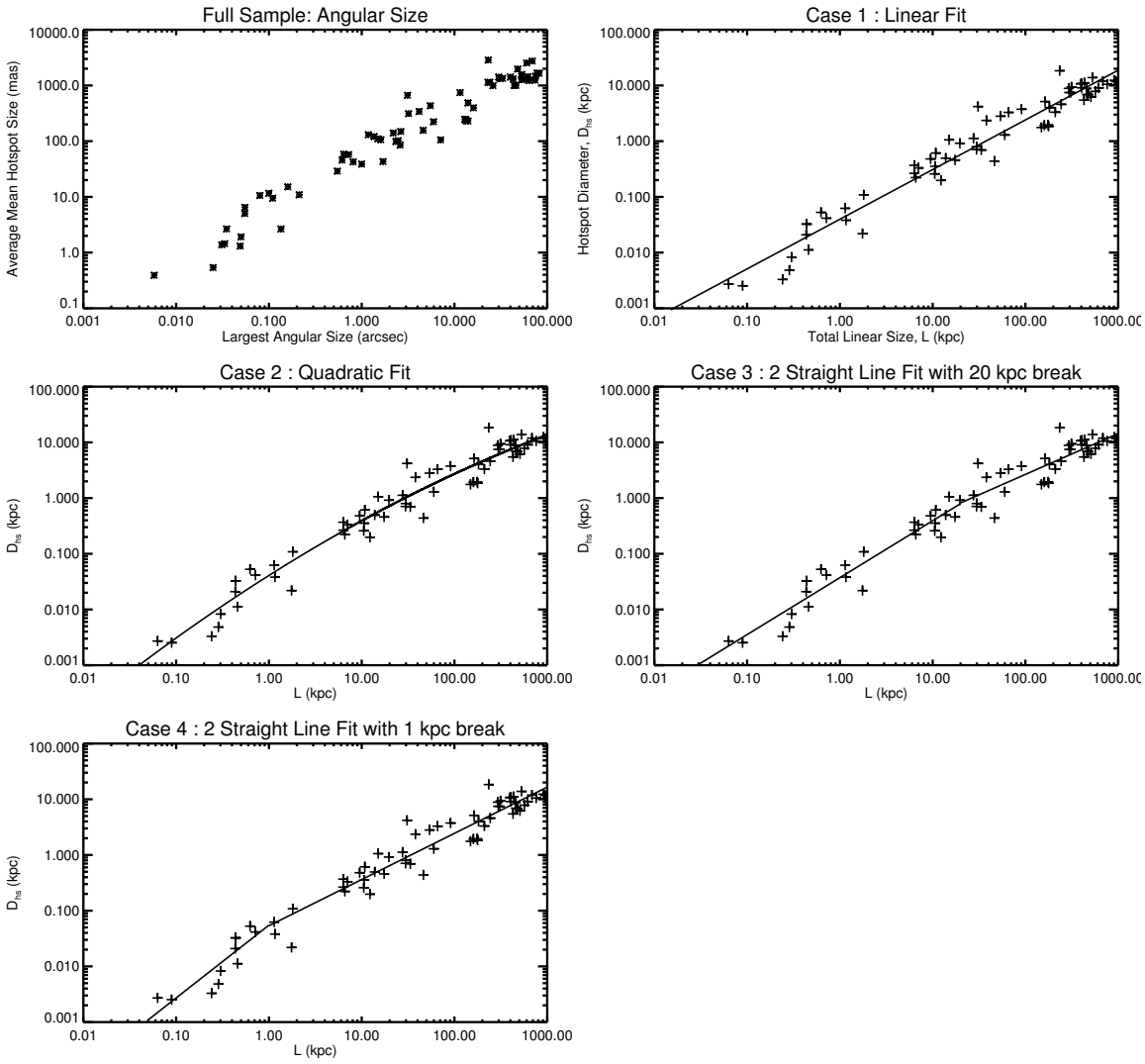

Figure 5.1: Various curve fits to [D_{hs}–L] data of Jeyakumar & Saikia (2000). The *upper-left* panel shows the actual data, the angular hotspot size vs. the linear size. The other panels show the different cases of curve fits to the data (Section 5.1).

5.2.1 BRW-Modified

In the BRW-modified model the hotspot size (and area) rises according to Equation (5.9). It otherwise follows the prescription of the original BRW model described in Section 2.5. During a source's evolution several additional quantities (which were fixed for a source when a constant hotspot size was assumed) also varied with its age. Some of these are the hotspot pressure p_{hs} (Equation 2.21), the hotspot magnetic field B_{hs} (Equation 2.22), the break frequencies ν_{bs} and ν_{bf} (Equation 2.23), and the

critical Lorentz factors γ_{bs} and γ_{bf} (Equation 2.24).

5.2.2 MK-Modified

The MK-modified model incorporates a rising hotspot size (and area) according to Equation (5.9). In the MK model, the characteristic time, t_0, (Equation 2.33) when the size of the head was comparable to the hotspot size, depends on "an initial" hotspot area $A_{hs(t_0)}$, which we must now distinguish from the normal rising hotspot area A_{hs}. We found this "initial" hotspot area using $r_{hs(t_0)} = 0.02$ kpc. We chose this value as it gave the best 1-D K-S results when we compared the statistics of 6 MK-modified simulation runs done using $r_{hs(t_0)} = 0.01 - 0.06$ kpc, computed at intervals of 0.01 kpc. So in the MK-modified model, t_0 is,

$$t_0 = \left[\frac{3c_1^{2-\beta} c A_{hs(t_0)}}{(\Gamma_x + 1)(5-\beta)^2}\right]^{1/a} \left(\frac{\rho_0 a_0^{\beta}}{Q_0}\right)^{3/(4+\beta)}, \tag{5.10}$$

with $A_{hs(t_0)} = \pi r_{hs(t_0)}^2 = \pi\,(0.02\text{ kpc})^2$.

This model otherwise follows the prescription of the original MK model described in Section 2.6.

5.3 KDA-Modified Model with Increasing Axial Ratio

The axial ratio R_T, or the ratio of the length of a source to its maximum width, is varied with time in the KDA-modified model. It otherwise essentially follows the original KDA model described in Section 2.4. The [r_{hs}–L] data from Jeyakumar & Saikia (2000) was used to constrain the rate of increase of the axial ratio, where here R'_T was assumed to be equal to the ratio of the source length and its hotspot diameter, $R'_T = L/D_{hs} = L/(2r_{hs})$. The axial ratio was considered to be growing with the source linear size as a first order polynomial (power law),

$$R'_T = F_0 \left(\frac{L}{L_0}\right)^y, \tag{5.11}$$

where L_0 is a normalizing scale length taken as $L_0 = 1$ kpc. Values of F_0 and y were initially adopted from a single linear fit to R'_T (assumed as above) vs. L data from Jeyakumar & Saikia (2000). Because there was a substantial scatter between R'_T and

L, no very good fit to expression (5.11) could be obtained directly from this dataset.

Therefore, the parameters F_0 and y were varied in search of values which gave the best overall fit when compared with respect to the following two criteria. One was statistical fit (based on combined 1-D K-S probabilities) to the observational data (3C, 6C, 7C) when multi-dimensional Monte Carlo simulations were done according to the prescriptions in Section 3.3. The other criterion was closeness of the [P–D] tracks of the KDA-modified model to those of the original KDA tracks.

The best fit statistical results along with closest [P–D] tracks were obtained using $F_0 = 5$ and $y = 0.06$. Hence, these values were used as the growing axial ratio parameters in the KDA-modified model.

In the original KDA model the source linear size (Equation 2.2) depends on c_1, and c_1 from Equation (2.5) depends on R_T albeit defined there as the lobe length to width ratio. In the KDA-modified model R'_T depends on the linear size according to Equation (5.11), and an implicit proportionality between R_T and R'_T exists. The implementation incurs an "infinite loop" problem here, which is resolved by considering a constant value of $c_1 = 1.8$ (following BRW) in the KDA-modified model.

5.4 Results of Modified Models

5.4.1 [P–D] Tracks

The power (P) vs. linear-size (D), or, [P–D] tracks of the BRW-modified, MK-modified, and KDA-modified models, as compared to the original BRW, MK, and KDA models, respectively, are shown in Figures 5.2, 5.3, and 5.4.

The modified models follow the same general trends as do the original models described in Section 4.1. The tracks are generated using the modified models (described in Sections 5.2 and 5.3) with the default values of parameters for dynamical and power evolution from each of the original models (given in Table 2.1). Each source (with beam powers and redshifts given in the plot) had been evolved at frequency $\nu = 151$ MHz. For this Figure (alone) the total linear sizes were converted to the projected sizes assuming an average viewing angle to the line of sight of 39.5° (following KDA), i.e.

$$D_{proj} = D(t) \times \sin 39.5^\circ. \tag{5.12}$$

The rate of steepening of the tracks is different in the three models, as seen from

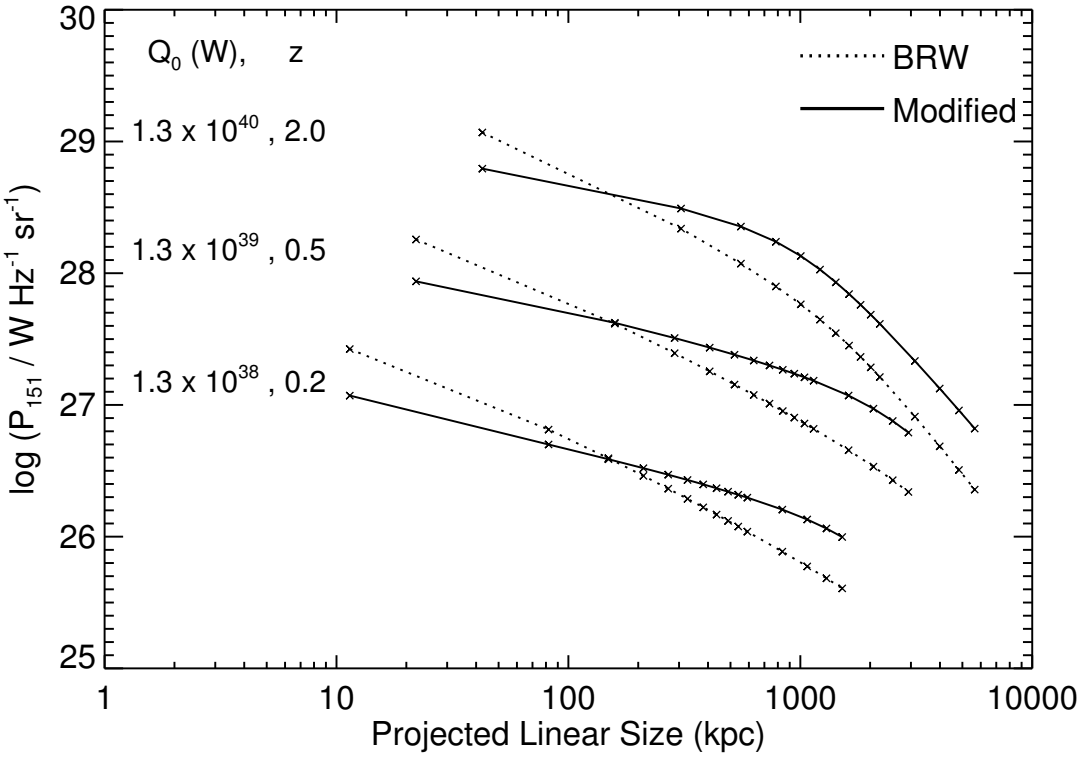

Figure 5.2: $[P$–$D]$ tracks of three sources with jet powers (Q_0) in Watts and redshifts (z) of $[1.3 \times 10^{40}, 2.0]$, $[1.3 \times 10^{39}, 0.5]$, $[1.3 \times 10^{38}, 0.2]$ (from top to bottom). Each of the *solid* and *dotted* curves correspond to the tracks predicted by the BRW-modified model and the default BRW model, respectively. The crosses on the tracks denote source lifetimes of 1, 10, 20, 30, ..., 90, 100, 150, 200, 250, 300 Myr.

the figures. The BRW-modified tracks (Figure 5.2) are less steep than the original BRW tracks, for all jet powers and redshifts. Among the three original models, KDA, BRW and MK, BRW gave the worst fit to the data, when compared with respect to K-S statistical tests (from the results in Chapter 4 and the conclusions in Section 8.2). If the reason can be identified with the fact that BRW gave the steepest $[P$–$D]$ tracks (in Figure 4.1), then this "shallowing" of the tracks in the BRW-modified model could be a favorable trend. This indicates that the K-S statistical fits to the data might be better for the BRW-modified model (which is indeed true from the results in Section 5.4.2, as discussed in Section 5.5). The MK-modified track (Figure 5.3) is steeper than the original MK track for the high jet power and high redshift case, slightly steeper for the intermediate power and redshift case, and less steep for the low

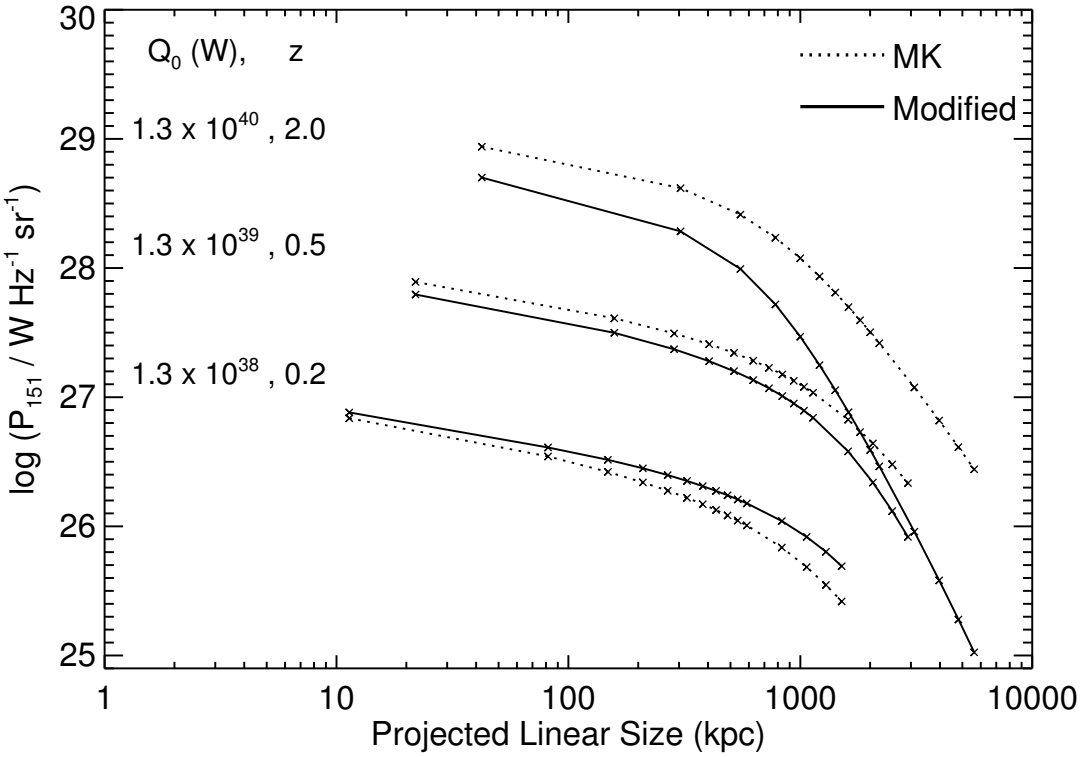

Figure 5.3: [P–D] tracks of three sources with jet powers (Q_0) in Watts and redshifts (z) of $[1.3 \times 10^{40}, 2.0]$, $[1.3 \times 10^{39}, 0.5]$, $[1.3 \times 10^{38}, 0.2]$ (from top to bottom). Each of the *solid* and *dotted* curves correspond to the tracks predicted by the MK-modified model and the default MK model, respectively. The crosses on the tracks denote source lifetimes of 1, 10, 20, 30, ..., 90, 100, 150, 200, 250, 300 Myr.

power and redshift case. The KDA-modified tracks (Figure 5.4) are either comparable to, or slightly more steep than, the original KDA tracks, for all beam powers and redshifts.

The "youth–redshift degeneracy" (described in Section 4.1) is clear in these [P–D] tracks. A high-power, high-redshift, source shows a faster fall off in its specific 151 MHz luminosity with time, and can even fall below the limiting flux of a radio survey at a younger age, as compared to a lower-power but also a lower-redshift source.

5.4.2 Simulations and Preliminary Statistical Tests

Similarly to our treatment of the original models in Section 4.2, 1-D K-S test results were used as a statistical tool for primary quantitative comparisons between different

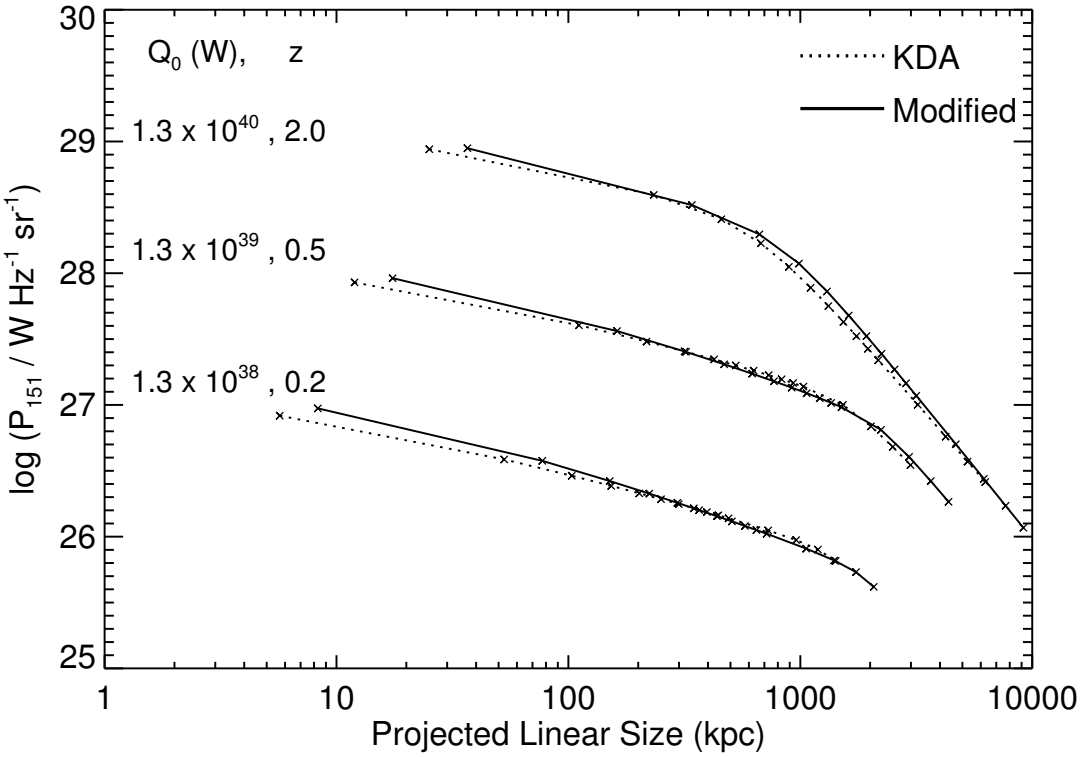

Figure 5.4: [*P–D*] tracks of three sources with jet powers (Q_0) in Watts and redshifts (z) of $[1.3 \times 10^{40}, 2.0]$, $[1.3 \times 10^{39}, 0.5]$, $[1.3 \times 10^{38}, 0.2]$ (from top to bottom). Each of the *solid* and *dotted* curves correspond to the tracks predicted by the KDA-modified model and the default KDA model, respectively. The crosses on the tracks denote source lifetimes of 1, 10, 20, 30, ..., 90, 100, 150, 200, 250, 300 Myr.

parameter variations of the modified models. For each model some parameters were chosen as "better" (in providing 1-D K-S fits to the data); for these further simulations and additional statistical tests (Section 5.4.3) were done. Finally all the models were compared with respect to the different statistical fits they provide for the data.

The simulation runs were done and the results are presented in ways analogous to those of the three original models discussed in Chapter 4. The procedures followed are briefly discussed here; for complete details see Chapter 4. Tables 5.2, 5.5, 5.6 and 5.9 give our results for the BRW-modified model; Tables 5.3, 5.7 and 5.10 give those for the MK-modified model; Tables 5.4 and 5.8 provide them for the KDA-modified model. The tables follow the same format and pattern as the corresponding previous tables for the original models. Explanations of the table entries are given

Table 5.2: BRW-modified Model Results: Different Initial Ensemble Parameters [a]

x	Survey	Ratio_{3C}	$\mathcal{P}(K\text{–}S)$				$\mathcal{P}_{[P,D,z,\alpha]}$
T_{MaxAge} [b]		Ratio_{6C}	$\mathcal{P}(P)$	$\mathcal{P}(D)$	$\mathcal{P}(z)$	$\mathcal{P}(\alpha)$	$\mathcal{P}_{[P,2D,z,\alpha]}$
Ensemble Size		Ratio_{7C}					
2.6	3C	1 (2.87) [c]	3.69e-04	5.78e-10	0.00250	6.44e-11	0.404
500	6C	0.625	0.202	4.26e-04	0.420	3.58e-10	0.407
4397469	7C	0.760	0.00125	0.00487	0.00317	0.00601	
2.6	3C	1 (1.48)	8.42e-06	9.61e-08	6.86e-04	2.80e-11	0.451
250	6C	0.779	0.0709	0.00193	0.439	9.98e-11	0.578
1466378	7C	0.753	5.11e-05	0.207	8.34e-05	0.00316	
3.0	3C	1 (1.22)	0.0325	0.0502	0.0616	7.42e-09	1.10
50	6C	1.58	0.212	0.258	0.413	3.66e-10	1.71
999361	7C	1.95	8.20e-06	0.647	1.16e-06	3.15e-06	
3.0	3C	1 (2.83)	0.0327	0.0957	0.193	4.74e-12	1.18
100	6C	1.19	0.310	0.00732	0.312	9.98e-11	1.75
3508016	7C	1.70	2.72e-04	0.761	8.95e-05	6.71e-04	
3.0	3C	1 (2.99)	0.198	0.0940	0.387	7.50e-15	1.56
150	6C	1.16	0.434	0.0715	0.312	3.58e-10	2.06
4861474	7C	1.56	4.52e-04	0.589	0.00124	0.00304	
3.0	3C	1 (1.86)	0.198	0.0366	0.483	8.12e-13	1.88
150	6C	1.17	0.583	0.174	0.432	3.58e-10	2.43
3045199	7C	1.66	2.89e-05	0.668	1.53e-05	6.91e-04	
3.0	3C	1 (1.74)	0.152	0.00101	0.484	4.74e-12	1.29
150	6C	1.31	0.434	0.00693	0.574	3.58e-10	1.31
3045199_1	7C	1.63	1.69e-04	0.0173	2.85e-05	7.21e-04	
3.0	3C	1 (1.61)	0.197	0.0926	0.485	1.31e-13	1.48
150	6C	1.43	0.583	0.00764	0.211	3.66e-10	1.77
3045199_2	7C	1.77	8.11e-04	0.319	8.95e-05	5.45e-05	
3.0	3C	1 (1.23)	0.175	0.0182	0.131	3.15e-13	0.885
200	6C	1.22	0.310	9.92e-04	0.437	9.98e-11	0.990
2979285	7C	1.70	0.00133	0.141	0.00125	0.0227	
3.0	3C	1 (1.41)	0.253	1.59e-05	0.367	1.92e-14	1.19
250	6C	1.13	0.212	0.356	0.286	3.58e-10	1.43
3355926	7C	1.53	0.00768	0.0290	0.00751	0.0121	

Continued on next page ...

Table 5.2: continued from previous page ...

x T_{MaxAge} [b] Ensemble Size	Survey	Ratio_{3C} Ratio_{6C} Ratio_{7C}	$\mathcal{P}(K\text{–}S)$				$\mathcal{P}_{[P,D,z,\alpha]}$ $\mathcal{P}_{[P,2D,z,\alpha]}$
			$\mathcal{P}(P)$	$\mathcal{P}(D)$	$\mathcal{P}(z)$	$\mathcal{P}(\alpha)$	
3.0	3C	1 (1.68)	0.177	8.37e-05	0.171	3.29e-13	1.73
300	6C	1.15	0.481	0.0402	0.897	3.58e-10	2.23
4963343	7C	1.58	0.00202	0.787	4.54e-04	0.00296	
3.0	3C	1 (1.78)	0.290	1.02e-07	0.354	1.31e-13	1.61
300	6C	1.18	0.583	0.509	0.295	9.98e-11	2.02
4963343_1	7C	1.55	0.00207	0.142	0.00200	0.00316	
3.0	3C	1 (1.85)	0.320	9.70e-04	0.581	2.69e-11	1.75
300	6C	1.12	0.897	0.0709	0.131	9.98e-11	1.95
4963343_2	7C	1.47	2.80e-04	0.248	7.56e-04	0.00148	
3.0	3C	1 (1.99)	0.227	2.35e-04	0.220	5.35e-14	1.34
300	6C	0.964	0.887	0.0136	0.298	9.98e-11	1.48
4963343_3	7C	1.38	4.60e-04	0.218	0.00126	0.00154	
3.0	3C	1 (0.690)	0.358	6.06e-05	0.280	3.00e-10	0.985 [d]
350	6C	1.02	0.123	0.196	0.327	6.15e-09	1.17 [d]
2138676	7C	1.46	0.00541	0.134	0.0264	0.0119	
3.0	3C	1 (1.19)	0.0554	4.87e-06	0.0990	1.11e-15	1.06
500	6C	1.18	0.915	0.00708	0.404	3.66e-10	1.12
4886474	7C	1.49	0.00512	0.0883	0.0117	0.00671	
3.0	3C	1 (1.27)	0.176	7.95e-05	0.176	7.77e-13	1.25
600	6C	0.965	0.879	4.44e-04	0.427	9.98e-11	1.28
5020623	7C	1.37	0.0125	0.0532	0.0239	0.0106	

[a] Runs done using different x and T_{MaxAge} (as mentioned) in the initial random ensembles. The model parameters are set equal to the default version of BRW-modified, where the hotspot size grows (Jeyakumar & Saikia 2000) with source age, according to Case 2 (quadratic fit) from Section 5.1. The other model parameters for dynamical and power evolution are same as in the default BRW (Blundell, Rawlings, & Willott 1999) case.

[b] T_{MaxAge} in units of Myr.

[c] From its definition, $\text{Ratio}_{3C} = 1$. The number in parentheses gives the ratio of the number of sources detected in 3C simulation (with given ensemble size) as compared to the real 3C survey.

[d] One cannot be confident of the validity of the K-S statistic as the detected sample in the simulation is smaller (or, much smaller) than in the actual catalog.

Table 5.3: MK-modified Model Results: Different Initial Ensemble Parameters [a]

x	Survey	Ratio_{3C}	$\mathcal{P}(K\text{–}S)$				$\mathcal{P}_{[P,D,z,\alpha]}$
T_{MaxAge} [b]		Ratio_{6C}	$\mathcal{P}(P)$	$\mathcal{P}(D)$	$\mathcal{P}(z)$	$\mathcal{P}(\alpha)$	$\mathcal{P}_{[P,2D,z,\alpha]}$
Ensemble Size		Ratio_{7C}					
2.6	3C	1 (0.710)	0.0931	0.00650	0.124	2.80e-45	0.727 [c]
500	6C	0.971	0.105	0.0283	0.575	1.82e-21	0.767 [c]
4397469	7C	1.28	0.0356	0.0309	0.130	7.92e-22	
2.6	3C	1 (3.15)	0.00363	0.0406	0.0836	0	0.677
50	6C	0.895	0.176	0.0371	0.418	1.83e-24	0.890
2892934	7C	1.18	5.15e-08	0.245	7.67e-05	4.15e-20	
2.6	3C	1 (3.01)	1.37e-04	0.168	0.0616	0	0.596
50	6C	0.950	0.0709	7.20e-04	0.295	1.83e-24	0.899
2892934_1	7C	1.23	1.06e-07	0.221	7.74e-05	4.15e-20	
2.6	3C	1 (2.31)	3.76e-04	0.0263	0.273	0	1.09
100	6C	0.727	0.378	0.0609	0.380	1.83e-24	1.42
3508016	7C	1.20	4.26e-05	0.428	0.0161	4.15e-20	
2.6	3C	1 (2.0)	0.00557	0.0373	0.474	0	1.46
150	6C	0.621	0.0460	0.241	0.580	2.99e-26	2.02
3888492	7C	0.992	2.69e-04	0.610	0.0251	5.38e-21	
2.6	3C	1 (1.54)	0.0913	0.340	0.280	0	1.39
150	6C	0.913	0.469	0.0350	0.408	1.83e-24	1.78
3888492_1	7C	1.21	0.00763	0.0465	0.0713	4.15e-20	
2.6	3C	1 (1.77)	0.0491	0.521	0.535	0	2.12
150	6C	1.08	0.624	0.102	0.506	1.83e-24	2.88
3888492_2	7C	1.06	0.00187	0.301	0.0491	6.13e-21	
2.6	3C	1 (1.66)	0.0122	0.420	0.360	0	1.91
150	6C	1.02	0.564	0.0643	0.556	1.83e-24	2.73
3888492_3	7C	1.34	1.34e-04	0.584	0.0161	4.15e-20	
2.6	3C	1 (1.22)	0.0497	0.129	0.294	0	1.31
200	6C	0.980	0.471	0.00594	0.408	1.83e-24	1.69
3831459	7C	1.18	6.97e-04	0.412	0.0247	4.15e-20	
2.6	3C	1 (1.21)	0.0353	0.0508	0.220	0	0.751
200	6C	0.858	0.416	0.0357	0.0425	1.83e-24	0.946

Continued on next page ...

Table 5.3: continued from previous page ...

x T_{MaxAge} [b] Ensemble Size	Survey	Ratio_{3C} Ratio_{6C} Ratio_{7C}	$\mathcal{P}(K\text{–}S)$				$\mathcal{P}_{[P,D,z,\alpha]}$ $\mathcal{P}_{[P,2D,z,\alpha]}$
			$\mathcal{P}(P)$	$\mathcal{P}(D)$	$\mathcal{P}(z)$	$\mathcal{P}(\alpha)$	
3831459_1	7C	1.38	7.74e-05	0.199	0.0112	4.15e-20	
2.6	3C	1 (1.16)	0.0668	0.00569	0.294	0	0.874
250	6C	1.00	0.458	0.0111	0.252	1.83e-24	0.913
4195764	7C	1.40	0.00110	0.0436	0.0250	5.91e-21	
2.6	3C	1 (1.33)	0.0350	0.125	0.496	0	1.57
250	6C	0.899	0.869	0.232	0.267	1.83e-24	1.85
4195764_1	7C	1.11	0.00307	0.0144	0.0362	6.13e-21	
2.6	3C	1 (1.39)	9.76e-04	0.216	0.421	0	1.64
250	6C	0.756	0.0935	3.44e-04	0.681	1.83e-24	2.36
4195764_2	7C	1.08	2.38e-05	0.827	0.0115	4.30e-20	
2.6	3C	1 (1.16)	0.319	0.0507	0.282	0	1.33
250	6C	0.755	0.904	7.01e-04	0.103	1.83e-24	1.39
4195764_3	7C	1.29	0.00742	0.00758	0.0363	5.91e-21	
2.6	3C	1 (1.10)	0.00152	0.0125	0.421	0	1.72
300	6C	0.782	0.641	0.252	0.0709	1.83e-24	2.34
4342468	7C	0.984	0.0105	0.732	0.235	6.13e-21	
2.6	3C	1 (1.11)	0.0121	6.30e-04	0.280	0	1.05
300	6C	0.788	0.655	3.44e-04	0.0667	1.83e-24	1.31
4342468_1	7C	1.18	6.56e-04	0.431	0.0337	4.30e-20	
2.6	3C	1 (1.21)	0.00553	0.00377	0.622	0	1.18
300	6C	0.621	0.179	0.00158	0.536	1.83e-24	1.23
4342468_2	7C	0.993	0.00108	0.0785	0.0486	6.13e-21	
2.6	3C	1 (1.07)	0.122	0.00572	0.0200	0	0.956
300	6C	0.585	0.806	0.0604	0.252	1.83e-24	1.08
4342468_3	7C	1.28	4.03e-04	0.128	0.0243	4.15e-20	
2.6	3C	1 (0.855)	0.00680	0.0227	0.210	0	1.03 [c]
350	6C	1.15	0.980	0.110	0.103	4.74e-24	1.16 [c]
4280738	7C	1.18	0.00111	0.0785	0.0235	4.15e-20	
3.0	3C	1 (1.07)	1.21e-07	0.0366	1.47e-08	0	0.558

Continued on next page ...

Table 5.3: continued from previous page ...

x T_{MaxAge} [b] Ensemble Size	Survey	Ratio_{3C} Ratio_{6C} Ratio_{7C}	$\mathcal{P}(K\text{–}S)$				$\mathcal{P}_{[P,D,z,\alpha]}$ $\mathcal{P}_{[P,2D,z,\alpha]}$
			$\mathcal{P}(P)$	$\mathcal{P}(D)$	$\mathcal{P}(z)$	$\mathcal{P}(\alpha)$	
150	6C	0.984	0.212	0.371	0.0265	2.99e-26	0.911
4861474	7C	1.75	0.00341	0.134	0.0541	7.92e-22	
3.0	3C	1 (0.366)	2.30e-04	0.195	6.52e-05	1.58e-31	0.410 [c]
500	6C	1.27	0.154	0.0125	0.00722	8.88e-16	0.611 [c]
4886474	7C	1.59	0.145	0.128	0.0532	6.13e-21	

[a] These runs are done with different initial random ensembles with values of x and T_{maxage} as listed. In these MK-modified model simulations, the hotspot size grows (Jeyakumar & Saikia 2000) with source age according to Case 2 (quadratic fit) from Section 5.1, and a fixed $r_{hs(t_0)} = 0.02$ kpc (Section 5.2), is used. Otherwise the model parameters for dynamical and power evolution are same as in the default MK (Manolakou & Kirk 2002) case.

[b] T_{MaxAge} in units of Myr.

[c] One cannot be confident of the validity of the K-S statistic as the detected sample in the simulation is smaller (or, much smaller) than in the actual catalog.

in Sections 4.2 and 4.6. All the statistical test (K-S and correlations) results for the modified models include the 1 kpc cutoff of source size, i.e., the statistics are calculated by excluding sources with linear size, $D < 1$ kpc. The relevant reasons are given in Section 4.5.

An initial ensemble, generated using the default parameters from BRW for the RG population generation, was evolved according to each of the modified models. The sources in the simulated surveys (according to the prescription in Section 3.3) were compared to the data samples of the 3C, 6C and 7C catalogs. We examined the 1-D K-S test statistics of the first entry (the very first 3 rows) of Tables 5.2, 5.3 and 5.4 (modified model results) and compared those to the first entries of Tables 4.2, 4.3 and 4.1, respectively (original model results). From this single comparison we can say the following. The BRW-modified model is significantly better (the combined 1-D K-S probabilities are $\sim 10 - 20$ times higher, which is $\sim 4\sigma$ better) than the original BRW model. The MK-modified and KDA-modified models are slightly better than the original MK and KDA models, respectively.

In search of further improvements of the combined 1-D K-S statistics, we steepened the beam power distribution function of the sources generated in the initial population

Table 5.4: KDA-modified Model Results: Different Initial Ensemble Parameters [a]

x T_{MaxAge} [b] Ensemble Size	Survey	Ratio_{3C} Ratio_{6C} Ratio_{7C}	$\mathcal{P}(K\text{–}S)$				$\mathcal{P}_{[P,D,z,\alpha]}$ $\mathcal{P}_{[P,2D,z,\alpha]}$
			$\mathcal{P}(P)$	$\mathcal{P}(D)$	$\mathcal{P}(z)$	$\mathcal{P}(\alpha)$	
2.6	3C	1 (1.83) [c]	9.56e-08	1.35e-04	2.70e-06	1.47e-08	1.20
500	6C	0.535	0.678	0.145	0.862	6.89e-07	1.41
4397469	7C	0.675	0.0105	0.199	0.00183	0.00481	
3.0	3C	1 (3.54)	0.0177	0.0186	0.148	2.40e-07	0.912
50	6C	1.11	0.416	0.00622	0.727	6.89e-07	0.935
4452567	7C	1.80	3.96e-04	9.64e-04	1.37e-04	0.0198	
3.0	3C	1 (1.71)	0.0357	0.0968	0.312	4.57e-07	1.51
100	6C	1.15	0.701	0.159	0.274	1.96e-06	2.06
3508016	7C	1.55	6.75e-04	0.575	0.00111	0.0183	
3.0	3C	1 (1.66)	0.332	0.0129	0.474	1.22e-07	2.02
150	6C	1.14	0.735	0.0117	0.556	6.89e-07	2.40
4861474	7C	1.52	0.00187	0.603	0.00290	0.0183	
3.0	3C	1 (1.66)	0.0488	0.00158	0.511	2.19e-07	2.05
150	6C	1.17	0.416	0.240	0.727	6.89e-07	2.79
4861474_3	7C	1.70	0.0115	0.971	0.0106	0.00117	
3.0	3C	1 (0.724)	0.379	0.0174	0.247	2.80e-04	1.64 [d]
200	6C	1.04	0.627	0.0443	0.435	1.48e-05	2.14 [d]
2979285	7C	1.55	0.0167	0.753	0.0212	0.00861	
3.0	3C	1 (1.27)	0.319	0.0699	0.680	1.13e-07	2.48
200	6C	0.887	0.848	0.0350	0.404	6.89e-07	3.14
4683659	7C	1.66	0.0169	0.932	0.0108	0.00214	
3.0	3C	1 (0.890)	0.450	0.00418	0.591	8.97e-10	2.21 [d]
250	6C	1.08	0.625	0.213	0.643	2.80e-06	2.56 [d]
3355926	7C	1.21	0.0631	0.343	0.0539	0.00230	
3.0	3C	1 (1.08)	0.0930	0.0357	0.513	3.34e-09	1.63
250	6C	0.929	0.539	0.485	0.118	6.89e-07	2.23
4720731	7C	1.50	0.0105	0.417	0.00182	0.0198	
3.0	3C	1 (1.01)	0.285	0.0260	0.220	3.05e-10	1.67
300	6C	1.08	0.811	0.232	0.252	6.89e-07	2.12
4963343	7C	1.34	0.0368	0.457	0.00455	0.00109	

Continued on next page ...

Table 5.4: continued from previous page ...

x T_{MaxAge} [b] Ensemble Size	Survey	Ratio_{3C} Ratio_{6C} Ratio_{7C}	$\mathcal{P}(K\text{–}S)$				$\mathcal{P}_{[P,D,z,\alpha]}$ $\mathcal{P}_{[P,2D,z,\alpha]}$
			$\mathcal{P}(P)$	$\mathcal{P}(D)$	$\mathcal{P}(z)$	$\mathcal{P}(\alpha)$	
3.0	3C	1 (0.352)	0.953	0.0984	0.980	8.41e-05	2.05 [d]
350	6C	0.965	0.657	0.427	0.427	9.37e-04	2.45 [d]
2138676	7C	1.69	0.0860	0.303	0.0718	0.00940	
3.0	3C	1 (0.752)	0.393	8.54e-05	0.574	8.81e-05	1.65 [d]
400	6C	1.02	0.803	0.0341	0.276	5.13e-06	1.86 [d]
4823869	7C	1.28	0.0145	0.312	0.00655	0.00247	
3.0	3C	1 (0.628)	0.124	0.00801	0.372	1.70e-07	1.81 [d]
500	6C	0.996	0.993	0.280	0.926	4.77e-05	2.23 [d]
4886474	7C	1.28	0.0374	0.454	0.0262	0.0198	
3.0	3C	1 (0.690)	0.122	0.00541	0.0892	2.10e-04	1.07 [d]
500	6C	1.14	0.472	0.125	0.196	4.36-06	1.59 [d]
6451283	7C	1.68	0.00100	0.732	0.00734	0.0198	
3.0	3C	1 (0.697)	0.117	0.0529	0.666	1.55e-07	1.77 [d]
600	6C	0.872	0.699	0.313	0.228	2.60e-05	2.22 [d]
5020623	7C	1.34	0.120	0.412	0.127	0.00101	

[a] Runs done using different initial random ensembles with values of x and T_{MaxAge} as mentioned. The model parameters are the same as in the default version of KDA-modified, where the axial ratio grows with source age according to Section 5.3. Otherwise the parameters for dynamical and power evolution are from the default KDA model (Kaiser, Dennett-Thorpe, & Alexander 1997).

[b] T_{MaxAge} in units of Myr.

[c] From its definition, $\text{Ratio}_{3C} = 1$. The number in parentheses gives the ratio of the number of sources detected in 3C simulation (with given ensemble size) as compared to the real 3C survey.

[d] One cannot be confident of the validity of the K-S statistic as the detected sample in the simulation is smaller (or, much smaller) than in the actual catalog.

Table 5.5: BRW-modified Results: K-S Statistics for First Set of Parameter Variations [a]

Model Ensemble Size	Survey	Ratio_{3C} Ratio_{6C} Ratio_{7C}	$\mathcal{P}(K\text{–}S)$ $\mathcal{P}(P)$	$\mathcal{P}(D)$	$\mathcal{P}(z)$	$\mathcal{P}(\alpha)$	$\mathcal{P}_{[P,D,z,\alpha]}$ $\mathcal{P}_{[P,2D,z,\alpha]}$
BRW-modified [b]	3C	1 (1.41)	0.253	1.59e-05	0.367	1.92e-14	1.19
	6C	1.13	0.212	0.356	0.286	3.58e-10	1.43
	7C	1.53	0.00768	0.0290	0.00751	0.0121	
$\beta = 1$	3C	1 (5.35)	0.00494	1.21e-08	0.0320	7.11e-08	0.189
	6C	0.973	0.0893	6.12e-06	0.141	3.83e-13	0.194
	7C	1.00	2.38e-06	0.00928	1.56e-04	7.53e-04	
$a_0 = 7.5$ kpc	3C	1 (0.931)	0.102	7.12e-07	0.0411	1.36e-16	0.618
	6C	1.24	0.140	0.170	0.312	3.66e-10	0.776
	7C	1.57	0.00831	0.0836	0.0248	0.00277	
$a_0 = 20$ kpc	3C	1 (3.67)	0.0859	8.84e-06	0.112	9.34e-07	0.610
	6C	1.08	0.0893	0.109	0.141	8.47e-14	0.877
	7C	1.36	2.93e-05	0.324	1.56e-04	3.26e-06	
$\rho_0 = \rho_1$ [c]	3C	1 (0.759)	0.0634	3.12e-09	0.0266	5.63e-19	0.770 [e]
	6C	1.07	0.760	0.0322	0.170	1.30e-08	0.844 [e]
	7C	1.44	0.0317	0.0907	0.0587	7.19e-06	
$\rho_0 = \rho_2$ [d]	3C	1 (2.73)	0.0624	2.35e-04	0.247	3.34e-06	0.733
	6C	1.04	0.0893	0.0685	0.214	3.83e-13	0.963
	7C	1.44	2.86e-04	0.306	0.00124	2.26e-05	
$\gamma_{max(hs)} = 10^{10}$	3C	1 (1.41)	0.253	8.49e-06	0.367	1.92e-14	1.07
	6C	1.15	0.212	0.111	0.286	3.58e-10	1.19
	7C	1.54	0.00537	0.0836	0.00751	0.00296	
$p = 2.001$	3C	1 (0.828)	0.0619	6.01e-05	0.0215	1.53e-16	0.414 [e]
	6C	0.979	0.249	0.00174	0.170	4.23e-09	0.418 [e]
	7C	1.54	0.00582	0.00481	0.0840	0.00296	
$p = 2.999$	3C	1 (2.34)	0.196	1.42e-06	0.232	6.82e-11	0.842
	6C	1.07	0.212	0.0141	0.214	9.98e-11	0.986
	7C	1.51	1.52e-05	0.221	2.64e-04	0.00624	
$t_{bs} = 10^3$ yr	3C	1 (1.03)	0.135	3.91e-07	0.0411	1.57e-16	0.719
	6C	1.16	0.310	0.0243	0.308	3.66e-10	0.816
	7C	1.57	0.00828	0.134	0.0508	0.00144	

Continued on next page ...

Table 5.5: continued from previous page ...

Model Ensemble Size	Survey	Ratio_{3C} Ratio_{6C} Ratio_{7C}	$\mathcal{P}(K$–$S)$				$\mathcal{P}_{[P,D,z,\alpha]}$ $\mathcal{P}_{[P,2D,z,\alpha]}$
			$\mathcal{P}(P)$	$\mathcal{P}(D)$	$\mathcal{P}(z)$	$\mathcal{P}(\alpha)$	
	3C	1 (1.21)	0.00425	4.88e-05	0.00114	3.34e-09	0.891
$t_{bs} = 10^7$ yr	6C	1.21	0.434	0.356	0.127	3.83e-13	1.38
	7C	1.69	0.00341	0.435	0.0385	8.76e-06	
	3C	1 (1.30)	0.198	4.70e-05	0.138	1.37e-16	0.776
$t_{bf} = 0.01$ yr	6C	1.22	0.212	0.0250	0.286	3.58e-10	0.873
	7C	1.58	0.0125	0.134	0.0169	7.21e-04	
	3C	1 (1.57)	0.197	6.30e-04	0.367	4.96e-17	1.17
$t_{bf} = 100$ yr	6C	1.15	0.310	0.0141	0.310	9.98e-11	1.38
	7C	1.55	0.00341	0.326	0.00495	6.71e-04	

[a] These runs are done with an initial ensemble of size 3355926 generated using $x = 3.0, T_{MaxAge} =$ 250 Myr. In these simulations, the parameter for dynamical and power evolution listed in the first column is varied, the rest are from the default version of the BRW-modified model (Section 5.2).

[b] Parameter values set equal to those given in the BRW model (Blundell et al. 1999), except for assuming that the hotspot size grows with source age according to Jeyakumar & Saikia (2000).

[c] $\rho_1 = \rho_{0\ (\text{Default})}/2 = 8.35 \times 10^{-24}$ kg m^{-3}.

[d] $\rho_2 = 2 \times \rho_{0\ (\text{Default})} = 3.34 \times 10^{-23}$ kg m^{-3}.

[e] One cannot be confident of the validity of the K-S statistic as the detected sample in the simulation is smaller (or, much smaller) than in the actual catalog.

as we did earlier (Section 4.4). The exponent in the intial jet power distribution, x (Equation 3.9), was increased as described in Section 4.4. For the BRW-modified and KDA-modified models the overall statistics improved the most at $x = 3.0$, while for the MK-modified model $x = 2.6$ now gave better fits. The values of x which gave better 1-D K-S results were then used for the later simulations.

The initial population generated with $x = 3$ (but otherwise using the BRW prescription), was evolved according to the BRW-modified power evolution model. The corresponding 1-D K-S statistics are given in the last but one entry in Table 5.2, and show the improved fit (w.r.t. the first entry of the same table) on steepening the jet power distribution to $x = 3.0$. To search for possible further improvements we varied the other parameters prescribing the power evolution in the models, which are described next. Simulated surveys were constructed using the parameter listing given in Table 5.5 (each variation done one at a time) of the BRW-modified power

Table 5.6: BRW-modified Model Results: K-S Statistics for Best Initial Ensemble [a]

T_{MaxAge} [b]	$\mathcal{P}(K\text{–}S)$	Run 1	Run 2	Run 3	Run 4	Mean	S.D. (σ)	Rank [c]
150 [d]	$\mathcal{P}_{[P,D,z,\alpha]}$	1.558	1.877	1.291	1.477	1.551	0.2448	2
	$\mathcal{P}_{[P,2D,z,\alpha]}$	2.056	2.432	1.306	1.770	1.891	0.4749	
300 [e]	$\mathcal{P}_{[P,D,z,\alpha]}$	1.727	1.610	1.749	1.341	1.607	0.1875	1
	$\mathcal{P}_{[P,2D,z,\alpha]}$	2.233	2.019	1.946	1.483	1.920	0.3159	

[a] In these BRW-modified model simulations, the hotspot size grows (Jeyakumar & Saikia 2000) with source age according to Case 2 (quadratic fit) from Section 5.1. Each run is done using an initial population with $x = 3.0$, and T_{MaxAge} as listed. The 4 runs averaged here differ in their initial random seeds.

[b] T_{MaxAge} in units of Myr.

[c] Rank according to mean $\mathcal{P}_{[P,D,z,\alpha]}$.

[d] Initial ensembles for the 4 runs are of sizes 4861474 (1 run), and 3045199 (3 runs).

[e] Initial ensembles for the 4 runs are of size 4963343.

Table 5.7: MK-modified Model Results: K-S Statistics for Best Initial Ensemble [a]

T_{MaxAge} [b]	$\mathcal{P}(K\text{–}S)$	Run 1	Run 2	Run 3	Run 4	Mean	S.D. (σ)	Rank [c]
150 [d]	$\mathcal{P}_{[P,D,z,\alpha]}$	1.461	1.391	2.116	1.913	1.720	0.3508	1
	$\mathcal{P}_{[P,2D,z,\alpha]}$	2.024	1.781	2.885	2.730	2.355	0.5357	
250 [e]	$\mathcal{P}_{[P,D,z,\alpha]}$	0.8741	1.567	1.643	1.334	1.355	0.3464	2
	$\mathcal{P}_{[P,2D,z,\alpha]}$	0.9134	1.848	2.364	1.390	1.629	0.6212	
300 [f]	$\mathcal{P}_{[P,D,z,\alpha]}$	1.722	1.045	1.178	0.9558	1.225	0.3433	3
	$\mathcal{P}_{[P,2D,z,\alpha]}$	2.340	1.309	1.231	1.078	1.490	0.5752	

[a] In these MK-modified model simulations, the hotspot size grows (Jeyakumar & Saikia 2000) with source age according to Case 2 (quadratic fit) from Section 5.1, and a fixed $r_{hs(t_0)} = 0.02$ kpc (Section 5.2), is used. Each run is done using an initial population with $x = 2.6$, and T_{MaxAge} as listed. The 4 runs averaged here are of same ensemble size but differ in the initial random seeds.

[b] T_{MaxAge} in units of Myr.

[c] Rank according to mean $\mathcal{P}_{[P,D,z,\alpha]}$.

[d] Initial ensembles for the 4 runs are of size 3888492.

[e] Initial ensembles for the 4 runs are of size 4195764.

[f] Initial ensembles for the 4 runs are of size 4342468.

evolution model. The total 1-D K-S statistics, as seen from Table 5.5, are comparable to or better than the original BRW model results (Tables 4.2, 4.5 and 4.8).

In order to find the best-fit maximum RG age, we performed simulation runs using initial populations with $x = 3$ (for BRW-modified and KDA-modified), and $x = 2.6$ (for MK-modified), similar to the original models in Section 4.5. In these we employed different varied T_{MaxAge}, and obtained the following results.

In the BRW- and MK-modified models, the combined 1-D K-S probabilities, $[\mathcal{P}(P) + \mathcal{P}(D) + \mathcal{P}(z) + \mathcal{P}(\alpha)]$ or $[\mathcal{P}(P) + 2\mathcal{P}(D) + \mathcal{P}(z) + \mathcal{P}(\alpha)]$, did not quite vary smoothly over the range in maximum age considered. Hence, we picked some of the "superior" (giving better 1-D K-S fits) T_{MaxAge} values, and performed three more simulation runs using the same parameters, but with different initial random seeds. The relevant 1-D K-S statistics of the runs are shown in Tables 5.2 and 5.3. We then found the means and standard deviations (σ) of the combined 1-D K-S statistics for the 4 runs with selected T_{MaxAge}'s. The results are shown in Tables 5.6 and 5.7.

The T_{MaxAge} that gave the highest mean statistics ($\mathcal{P}_{[P,D,z,\alpha]}$ and $\mathcal{P}_{[P,2D,z,\alpha]}$) was chosen as the best maximum age at the considered x. In the BRW-modified model the highest mean statistic was seen at $T_{MaxAge} = 300$ Myr (when compared between 150 and 300 Myr, for $x = 3.0$). The MK-modified model performed its best at $T_{MaxAge} = 150$ Myr (when compared between 150, 250 and 300 Myr, for $x = 2.6$). Hence we used initial populations with $x = 2.6$ or 3.0, and the above "optimal" T_{MaxAge} values for each model in subsequent runs.

From Table 5.4, the combined 1-D K-S probability $[\mathcal{P}(P) + \mathcal{P}(D) + \mathcal{P}(z) + \mathcal{P}(\alpha)]$, for the KDA-modified model, varied more or less smoothly over the range of T_{MaxAge}'s considered. As a check, a second simulation run was done using some of the T_{MaxAge} values which appeared to give better fits to the data. Comparing the 1-D K-S statistics for all the runs, $T_{MaxAge} = 200$ Myr gave the closest fit. Hence we used initial populations with $x = 3.0$ and $T_{MaxAge} = 200$ Myr for the subsequent runs of the KDA-modified model.

As seen from the tables showing the individual 1-D K-S statistic probabilities (Tables 5.2, 5.3, 5.4, 5.5 and 5.8), often some of the 12 K-S probabilities for some cases give acceptable fits, but it is difficult to find a single model where all are really good fits. In other words, the modified models also do not give good simultaneous fits to the $[P, D, z, \alpha]$ data from all three of the radio surveys considered (3C, 6C and 7C).

Following a prescription similar to that used in Section 4.6, Monte-Carlo simulations were done using the same large population and varying the model parameters

Table 5.8: KDA-modified Results: K-S Statistics for First Set of Parameter Variations [a]

Model Ensemble Size	Survey	Ratio_{3C} Ratio_{6C} Ratio_{7C}	$\mathcal{P}(K\text{–}S)$ $\mathcal{P}(P)$	$\mathcal{P}(D)$	$\mathcal{P}(z)$	$\mathcal{P}(\alpha)$	$\mathcal{P}_{[P,D,z,\alpha]}$ $\mathcal{P}_{[P,2D,z,\alpha]}$
	3C	1 (1.80) [c]	0.0252	0.0495	0.420	1.57e-06	1.56
KDA-modified [b]	6C	0.942	0.539	0.471	0.287	6.89e-07	2.10
	7C	1.48	0.0350	0.321	0.0160	0.00917	
	3C	1 (1.69)	0.0250	0.0357	0.612	3.07e-09	1.22
KDA-modified [b]	6C	1.31	0.272	0.0350	0.0425	6.89e-07	1.56
	7C	1.76	0.0362	0.459	0.0106	0.00101	
	3C	1 (1.86)	0.396	0.0525	0.680	5.57e-08	2.37
KDA-modified [b]	6C	1.00	0.843	0.102	0.380	6.89e-07	2.84
	7C	1.58	0.0367	0.584	0.0106	0.00468	
	3C	1 (1.94)	0.396	0.0917	0.680	1.47e-08	1.95
KDA-modified [b]	6C	1.16	0.501	0.0593	0.194	1.92e-06	2.36
	7C	1.38	0.0160	0.459	0.0161	0.0356	
	3C	1 (2.61)	0.0681	2.50e-08	0.580	3.10e-10	1.49
BRW Env. [d]	6C	0.929	0.690	2.50e-05	0.270	7.62e-08	1.61
β, a_0, ρ_0	7C	1.16	0.0367	0.190	0.0946	0.00438	
	3C	1 (23.1)	3.16e-04	4.31e-04	0.00319	0	0.240
$\beta = 1.0$	6C	0.855	0.0809	4.05e-06	0.198	6.99e-22	0.300
	7C	1.01	1.78e-10	0.0978	9.25e-07	1.10e-14	
	3C	1 (1.19)	0.0678	2.37e-04	0.423	5.36e-06	0.830
$\beta = 2.02$	6C	0.898	0.187	0.242	0.0441	5.35e-06	1.00
	7C	1.66	0.0170	0.0292	0.00699	0.00976	
	3C	1 (1.08)	0.0670	0.0124	0.500	1.41e-09	1.17
$a_0 = 1.5$ kpc	6C	0.858	0.185	0.331	0.0709	5.35e-06	1.52
	7C	1.62	0.0680	0.209	0.0340	9.93e-04	
	3C	1 (7.32)	0.0847	0.0125	0.0836	1.72e-08	1.13
$a_0 = 5$ kpc	6C	0.970	0.416	0.0371	0.287	5.79e-13	1.64
	7C	1.32	1.27e-05	0.781	2.34e-04	2.00e-07	
	3C	1 (0.938)	0.0702	0.00508	0.574	1.24e-10	0.991 [g]
$\rho_0 = \rho_1$ [e]	6C	0.857	0.102	0.184	0.0341	5.40e-05	1.23 [g]
	7C	1.68	0.0424	0.209	0.00632	9.93e-04	

Continued on next page ...

Table 5.8: continued from previous page ...

Model Ensemble Size	Survey	Ratio_{3C} Ratio_{6C} Ratio_{7C}	$\mathcal{P}(K\text{–}S)$				$\mathcal{P}_{[P,D,z,\alpha]}$ $\mathcal{P}_{[P,2D,z,\alpha]}$
			$\mathcal{P}(P)$	$\mathcal{P}(D)$	$\mathcal{P}(z)$	$\mathcal{P}(\alpha)$	
$\rho_0 = \rho_2$ [f]	3C	1 (6.77)	0.0625	0.0125	0.112	1.44e-07	0.817
	6C	0.997	0.416	0.159	0.287	9.87e-12	1.01
	7C	1.33	1.27e-05	0.138	2.36e-04	1.88e-06	
$\Gamma_B = 5/3$	3C	1 (1.59)	0.0497	0.0129	0.340	1.07e-11	1.30
	6C	0.919	0.389	0.251	0.0735	1.41e-05	1.85
	7C	1.49	0.0522	0.629	0.0107	9.78e-04	
$\Gamma_C = 5/3$	3C	1 (0.772)	0.358	0.0223	0.321	3.56e-08	0.874 [g]
	6C	0.670	0.134	0.100	0.00952	7.45e-05	0.944 [g]
	7C	1.58	0.0874	0.00818	0.0526	0.0198	

[a] These runs are done with initial ensembles of size 6814314 generated using $x = 3.0, T_{MaxAge} =$ 200 Myr. In these simulations, the model parameter for dynamical and power evolution listed in the first column is varied, the rest are same from default version of the KDA-modified model.

[b] Parameter values set equal to those given in the KDA model (Kaiser et al. 1997), except for assuming that the axial ratio grows with source age according to Section 5.3. Initial ensembles for the 1st 4 simulation runs (the default KDA-modified cases) are of same size 6814314, but have different random seeds.

[c] Always, $\text{Ratio}_{3C} = 1$, because of the way it is defined. The number in parentheses gives the ratio of the number of sources detected in 3C simulation (with given ensemble size) as compared to the real 3C survey.

[d] Parameters defining external environment density profile are set to those of the BRW model, namely $\beta = 1.6, a_0 = 10$ kpc, $\rho_0 = 1.67 \times 10^{-23}$ kg m^{-3}.

[e] $\rho_1 = \rho_{0\ \text{(Default)}}/2 = 3.6 \times 10^{-22}$ kg m^{-3}.

[f] $\rho_2 = 5 \times \rho_{0\ \text{(Default)}} = 3.6 \times 10^{-21}$ kg m^{-3}.

[g] One cannot be confident of the validity of the K-S statistic as the detected sample in the simulation is smaller (or, much smaller) than in the actual catalog.

around their default values (as in Section 4.4.2). The KDA-modified simulations were done with initial population generated using $x = 3.0$ and $T_{MaxAge} = 200$ Myr. The results are displayed in Table 5.8. As seen from the combined 1-D K-S probabilities, $[\mathcal{P}(P) + \mathcal{P}(D) + \mathcal{P}(z) + \mathcal{P}(\alpha)]$ or $[\mathcal{P}(P) + 2\mathcal{P}(D) + \mathcal{P}(z) + \mathcal{P}(\alpha)]$, simple variations of the dynamical and power evolution parameters in the KDA-modified model do not give improved statistical fits as compared to the default version (KDA-modified, e.g., KDA model with axial ratio increasing according to Section 5.3). Hence we decided to stop exploring further parameter variations of the KDA-modified model.

Table 5.9: BRW-modified Results: K-S Statistics for Best-Fit Parameter Variations [a]

Model	$\mathcal{P}(K\text{–}S)$	Run 1	Run 2	Run 3	Run 4	Mean	S.D. (σ)	Rank [b]
BRW-Modified	$\mathcal{P}_{[P,D,z,\alpha]}$	1.341	1.749	1.610	1.727	1.607	0.1875	8
	$\mathcal{P}_{[P,2D,z,\alpha]}$	1.483	1.946	2.019	2.233	1.920	0.3159	9 – 10
1-Change [c]								
KDA Env. [d]	$\mathcal{P}_{[P,D,z,\alpha]}$	1.829	2.275	1.621	1.810	1.884	0.2773	3
β, a_0, ρ_0	$\mathcal{P}_{[P,2D,z,\alpha]}$	2.235	2.566	1.656	1.812	2.067	0.4126	8
$a_0 = 15$ kpc	$\mathcal{P}_{[P,D,z,\alpha]}$	2.070	1.555	2.317	1.543	1.871	0.3856	5
	$\mathcal{P}_{[P,2D,z,\alpha]}$	2.616	1.757	3.104	1.800	2.319	0.6556	6
$a_0 = 20$ kpc	$\mathcal{P}_{[P,D,z,\alpha]}$	0.8655	1.292	0.8623	0.9013	0.9803	0.2087	14
	$\mathcal{P}_{[P,2D,z,\alpha]}$	0.9817	1.569	1.125	1.013	1.172	0.2713	14
$\rho_0 = \rho_2$ [e]	$\mathcal{P}_{[P,D,z,\alpha]}$	1.509	1.524	1.388	1.771	1.548	0.1609	10 – 11
	$\mathcal{P}_{[P,2D,z,\alpha]}$	1.611	1.751	1.736	2.260	1.839	0.2876	11
$\gamma_{min(hs)} = 10$	$\mathcal{P}_{[P,D,z,\alpha]}$	2.030	1.609	1.893	2.311	1.961	0.2919	1
	$\mathcal{P}_{[P,2D,z,\alpha]}$	2.394	1.845	2.271	2.811	2.330	0.3978	1
$\gamma_{max(hs)} = 10^{10}$	$\mathcal{P}_{[P,D,z,\alpha]}$	1.145	1.574	1.875	2.291	1.721	0.4841	7
	$\mathcal{P}_{[P,2D,z,\alpha]}$	1.332	1.943	2.528	3.008	2.203	0.7257	3 – 4
$p = 2.5$	$\mathcal{P}_{[P,D,z,\alpha]}$	1.734	1.411	1.467	1.788	1.600	0.1885	10 – 11
	$\mathcal{P}_{[P,2D,z,\alpha]}$	1.830	1.800	1.536	2.062	1.807	0.2156	12
$p = 2.999$	$\mathcal{P}_{[P,D,z,\alpha]}$	1.791	1.529	1.591	1.222	1.533	0.2357	9
	$\mathcal{P}_{[P,2D,z,\alpha]}$	2.340	2.281	1.928	1.431	1.995	0.4179	7
$t_{bf} = 10$ yr	$\mathcal{P}_{[P,D,z,\alpha]}$	1.224	1.326	1.303	2.063	1.479	0.3917	13
	$\mathcal{P}_{[P,2D,z,\alpha]}$	1.311	1.450	1.408	2.470	1.660	0.5431	13
$t_{bf} = 100$ yr	$\mathcal{P}_{[P,D,z,\alpha]}$	2.314	1.272	1.795	2.655	2.009	0.6052	4
	$\mathcal{P}_{[P,2D,z,\alpha]}$	2.999	1.459	2.165	3.340	2.491	0.8465	2
$t_{bf} = 10^3$ yr	$\mathcal{P}_{[P,D,z,\alpha]}$	1.841	1.721	2.090	2.054	1.927	0.1756	2
	$\mathcal{P}_{[P,2D,z,\alpha]}$	2.226	2.129	2.505	2.231	2.273	0.1615	3 – 4
2-Changes [f]								
$t_{bf} = 100$ yr	$\mathcal{P}_{[P,D,z,\alpha]}$	2.237	1.489	1.605	2.111	1.861	0.3686	6
$\gamma_{min(hs)} = 10$	$\mathcal{P}_{[P,2D,z,\alpha]}$	2.752	1.760	1.822	2.623	2.239	0.5208	5
$t_{bf} = 100$ yr	$\mathcal{P}_{[P,D,z,\alpha]}$	1.454	1.469	1.499	1.579	1.500	0.0560	12
$a_0 = 15$ kpc	$\mathcal{P}_{[P,2D,z,\alpha]}$	1.828	1.955	1.729	2.234	1.937	0.2191	9 – 10

[a] Each run is done using $x = 3.0$ and $T_{MaxAge} = 300$ Myr for the initial population of size 4963343; the 4 runs averaged here differ in the initial random seeds.

[b] Overall rank (obtained by averaging separate ranks from the four runs) of each of the 14 BRW-modified cases shown here; two values indicate a tie.

[c] Value of only 1 parameter, as listed in the first column, is changed w.r.t. the default version of the BRW-modified model.

[d] Parameters defining external environment density profile are set to those of the KDA model, namely, $\beta = 1.9, a_0 = 2$ kpc, $\rho_0 = 7.2 \times 10^{-22}$ kg m^{-3}.

[e] $\rho_2 = 2 \times \rho_{0\ \text{(Default)}} = 3.34 \times 10^{-23}$ kg m^{-3}.

[f] Values of 2 parameters, as listed in the first column, are changed w.r.t. the default version of the BRW-modified model.

To study the dependence on other model parameters, the initial populations were generated using $x = 3.0$ and $T_{MaxAge} = 300$ Myr for the BRW-modified simulations. For the MK-modified model the relevant birth function parameters used were $x = 2.6$ and $T_{MaxAge} = 150$ Myr. The 1-D K-S results of the first set of runs employing the same "optimal" initial population (with the mentioned x and T_{MaxAge}) and varying the power evolution model parameters to several alternate values, are in Tables B.1 and B.6, for the BRW-modified and MK-modified models.

Now only those cases that gave any improvement in statistics over the default case or were essentially as good as the default were considered further. Three more runs (making a total of four runs) of these picked parameter sets were done using the same big population size but with different pseudo-random seeds, and the means and standard deviations of the relevant 1-D K-S statistics, were found. Some "2-change" cases, i.e., models where two "superior" parameter variations (those giving high 1-D K-S probabilities) were simultaneously employed (as described in Section 4.6 for the original models), also were explored. The means and standard deviations of the combined 1-D K-S probabilities (or, $\mathcal{P}_{[P,D,z,\alpha]}$ and $\mathcal{P}_{[P,2D,z,\alpha]}$) for some "1-change" and "2-change" simulations, are given in Tables 5.9 and 5.10 for the BRW-modified and MK-modified models, respectively.

The 1-D K-S statistic results of these sets of four runs (described in the previous paragraph) for the parameter variations of the 2 modified models are given in Appendix B. Tables B.1, B.2, B.3 and B.4 give the results for the 4 simulation runs of the BRW-modified model; Tables B.6, B.7, B.8 and B.9 do the same for the MK-modified model. The ranks of the combined statistics, $\mathcal{P}_{[P,D,z,\alpha]}$ and $\mathcal{P}_{[P,2D,z,\alpha]}$, in the 4 runs are shown in Tables B.5 and B.10 for the BRW-modified and MK-modified models, respectively.

For the BRW-modified simulations (using the initial ensemble with $x = 3.0$ and $T_{MaxAge} = 300$ Myr) the models which produced combined 1-D K-S statistics within

Table 5.10: MK-modified Results: K-S Statistics for Best-Fit Parameter Variations [a]

Model	$\mathcal{P}(K\text{–}S)$	Run 1	Run 2	Run 3	Run 4	Mean	S.D. (σ)	Rank [b]
MK-Modified	$\mathcal{P}_{[P,D,z,\alpha]}$	1.461	1.391	2.116	1.913	1.720	0.3508	5 – 6 – 7
	$\mathcal{P}_{[P,2D,z,\alpha]}$	2.024	1.781	2.885	2.730	2.355	0.5357	6 – 7
1-Change [c]								
KDA Env. [d]	$\mathcal{P}_{[P,D,z,\alpha]}$	1.546	1.427	1.912	1.159	1.511	0.3128	11
β, a_0, ρ_0	$\mathcal{P}_{[P,2D,z,\alpha]}$	2.150	1.843	2.583	1.464	2.010	0.4740	11
$\beta = 1.6$	$\mathcal{P}_{[P,D,z,\alpha]}$	2.065	2.734	1.576	1.578	1.988	0.5475	2
	$\mathcal{P}_{[P,2D,z,\alpha]}$	3.223	4.044	2.177	2.079	2.881	0.9324	1 – 2
$a_0 = 7.5$ kpc	$\mathcal{P}_{[P,D,z,\alpha]}$	1.520	1.979	1.614	2.122	1.809	0.2879	5 – 6 – 7
	$\mathcal{P}_{[P,2D,z,\alpha]}$	2.323	2.910	2.089	2.840	2.540	0.3987	4
$a_0 = 20$ kpc	$\mathcal{P}_{[P,D,z,\alpha]}$	1.740	2.279	1.065	1.299	1.596	0.5347	10
	$\mathcal{P}_{[P,2D,z,\alpha]}$	2.642	3.640	1.216	1.783	2.320	1.057	8 – 9
$\rho_0 = \rho_2$ [e]	$\mathcal{P}_{[P,D,z,\alpha]}$	1.581	1.105	1.569	1.085	1.335	0.2774	12
	$\mathcal{P}_{[P,2D,z,\alpha]}$	2.132	1.179	1.818	1.387	1.629	0.4279	12
$\gamma_{max(hs)} = 3 \times 10^8$	$\mathcal{P}_{[P,D,z,\alpha]}$	1.661	1.686	1.232	1.615	1.548	0.2132	9
	$\mathcal{P}_{[P,2D,z,\alpha]}$	2.294	2.027	1.437	2.008	1.941	0.3609	10
$p = 2.3$	$\mathcal{P}_{[P,D,z,\alpha]}$	2.015	1.502	1.988	1.595	1.775	0.2646	3 – 4
	$\mathcal{P}_{[P,2D,z,\alpha]}$	3.199	1.894	2.838	1.828	2.440	0.6847	5
$\epsilon = 1.4$	$\mathcal{P}_{[P,D,z,\alpha]}$	1.983	2.223	2.389	1.582	2.044	0.3505	1
	$\mathcal{P}_{[P,2D,z,\alpha]}$	2.962	3.184	3.607	2.040	2.948	0.6621	1 – 2
2-Changes [f]								
$\epsilon = 1.4$	$\mathcal{P}_{[P,D,z,\alpha]}$	1.640	1.981	2.039	1.607	1.817	0.2247	3 – 4
$\beta = 1.6$	$\mathcal{P}_{[P,2D,z,\alpha]}$	2.488	2.759	2.911	2.219	2.594	0.3054	3
$\epsilon = 1.4$	$\mathcal{P}_{[P,D,z,\alpha]}$	1.175	2.035	2.411	1.433	1.764	0.5624	8
$a_0 = 7.5$ kpc	$\mathcal{P}_{[P,2D,z,\alpha]}$	1.705	2.903	3.704	1.962	2.568	0.9154	6 – 7
$\beta = 1.6$	$\mathcal{P}_{[P,D,z,\alpha]}$	1.268	2.256	2.322	1.341	1.797	0.5695	5 – 6 – 7
$a_0 = 7.5$ kpc	$\mathcal{P}_{[P,2D,z,\alpha]}$	1.918	3.133	3.278	1.489	2.455	0.8865	8 – 9

[a] Each run is done using $x = 2.6$ and $T_{MaxAge} = 150$ Myr for the initial population of size 3888492; the 4 runs averaged here differ in the initial random seeds.

[b] Overall rank (obtained by averaging separate ranks from the four runs) of each of the 12 MK-modified cases shown here; two or more values indicate a tie.

[c] Value of 1 parameter, as listed in the first column, is changed w.r.t. the default version of the MK-modified model.

[d] Parameters defining external environment density profile are set to those of the KDA model, namely, $\beta = 1.9, a_0 = 2$ kpc, $\rho_0 = 7.2 \times 10^{-22}$ kg m^{-3}.

[e] $\rho_2 = 2 \times \rho_{0\ \text{(Default)}} = 3.4 \times 10^{-23}$ kg m^{-3}.

[f] Values of 2 parameters, listed in the first column, are changed w.r.t. the default version of the MK-modified model.

1σ of each other consist of the parameter variations listed in Table 5.9. The 1-D K-S statistical results are substantially better for the BRW-modified model than for the default BRW version. The 1-D K-S probabilities for α are sometimes better (especially for 7C) and in few cases (Tables B.1, B.2, B.3 and B.4) approach the value 0.01 for which a model spectral index fit is not firmly rejected.

The MK-modified simulation results (means and standard deviations of relevant K-S statistics) with different parameter variations, using the initial ensemble with $x = 2.6$ and $T_{MaxAge} = 150$ Myr, are shown in Table 5.10. The 1-D K-S statistics of the MK-modified model are comparable to or better than the default MK results.

5.4.3 Additional Statistical Tests

Similarly to what we did in Section 4.8 for the original models, we performed additional statistical analyses on the modified models, to make a more robust comparison both between them and with the original models. For each modified model the 1-D K-S best-fit parameter variation cases, i.e., those which gave the highest combined probability $\mathcal{P}_{[P,D,z,\alpha]}$, according to the results from Section 5.4.2 were selected. Additional statistical tests (with results described next) were performed on the simulations of the modified models with these selected parameters. The modified models were then compared with each other and the original models (from the results in Section 4.8).

5.4.3.1 2-Dimensional Kolmogorov-Smirnov Tests:

The 2-D K-S test results for both the default versions of the modified models and the parameter sets (denoted as "varied") giving the highest total 1-D K-S probability for each model (described in the last 2 paragraphs of Section 5.4.2), are given in Table 5.11. The results are listed in a similar way as are the 1-D K-S statistics in previous tables. An explanation of the table entries is given in Section 4.8.1 for the original models.

The general trends of the 2-D K-S results are discussed in Section 5.5.2.

Table 5.11: 2-D K-S Test Results for the Three Modified Models [a]

Model Parameters	Survey	2-D K-S Probability, $\mathcal{P}(K–S)$					
		$\mathcal{P}(P–z)$	$\mathcal{P}(P–D)$	$\mathcal{P}(z–D)$	$\mathcal{P}(P–\alpha)$	$\mathcal{P}(z–\alpha)$	$\mathcal{P}(D–\alpha)$
KDA-modified	3C	7.57e-07	3.08e-10	1.19e-08	3.29e-09	9.80e-08	1.91e-09
Default [b]	6C	0.682	0.0687	0.160	4.65e-05	9.74e-05	1.24e-04
	7C	0.00170	0.00479	0.00160	0.00259	6.86e-04	0.00101
KDA-modified	3C	0.329	0.0622	0.116	5.60e-06	2.67e-05	1.33e-14
Varied [c]	6C	0.473	0.192	0.195	1.30e-05	1.98e-05	1.29e-04
	7C	0.00719	0.0341	0.0211	0.00373	0.00255	9.91e-05
BRW-modified	3C	0.00234	4.17e-10	2.10e-08	8.27e-08	6.07e-08	5.47e-12
Default [d]	6C	0.458	0.00506	0.00667	1.46e-06	1.48e-06	1.53e-04
	7C	0.00309	8.54e-04	0.00222	0.00733	0.00648	0.0112
BRW-modified	3C	0.299	0.00119	0.00246	5.99e-11	3.86e-10	4.64e-14
Varied [e]	6C	0.781	0.434	0.496	3.21e-06	7.85e-06	2.76e-04
	7C	1.60e-04	0.00297	0.00237	6.00e-05	6.28e-05	0.00228
MK-modified	3C	0.0366	1.48e-04	0.00444	2.29e-40	2.28e-39	1.88e-32
Default [f]	6C	0.0656	0.0325	0.183	1.70e-17	2.32e-18	3.76e-16
	7C	0.0151	0.00180	0.00355	3.53e-15	5.25e-14	2.88e-13
MK-modified	3C	0.147	0.143	0.421	8.35e-40	5.53e-37	8.64e-30
Varied [g]	6C	0.254	0.282	0.235	1.53e-17	2.08e-18	2.22e-14
	7C	0.0203	0.00627	0.0290	2.27e-14	2.96e-13	2.91e-12

[a] 2-D K-S probabilities for different modified model runs, mentioned in the first column. The "Varied" models correspond to the parameter variation cases that gave the highest combined 1-D K-S probability for each model.

[b] KDA-modified simulations with the respective model parameters as described in Section 5.3. Initial population (of size 4397469) is generated using $x = 2.6$, $T_{MaxAge} = 500$ Myr. The 1-D K-S statistics for this case are in the first entry of Table 5.4.

[c] KDA-modified model simulation using initial population with $x = 3.0$, $T_{MaxAge} = 200$ Myr. The power evolution is with respective model parameters as described in Section 5.3. for a run with initial source population size = 4683659. The 1-D K-S statistics for this case are in Table 5.4 (7th entry).

[d] BRW-modified simulations with the respective model parameters as described in Section 5.2. Initial population (of size 4397469) is generated using $x = 2.6$, $T_{MaxAge} = 500$ Myr. The 1-D K-S statistics for this case are in the first entry of Table 5.2.

[e] BRW-modified model simulation using initial population with $x = 3.0$, $T_{MaxAge} = 300$ Myr. The power evolution is with parameter change $t_{bf} = 100$ yr, other parameters set to their default values as in the BRW-modified model, for Run 4 with initial source population size = 4963343. The 1-D K-S statistics for this case are in Table B.4 (11th entry).

[f] MK-modified simulations with the respective model parameters as described in Section 5.2. Initial population (of size 4397469) is generated using $x = 2.6$, $T_{MaxAge} = 500$ Myr. The 1-D K-S statistics for this case are in the first entry of Table 5.3.

[g] MK-modified model simulation using initial population with $x = 2.6$, $T_{MaxAge} = 150$ Myr. The power evolution is with parameter change $\beta = 1.6$, other parameters set to their default values as in the MK-modified model, for Run 2 with initial source population size = 3888492. The 1-D K-S statistics for this case are in Table B.7 (3rd entry).

5.4.3.2 Correlation Coefficient Analyses:

Spearman partial rank correlation coefficients were calculated for those cases for which the 2-D K-S tests were done. As explained in Section 4.8.2, we combined together the $[P, D, z, \alpha]$ data from the 3 surveys: 3C, 6C and 7C-III, for the actual observations or the model simulations, and computed correlations between them. This was done in order to subdue the tight [P–z] correlation present in a single flux-limited complete survey, and to thereby discover any correlations which exist between the other source characteristics.

Table 5.12 gives the four-variable Spearman partial rank correlation coefficients ($r_{PD,z\alpha}, r_{Pz,D\alpha}$, etc) which were computed on the combined data of the modified models. We found the three-variable correlation coefficients ($r_{PD,z}, r_{Pz,D}$ and $r_{Dz,P}$) for the combined $[P, D, z]$ data from all the surveys (3C, 6C and 7C I+II+III). These results are shown in Table 5.13.

We also examined the corresponding 2-variable and 3-variable correlations. A similar trend is seen in the [P–D] correlation for the modified models, as for the original models in Section 4.8.2. The 2-variable correlation r_{PD}, is always negative. But, when the 4-variable correlation between P and D is found with the effects of z and α removed, a small positive correlation is seen between P and D (i.e., positive $r_{PD,z\alpha}$).

5.5 Discussion of the Performance of the Modified Models

The primary modification done to the models, by incorporating a growing hotspot size and axial ratio in them, produced the following major results, judged from the combined 1-D K-S probabilities. The BRW-modified model (results in Section 5.4.2) is a better fit to the data than the original BRW model (Chapter 4), by $\sim 2.5\sigma$, when

Table 5.12: 4-variable Spearman Partial Rank Correlation Analyses for Modified Models

Correlation Coefficient	Data	Model (combining all surveys [a])					
		KDA-modified		BRW-modified		MK-modified	
	All [a]	Default [b]	Varied [b]	Default [b]	Varied [b]	Default [b]	Varied [b]
$r_{PD,z\alpha}$ [c]	0.0303	0.127	0.110	0.183	0.0309	0.160	0.127
$\Sigma_{PD,z\alpha}$ [d]	0.478	2.03	1.75	2.94	0.489	2.57	2.02
$r_{Pz,D\alpha}$	0.716	0.683	0.592	0.667	0.649	0.0754	-0.103
$\Sigma_{Pz,D\alpha}$	14.2	13.2	10.8	12.8	12.2	1.20	-1.64
$r_{Dz,P\alpha}$	-0.268	-0.274	-0.0665	-0.348	-0.237	0.218	0.00189
$\Sigma_{Dz,P\alpha}$	-4.33	-4.46	-1.06	-5.77	-3.83	3.52	0.0300
$r_{P\alpha,Dz}$	0.147	0.0990	0.326	-0.0163	-0.0139	-0.640	-0.750
$\Sigma_{P\alpha,Dz}$	2.33	1.57	5.35	-0.259	-0.219	-12.1	-15.4
$r_{D\alpha,Pz}$	0.472	-0.339	-0.654	0.0649	-0.275	0.605	0.346
$\Sigma_{D\alpha,Pz}$	8.08	-5.60	-12.4	1.03	-4.47	11.2	5.72
$r_{z\alpha,PD}$	-0.0234	0.0388	0.0183	0.132	0.194	-0.590	-0.609
$\Sigma_{z\alpha,PD}$	-0.369	0.615	0.291	2.12	3.12	-10.8	-11.2

[a] The four observables $[P, D, z, \alpha]$ for the 3C, 6C and 7C III surveys (whether real or simulated), combined together in a single sample.

[b] The model parameters used are the same as those in Table 5.11 for each of the "Default" and "Varied" cases of the KDA-modified, BRW-modified and MK-modified models.

[c] Spearman partial rank correlation coefficient between two variables P and D, independent of the other two variables z and α.

[d] Significance level associated with the correlation between P and D, independent of z and α.

comparing the 1-D K-S best-fit cases of each. The MK-modified and KDA-modified models produced fitting statistics (Section 5.4.2) which were slightly better than or comparable to the original MK and KDA model fits (Chapter 4).

We have explored the modified models through our extensive multi-dimensional Monte Carlo simulation procedures and parameter variations in the models. But here too, similar to what we found for the original models in Section 4.9, we found that no modified model gives acceptable fits to the source characteristics $[P, D, z, \alpha]$, for all the three surveys 3C, 6C and 7C, simultaneously.

Steepening the power law index for the initial beam power distribution (Equation 3.9) to $x = 3$ (from $x = 2.6$ used by BRW) while using the default maximum age $T_{MaxAge} = 500$ Myr, improved the 1-D K-S statistics for the BRW-modified model,

Table 5.13: 3-variable Spearman Partial Rank Correlation Analyses for Modified Models

Correlation Coefficient	Data	Model (combining all surveys [a])					
		KDA-modified		BRW-modified		MK-modified	
	All [a]	Default [b]	Varied [b]	Default [b]	Varied [b]	Default [b]	Varied [b]
$r_{PD,z}$ [c]	0.0731	0.0961	-0.0874	0.144	-0.0449	-0.165	-0.150
$\Sigma_{PD,z}$ [d]	1.32	1.74	-1.58	2.62	-0.812	-3.01	-2.72
$r_{Pz,D}$	0.672	0.623	0.553	0.604	0.551	0.670	0.593
$\Sigma_{Pz,D}$	14.6	13.2	11.2	12.7	11.2	14.7	12.3
$r_{Dz,P}$	-0.322	-0.305	-0.136	-0.350	-0.275	-0.174	-0.218
$\Sigma_{Dz,P}$	-5.99	-5.69	-2.48	-6.62	-5.09	-3.19	-4.00

[a] The three RG observables $[P, D, z]$ for the 3C, 6C and 7C I+II+III surveys (whether real or simulated), combined together in a single sample.

[b] The model parameters used are the same as those in Table 5.11 for each of the "Default" and "Varied" cases of the KDA-modified, BRW-modified and MK-modified models.

[c] Spearman partial rank correlation coefficient between two variables P and D, when the other variable z is kept fixed. The null hypothesis is "correlation between P and D arises entirely from those of z with P and D separately".

[d] The significance level associated with the correlation between P and D, independent of z. $\Sigma_{PD,z}$ is normally distributed about 0 with variance = 1, if the null hypothesis is true.

as can be seen from Table 5.2. However, in the MK-modified model $x = 2.6$ gave better results, as compared to $x = 3$ (Table 5.3). This is the only model (among the 6 extensive comparisons: KDA, BRW, MK and their corresponding modifications) which gave better 1-D K-S fits with the beam power distribution index set to its default value, $x = 2.6$. Simulations done by co-varying T_{MaxAge} and x (Tables 5.2, 5.3 and 5.4) gave better fits at a maximum age of 300 Myr (BRW-modified), 150 Myr (MK-modified) and 200 Myr (KDA-modified), when combined with the above "optimal" x. These "best-fit" values of x and T_{MaxAge} for the modified models (except x for MK-modified) are comparable to those in the original models (Section 4.4 and 4.5).

5.5.1 Comparison of Number of Sources Detected

We examined the trends for the ratios of number of sources detected in the 6C and 7C simulations with the number in the actual catalogs, as proportionate to the corresponding 3C fraction (Ratio_{6C} and Ratio_{7C}, defined in Equation 3.16). For the

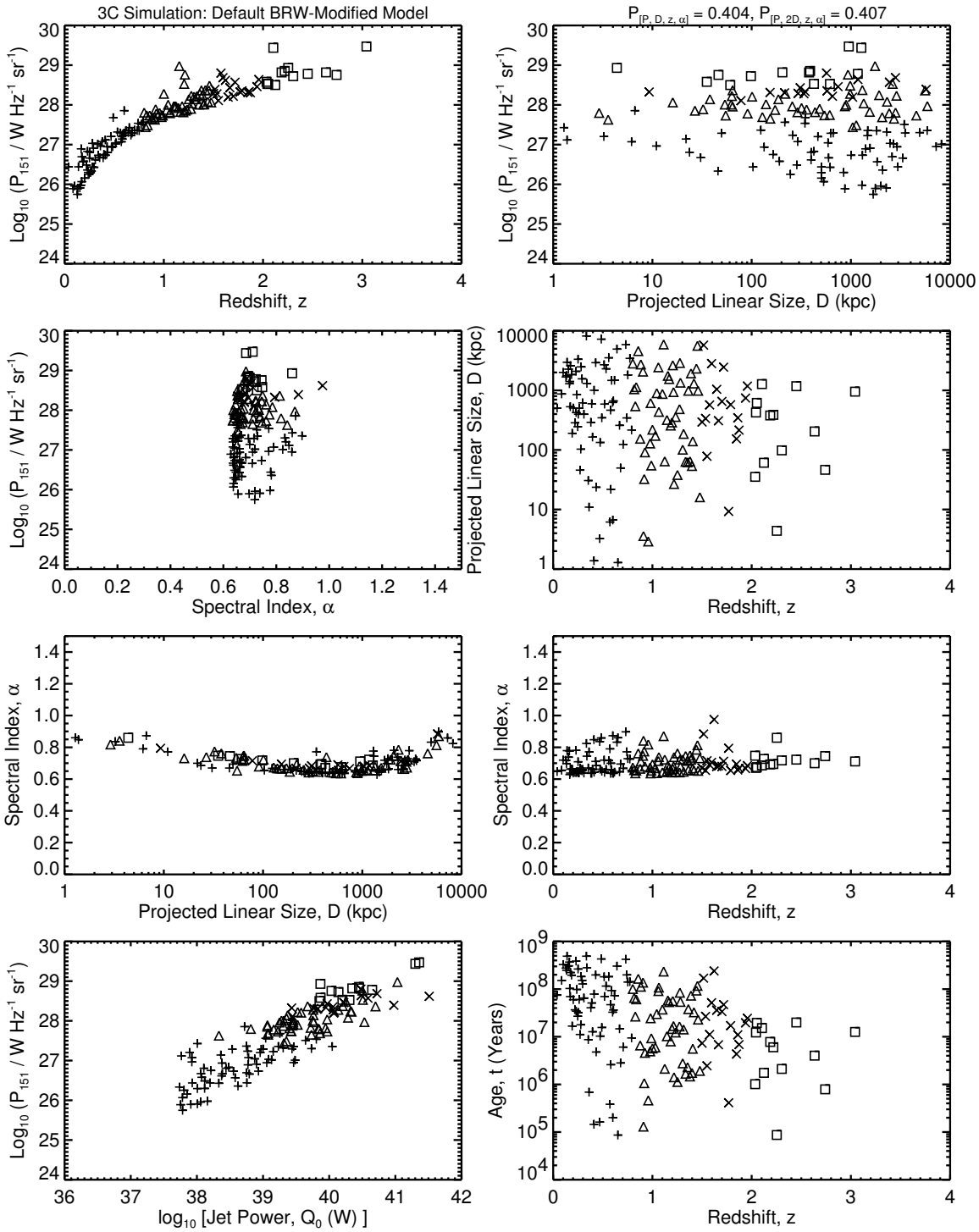

Figure 5.5a: The $[P$–D–z–$\alpha]$ planes for the 3C simulations of the default BRW-modified model. The initial ensemble (of size 4397469) is generated using $x = 2.6$, $T_{MaxAge} = 500$ Myr; the power evolution is with parameter values as used by the authors in the BRW model, with the hotspot growing in size according to Section 5.2. The 1-D K-S statistics for this case are in the first entry of Table 5.2. Compare to Figure 3.1a.

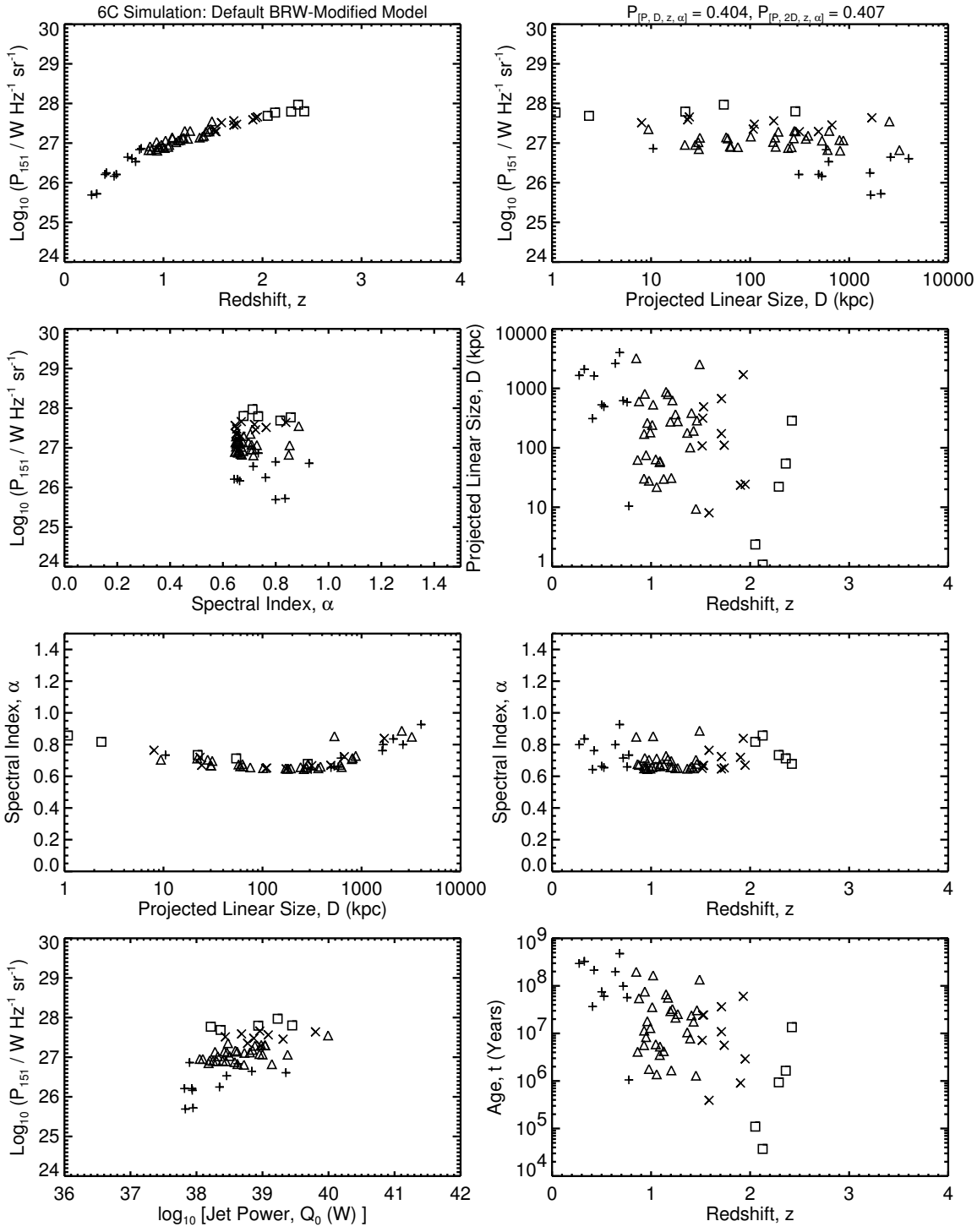

Figure 5.5b: The $[P$–D–z–$\alpha]$ planes for the 6C simulations of the default BRW-modified model, which is the same as in Figure 5.5a. Compare to Figure 3.1b.

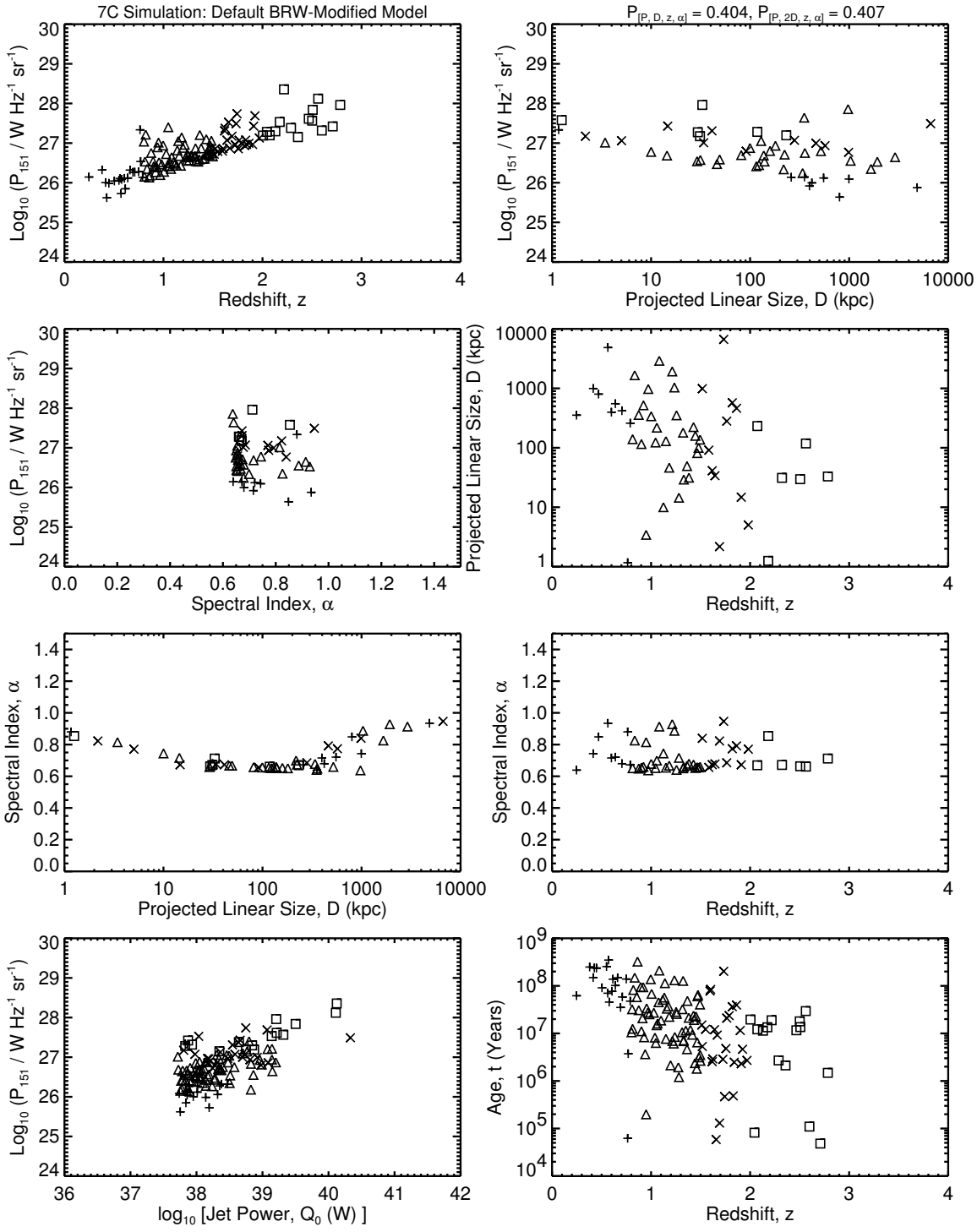

Figure 5.5c: The [P–D–z–α] planes for the 7C simulations of the default BRW-modified model, which is the same as in Figure 5.5a. Compare to Figure 3.1c.

BRW-modified and KDA-modified models, the detection number ratio was more consistent for the 6C than it was for the 7C simulations; i.e., Ratio_{6C} was closer to 1.0 (which it should equal ideally) than was Ratio_{7C}. For the MK-modified model, the detection number ratios for 6C and 7C were equally consistent, and were usually better than both the BRW-modified and KDA-modified predictions. Comparing the modified models by these detection number ratios, the MK-modified model gives the best fit to the data, followed by KDA-modified and finally BRW-modified.

In most of the cases with $x = 3$, the BRW-modified models gave overdetection in both 6C and 7C simulations when compared to 3C, with the overdetection factor greater in 7C. The Ratio_{6C} was mostly in the range $(1.0 - 1.2)$, and Ratio_{7C} usually in between $1.3 - 1.6$.

The detection number ratios were the best (closest to 1.0) for the MK-modified models. In general, there were both underdetection and overdetection in 6C, and overdetection in 7C when compared to 3C. The Ratio_{6C} was mostly in the range $(0.7 - 1.1)$, and the Ratio_{7C} in between $(1.0 - 1.3)$ for the MK-modified simulations.

The KDA-modified models gave a mixture of underdetections and overdetections in the 6C simulations, but only overdetections in 7C, when compared to 3C (as in the MK-modified model). For the simulations done with $x = 3$, the Ratio_{6C} was in the range $(0.9 - 1.2)$; the Ratio_{7C} was usually between 1.1 and 1.6, and went up to 1.7-1.8 for a few cases.

The behaviors of the modified models in producing "good" detection ratios are consistent with the trends of the original models. This implies that the modifications done to the models in this Chapter have little impact on the number of sources detected in the different flux-limited virtual surveys. Though we calculated the detection number ratios and here discuss the model performances on this basis, we do not formally consider them in comparing the models, due to reasons discussed in the last paragraph of Section 4.9.1.

5.5.2 Comparing Modified Models with Additional Statistical Tests

Examining the 2-D K-S test results from Table 5.11 we can say that the [P–z], [P–D] and [z–D] planes can be reasonably fitted by the "varied" cases of the modified models. Six of these non-α 2-D probabilities are > 0.1 for the MK-modified "varied" model; this is true for 5 $\mathcal{P}$'s in the KDA-modified, and 4 $\mathcal{P}$'s in the BRW-modified

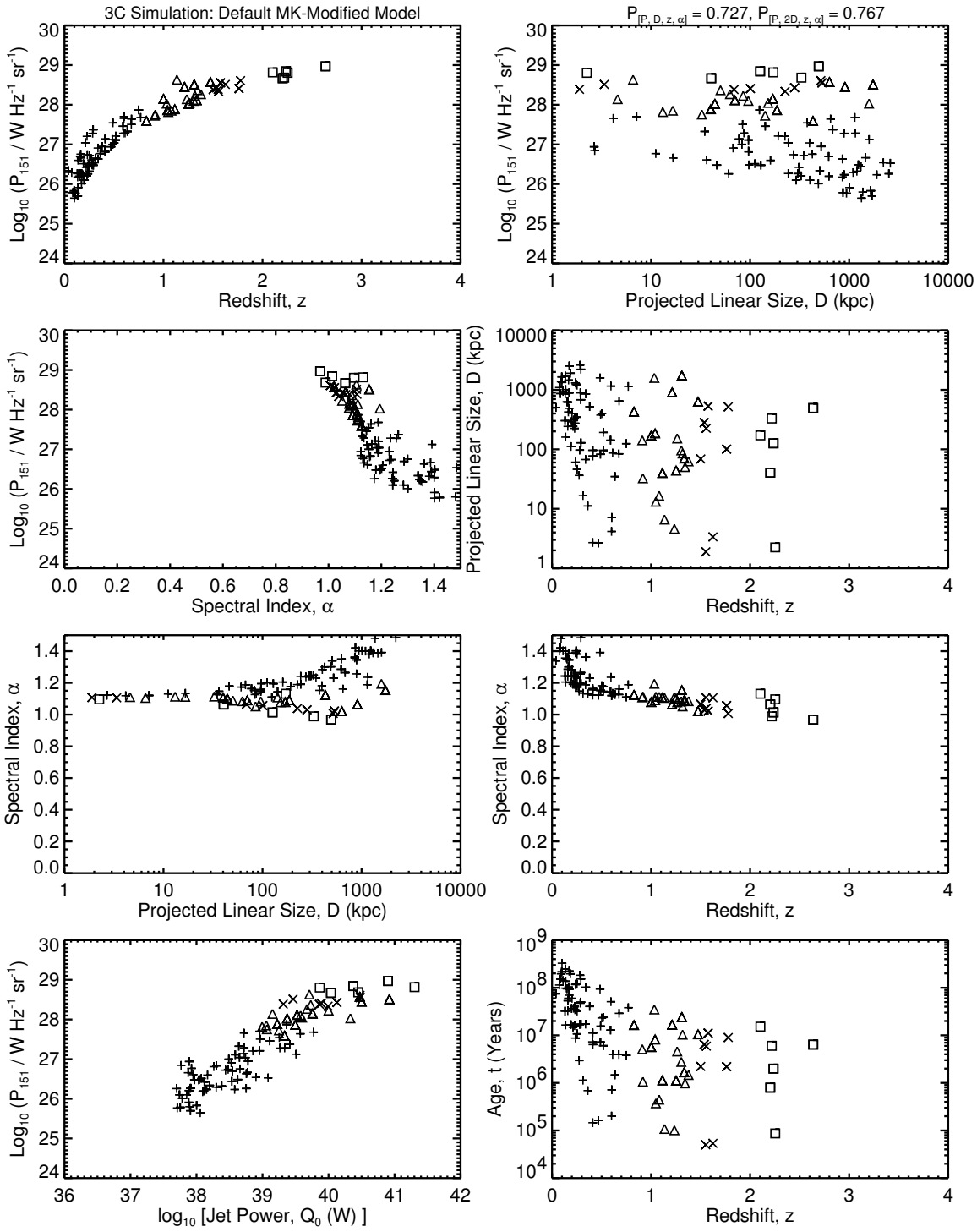

Figure 5.6a: The $[P$–D–z–$\alpha]$ planes for the 3C simulations of the default MK-modified model. The initial ensemble (of size 4397469) is generated using $x = 2.6$, $T_{MaxAge} =$ 500 Myr; the power evolution is with parameter values as used by the authors in the MK model, with the hotspot growing in size according to Section 5.2. The 1-D K-S statistics for this case are in the first entry of Table 5.3. Compare to Figure 3.1a.

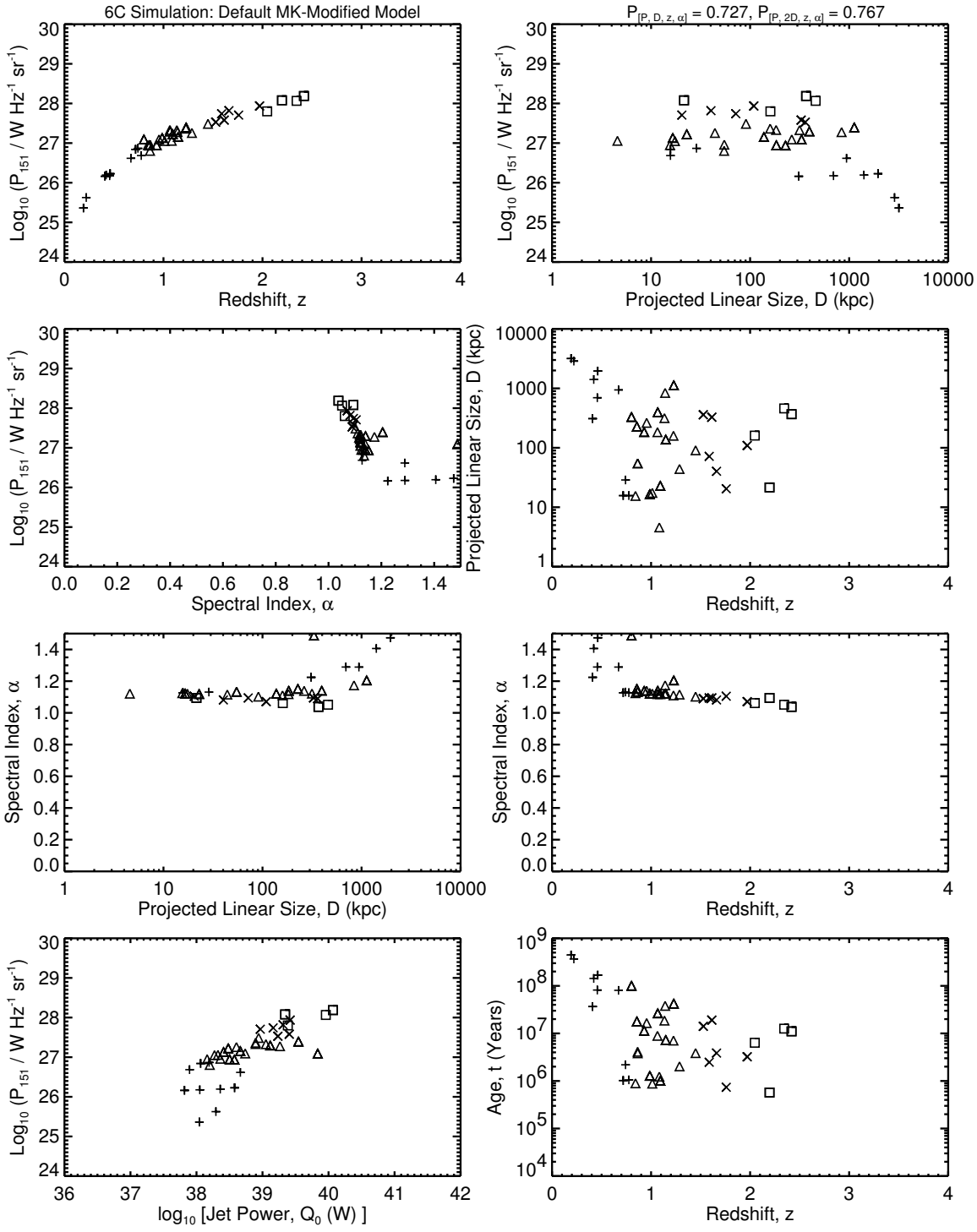

Figure 5.6b: The [P–D–z–α] planes for the 6C simulations of the default MK-modified model, which is the same as in Figure 5.6a. Compare to Figure 3.1b.

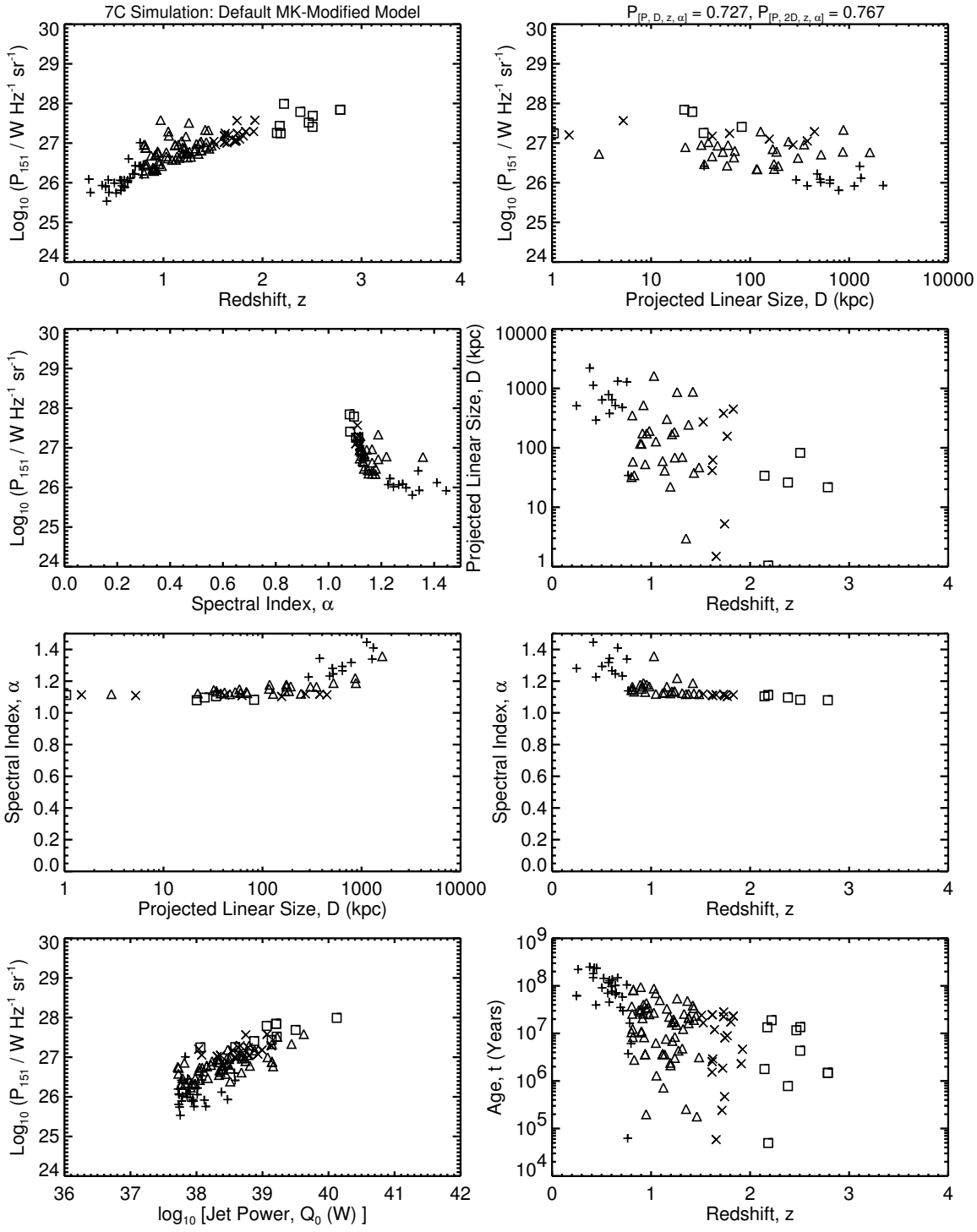

Figure 5.6c: The [P–D–z–α] planes for the 7C simulations of the default MK-modified model, which is the same as in Figure 5.6a. Compare to Figure 3.1c.

cases. All of the 2-D $\mathcal{P}$'s of the "varied" MK-modified model are higher than those of the default MK-modified. When compared to the corresponding default versions, improvements are seen for 8 of 9 of the 2-D $\mathcal{P}$'s not involving α, in the "varied" KDA-modified and BRW-modified models. These 2-D results provide support for the superiority of the "varied" models (selected from 1-D K-S tests) in fitting the data, as both the 1-D and 2-D statistics point in the same direction.

Comparing the "varied" cases of the modified models among themselves in the 9 planes not involving α (the [P–z], [P–D], [z–D] planes of each of 3C, 6C and 7C), 6 of the 2-D $\mathcal{P}$'s for the MK-modified model are higher than those of KDA-modified and BRW-modified; and, 5 of the the 2-D $\mathcal{P}$'s for the KDA-modified are higher than BRW-modified. All the α-related 2-D K-S probabilities are ≤ 0.008 for every modified model. Similar to the original models (as discussed in Section 4.9.2), the modified models also cannot fit any plane involving α.

From the 2-D K-S probabilities of the modified models in Table 5.11, we conclude that the MK-modified model is the best (having the highest number of 2-D $\mathcal{P}$'s close to 1) in fitting the observational data, very closely followed by KDA-modified, and we find the BRW-modified as worst.

From the Spearman partial rank correlation analyses on the combined data of the 3 surveys (3- and 4-variable coefficients in Tables 5.12 and 5.13) we can conclude that the KDA-modified model is able to match the survey data correlations very closely (particularly for $[P, D, z]$). Some matches to the data correlations are acceptable for the BRW-modified, but they are less good for the MK-modified model.

The parameter variation cases which were the best fits (i.e., gave the highest combined probability, $\mathcal{P}_{[P,D,z,\alpha]}$) from the 1-D K-S results, or the "varied" cases in Tables 5.11, 5.12 and 5.13, are not necessarily the better fits according to the correlation analyses. Comparing the 4-variable correlation coefficients of the different models, 4 out of 6 of them are better match to the data correlations in the default than the "varied" KDA-modified model. For the BRW-modified and MK-modified models the default and the "varied" cases perform comparably, as 3 coefficients are better in the default and the remaining 3 are better in the "varied" models. Examining the 3-variable coefficients, the default models are better than the "varied" for the KDA-modified and BRW-modified models in matching the real data correlations, while for MK-modified the "varied" is better than the default.

Considering the signs of the four-variable coefficients of the combined surveys,

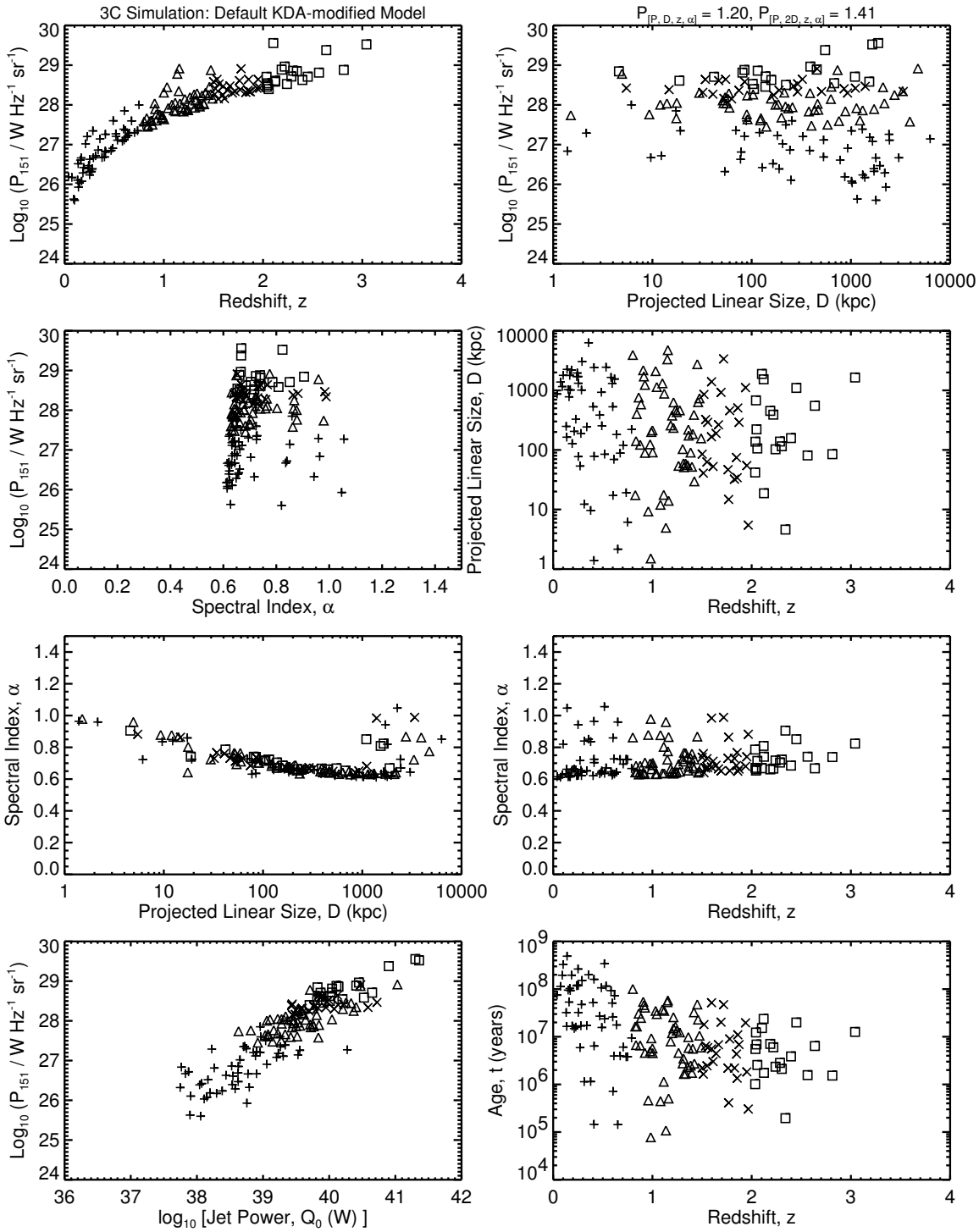

Figure 5.7a: The $[P$–D–z–$\alpha]$ planes for the 3C simulations of the default KDA-modified model. The initial ensemble (of size 4397469) is generated using $x = 2.6$, $T_{MaxAge} = 500$ Myr; the power evolution is with parameter values as used by the authors in the KDA model, with the axial ratio growing in size according to Section 5.3. The 1-D K-S statistics for this case are in the first entry of Table 5.4. Compare to Figure 3.1a.

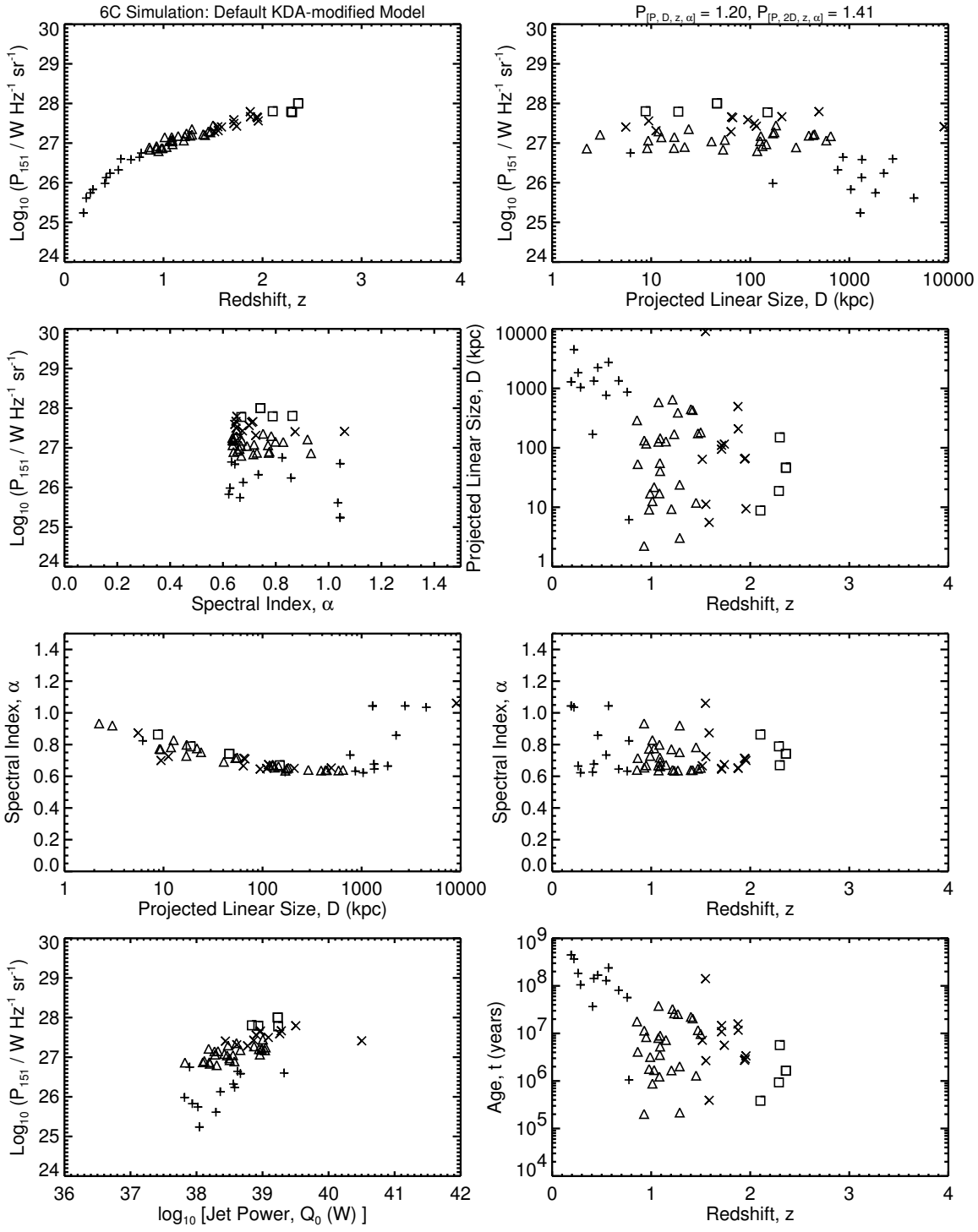

Figure 5.7b: The $[P$–D–z–$\alpha]$ planes for the 6C simulations of the default KDA-modified. The model is the same as in Figure 5.7a. Compare to Figure 3.1b.

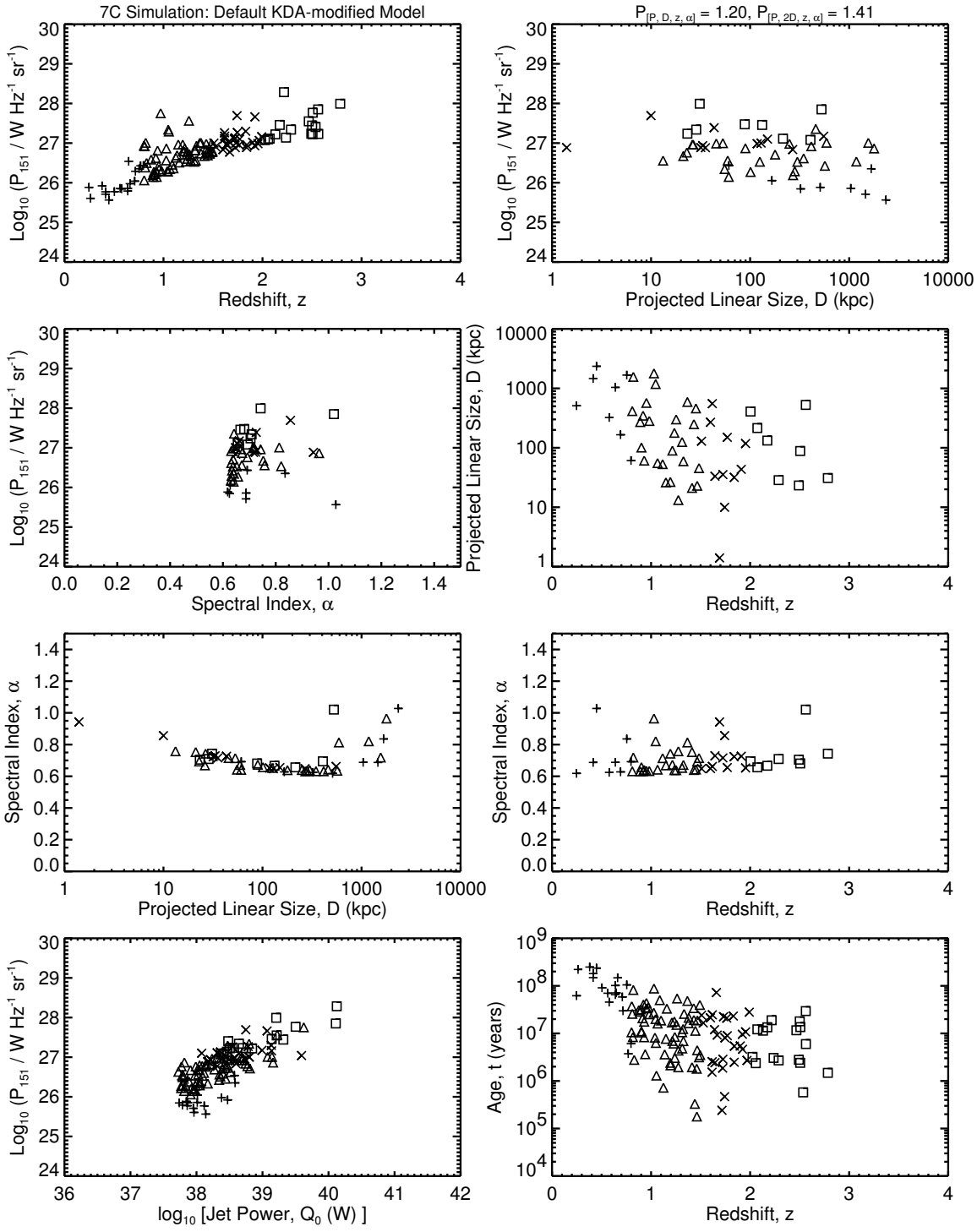

Figure 5.7c: The $[P$–D–z–$\alpha]$ planes for the 7C simulations of the default KDA-modified. This model is the same as in Figure 5.7a. Compare to Figure 3.1c.

the MK-modified model predicts [P–α] anti-correlation, [D–z] correlation, and its "varied" case produces [P–z] anti-correlation. All these are trends opposite to the survey data and to the other models, except that the BRW-modified model also predicts [P–α] anti-correlation. The signs of the [D–α] and [z–α] correlations of the combined surveys are only predicted by both the MK-modified models ([D–α] correlation is also exhibited weakly by the BRW-modified default case), while the other models produce opposite correlations. However, this advantage is meaningless as the MK-modified model gives very poor α-distribution.

From the correlation coefficient analyses done by combining data from all the surveys (3C, 6C and 7C) together we conclude that the KDA-modified model fits the data most closely, immediately followed by BRW-modified, and finally MK-modified. Similar trends emerge if we examine the 3-variable correlation coefficients from Table 5.13.

The BRW-modified model provides the best fit to the 4-variable [P–D] correlation, $r_{PD,z\alpha}$. This indicates that in the BRW model a growing hotspot is able to reproduce the P–D evolution (seen in 3C, 6C and 7C survey data) better than assuming a constant hotspot size (the original BRW model).

5.5.3 Discussion of [P–D–z–α] Planes

As for the original models shown in Section 4.9.3, we plotted planes through the [P–D–z–α] volume for the new simulated surveys, and compared them with the overall trends in the [P–D–z–α] slices of the actual data. For the sources in the simulated surveys, we also show the P vs. Q_0 (the jet power), and t (source age) vs. z diagrams.

The actual 3C, 6C and 7C data are shown in Figures 3.1a, 3.1b and 3.1c. The simulated data (3C, 6C and 7C virtual surveys) for the default versions of the BRW-modified, MK-modified and KDA-modified models are shown in Figures 5.5, 5.6 and 5.7, respectively. The "best-fit" parameter sets for each model (those which give the highest total 1-D K-S probability within each modified model) are the simulations plotted in Figures 5.8, 5.9 and 5.10, for the BRW-modified, MK-modified and KDA-modified models, respectively. These are the cases which were explored further by performing additional statistical tests on them (Sections 5.4.3 and 5.5.2). The parameter sets of these figures are denoted as "varied" in Tables 5.11, 5.12 and 5.13.

The main features of the [P–D–z–α] planes of the modified models are analogous to those of the original models in Section 4.9.3. So these are only discussed briefly,

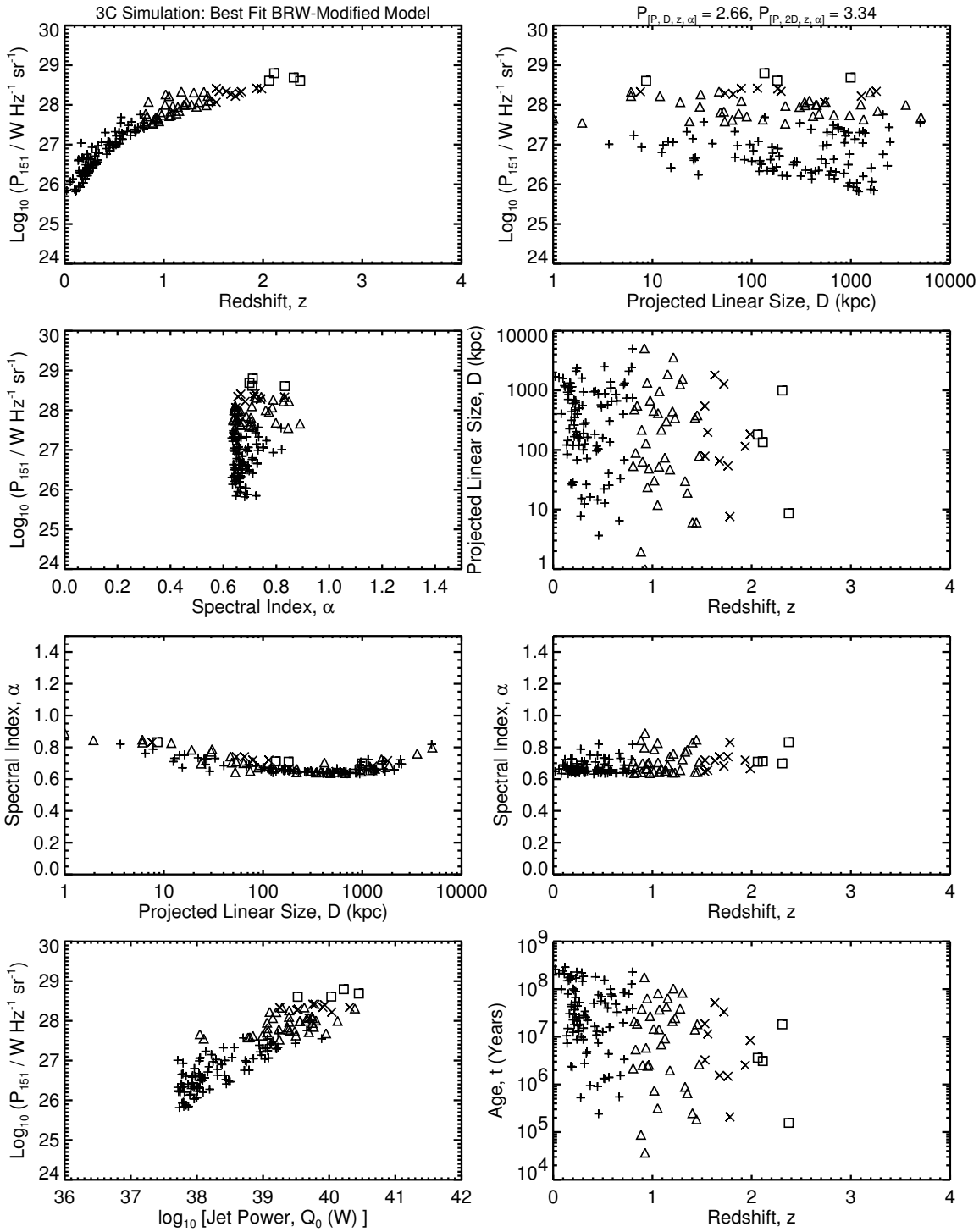

Figure 5.8a: The $[P$–D–z–$\alpha]$ planes for the 3C simulations of the best-fit BRW-modified model. The initial ensemble (of size 4963343 – Set 4) is generated using $x = 3.0$, $T_{MaxAge} = 300$ Myr; the power evolution is with the parameter variation of $t_{bf} = 100$ yr, with the rest being their default values as in the BRW-modified model. The 1-D K-S statistics for this case are in Table 5.9 (11th row, Run 4), and in Table B.4 (11th entry). Compare to Figure 3.1a.

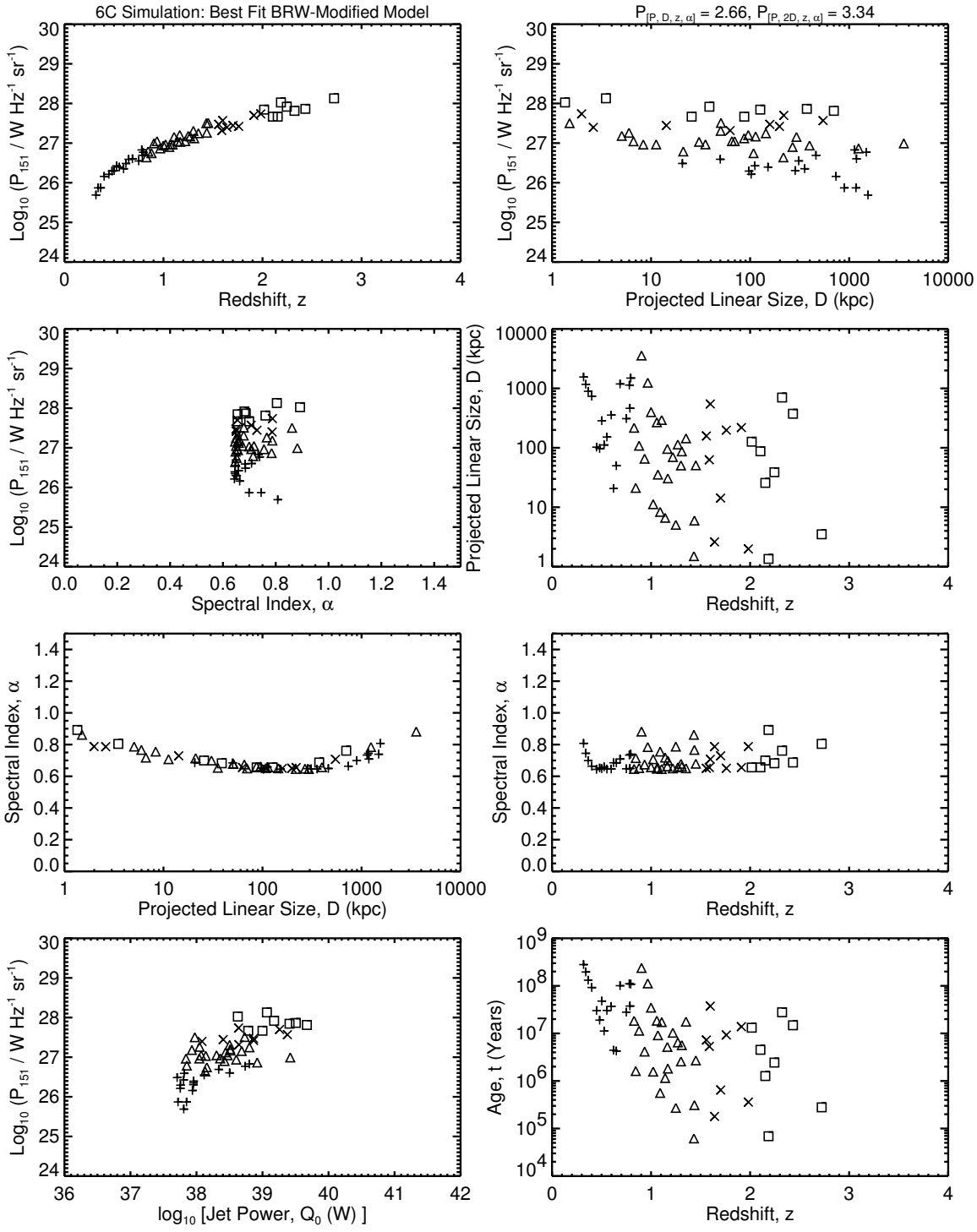

Figure 5.8b: The [P–D–z–α] planes for the 6C simulations of the best fit BRW-modified model, which is the same as in Figure 5.8a. Compare to Figure 3.1b.

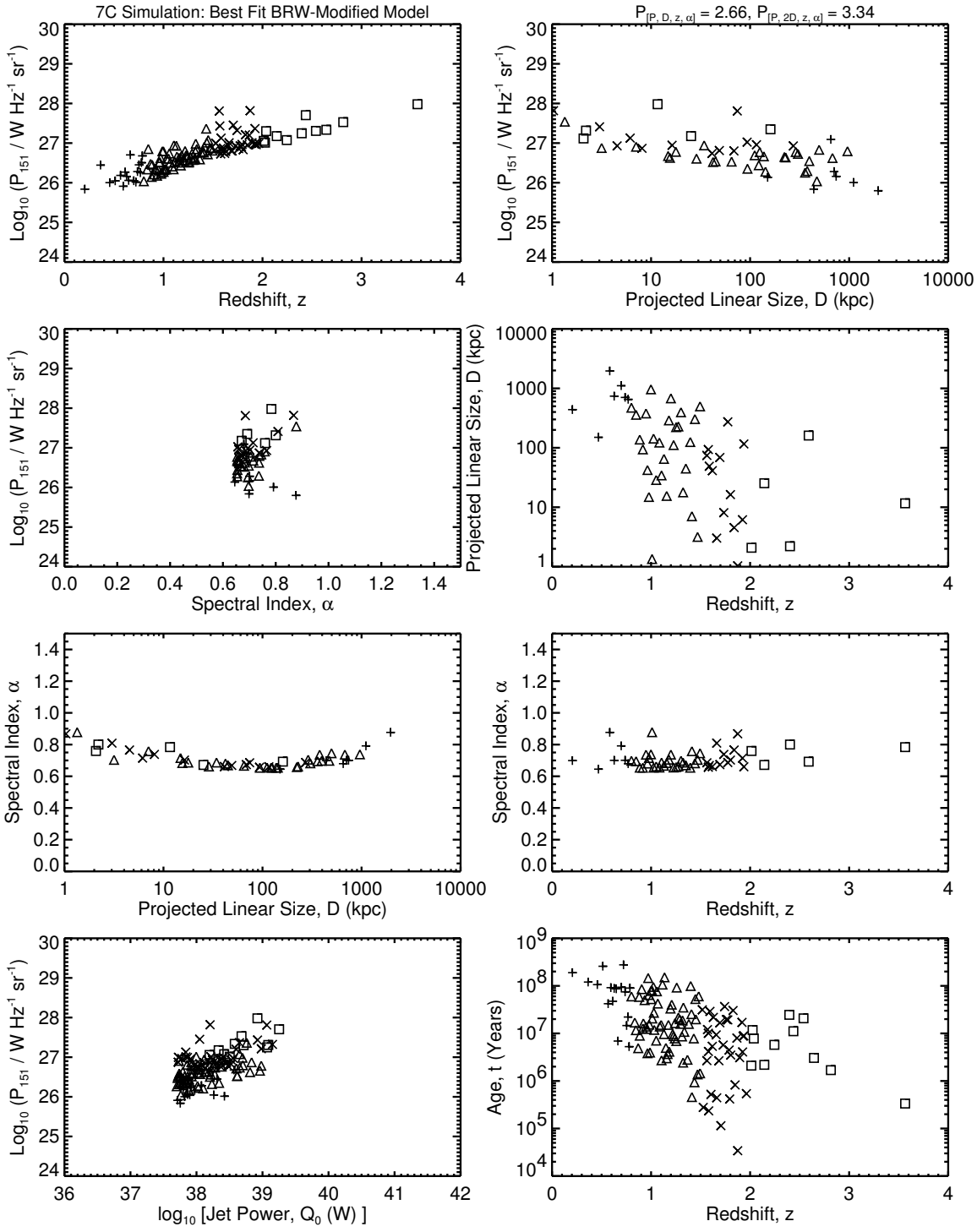

Figure 5.8c: The [P–D–z–α] planes for the 7C simulations of the best fit BRW-modified model, which is the same as in Figure 5.8a. Compare to Figure 3.1c.

with the stress on any new feature(s).

5.5.3.1 [P–z] Plane:

All of our simulated surveys of all the modified models miss many of the low-P sources seen in the data. Too few low-z/low-P sources are produced in all the simulated 7C surveys. There is underproduction of very high-z sources ($z > 2$) in the 7C simulations and a similar, but less pronounced, trend is also present for 6C.

5.5.3.2 [P–D] Plane:

The BRW-modified and KDA-modified models predict similar trends in the [P–D] plane, with some more scatter along P in the KDA-modified case. These models overproduce large powerful sources in 3C, and underproduce the large weaker sources. There is over-production of small sources in the KDA-modified model. The 6C and 7C [P–D] planes of all the modified models show a tighter correlation as compared to the data, which present more scatter. Given that additional physics not included in the models would tend to broaden this distribution, this result is expected.

There is P–D anti-correlation in the MK-modified model in all of the 3C, 6C and 7C simulations. Such P–D evolution is also seen in the BRW-modified model where it is more pronounced in the 6C and 7C simulations; such P–D anti-correlation trends are weaker in the KDA-modified model. An important improvement in the BRW-modified model is that the strong P–D anti-correlation of the original BRW is diluted after the modification which incorporates a growing hotspot.

5.5.3.3 [D–z] Plane:

The BRW-modified and KDA-modified models predict similar trends in the [D–z] plane. The KDA-modified model overproduces very small and very large 3C sources at all redshifts, while the BRW-modified model overproduces only the larger 3C sources.

The MK-modified model's (best-fit case) [D–z] planes seem to be a good fit (by eye) to the data (especially the 3C [D–z] planes), with the right amount of D–z anti-correlation. The BRW-modified model produces a weaker D–z anti-correlation than does the data in 3C, but stronger than the data in 6C and 7C. The D–z anti-correlation is almost negligible in 3C, and very weak in the 6C and 7C simulations of

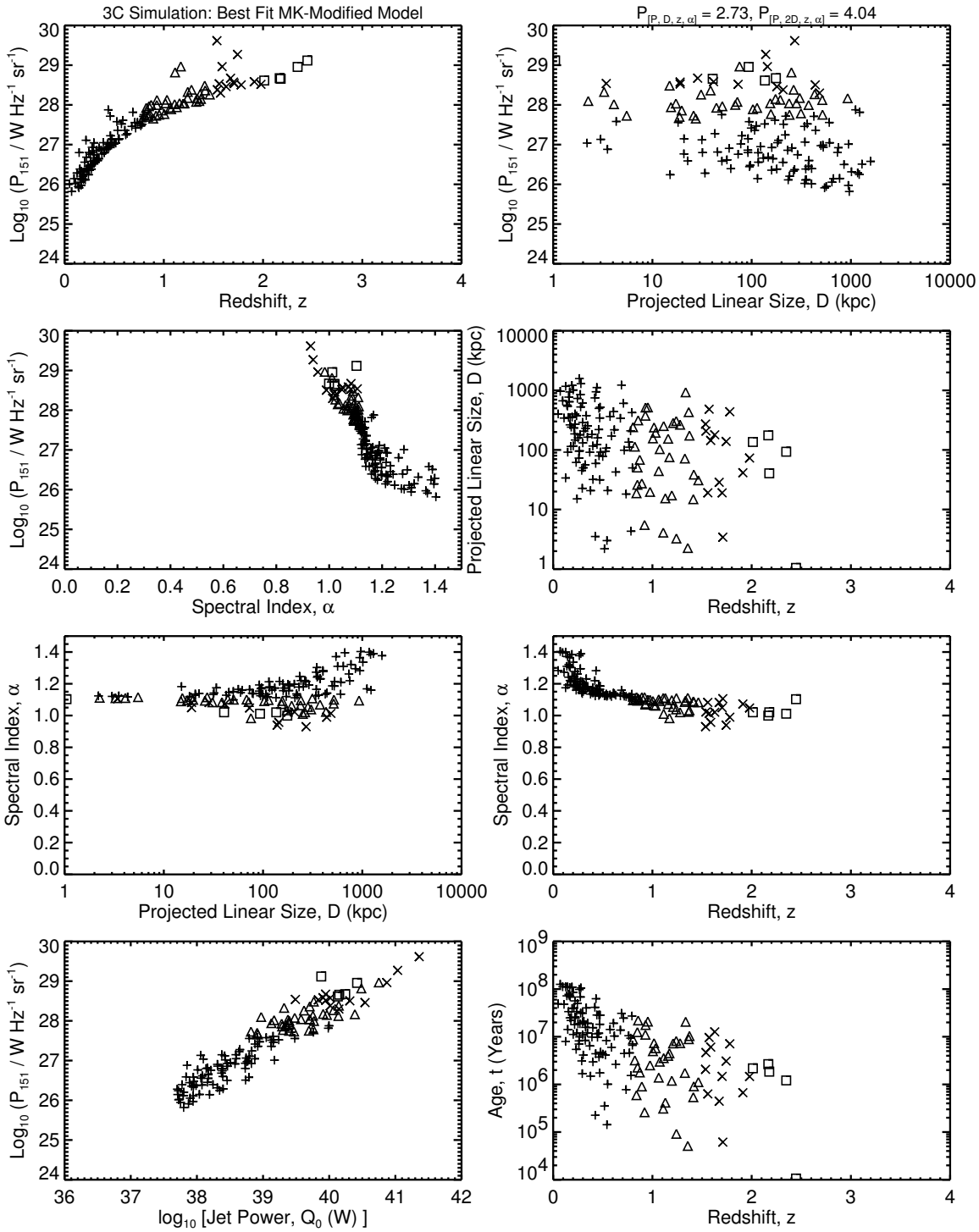

Figure 5.9a: The $[P$–D–z–$\alpha]$ planes for the 3C simulations of the best fit MK-modified model. The initial ensemble (of size 3888492 – Set 2) is generated using $x = 2.6$, $T_{MaxAge} = 150$ Myr; the power evolution is with parameter variation $\beta = 1.6$, the rest of the parameters having their default values of the MK-modified model. The 1-D K-S statistics for this case are in Table 5.10 (3rd row, Run 2), and in Table B.7 (3rd entry). Compare to Figure 3.1a.

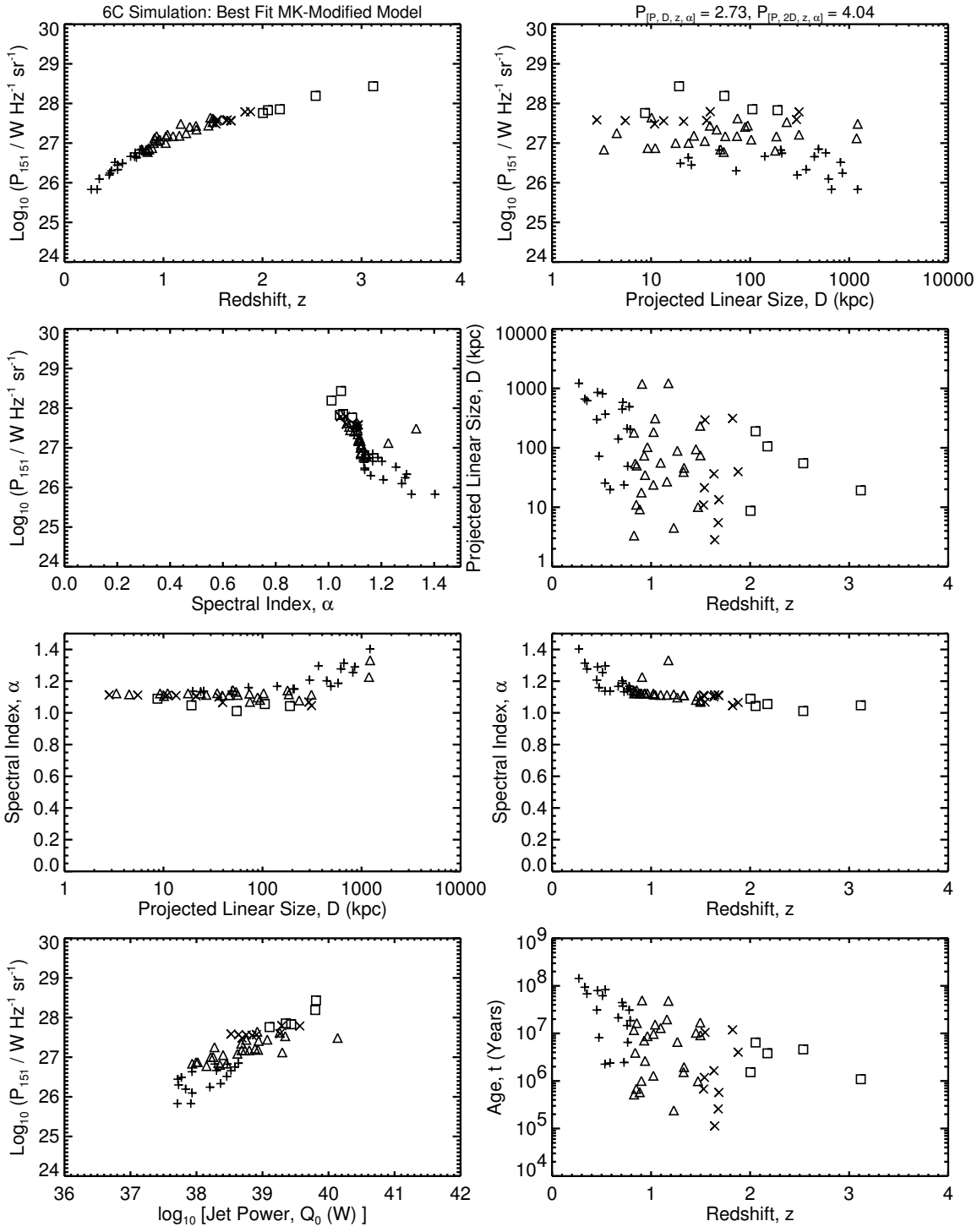

Figure 5.9b: The $[P$–D–z–$\alpha]$ planes for the 6C simulations of the best fit MK-modified model, which is the same as in Figure 5.9a. Compare to Figure 3.1b.

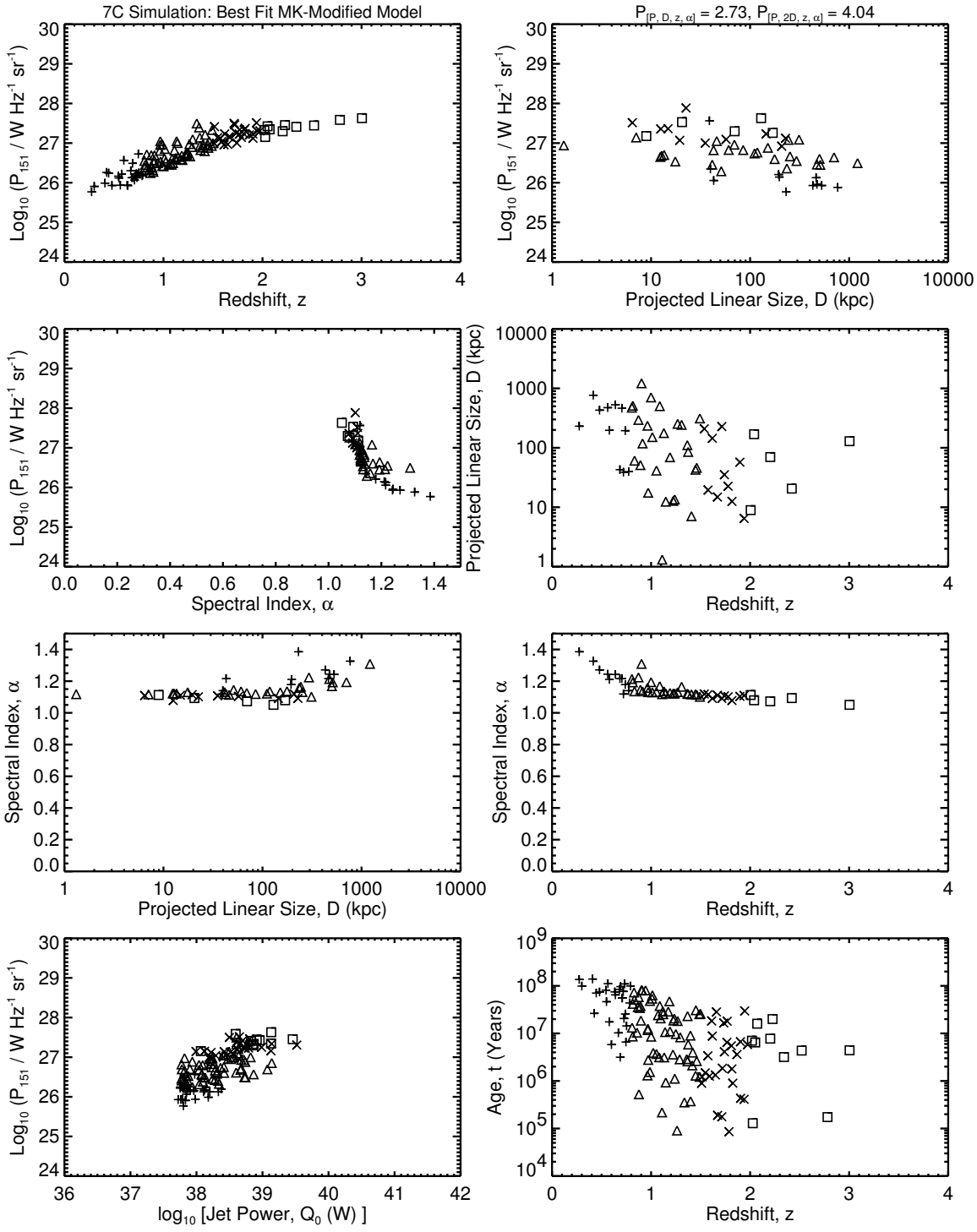

Figure 5.9c: The [P–D–z–α] planes for the 7C simulations of the best fit MK-modified model, which is the same as in Figure 5.9a. Compare to Figure 3.1c.

the KDA-modified model. An explanation of the D–z evolution (effect of the "youth-redshift degeneracy", discussed in Section 4.1) in given while discussing the original model planes in Section 4.9.3.

From these trends we conclude that the MK-modified model is the best fit (by eye) to the [D–z] planes of the 3C, 6C and 7C data.

5.5.3.4 [P–α] and [α–z] Planes:

There are tight correlations with the spectral index of all the other characteristics examined in the simulations. The data shows high scatter in α, which is not seen in any of the models.

In the BRW-modified model, the spectral indices are distributed between $0.6 < \alpha < 0.9$, with a greater number of sources at $\alpha \sim 0.6$. It does not produce any source with very flat or with very steep spectra, and some of these are seen in the real data.

The MK-modified model always produces too many steep spectrum sources, with the spectral indices distributed between $0.9 < \alpha < 1.5$. There exists a dense collection of sources at $\alpha \sim 1.0 - 1.1$, and the number decreases at higher α. In the [$\alpha - z$] plane there is a trend of α decreasing as z increases, which is manifested as P decreasing as α increases in the [P–α] plane.

The KDA-modified model presents similar trend to the BRW-modified model in the [P–α] and [α–z] planes, but with a larger scatter in α. A large subset of all the simulated sources pile up at $\alpha \geq 0.6$, and their numbers decrease at higher spectral index values, with sources existing only until $\alpha \sim 1.0$. So the KDA-modified model fails to produce any source flatter than $\alpha \sim 0.6$. It also underproduces some of the less powerful and steep sources in the $0.6 < \alpha < 1.0$ range.

5.5.3.5 [α–D] Plane:

In the BRW-modified model, there is a weak trend of α decreasing as D increases, but the trend reverses, so that α increases with D, at linear sizes greater than $\sim$ few $100 - 1000$ kpc. The initial trend is opposite to that seen in data where α shows a weak trend of increasing with D.

In the MK-modified model initially α remains almost constant as D increases, but at higher sizes ($> 100 - 200$ kpc) there is a trend of α increasing as D increases. The latter trend is similar to that seen in the data, but the MK spectra are always too

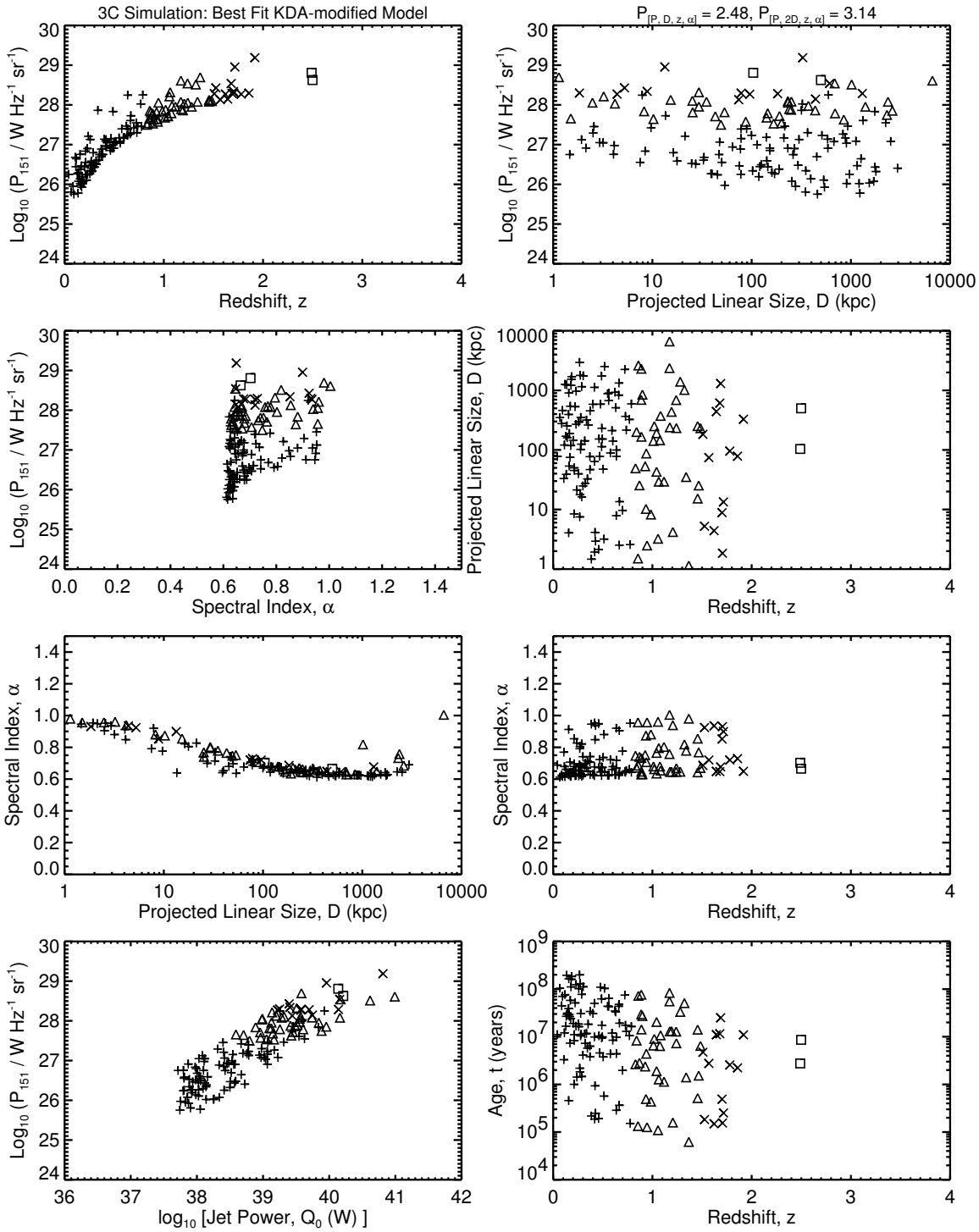

Figure 5.10a: The $[P$–D–z–$\alpha]$ planes for the 3C simulations of the best fit KDA-modified model. The initial ensemble (of size 4683659) is generated using $x = 3.0$, $T_{MaxAge} = 200$ Myr; the power evolution is with parameter values as used by the authors in the KDA model, with the axial ratio growing in size according to Section 5.3. The 1-D K-S statistics for this case are in Table 5.4 (7th entry). Compare to Figure 3.1a.

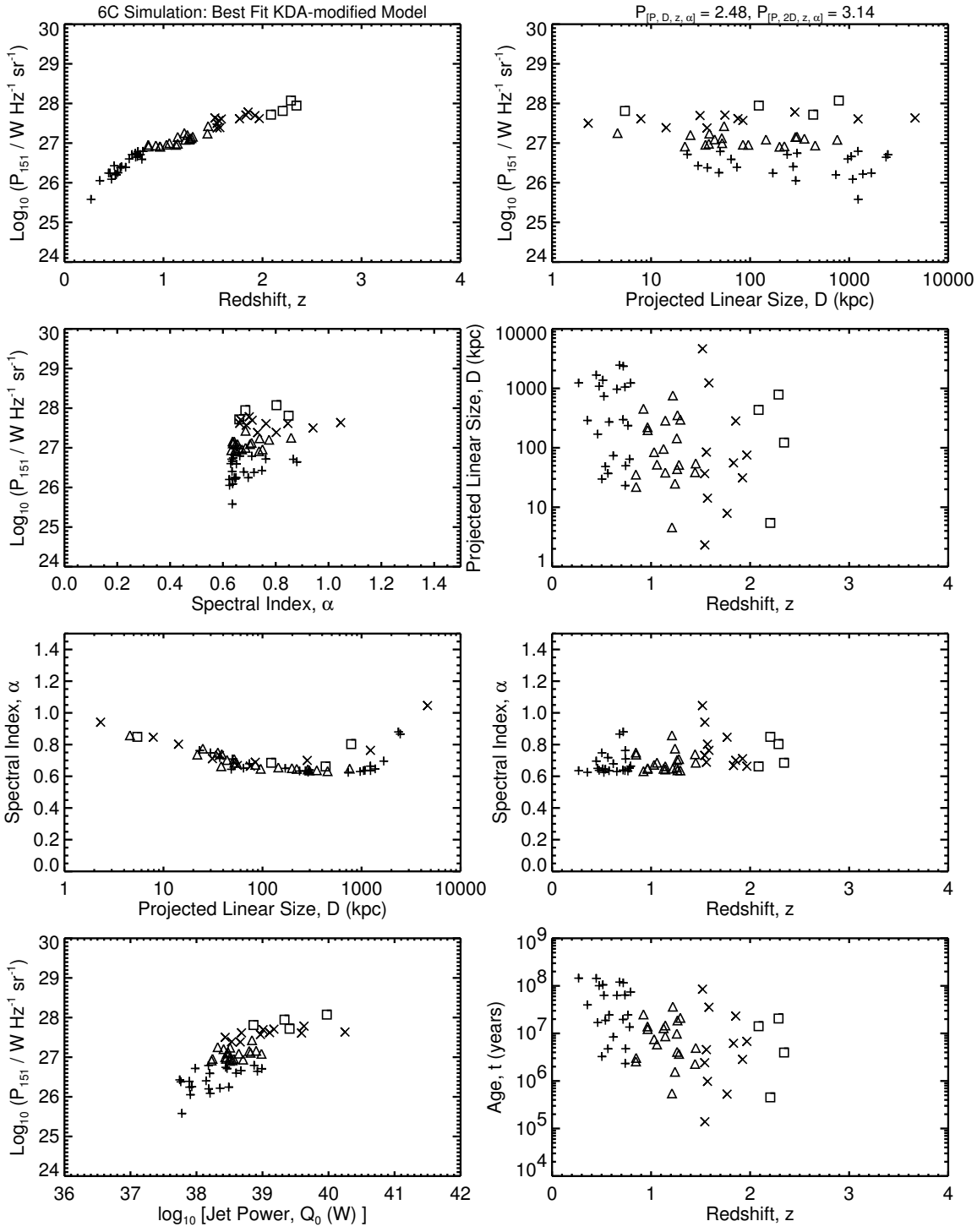

Figure 5.10b: The $[P$–D–z–$\alpha]$ planes for the 6C simulations of the best fit KDA-modified model, which is the same as in Figure 5.10a. Compare to Figure 3.1b.

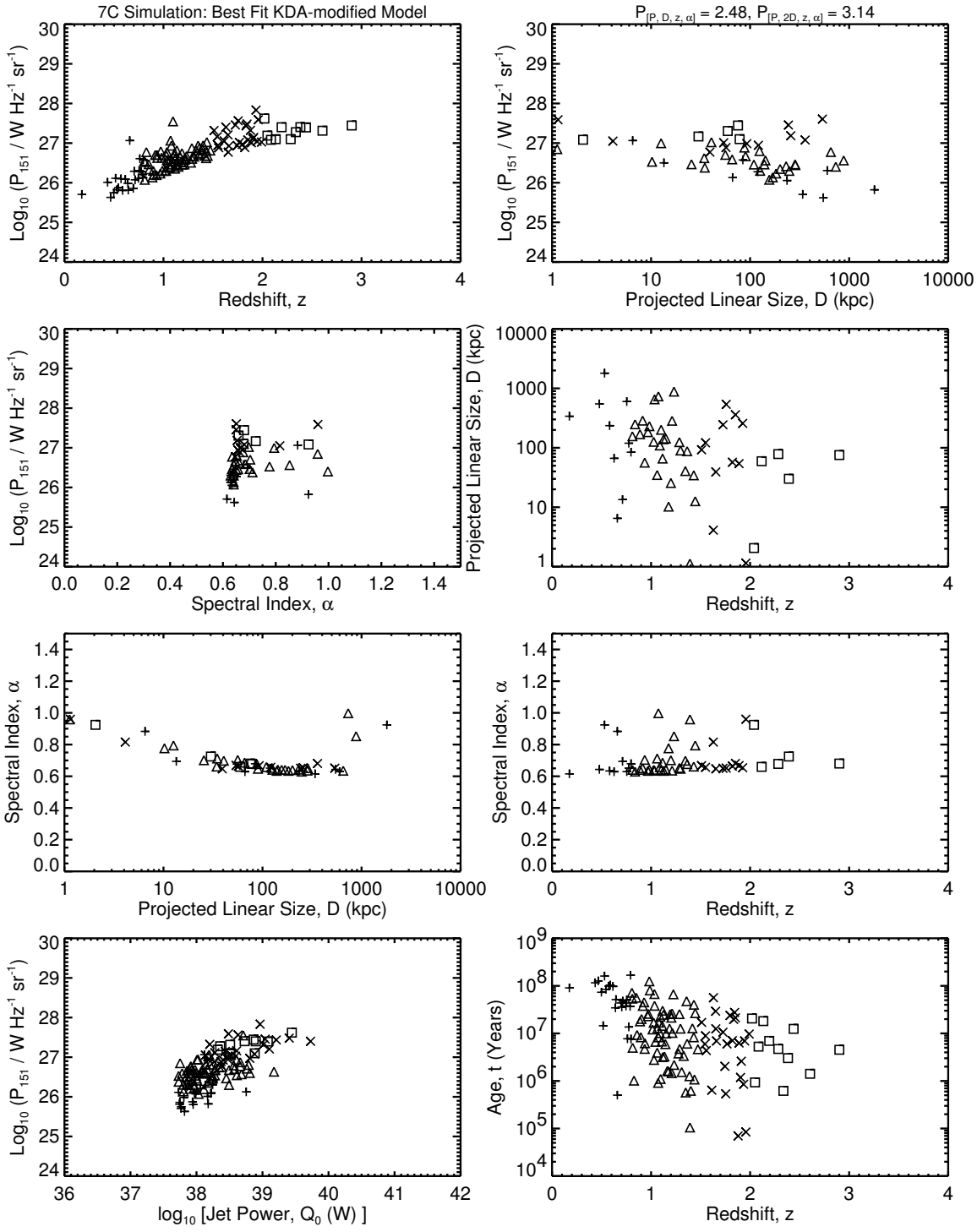

Figure 5.10c: The $[P$–D–z–$\alpha]$ planes for the 7C simulations of the best fit KDA-modified model, which is the same as in Figure 5.10a. Compare to Figure 3.1c.

steep as compared to the data.

The [α–D] plane of the KDA-modified model shows a tendency of α decreasing as D increases most of the time, but the trend reverses, so that α increases with D, at linear sizes greater than ~ 1 Mpc. The initial trend is opposite to that seen in the data.

– 6 –

Additional Models

Apart from the three previously published models of radio galaxy evolution described in Chapter 2 and the results for which are in Chapter 4, and their extensive modifications discussed in Chapter 5, I considered some other models. I investigated a modification given by Kaiser (2000) to the KDA model, which is described in Section 6.1. Some alternative Radio Luminosity Functions also were explored, as described in Section 6.2. All the model parameters used in this Chapter have the same meaning as their original definitions in Chapters 2, 4 and 5.

6.1 Kaiser (2000) Model: Modification to KDA

6.1.1 Model Description

Kaiser (2000, hereafter K2000) proposed a modification to the KDA (Kaiser, Dennett-Thorpe, & Alexander 1997) model, which essentially follows the formulation in KDA but which has the following differences.

The total integrated volume of a cocoon formed by injection of particles over the age of the source is equated to the following volume (due to self-similar expansion),

$$V_{\rm cocoon} = c_3 L_j^3, \qquad L_j = \frac{D(t)}{2}. \tag{6.1}$$

Here c_3 is a dimensionless contant depending on the cocoon geometry, and L_j is the length of a single jet. Hence the constant c_1 in the source linear size $D(t)$, Equation (2.2), is given by,

$$c_1 = \left[\left(\frac{p_h}{p_c} \right)^{1/\Gamma_c} \frac{\Gamma_c \left(\Gamma_c - 1\right) \left(\Gamma_x + 1\right) \left(5 - \beta\right)^3}{18 c_3 \left(9\Gamma_c - 4 - \beta\right)} \right]^{1/(5-\beta)}. \tag{6.2}$$

The Kaiser & Alexander (1997, KA) and the KDA model considered a cylindrical geometry for the cocoon, where the hotspot pressure p_h drives the source expansion along the jet axis and the expansion perpendicular to the axis is governed by the cocoon pressure p_c. Hence it was assumed in the KDA model that

$$\frac{p_h}{p_c} = 4R_T^2, \tag{6.3}$$

where R_T is the axial ratio, or the ratio of the length of the source to the full width of a lobe half way down the jet.

In subsequent studies of the shocked gas flow between the bow shock and the cocoon, Kaiser & Alexander (1999b) empirically fitted (p_h/p_c) as functions of β and R_T. Such investigations appeared to show that the (p_h/p_c) ratio of the KDA model (reproduced in Equation 6.3 before) was an overestimate. To correct this problem K2000 claimed that a better empirical formula was given by

$$\frac{p_h}{p_c} = (2.14 - 0.52\beta)\, R_T^{2.04-0.25\beta}. \tag{6.4}$$

Assuming $\gamma_{min} = 1$ and some finite γ_{max}, for particle energy power law index $p = 2$, the normalization of the energy spectrum is then given by,

$$n_0(t_i) = \frac{u_e(t_i)}{m_e c^2} \left[\log(\gamma_{max}) + \left(\frac{1}{\gamma_{max}} - 1\right)\right]^{-1}. \tag{6.5}$$

Since most FR II radio sources have cocoons of a relatively undistorted ellipsoidal shape (Leahy et al. 1989), K2000 parameterized the cocoon boundary as

$$r_c = \alpha_0 \left(1 - l^{\alpha_1}\right)^{\alpha_2}, \tag{6.6}$$

where α_0, α_1 and α_2 are constants to be obtained from cocoon radio maps. From the definition of R_T,

$$\alpha_0 = \frac{L_j}{2R_T} \left[1 - \left(\frac{1}{2}\right)^{\alpha_1}\right]^{-\alpha_2}. \tag{6.7}$$

Hence,

$$c_3 = \pi \frac{\alpha_0^2}{\alpha_1 L_j^2} B\left(2\alpha_2 + 1; 1/\alpha_1\right), \tag{6.8}$$

where $B(\mu;\nu)$ is the complete Beta-function.

Kaiser (2000) prescribed some fiducial model parameters which are listed in Column 2 of Table 6.1. Then he applied the model to the observed data of three FR II sources, the narrow line radio galaxy Cygnus A ($z = 0.056$), the broad line radio galaxy 3C 219 ($z = 0.1744$) and the radio loud quasar 3C 215 ($z = 0.411$). The best fit model parameters (obtained by K2000) compared to the observed parameters for the environments and other characterictics of the sources are given in Columns 3 – 8 of Table 6.1.

6.1.2 Results

Table 6.1: Parameter Values (Model and Observational) for 3 RGs in the K2000 Model [a]

Parameter	Fiducial [b]	CygA$_M$	CygA$_O$	3C219$_M$	3C219$_O$	3C215$_M$	3C215$_O$
β	1.5	1.5		1.5		1.5	
a_0 (kpc)	10	24	24	140	140	204	204
ρ_0 ($\times 10^{-23}$ kg m^{-3})	50.0	2.075	2.4	0.0515	0.92	0.0116	0.96
Γ_x	5/3	5/3		5/3		5/3	
Γ_c	4/3	4/3		4/3		4/3	
Γ_B	4/3	4/3		4/3		4/3	
$\gamma_{min(hs)}$	1	1		1		1	
$\gamma_{max(hs)}$	$10^{4.5}$	$10^{4.5}$		$10^{4.5}$		$10^{4.5}$	
p	2.00	2.075		2.03		2.22	
$R_T^{'}$			2.2		1.6		1.2
R_T [c]	2.3	2.27		3.02		2.26	
α_1	2	2		2		2	
α_2	1/3	1/3		1/3		1/3	
z			0.056		0.1744		0.411
Q_0 ($\times 10^{38}$ W)		6.54		1.75		4.85	
θ (degrees) [d]		80	76	62	32	37	32
T_{age} ($\times 10^6$ yr)		15.04		39.8		36.85	

[a] Subscript M denotes the model parameter (assumed or best-fit), and subscript O denotes the observed parameter value, for each radio galaxy.

[b] Values used by Kaiser (2000) as the fiducial model parameters (his Table 2).

[c] The axial ratios are from $R_T = R_T^{'}/\sin(\theta_O)$.

[d] Angle to the line of sight.

The power versus linear size diagrams ([P–D] tracks) computed for the K2000 model (using the fiducial model parameters), are shown in Figure 6.1. For comparison, the default KDA model tracks are also shown for the same jet powers and redshifts of the model sources. Clearly the K2000 tracks are much flatter than the KDA tracks. The [P–D] tracks for the three unique RGs studied in K2000 are shown in Figure 6.2, using both the best-fit model and the observed parameters of the sources.

We then performed multi-dimensional Monte Carlo simulations to realise the virtual surveys following the prescription in Section 3.3, but now using the K2000 formulation as the dynamical and radio power evolution model for sources, after generating

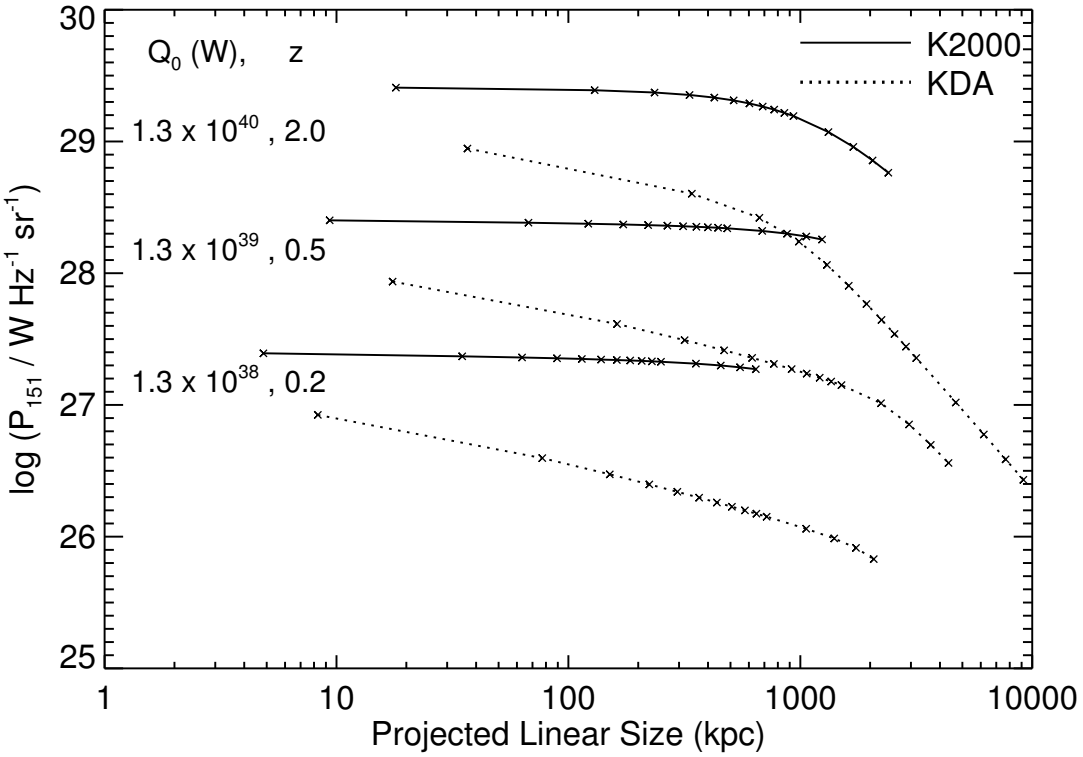

Figure 6.1: $[P$–$D]$ tracks of three model sources with jet powers (Q_0) in Watts and redshifts (z) of $[1.3 \times 10^{40}, 2.0]$, $[1.3 \times 10^{39}, 0.5]$, $[1.3 \times 10^{38}, 0.2]$ (from top to bottom). Each of the *solid* and *dotted* curves correspond to the tracks predicted by the K2000 model and the default KDA model, respectively. The crosses on the tracks denote source lifetimes of 1, 10, 20, 30, ..., 90, 100, 150, 200, 250, 300 Myr. Clearly the K2000 tracks are very flat and do not reasonably represent those followed by typical RGs over cosmological ages.

the initial ensemble from the BRW prescription. The simulated sources detected were compared to the actual data in the 3C, 6C, and 7C catalogs using the 1-D K-S tests described in Section 4.2. The resulting statistics are enlisted in Table 6.2. It is clear that the model fits are all very poor.

6.1.3 Conclusions

All the $[P$–$D]$ tracks for the K2000 model are much flatter than the corresponding typical tracks of the KDA, BRW and MK models. Also, the 1-D K-S statistical results obtained in the multi-dimensional Monte Carlo simulations are much worse

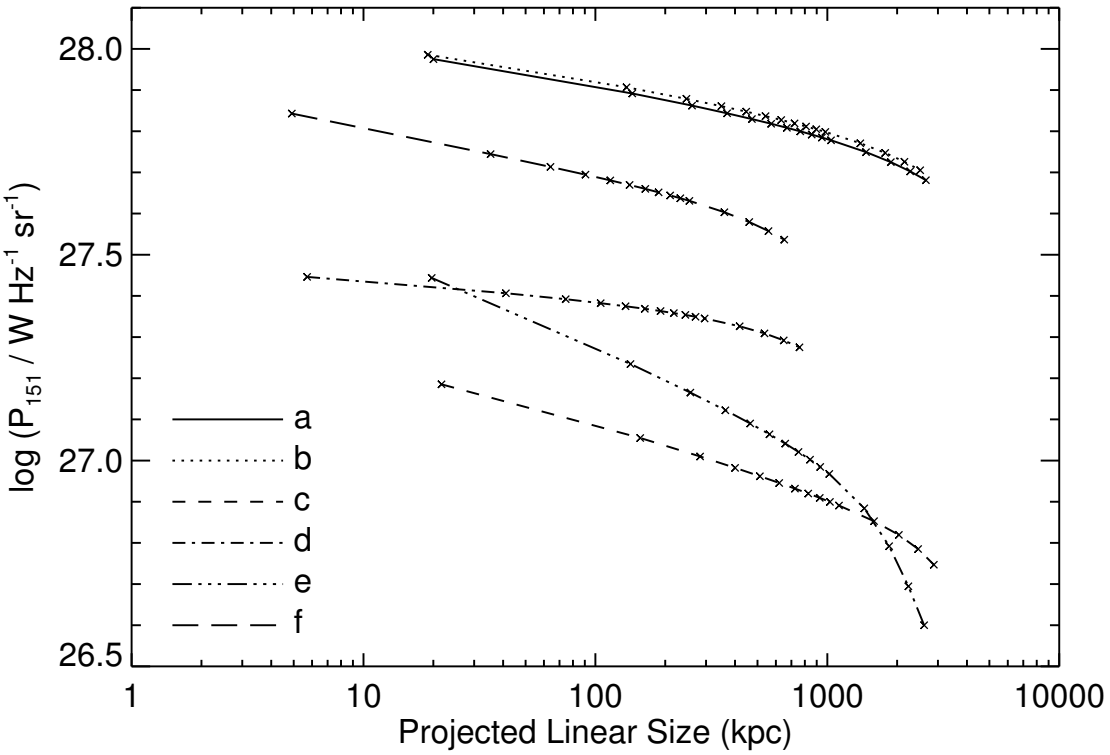

Figure 6.2: [P–D] tracks of three sources which are investigated by Kaiser (2000) in the K2000 model. The different curves correspond to the following legends, a: Cygnus A – Model; b: Cygnus A – Obs; c: 3C219 – Model; d: 3C219 – Obs; e: 3C215 – Model; f: 3C215 – Obs. See Section 6.1.1 and Table 6.1 for details. The crosses on the tracks denote source lifetimes of 1, 10, 20, 30, ..., 90, 100, 150, 200, 250, 300 Myr.

compared to any of the default models studied before. So we conclude that the K2000 model with the nominal parameter set cannot well reproduce the trends of observed properties in the low frequency radio surveys, 3C, 6C and 7C.

A reason for such poor behavior of this model might be that it was designated specifically to describe the environments and ages of three local and rather atypical FR II sources. So this model is biased towards describing special environments. The parameters used here cannot be applied globally and hence this model cannot explain the cosmological evolution of RGs. Since this cosmic RG evolution is the crux of this dissertation, we did not consider the K2000 model any further.

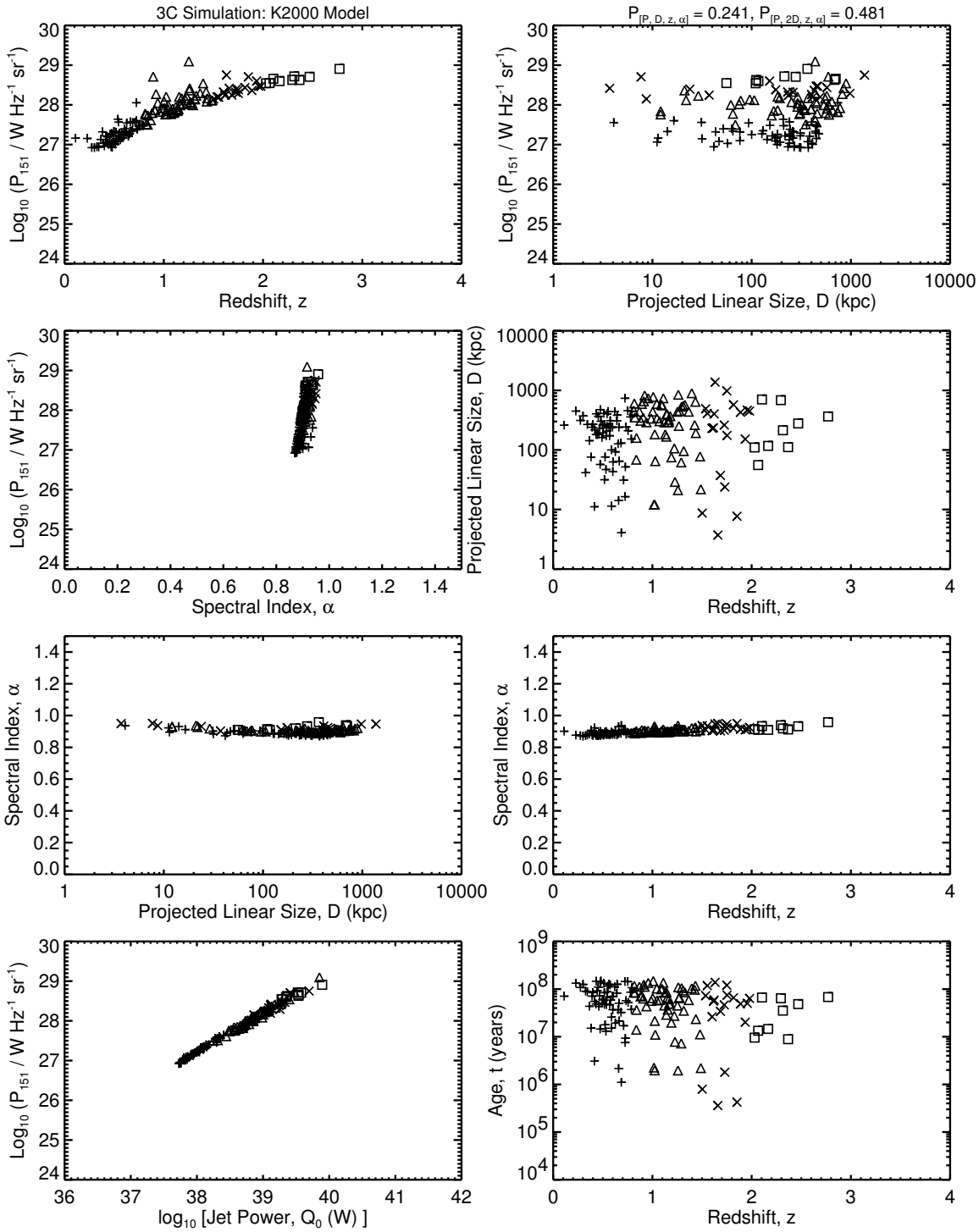

Figure 6.3a: The $[P$–D–z–$\alpha]$ planes for the 3C simulations of one K2000 model. The initial ensemble (of size 111072) is formed using $x = 3.0$, $T_{MaxAge} = 150$ Myr; the power evolution is with default (fiducial in Table 6.1) parameter values of the K2000 model. The 1-D K-S statistics for this case are in Table 6.2 (3rd model entry from top). Compare to Figure 3.1a.

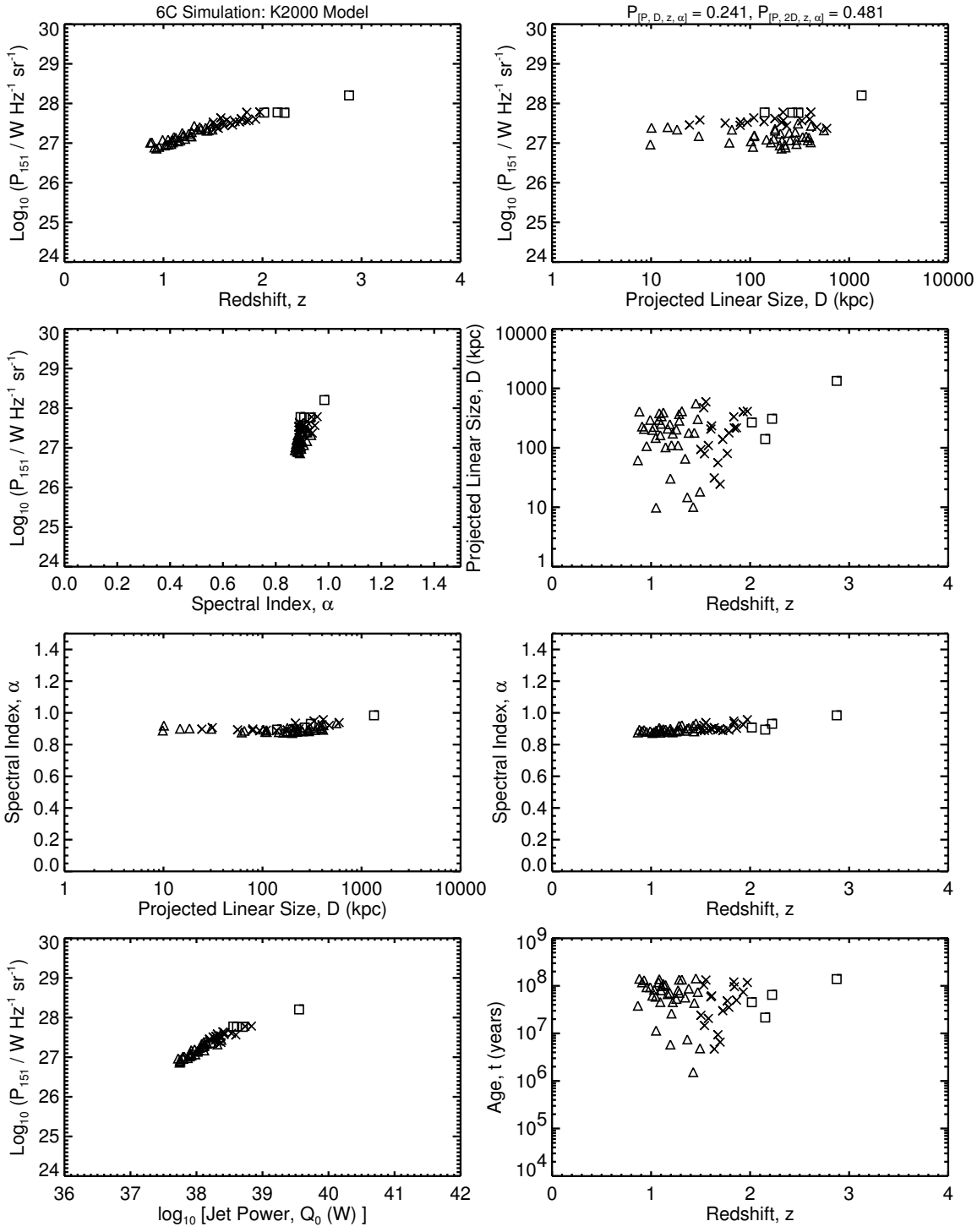

Figure 6.3b: The [P–D–z–α] planes for the 6C simulations of the K2000 model, with parameters as in Figure 6.3a. Compare to Figure 3.1b.

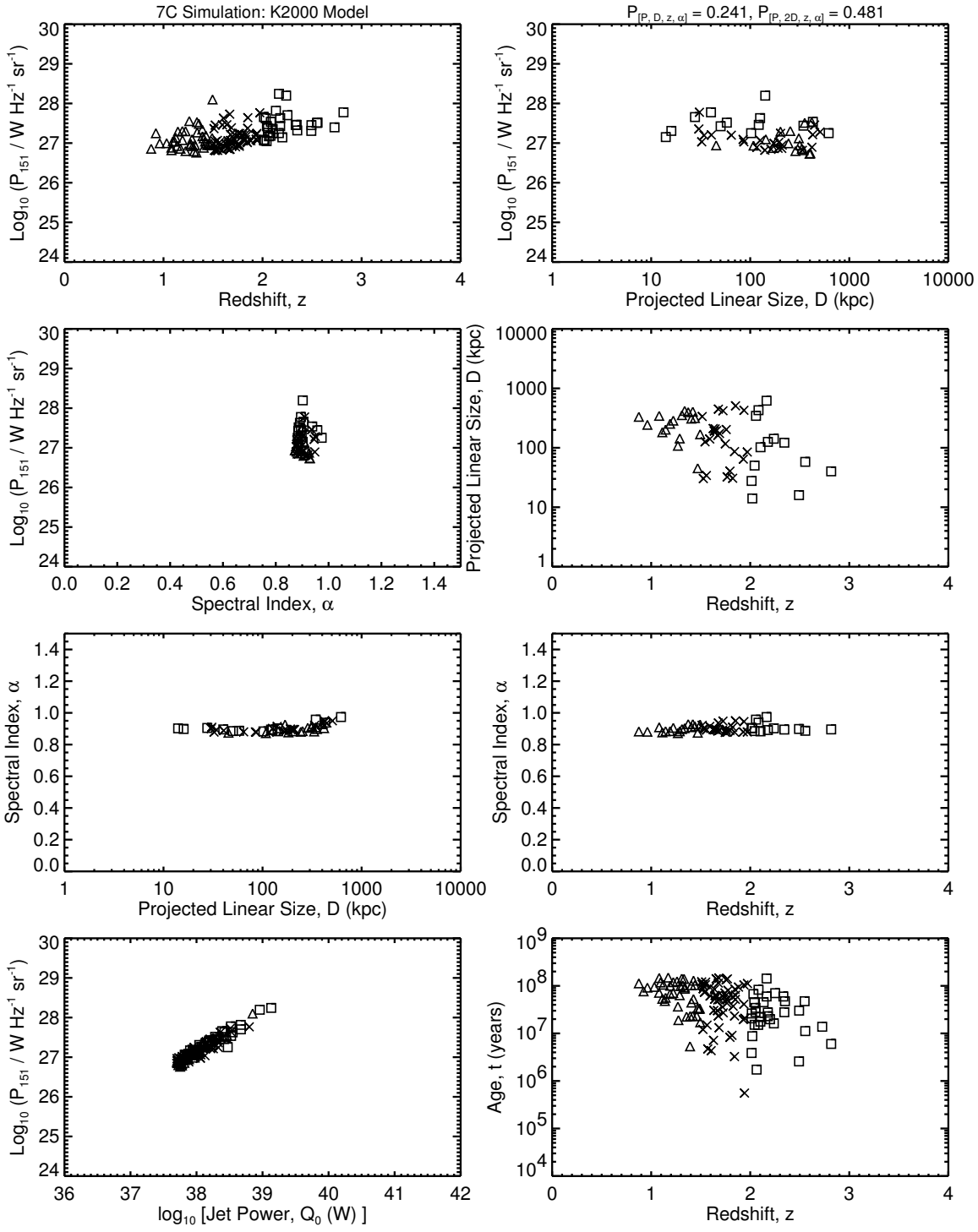

Figure 6.3c: The $[P$–D–z–$\alpha]$ planes for the 7C simulations of the K2000 model, with parameters as in Figure 6.3a. Compare to Figure 3.1c.

Table 6.2: K2000 Model Results: 1-D K-S Statistics [a]

x / T_{MaxAge} [b] / Ensemble Size	Survey	Ratio_{3C} / Ratio_{6C} / Ratio_{7C}	$\mathcal{P}(K\text{–}S)$				$\mathcal{P}_{[P,D,z,\alpha]}$ / $\mathcal{P}_{[P,2D,z,\alpha]}$
			$\mathcal{P}(P)$	$\mathcal{P}(D)$	$\mathcal{P}(z)$	$\mathcal{P}(\alpha)$	
K2000 parameters							
2.6	3C	1 (3.10) [c]	5.95e-11	4.06e-12	8.21e-07	3.89e-42	0.0127
500	6C	0.351	0.00110	3.59e-09	0.0185	1.80e-24	0.0130
114900	7C	0.318	9.89e-17	5.39e-04	1.24e-09	1.91e-13	
3.0	3C	1 (94.4)	8.30e-09	0.0151	2.69e-07	3.89e-42	0.152
150	6C	0.796	3.05e-06	2.13e-04	0.00264	1.80e-24	0.302
4861474	7C	0.710	1.04e-19	0.221	1.48e-13	1.91e-13	
3.0	3C	1 (2.15)	8.30e-09	0.0200	3.53e-06	2.00e-41	0.241
150	6C	0.871	8.19e-05	1.52e-04	0.00211	4.92e-21	0.481
111072	7C	0.741	4.28e-21	0.360	9.20e-14	2.78e-13	
KDA parameters							
3.0	3C	1 (11.3)	0.00743	0.164	0.0107	1.99e-06	0.698
150	6C	0.906	0.0549	0.0250	0.0900	8.26e-14	1.29
4861474	7C	1.09	1.46e-08	0.668	2.26e-06	8.76e-06	
3.0	3C	1 (0.310)	0.0961	0.0169	0.134	0.00195	0.684 [d]
150	6C	0.863	0.490	0.235	0.594	2.57e-04	0.892 [d]
111072	7C	0.921	4.79e-05	0.201	2.61e-05	6.46e-07	

[a] K2000 model results with different values of x and T_{MaxAge} (as listed) of the initial ensemble used. The parameters for dynamical and power evolution are those of K2000 (1st 3 entries) or KDA (last 2 entries) model, as mentioned. These results incorporate the 1 kpc size cutoff, i.e., sources with total linear size $D(t) < 1$ kpc are excluded from the simulations.

[b] T_{MaxAge} in units of Myr.

[c] From its definition, $\text{Ratio}_{3C} = 1$. The number in parentheses gives the ratio of the number of sources detected in 3C simulation (with given ensemble size) as compared to the real 3C survey.

[d] One cannot be confident of the validity of the K-S statistic as the detected sample in the simulation is much smaller than in the actual catalog.

6.2 Alternative Radio Luminosity Function

6.2.1 Different RLFs

The model simulations we performed in Chapters 4, 5 and 7, and in Section 6.1, are done adopting the redshift birth function of radio sources (Section 3.1.2), or the RLF,

from Willott et al. (2001). To explore the effect of the redshift distribution of the sources generated in the initial ensemble on the simulation results, we performed a run for each of the original models using two other RLFs.

The redshift distribution (Equation 3.6) as reproduced here,

$$\rho(z) \propto \exp\left[-\frac{1}{2}\left(\frac{z-z_0}{\sigma_z}\right)^2\right], \tag{6.9}$$

is the common gaussian functional form of all the RLFs considered. The values of the peak redshift, z_0, and the redshift standard deviation, σ_z, are different in the newly investigated RLFs.

One of these other redshift birth functions is the RLF given by Grimes, Rawlings, & Willott (2004), which has $z_0 = 1.684$ and $\sigma_z = 0.447$. These values are adopted from Table 5 of Grimes et al. (2004) (z_{2a} and z_{2b} from their two-population generalised luminosity function).

The other redshift distribution we explored is arbitrary (i.e., chosen by us). Here we chose the RLF to have $z_0 = 1.7$ and $\sigma_z = 0.8$. The peak redshift of this RLF is essentially the same as Grimes et al. (2004)'s, but this one has a higher σ_z. Our aim was to explore the effect of a higher standard deviation in the redshift birth function.

6.2.2 Results and Discussion

6.2.2.1 1-D K-S Test:

An initial ensemble was generated using the default values of x (= 2.6) and T_{MaxAge} (= 500 Myr) and the Grimes et al. (2004) RLF (z_0 and σ_z). The arbitrary RLF was employed to generate another ensemble, where $x = 3$ and $T_{MaxAge} = 200$ Myr was used. Simulations were performed, whereby these ensembles were evolved according to each of the 3 original models: KDA, BRW and MK (Chapter 2), with the default dynamical and radio lobe power evolution parameters used by the respective authors (Kaiser et al. 1997; Blundell et al. 1999; Manolakou & Kirk 2002).

The 1-D K-S statistical test results are given in Table 6.3 for both the Grimes et al. (2004) and for the arbitrary RLF. The table follows the same format as the 1-D K-S test result tables for the original models in Chapter 4: Tables 4.4, 4.5, 4.6 etc in Section 4.4.2. The table entries are explained in the last two paragraphs of Section 4.2.

Table 6.3: 1-D K-S Statistical Results With Alternative RLFs [a]

Model	Survey	Ratio_{3C} Ratio_{6C} Ratio_{7C}	$\mathcal{P}(K\text{–}S)$ $\mathcal{P}(P)$	$\mathcal{P}(D)$	$\mathcal{P}(z)$	$\mathcal{P}(\alpha)$	$\mathcal{P}_{[P,D,z,\alpha]}$ $\mathcal{P}_{[P,2D,z,\alpha]}$
Grimes et al. (2004) RLF [b]							
KDA [d]	3C	1 (4.06) [c]	5.59e-08	8.84e-06	1.01e-04	3.01e-08	0.494
	6C	0.646	0.140	0.00193	0.310	3.66e-10	0.690
	7C	0.686	0.0122	0.319	0.00202	0.0106	
BRW [e]	3C	1 (4.98)	4.63e-07	5.54e-08	3.43e-05	8.34e-04	0.467
	6C	0.765	0.0770	0.0265	0.212	3.66e-10	0.751
	7C	0.811	5.04e-05	0.438	9.03e-05	0.00304	
MK [d]	3C	1 (2.37)	5.82e-11	1.27e-09	1.95e-05	0	0.712
	6C	0.465	0.161	0.00203	0.432	1.80e-24	1.05
	7C	0.510	1.55e-05	0.548	0.00126	1.58e-15	
Arbitrary RLF [f]							
KDA [e]	3C	1 (19.5)	1.20e-11	0.00379	1.20e-11	6.92e-23	0.114
	6C	0.470	9.18e-07	9.07e-04	9.18e-07	3.66e-10	0.228
	7C	0.379	4.10e-06	0.180	2.88e-05	1.11e-07	
BRW [d]	3C	1 (34.1)	4.63e-04	1.07e-07	3.43e-05	0.0138	0.608
	6C	0.432	0.114	0.174	0.0153	3.66e-10	0.987
	7C	0.323	0.103	0.441	0.0533	0.00624	
MK [e]	3C	1 (12.5)	6.23e-11	2.66e-06	1.42e-13	0	0.0543
	6C	0.356	4.41e-05	2.01e-04	3.33e-07	1.80e-24	0.108
	7C	0.303	2.74e-04	0.0883	1.08e-06	2.87e-16	

[a] Results for KDA, BRW and MK simulations with the respective default values of the radio lobe power and dynamical evolution model parameters, as used by the authors (Kaiser et al. 1997; Blundell et al. 1999; Manolakou & Kirk 2002).

[b] Simulations done with an initial ensemble of size 3712083 generated using RLF where the gaussian redshift distribution has $z_0 = 1.684$ and $\sigma_z = 0.447$; the other parameters are $x = 2.6$, $T_{MaxAge} = 500$ Myr.

[c] Always $\text{Ratio}_{3C} = 1$, because of the way it is defined. The number in parentheses gives the ratio of the number of sources detected in 3C simulation (with given ensemble size) as compared to the real 3C survey.

[d] Linear size, $D(t)$ cut off of 1 kpc is used in the simulations.

[e] Linear size, $D(t)$ cut off of 10 kpc is used in the simulations.

[f] Simulations done with an initial ensemble of size 3680508 generated using a RLF where the gaussian redshift distribution has $z_0 = 1.7$ and $\sigma_z = 0.8$; the other parameters are $x = 3.0$, $T_{MaxAge} = 200$ Myr.

The simulations for the two RLFs in this Section have been done with different x and T_{MaxAge}. The Grimes et al. (2004)'s RLF is tested using the default values of x and T_{MaxAge} (from BRW), and arbitrary values were picked for the arbitrary RLF. Hence it is not straight forward to extract the effect of the radio lumonosity function only from these simulations where all of x, T_{MaxAge}, z_0 and σ_z were changed. A more robust examination would require more simulation runs involving the variation of one/more of the parameters x, T_{MaxAge}, z_0 and σ_z (i.e., by considering different values of all possible permutations of the parameters), which we did not perform. The discussions below pertain to the values of x and T_{MaxAge} used for the corresponding RLFs.

The following trends are observed from the results of the simulation runs done using Grimes et al. (2004)'s RLF ($z_0 = 1.684, \sigma_z = 0.447$). An ensemble of size comparable to the simulations of the original models in Chapter 4, gives a higher 3C detection ratio here, i.e., a larger number of sources are detected in the virtual surveys as compared to the actual number in the 3C, 6C and 7C catalogs. The BRW model gives better detection number ratio in the 6C and 7C surveys (i.e., Ratio_{6C} and Ratio_{7C}, defined in Equation 3.16, close to 1), followed by KDA and finally by MK. Most of the K-S statistics are not wonderful, with only some individual probabilities for the 6C survey are acceptable. The MK model gives the highest total combined probabilities, $\mathcal{P}_{[P,D,z,\alpha]}$ and $\mathcal{P}_{[P,2D,z,\alpha]}$, with BRW and KDA following very close to each other.

The results of the arbitrary RLF ($z_0 = 1.7, \sigma_z = 0.8$) simulations indicate the following. The 3C detection ratios are much higher than those of Grimes et al. (2004), or those of the original models in Chapter 4. Evidently, with a wider redshift birth function, i.e., σ_z higher compared to that in Grimes et al. (2004) or Willott et al. (2001), an ensemble with a smaller size can detect the same number of sources in the virtual surveys as in the 3C, 6C and 7C catalogs. The 6C and 7C detection number ratios for all the models are bad. In general, none of the K-S statistics are wonderful. However, the individual 1-D K-S probabilities for P, D and z in the 6C and 7C surveys are acceptable for the BRW simulations. The BRW model gives the highest total probabilities, followed by KDA and finally MK.

All the spectral index fits are still very poor, using either of the alternative RLFs. So we can say that altering the redshift birth function has little effect on the major drawback of these models: the mismatch of the spectral index behavior between data

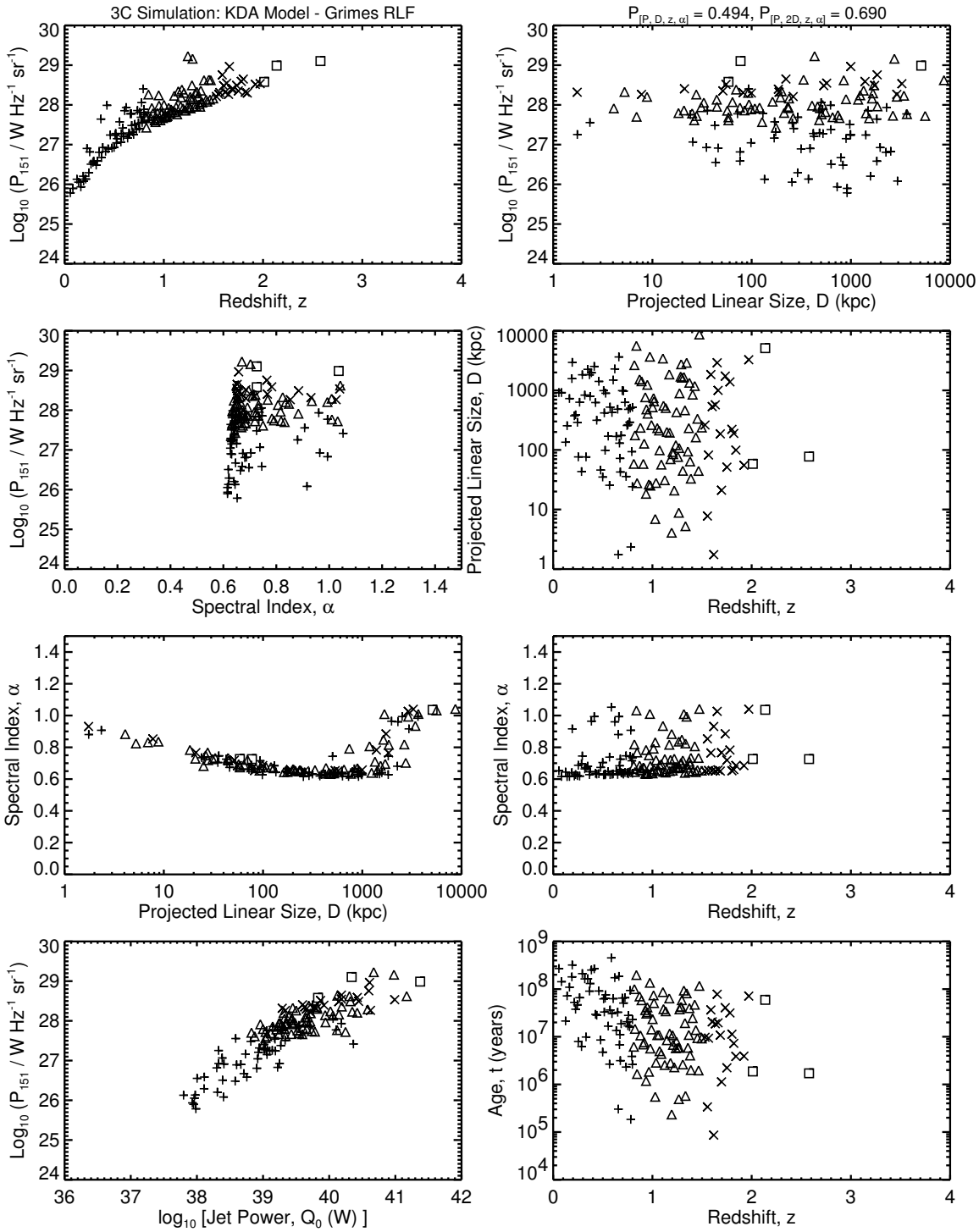

Figure 6.4a: The $[P$–D–z–$\alpha]$ planes for the 3C simulations of the default KDA model. The initial ensemble (of size 3712083) is generated using the redshift distribution from Grimes et al. (2004) ($z_0 = 1.684$, $\sigma_z = 0.447$) and $x = 2.6$, $T_{MaxAge} = 500$ Myr; the power evolution is with parameter values as used by the authors in the KDA model. The 1-D K-S statistics for this case are in the first entry of Table 6.3. Compare to Figure 3.1a.

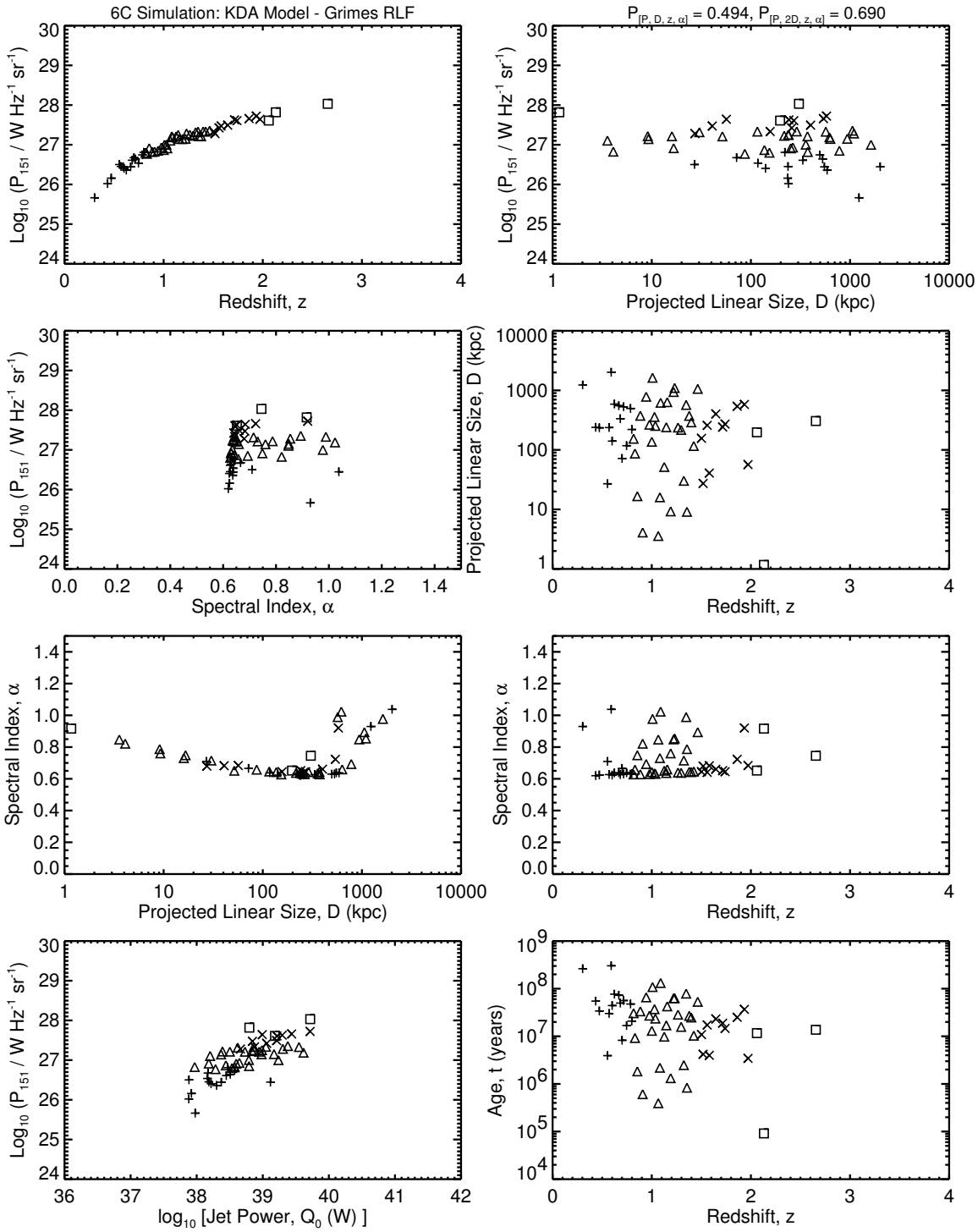

Figure 6.4b: The [P–D–z–α] planes for the 6C simulations of the default KDA using Grimes et al. (2004) RLF. The model is the same as in Figure 6.4a. Compare to Figure 3.1b.

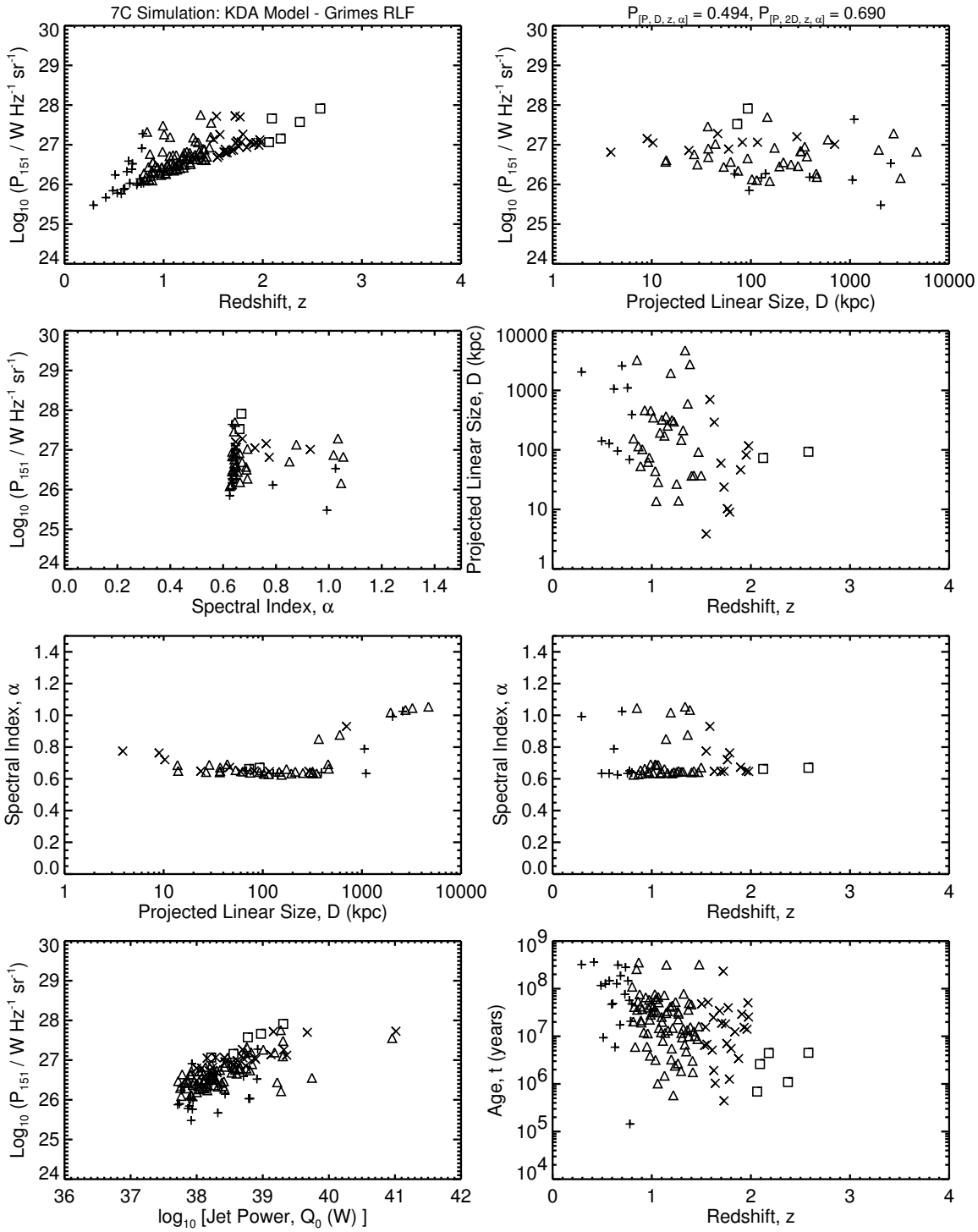

Figure 6.4c: The [P–D–z–α] planes for the 7C simulations of the default KDA using Grimes et al. (2004) RLF. This model is the same as in Figure 6.4a. Compare to Figure 3.1c.

and simulations.

6.2.2.2 [P–D–z–α] Planes:

The slices through the [P–D–z–α] volume using Grimes et al. (2004)'s RLF are shown in Figures 6.4, 6.5 and Figure 6.6, for the default KDA, BRW and MK model simulations, respectively. The following trends can be seen from the planes.

Inspecting the [P–z] planes, some very powerful, intermediate- to high-z sources are detected (mostly in MK) in the 3C simulations, which are not present in the data. The scatter in P values for the 3C pseudo-catalog increases with increasing z, giving substantially more scatter than that present in the 3C data for the high-P/high-z sources. The simulated 6C and 7C surveys produce too few low-z and high-z sources, compared to the numbers in the data. A reason for the overproduction of intermediate redshift sources is that Grimes et al. (2004)'s RLF is narrow and sharply peaks at $z_0 = 1.684$ (as it has a smaller standard deviation of $\sigma_z = 0.447$), so more sources are produced around z_0.

Examining the [P–D] planes of the simulations, we find that in the KDA and MK models an excessive number of large ($D > 1$ Mpc), and powerful sources are produced in the 3C simulations. Similar to the data (mainly in 3C), a $P-D$ evolution (decrease of P as D increases) is seen in the BRW model. This is an advantage of using Grimes et al. (2004)'s RLF in the BRW model. The too strong $P - D$ evolution seen in the original BRW model with Willott et al. (2001)'s RLF (Section 4.9.3) is diluted here. The KDA and MK models show a very weak P–D anti-correlation in the 3C results.

The [D–z] planes of KDA and MK models clearly demonstrate the overproduction of very large sources in 3C (discussed in the previous paragraph). The anti-correlation of linear size with redshift is present more or less in all the models, and most evidently in BRW which is consistent with the trend present in the 3C data. The cause of this D–z evolution was discussed in Section 4.9.3.

The spectral index trends are similar to the discussion of [P–α], [α–z] and [α–D] planes of the original models (using Willott et al. (2001)'s RLF) in Section 4.9.3. Although we did not conduct a wide-ranging exploration of parameter space using these additional modifications, the preliminary work done in this Section indicates that using these different RLFs is unlikely to improve the fits to the data.

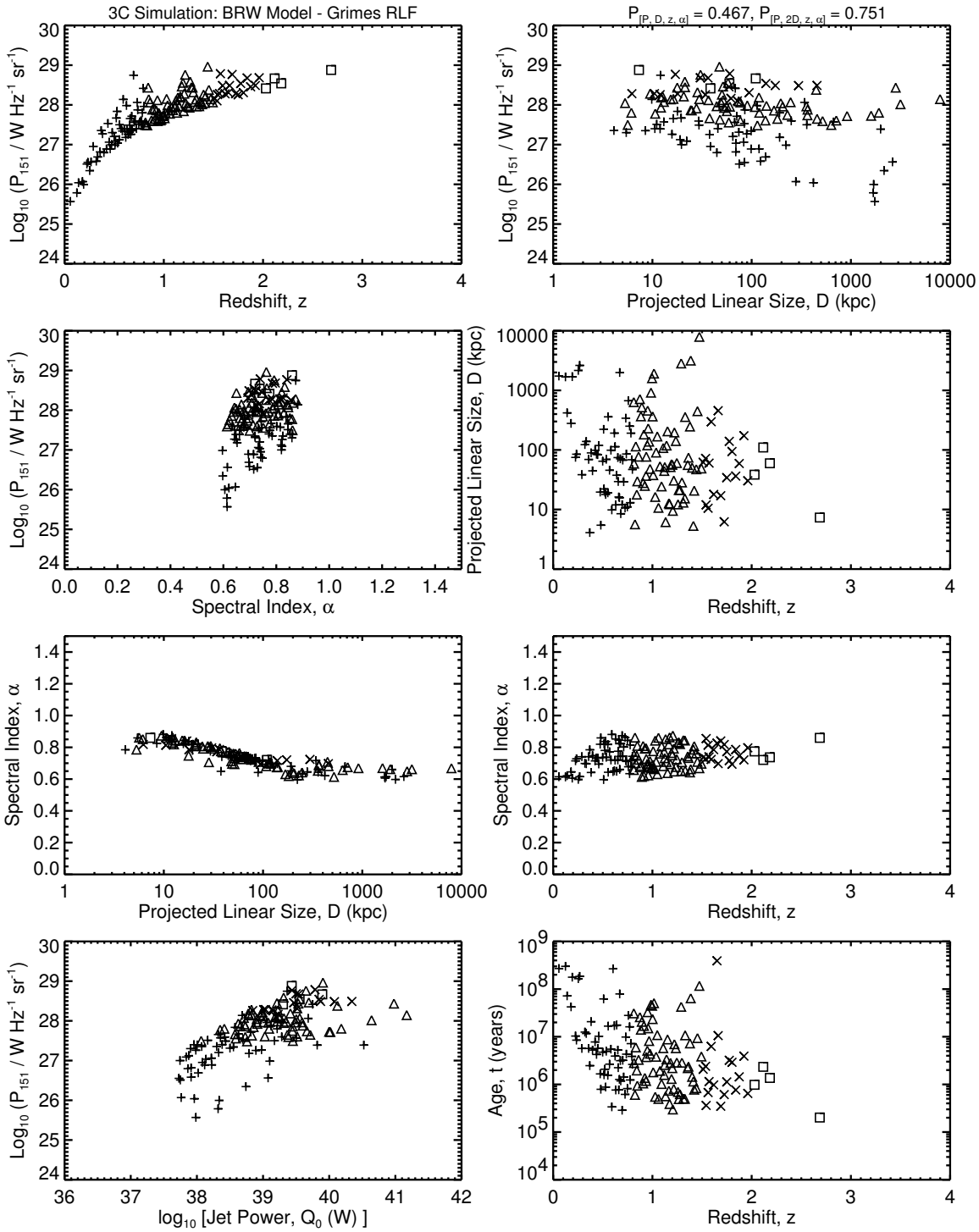

Figure 6.5a: The $[P$–D–z–$\alpha]$ planes for the 3C simulations of the default BRW model. The initial ensemble (of size 3712083) is generated using the redshift distribution from Grimes et al. (2004) ($z_0 = 1.684$, $\sigma_z = 0.447$) and $x = 2.6$, $T_{MaxAge} = 500$ Myr; the power evolution is with parameter values as used by the authors in the BRW model. The 1-D K-S statistics for this case are in the second entry of Table 6.3. Compare to Figure 3.1a.

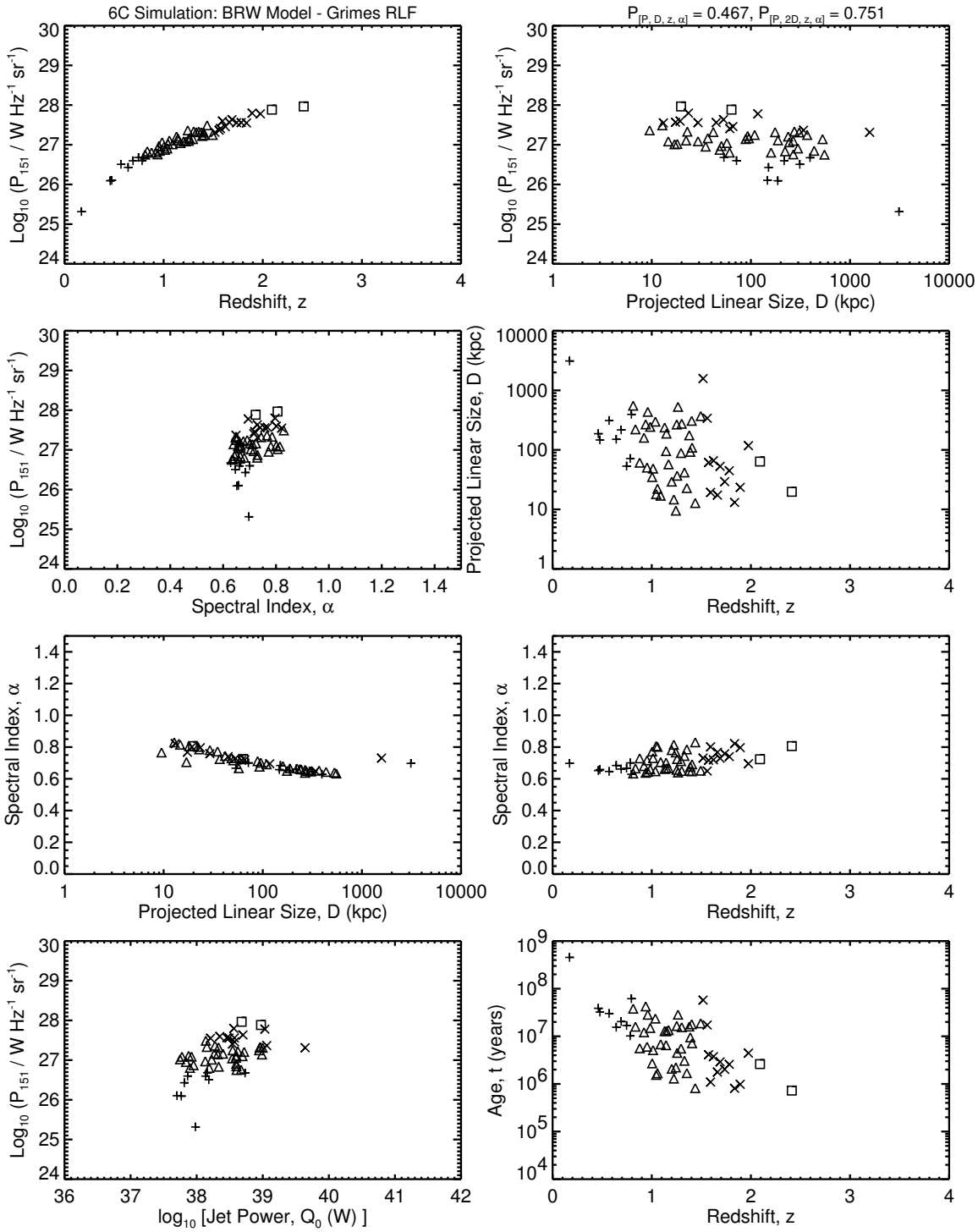

Figure 6.5b: The [P–D–z–α] planes for the 6C simulations of the default BRW model using Grimes et al. (2004) RLF, which is the same as in Figure 6.5a. Compare to Figure 3.1b.

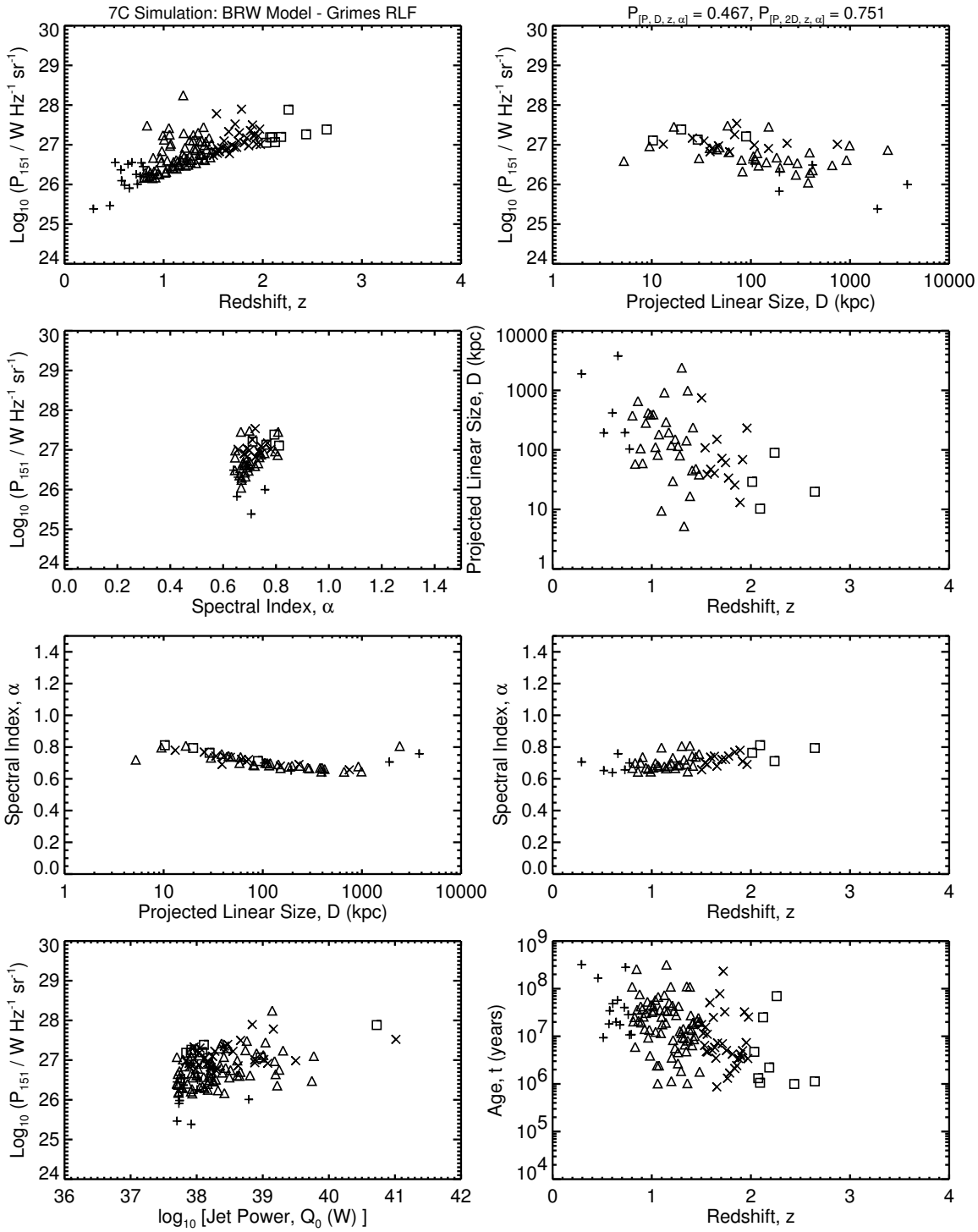

Figure 6.5c: The $[P$–D–z–$\alpha]$ planes for the 7C simulations of the default BRW model using Grimes et al. (2004) RLF, which is the same as in Figure 6.5a. Compare to Figure 3.1c.

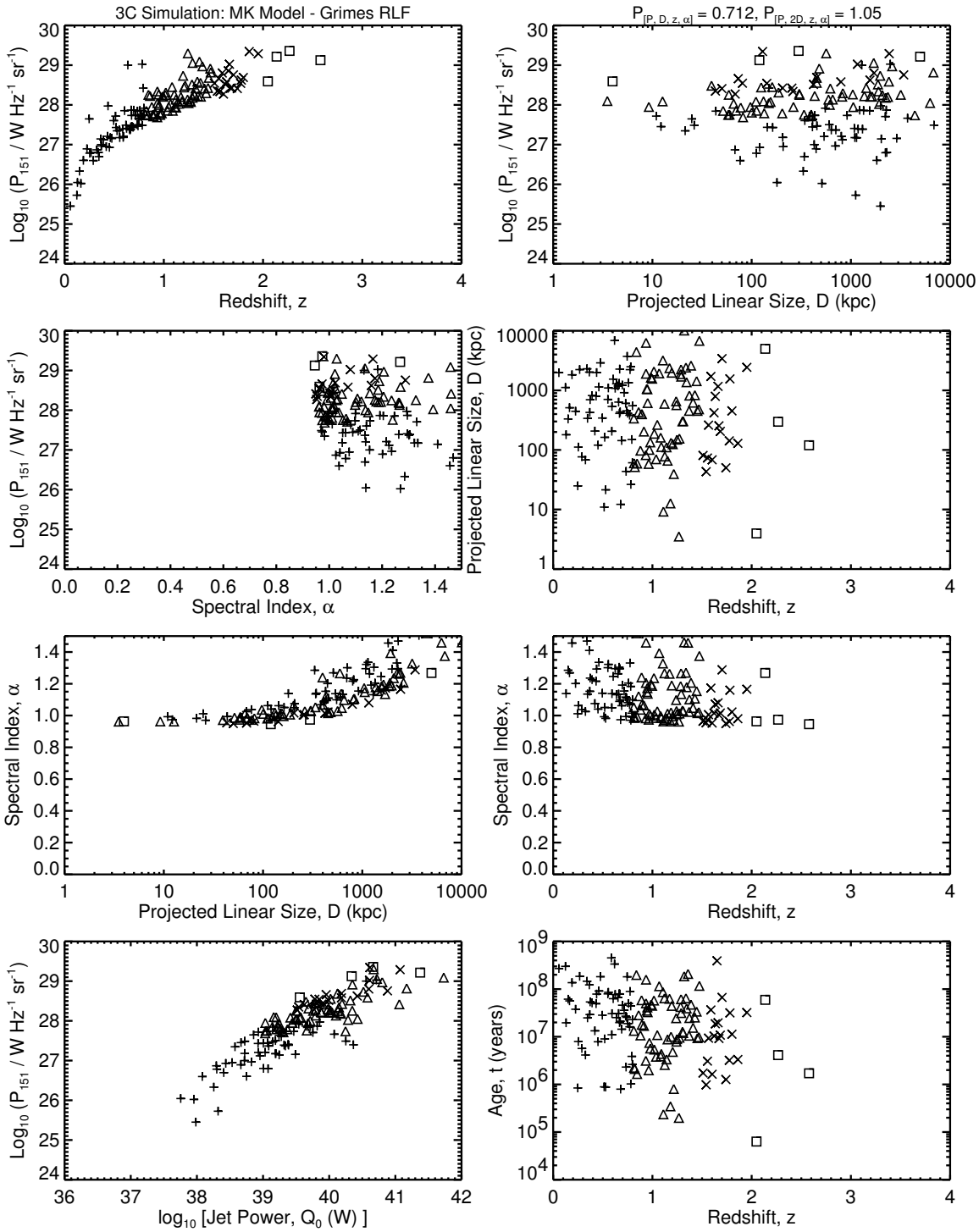

Figure 6.6a: The $[P$–D–z–$\alpha]$ planes for the 3C simulations of the default MK model. The initial ensemble (of size 3712083) is generated using the redshift distribution from Grimes et al. (2004) ($z_0 = 1.684$, $\sigma_z = 0.447$) and $x = 2.6$, $T_{MaxAge} = 500$ Myr; the power evolution is with parameter values as used by the authors in the MK model. The 1-D K-S statistics for this case are in the third entry of Table 6.3. Compare to Figure 3.1a.

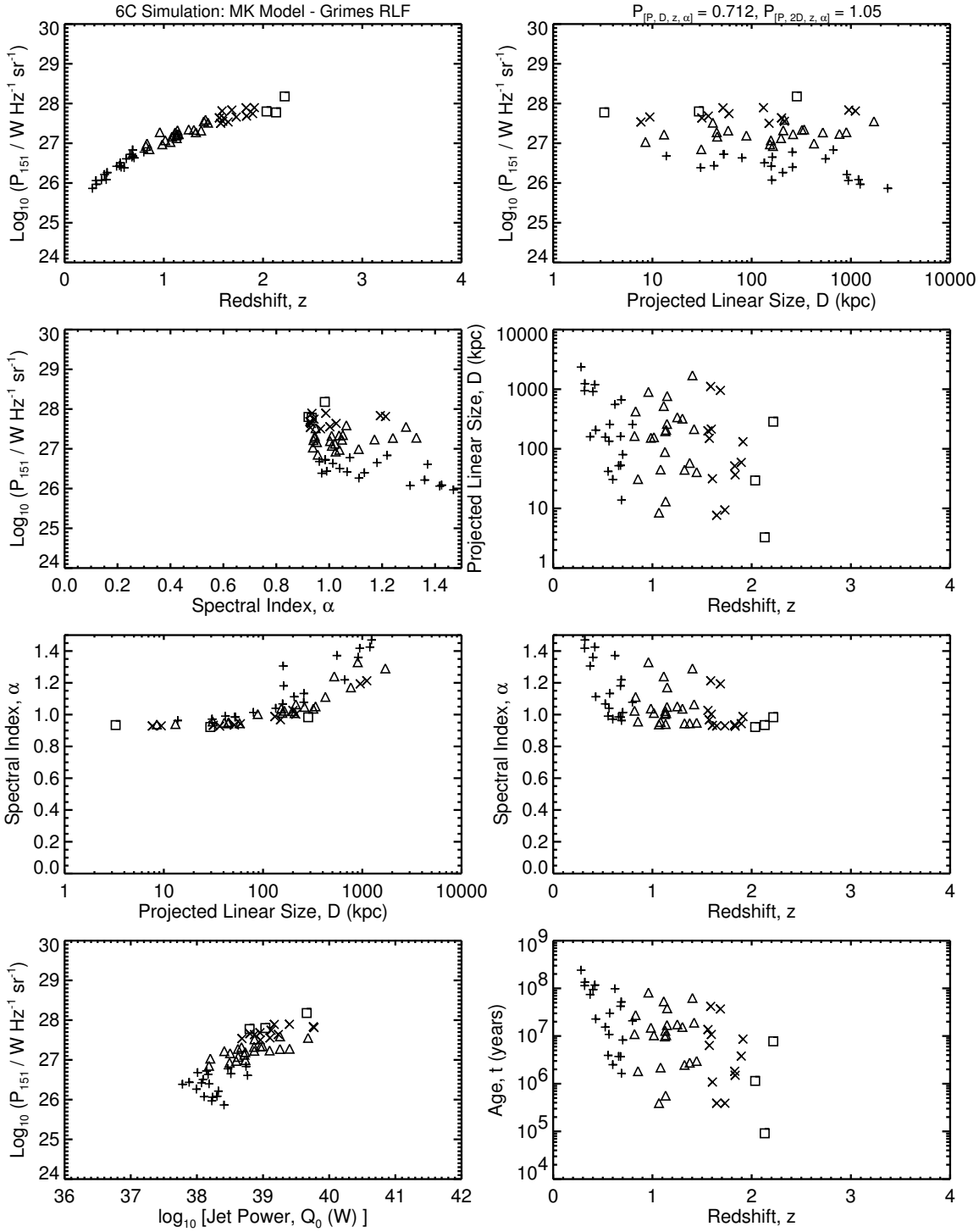

Figure 6.6b: The [P–D–z–α] planes for the 6C simulations of the default MK model using Grimes et al. (2004) RLF, which is the same as in Figure 6.6a. Compare to Figure 3.1b.

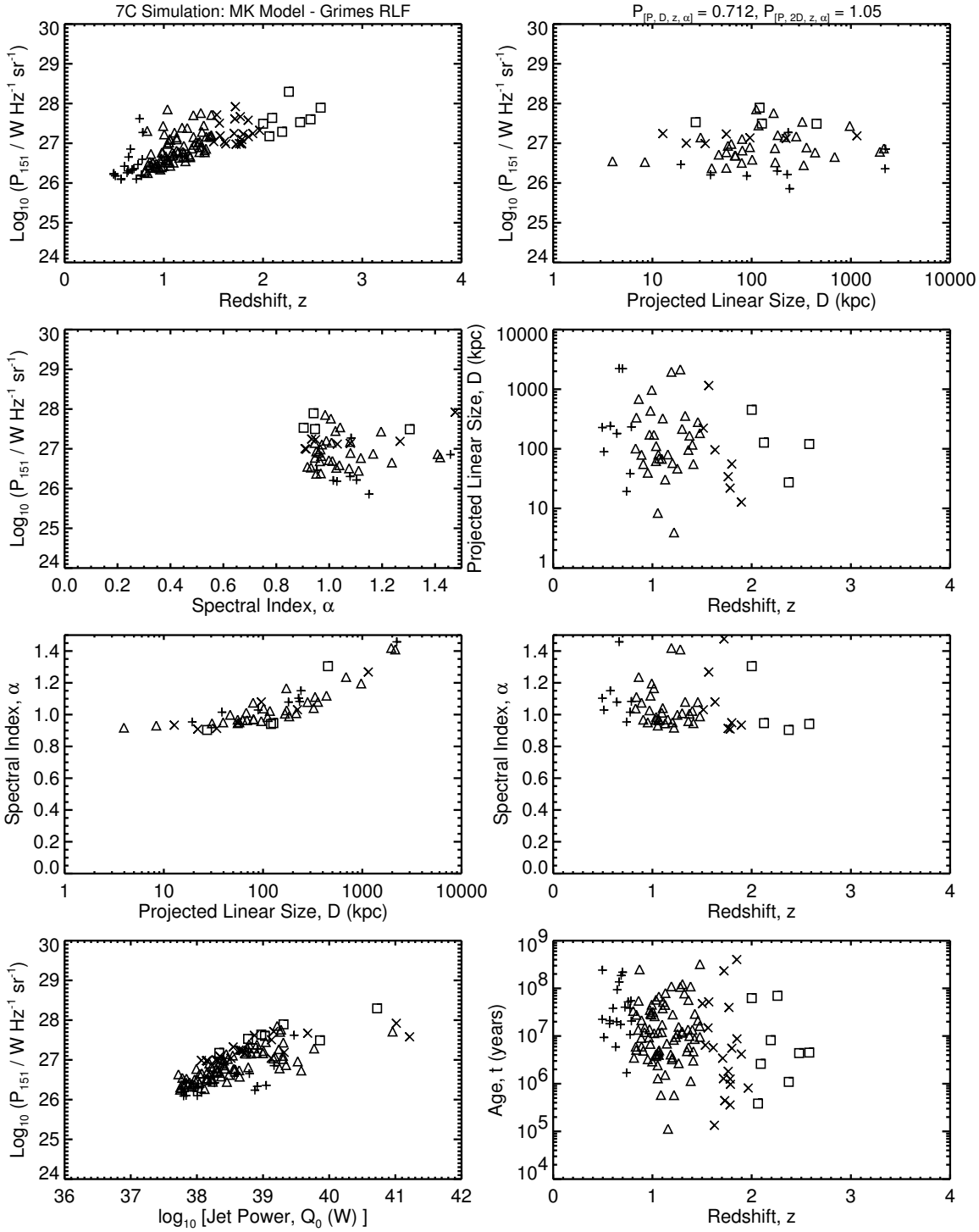

Figure 6.6c: The [P–D–z–α] planes for the 7C simulations of the default MK model using Grimes et al. (2004) RLF, which is the same as in Figure 6.6a. Compare to Figure 3.1c.

– 7 –

Relevant Volume Filling Fraction

One of the most important goals of this thesis work is to address the question of what fraction of the relevant volume of the universe (volume containing most of the cosmic baryons) did the radio lobes occupy during the quasar era. This key motivation was described briefly in Section 1.2. In this Chapter we give the details of such studies, where we calculate the total volume filled by the RGs over the quasar era (when their population peaked), as a fraction of the relevant volume of the universe.

7.1 The Relevant Universe

The volume of our "Relevant Universe", is the volume of the cosmic baryons which exist as the WHIM and have temperatures $10^5 < T < 10^7$ K (e.g., Cen & Ostriker 1999, 2006; Davé et al. 2001). This warm/hot intergalactic gas contains the majority of the baryons ($\sim 40 - 50\%$ by mass) in the universe at the present epoch. These warm/hot baryons permeate the universe as extended large-scale filamentary structures, the junctions of which are the sites of galaxy and cluster formation.

The WHIM comprise the main repository of cosmic baryons which can potentially collapse to form self-gravitating (gravitationally bound) entities like stars. So the radio lobes need to penetrate a significant portion of this "relevant volume of the universe", or the warm/hot baryonic filaments, in order to have a significant role in impacting star formation and spreading magnetic fields and metals (Section 1.1).

The baryons in the "relevant universe", or the WHIM, occupied ∼3% of the total volume of the universe during most of the quasar epoch (i.e., between $2 \leq z \leq 3$); they pervade ∼10% of the volume today. The mass of the WHIM as a fraction of the total baryonic mass in the universe was ∼15% during the quasar era, and has grown dramatically since then to reach ∼50% today (Cen & Ostriker 1999). The increase in fractional WHIM mass is due to gravitational accretion of matter from cold dark matter halos into the warm/hot intergalactic phase, and the heating this gas undergoes as it virializes.

7.2 Methodology

The volume fraction of the relevant universe filled by RGs is calculated from the following prescriptions. An initial ensemble of sources generated to do the simulated surveys (following Section 3.1), is considered as the population of RGs existing out there. Among the millions of RGs generated in the ensemble, only a few tens are detected in the simulated surveys. This is also what happens in reality: among the millions of RGs born through the quasar era, we can now detect only a few in our flux-limited radio surveys. Severe energy losses (adiabatic, synchrotron and IC losses) make most of the sources fall below our current flux limits; these are discussed in detail in Gopal-Krishna, Wiita, & Saripalli (1989); Blundell & Rawlings (1999); Blundell, Rawlings, & Willott (1999); Gopal-Krishna & Wiita (2001, 2003a,b); Gopal-Krishna, Wiita, & Osterman (2003); Gopal-Krishna, Wiita, & Barai (2004). Such power losses are evident in the simulations from the steeply falling [P–D] tracks of Section 4.1.

For a complete estimate of the relevant volume filling fraction we consider the volumes of all the sources generated in the initial population, as weighted by the factors discussed below. We also take note of the contributions of the sources born in several generations during the quasar era.

The universe is divided into redshift bins (shells), and the relevant volume fraction is calculated in each z-bin. Let the minimum and maximum redshifts of a shell be z_{min} and z_{max} ($z = 0$ at the present epoch, and $z \rightarrow \infty$ at the Big Bang). The bin-width is taken as $\Delta z = 0.02 = (z_{max} - z_{min})$. The mid-redshift of a bin, $z_{mid} = (z_{min} + z_{max})/2$, is considered as the epoch of that bin. The formulations in the following subsections refer to the volume of the relevant universe or the RGs inside a typical z-shell. The distribution of the volume fraction is estimated as a function of redshift, which is then integrated over the entire quasar era epoch to get the total volume contribution of several generations of RGs in the universe.

7.2.1 Relevant WHIM Volume in the Universe

As mentioned in Section 3.1, we assume a consensus flat, dark-energy dominated universe. The present value of the Hubble constant $H_0 = 71$ km s^{-1} Mpc^{-1}, the matter density parameter $\Omega_M = 0.3$, and the vacuum energy density parameter $\Omega_\Lambda = 0.7$, come from WMAP results (Spergel et al. 2003, 2006). The cosmological equations used in this Chapter are adopted from Hogg (1999), which are basically the same as

in Peacock (1999).

Following Equation (14) of Hogg (1999) we define for a spatially flat universe (i.e., a universe which has zero curvature and whose spatial slices can be described by 3-dimensional Euclidean geometry),

$$E(z) \equiv \sqrt{\Omega_M \left(1+z\right)^3 + \Omega_\Lambda} \tag{7.1}$$

The total comoving volume, $V_{\rm comov}$, all-sky, out to redshift z_0 can be written as (Hogg 1999: Equations 29, 16, 15),

$$V_{\rm comov} = \frac{4\pi}{3}\left(\frac{c}{H_0}\right)^3 \left[\int_0^{z_0} \frac{dz}{E(z)}\right]^3. \tag{7.2}$$

Hence the comoving volume over all-sky (4π steradians) in a redshift shell, or the region of the universe between redshifts z_{min} and z_{max} is,

$$\Delta V_{\rm comov} = \frac{4\pi}{3}\left(\frac{c}{H_0}\right)^3 \left(\chi_2^3 - \chi_1^3\right), \tag{7.3}$$

where,

$$\chi_2 = \int_0^{z_{max}} \frac{dz}{E(z)}, \quad \chi_1 = \int_0^{z_{min}} \frac{dz}{E(z)}. \tag{7.4}$$

The same expression is also obtained by integrating the comoving volume element (Equation 3.85) of Peacock (1999), using his Equation (3.76).

The flux-limited surveys (real and simulated) explored in this thesis do not consider radio sources over all of the sky; these detect sources within the survey sky areas only. The big ensemble (initial population) explicitly detects sources over the 3CRR survey area, $\mathrm{Area}_{3C} = 4.23$ sr. So the RG population from which these sources are detected lies within a smaller comoving volume extending over only the 3CRR sky area.

In these simulations the number of sources is taken proportionate to the sky area over which they are detected. This has been discussed in Section 3.3, where the sources of the initial ensemble to perform 6C and 7C simulations were picked from the 3C ensemble, according to the corresponding sky area ratios (Equation 3.15). Now if a simulation detects $N_{\rm sim(3C)}$ sources, where there are $N_{\rm samp(3C)} = 145$ sources in the real 3C survey, then the 3C detection ratio is written as (similar to the 6C and

7C detection ratios in Section 3.3),

$$\text{Ratio}_{3C} = \frac{N_{\text{sim}(3C)}}{N_{\text{samp}(3C)}}. \tag{7.5}$$

So following our earlier argument, it is assumed that the simulation is detecting sources over an effective sky area given by,

$$\text{Area}_{3C(\text{effec})} = \text{Area}_{3C} \times \text{Ratio}_{3C}. \tag{7.6}$$

If ΔV_{comov} (Equation 7.3) gives the comoving volume of a z-shell over all-sky, then the comoving volume over the effective 3C survey area is,

$$\Delta V_{\text{comov},3C(\text{effec})} = \Delta V_{\text{comov}} \frac{\text{Area}_{3C(\text{effec})}}{4\pi} = \Delta V_{\text{comov}} \frac{\text{Area}_{3C} \times \text{Ratio}_{3C}}{4\pi}. \tag{7.7}$$

The effective comoving volume of the z-shell is converted to the proper volume it had at that epoch (or the mid redshift, z_{mid}, of the bin),

$$\Delta V_{\text{proper}} = \frac{\Delta V_{\text{comov},3C(\text{effec})}}{(1 + z_{mid})^3}. \tag{7.8}$$

The effective relevant volume of the z-shell is then the fraction of the proper cosmological volume of the shell occupied by WHIM. This final "relevant volume" is found by multiplying the effective proper volume of the shell, ΔV_{proper} by the WHIM volume fraction at that epoch (at z_{mid}).

The WHIM volume fraction is adopted from the large-scale cosmological simulations of Cen & Ostriker (1999). Cen & Ostriker (2006) give an improved WHIM fraction calculation by explicitly including galactic superwind feedback processes, but there is no significant difference from their previous results. We use the estimates from Cen & Ostriker (1999) Figure 2, which gives the evolution of WHIM volume fraction with redshift upto $z = 3$. We read out the points from the plot for $z = 0, 0.5, 1.0, 3.0$, and linearly interpolated between those redshifts to get the WHIM volume fraction as a function of redshift. At $z > 3$, the fraction was taken to be constant and equal to the value at $z = 3$.

In this way we obtain the final "relevant volume of the universe" inside a z-shell as,

$$\Delta V_{\text{WHIM}} = \Delta V_{\text{proper}} \times \text{WHIM Volume Fraction}. \tag{7.9}$$

Our $\Delta V_{\rm WHIM}$ gives the relevant volume in a z-shell of the universe, to which the total RG volume in that shell is compared.

7.2.2 Radio Galaxy Volumes

The RG volumes are calculated by assuming that the RGs are cylindrical in shape with total length $D(t)$ (given by Equation 2.2), at an age t. The axial ratio, R_T (mentioned in Section 2.4), gives the ratio of the source length and its width (or diameter). From these, the volume occupied by a RG at an age t is,

$$V_{RG}(t) = \pi \left[\frac{D(t)}{2R_T}\right]^2 D(t) = \frac{\pi D(t)^3}{4R_T^2}. \tag{7.10}$$

To get a conservative estimate, in all the volume computations $R_T = 5$ is used, irrespective of the model (unless otherwise noted). This value appears to be a reasonable average axial ratio based on observations (e.g., Gopal-Krishna & Wiita 2001, and references therein). The difference in this axial ratio used to calculate the volumes, from that in the KDA model where $R_T = 1.3$ gave the best fit to the [P–D–z] planes, and in the KDA-modified model where R_T varies, is noteworthy. If later work shows that $R_T < 5$ is preferable, then a typical radio galaxy volume $V_{RG}(t)$ will be larger, thus favoring our picture of substantial cosmological impact of RGs.

Let the cosmic times of the end points of the z-shell (defined at the beginning of Section 7.2) be denoted as t_{IN} (corresponding to redshift z_{min}) and t_{OUT} (corresponding to redshift z_{max}). These times correspond to $t = 0$ at the Big Bang, and $t = 13.7$ Gyr at the present epoch. It is assumed that all the RGs in an ensemble live out to their full T_{MaxAge}. Even if the vast majority of radio sources born through the quasar era fall below the flux limit to be detected now, they do expand as long as the AGN is feeding the jets (and the lobes in turn), and hence contribute to filling part of the universe.

In a shell (between z_{max} and z_{min}, or between t_{OUT} and t_{IN}), all the RGs are counted which have any portion of their lives falling in the time range of that z-bin. So a RG is counted in a shell if its t_{birth} satisfies one or both of the following conditions,

$$\begin{aligned} (t_{IN} - T_{MaxAge}) \leq \;& t_{birth} \;< t_{IN}, \\ \text{or,}\;\; (t_{OUT} - T_{MaxAge}) \leq \;& t_{birth} \;< t_{OUT}. \end{aligned} \tag{7.11}$$

The z-shell intercepts the volume of a RG between times t_{OUT} and t_{IN} only. The volume contribution of a RG in the z-bin is calculated as,

$$\Delta V_{RG}\,(z) = V_{RG}(t_{IN} - t_{birth}) - V_{RG}(t_{OUT} - t_{birth}). \tag{7.12}$$

For a RG which is born or dies within a shell, the following respectively hold:

$$\begin{aligned} t_{IN} > \quad & t_{birth} \quad > t_{OUT}, \\ t_{IN} > \quad & (t_{birth} + T_{MaxAge}) \quad > t_{OUT}. \end{aligned} \tag{7.13}$$

In such a case the volume contribution in the shell is calculated by setting the time arguments as follows. If $(t_{OUT} - t_{birth}) < 0$, then $(t_{OUT} - t_{birth}) = 0$ is taken. If $(t_{IN} - t_{birth}) > T_{MaxAge}$, then $(t_{IN} - t_{birth}) = T_{MaxAge}$ is used.

The volume contribution of all the RGs which are intercepted by a z-shell are then added to get the total RG volume $\Delta V_{RG(\mathrm{total})}$.

7.2.3 Volume Fraction

The relevant volume fraction in a z-shell is considered to be the fraction, $\Delta\iota(z)$, at the mid epoch of the shell or redshift z_{mid}. This is estimated from the volumes computed in Sections 7.2.1 and 7.2.2,

$$\Delta\iota(z) = \frac{\Delta V_{RG(\mathrm{total})}}{\Delta V_{\mathrm{WHIM}}}. \tag{7.14}$$

We stress that this quantity gives the relevant fraction within individual redshift shells. Integrating $\Delta\iota(z)$ over z gives the volume fraction as,

$$\iota = \int_0^{z_{early}} \Delta\iota(z) dz, \tag{7.15}$$

where, z_{early} is the earliest redshift of a source in the initial ensemble. However, there is another significant factor to be taken into account to estimate the total fraction correctly; this involves noting the contribution from the likelihood that there were several generations of RGs during the Quasar Era (QE), as discussed next.

We are interested in the total volume filled by the multiple generations of RGs in the universe over the whole QE. This was taken into account in GKW01 from the following qualitative arguments. Gopal-Krishna & Wiita (2001) considered the length of the QE as $t_{QE} \sim 2$ Gyr, and the maximum age of radio sources $T_{MaxAge} = 500$ Myr.

They argued that every place in the universe could have been potentially affected by $t_{QE}/T_{MaxAge} = 4$ generations of RGs during the entire QE. So they multiplied the peak of the corrected RLF by (t_{QE}/T_{MaxAge}) in their Section 2.2, to get the total proper density of intrinsically powerful radio sources in the universe.

In our simulations we obtain the total fraction in the following way. We add the values of $\Delta\iota(z)$ several times in intervals of T_{MaxAge} over the entire QE. The length of the QE is obtained from the temporal length of the epoch for which $\Delta\iota(z) \geq 5\%$ of its peak value. Starting from the high-z end-point of the QE, values of $\Delta\iota(z)$ are computed at intervals of T_{MaxAge} and summed, until the low-z end-point of the QE is reached or exceeded. This addition is done several times; each time the starting point is chosen differently by going back or forward from the original starting point by integral multiples of 50 Myr. The total $\Delta\iota(z)$ obtained from these several $(2n + 1)$ additions (each starting from a different cosmic time), are then averaged to get the mean total "relevant volume fraction" of the universe filled by generations of radio galaxies during the quasar era. This is denoted by ζ in Equation (4) of Gopal-Krishna & Wiita (2001), and is called the "fractional relevant volume that radio lobes born during the QE cumulatively cover". Mathemetically ζ can be expressed as,

$$\zeta = \sum_{\substack{\text{Over quasar era} \\ \text{In intervals of } T_{MaxAge}}} \Delta\iota(z). \tag{7.16}$$

7.2.4 Mean Radio Galaxy Volume

We now numerically estimate the mean proper volume attained by a typical radio galaxy at its maximum age, $\langle V(T_{MaxAge})\rangle$. This is done using the same z binning as for finding the relevant fractions, but the way the RGs are counted in the z-shells is different. The cosmic times have the same meanings as in Section 7.2.2.

To find this average volume a simulated source in the initial ensemble is considered only at its maximum age. A RG is counted in a z-bin if its t_{birth} satisfies the following condition:

$$t_{IN} > (t_{birth} + T_{MaxAge}) > t_{OUT}. \tag{7.17}$$

In this way, all the RGs which have their switch-off times within a z-bin are considered, and their total volume in the shell is computed. This total volume divided by the number of RGs in the shell gives the average volume of one radio galaxy. The volumes from all the shells over the whole redshift range are then averaged, to obtain the

resultant mean volume of a RG at its T_{MaxAge},

$$\langle V(T_{MaxAge})\rangle = \text{Mean}\left(\frac{\text{Total volume of RGs switching off in a z-shell}}{\text{Total number of such RGs in the shell}}\right). \quad (7.18)$$

7.3 Results and Discussion

Following the methodology in Section 7.2, the relevant volume fraction, ζ, was computed for a subset of the model simulations done in the previous Chapters for the 3 main models, KDA, BRW and MK, as well as for the modifications we have considered. The total volume of RGs in an initial ensemble of radio sources was compared to the relevant volume of the universe, to get the fraction filled as a function of z.

The model parameters which determine the relevant volume fraction can be enumerated as follows. The distribution function of redshift (Equation 3.6: z_0, σ_z), and that of jet power (Equation 3.9: x, Q_{min}, Q_{max}), according to which an initial ensemble of sources are generated (Section 3.1) following the presciption from BRW, along with the maximum age, T_{MaxAge}, are the parameters which are model-independent, i.e., they do not depend on the RG power evolution models. The RG volume, $V_{RG}(t)$ (Equation 7.10) depends on the models through the linear size, $D(t)$ (Equation 2.2), which explicitly involves the ambient density parameters (Equation 2.1: ρ_0, a_0, β). The other model-dependent factor is the detection ratio (Equation 7.5) which is obtained from the number of sources in the simulated surveys.

7.3.1 Cosmological Volumes

Figure 7.1 gives the cosmological volumes leading to the "relevant volume of the universe". The *left-top* panel shows the all-sky comoving volume, $\Delta V_{\rm comov}$ (Equation 7.3), in the different z-shells. This corresponds to the the proper volume distribution shown in the *left-bottom* panel, which is basically the comoving volume divided by $(1+z)^3$. The *right-top* panel gives the fractional volume of the WHIM compared to the total volume of the universe, which was interpolated from Cen & Ostriker (1999) as described toward the end of Section 7.2.1. The *right-bottom* panel is the final relevant WHIM volume inside the redshift shells over the effective 3CRR sky area, $\Delta V_{\rm WHIM}$ (Equation 7.9).

The *top-left* panel of Figure 7.2 shows the time-width corresponding to the z-bin

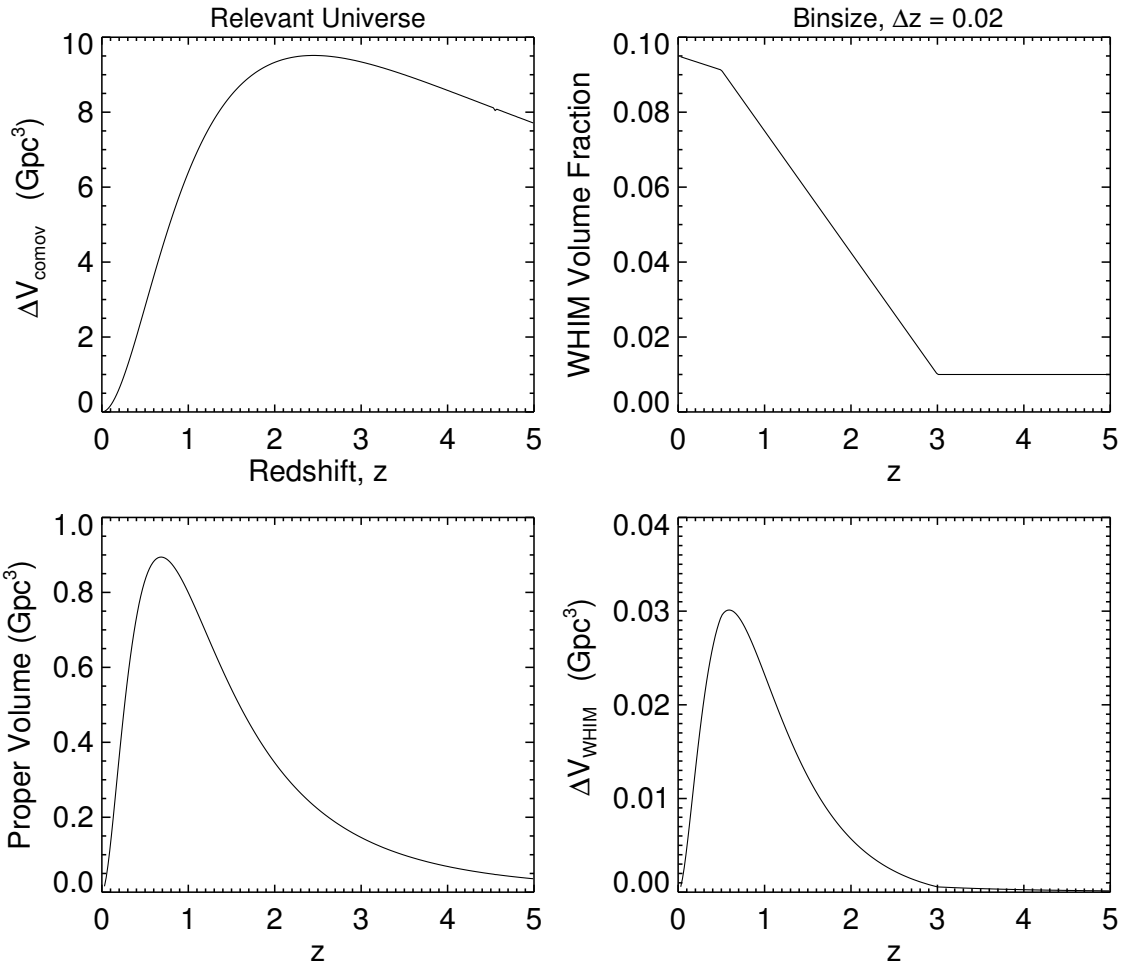

Figure 7.1: Relevant Volume of the Universe: WHIM volume over effective 3CRR sky area as a function of redshift. See Sections 7.2.1 and 7.3.1 for details.

width used, $\Delta z = 0.02$, over all relevant redshifts. From here it is clear that at higher redshifts ($z > 2$) a RG of $T_{MaxAge} = 100 - 500$ Myr spans many ($\sim 10 - 20$) bins; whereas, at lower redshifts ($z < 0.5$) a RG spans only one to a few bins. These results (comoving, proper, WHIM volumes and time-width) are solely dependent on cosmology, and remain constant for the simulations done for the three main RG evolution models (KDA, BRW and MK) and their modifications.

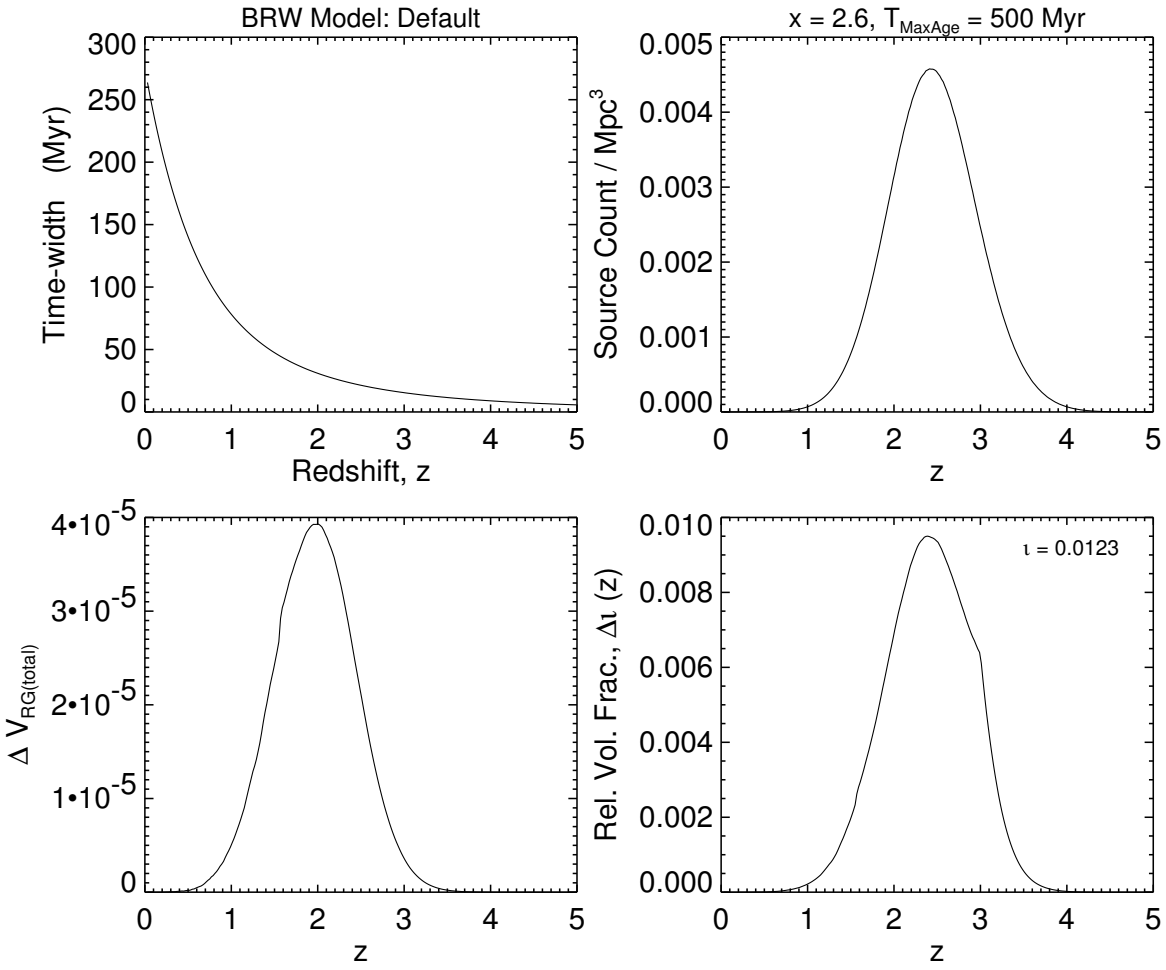

Figure 7.2: Relevant volume fraction of the universe filled by RGs from BRW simulation with default model parameters. The initial ensemble of size 1561417 is generated using $x = 2.6$, $T_{MaxAge} = 500$ Myr. See Section 7.3.2.1 for details.

7.3.2 Radio Galaxy Volumes and Relevant Fractions

7.3.2.1 BRW Default Model:

We discuss the RG volume fraction results and their implications for one model in detail, as they are similar for all. This chosen model is the BRW default simulation (done with initial ensemble of size 1561417 generated using $x = 2.6$, $T_{MaxAge} = 500$ Myr, which detected 167 sources in 3C), since this corresponds to the case for which ζ was computed by Gopal-Krishna & Wiita (2001). The quantitative relevant fraction results for all models are tabulated later.

The details of the RG volumes for this model (BRW default) are shown in Fig-

ure 7.2. The *top-right* panel shows the number of RGs counted in the z-shells per unit Mpc^3 volume of the shell. The *bottom-left* panel gives the total RG volume ($\Delta V_{RG(\text{total})}$, Section 7.2.2) in the z-bins. The *bottom-right* panel shows the relevant volume fraction $\Delta\iota(z)$ (Equation 7.14) as a funciton of redshift.

The following trends are noted from the redshifts at which the volume distributions peak. The RLF or redshift distribution (Equation 3.6) from which the sources in the initial ensemble are drawn is a gaussian with its peak at $z_0 = 2.2$, so the maximum number of sources in the initial ensemble are born at z_0. From Figure 7.2 we can see that the total RG volume, $\Delta V_{RG(\text{total})}$ peaks at $z \sim 2$, which is at a redshift lower than z_0. This difference can be explained as follows. The majority of sources born at z_0 remain active for $T_{MaxAge} = 500$ Myr, and are thus counted in several later z-bins. They contribute to the RG volume in increasing amounts as they grow in age, until the maximum age $T_{MaxAge} = 500$ Myr. Their combined increasing contributions at redshifts later than z_0, make $\Delta V_{RG(\text{total})}$ to peak at a $z < z_0$. This peak redshift of $\Delta V_{RG(\text{total})}$ should be around the cosmic epoch corresponding to $(t(z_0) - T_{MaxAge})$, as that is the epoch when the largest number of sources in the population reach their maximum volume.

On the other hand, the relevant volume fraction, $\Delta\iota(z)$, peaks at $z \sim 2.4$ (from Figure 7.2), which is at a redshift higher than z_0. The distribution of WHIM volume, ΔV_{WHIM} (Figure 7.1), can be invoked to explain this result. We see that ΔV_{WHIM} rises sharply from an early redshift $z \sim 3$, with increasing steepness, until it reaches a peak at $z \sim 0.7$. Such a behavior is because of the trends of proper volume of z-shells in our current consensus cosmology (Section 7.2.1). When the ratio of $\Delta V_{RG(\text{total})}$ to ΔV_{WHIM} is taken to get $\Delta\iota(z)$ at $z \sim z_0$, $\Delta V_{RG(\text{total})}$ is divided by a volume ΔV_{WHIM} which decreases with increasing redshift. So the result is that the peak relevant fraction is obtained at $z > z_0$.

A representation of how the volume contribution of multiple RG generations are added to get the total cumulative fraction over the entire QE is given in Figure 7.3. The methodology to calculate this total fraction was discussed in the last paragraph of Section 7.2.3. The solid black curve in the figure is the volume fraction $\Delta\iota(z)$ as a function of redshift. The symbols (of a single type and color) plotted on it are the values of $\Delta\iota(z)$ which are picked at intervals of $T_{MaxAge} = 500$ Myr over the QE, and added. The different plotting symbols denote the different starting points for the added fractions, which were finally averaged to get the cumulative fraction, ζ.

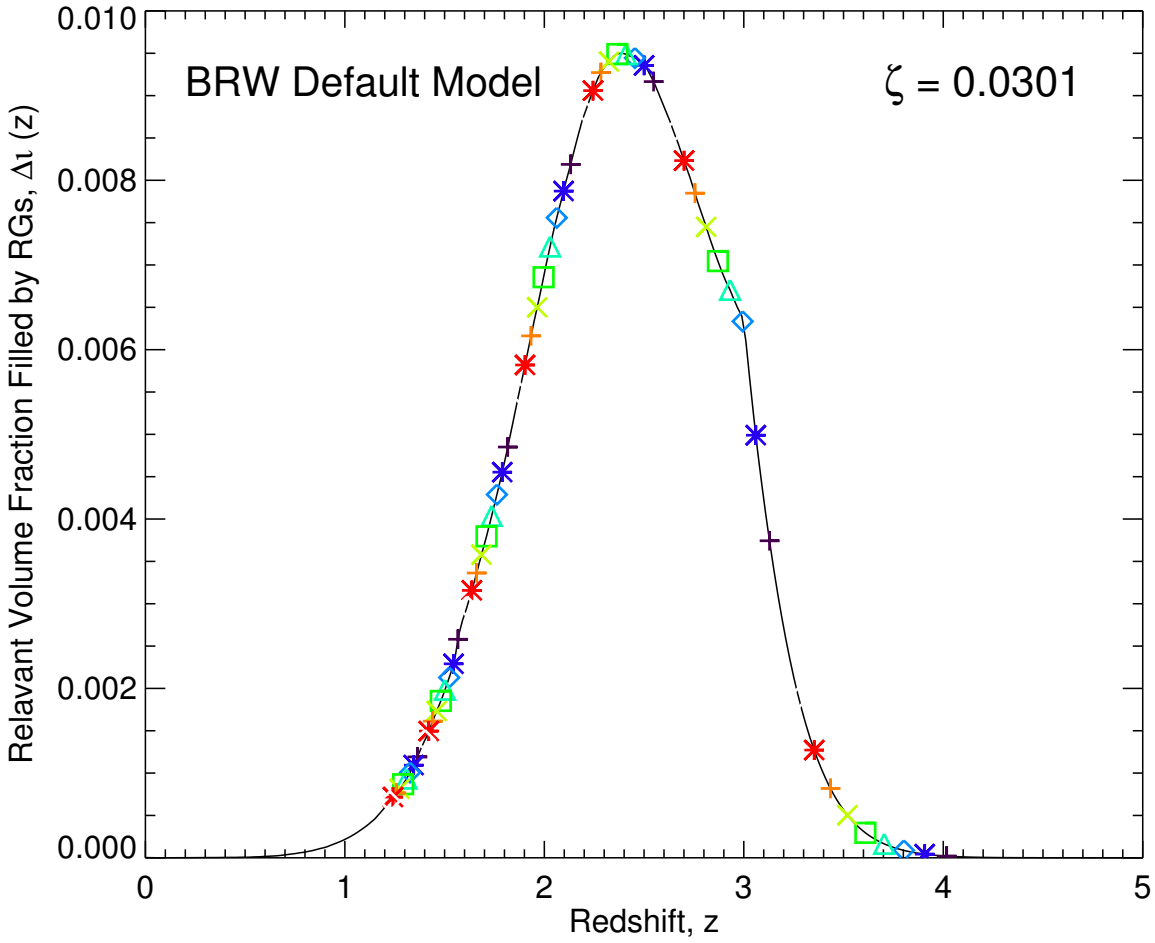

Figure 7.3: Total relevant volume fraction of the universe filled by RGs by adding the volume contributions of multiple generations of RGs over the quasar era. This is for the BRW simulation with default model parameters, for the initial ensemble of size 1561417 generated using $x = 2.6$, $T_{MaxAge} = 500$ Myr. See Section 7.3.2.1 for details.

For this model (BRW default) the quasar era spans the redshift range $z_{QE} = 3.52 - 1.16$, or the cosmic time range $1.74 - 5.10$ Gyr, corresponding to a quasar era of duration $t_{QE} = 3.36$ Gyr. Hence there are contributions from 7 generations of RGs in the case where $T_{MaxAge} = 500$ Myr. The final relevant fraction results for this model are:

$$\iota = 0.0123, \qquad \zeta = 0.0301. \tag{7.19}$$

Table 7.1: Relevant Volume Fractions for Selected BRW Models and Modifications

x	T_{MaxAge} (Myr)	Ensemble Size	Model Parameters	Ratio /3C	A_z ($\times 10^{-8}$) (Mpc^{-3})	Volume Fraction, ι	Total Vol-Frac, ζ
BRW Model [a]							
2.6	250	1466378	Default	2.12	0.931	0.00147	0.00623
2.6	500	1365839	Default	1.23	0.465	0.0102	0.0248
		1561417	Default	1.15	0.532	0.0123	0.0301
3.0	50	999361	Default	3.39	2.99	1.08e-05	0.000201
3.0	150	4861474	Default	6.03	4.99	0.000430	0.00285
3.0	200	1019403	Default	0.99	0.798	0.00107	0.00549
3.0	250	1571349	Default	1.33	0.997	0.00204	0.00863
		3355926	$a_0 = 7.5$ kpc [b]	0.869	2.13	0.00964	0.0408
3.0	300	2107441	Default	1.49	1.13	0.00366	0.0133
3.0	350	2138676	Default	1.25	0.997	0.00611	0.0197
3.0	500	2930490	Default	1.21	0.997	0.0179	0.0437
		6451283	$a_0 = 7.5$ kpc	1.03	2.19	0.0667	0.163
BRW-modified Model [c]							
2.6	500	4397469	Default	2.87	1.50	0.0139	0.0339
3.0	300	4963343	$t_{bf} = 100$ yr [d]	1.94	2.66	0.00658	0.0240

[a] Results for BRW model (Section 2.5).

[b] 1-D K-S best-fit case of BRW, whose main statistical results are given in Tables A.8, 4.10 and 4.14.

[c] Results for BRW-modified model (Section 5.2.1), where a hotspot size growing with the source age is incorporated.

[d] 1-D K-S best-fit case of BRW-modified, whose main statistical results are given in Tables B.4, 5.11 and 5.12.

7.3.2.2 Other Models:

We tabulate the relevant volume fraction results for selected models. Tables 7.1, 7.2 and 7.3 give the results for the BRW, KDA and MK models for several parameter variations and some modifications.

These tables follow the same format, so only the table entries for the BRW model (Table 7.1) are explained. The results for a particular parameter variation of the model are given in each row. Column 1 lists the value of the RG jet power distribution index x. Column 2 gives the T_{MaxAge} (in Myr) used for the initial population

generation in that model run. The initial population (ensemble) size used to realise the model simulation is listed in column 3. Column 4 gives the dynamical and power evolution model parameters used in the simulation, which are mostly "default", i.e., the parameters are set to the values used by the respective authors (Table 2.1); if some parameter is varied its value is listed. Column 5 lists the 3C detection ratio, Ratio_{3C} defined in Equation (7.5). Column 6 gives A_z, the normalizing factor in the redshift distribution (Section 3.1.2) which was used to generate the initial population; A_z is the factor by which $[V_C(z=0) \times \rho(z_{birth})]$ (Section 3.1.2) is multiplied to get the number, N_{born} of radio sources born within the relevant comoving volume, V_C. Column 7 gives the relevant volume fraction, ι, and Column 8 lists the total (cumulative) relevant volume fraction over multiple generations, ζ.

From Tables 7.1 – 7.3 the following trends are seen in the relevant volume fractions. The fractions, ι and ζ vary significantly between the models, and also change substantially when using different parameter values within the same model. So we see that, quite a wide range of relevant volume filling factors can be produced by the allowed range in model parameters.

For the default case, RGs in the BRW simulations cumulatively fill out ∼3% of the relevant universe. This number is ∼4.5% for the KDA model and ∼7% for the MK model. At the same x and T_{MaxAge}, and using default model parameters, the MK model gives the largest relevant fractions, followed by the KDA and finally by the BRW models. The reason for this is that a larger initial ensemble needs to be generated in the MK model to get the same number of sources detected compared to the other models.

The fractions for the "1-D K-S best-fit" cases (those giving highest total 1-D K-S probability within each model) of the models are: BRW: 4%, BRW-modified: 2.4%, KDA: 2.2%, KDA-modified: 4.4%, MK: 1.5%, MK-modified: 1.5%. These models are the "varied" cases for which additional statistical tests were done in Sections 4.8 (Tables 4.10 and 4.14) and 5.4.3 (Tables 5.11 and 5.12). The [P–D–z–α] planes for these cases are in Figures 4.5, 4.6, 4.7, 5.8, 5.9 and 5.10 for the best-fit KDA, BRW, MK, BRW-modified, MK-modified and KDA-modified models, respectively.

The runs involving parameter variations corresponding to "1-D K-S best-fit"s of the BRW and KDA models give higher fractions (by $\sim 4-5$ times) than do the corresponding "Default" models, for the same x and T_{MaxAge}. This is because the BRW best-fit is with $a_0 = 7.5$ kpc $< a_{0\ (\mathrm{Default})}$, and KDA best-fit is with $\rho_0 =$

Table 7.2: Relevant Volume Fractions for Selected KDA Models and Modifications

x	T_{MaxAge} (Myr)	Ensemble Size	Model Parameters	Ratio /3C	A_z ($\times 10^{-8}$) (Mpc^{-3})	Volume Fraction, ι	Total Vol-Frac, ζ
KDA Model [a]							
2.6	150	1553389	Default	2.17	1.60	0.000324	0.00215
2.6	500	4397469	Default	2.18	1.50	0.0183	0.0452
3.0	50	999361	Default	0.86	2.99	1.92e-05	0.000359
3.0	100	1993745	Default	1.14	3.03	0.000200	0.00193
3.0	150	1034594	Default	0.455	1.06	0.000787	0.00524
		1618248	Default	0.703	1.66	0.000796	0.00530
		4861474	p, ρ_0 [b, c]	0.993	4.99	0.00331	0.0220
3.0	200	2979285	Default	0.92	2.33	0.00240	0.0123
3.0	300	4963343	Default	1.25	2.66	0.00825	0.0303
3.0	500	2930490	Default	0.552	0.997	0.0372	0.0918
		3419466	Default	0.559	1.16	0.0428	0.106
		4886474	Default	0.807	1.66	0.0424	0.105
		6451283	p, ρ_0 [b]	0.393	2.19	0.225	0.555
3.0	600	1595208	Default	0.228	0.465	0.0738	0.160
		5020623	Default	0.848	1.46	0.0624	0.135
KDA-modified Model [d]							
2.6	500	4397469	Default ($\uparrow R_T$) [e]	1.83	1.50	0.00266	0.00653
		4397469	Default	1.83		0.0679	0.168
3.0	200	4683659	Default [f]	1.27	3.66	0.00848	0.0435

[a] Results for KDA model (Section 2.4).

[b] Parameter variations: $p = 2.12$ and $\rho_0 = \rho_{0\ (\text{Default})}/2 = 3.6 \times 10^{-22}$ kg m^{-3}.

[c] 1-D K-S best-fit case of KDA, with parameter variations as noted for which the main statistical results are given in Tables A.1, 4.10 and 4.14.

[d] Results for KDA-modified model (Section 5.3), where the KDA model is modified by incorporating a rising axial ratio. But, a fixed $R_T = 5.0$ is used to calculate the RG volumes, except otherwise noted.

[e] Increasing R_T (as used in the KDA-modified model) used to calculate the RG volumes.

[f] Default parameters of KDA-modified model also give the 1-D K-S best-fit for it, whose main statistical results are given in Tables 5.4, 5.11 and 5.12.

$\rho_{0\ (\text{Default})}/2$, both of which have the effect of increasing $D(t)$ and thence the RG volumes.

Table 7.3: Relevant Volume Fractions for Selected MK Models and Modifications

x	T_{MaxAge} (Myr)	Ensemble Size	Model Parameters	Ratio /3C	A_z ($\times 10^{-8}$) (Mpc^{-3})	Volume Fraction, ι	Total Vol-Frac, ζ
MK Model [a]							
2.6	150	3888492	Default	3.26	3.99	0.000772	0.00512
2.6	500	4397469	Default	1.37	1.50	0.0286	0.0699
3.0	50	4452567	Default	2.48	13.3	6.48e-05	0.00121
3.0	100	3508016	Default	1.20	5.32	0.000583	0.00559
3.0	150	4861474	Default	1.20	4.99	0.00213	0.0141
		4861474, Set2	$\gamma_{max(hs)}$ [b, c]	1.11	4.99	0.00230	0.0153
3.0	200	1019403	Default	0.193	0.798	0.00542	0.0277
		5109809	Default	0.883	3.99	0.00595	0.0304
3.0	300	2107441	Default	0.290	1.13	0.0185	0.0674
		4963343	Default	0.731	2.66	0.0172	0.0627
3.0	500	2930490	Default	0.310	0.997	0.0687	0.168
		3419466	Default	0.331	1.16	0.0751	0.183
		4886474	Default	0.421	1.66	0.0844	0.206
		4886474	$\gamma_{max(hs)}$ [b]	0.414	1.66	0.0858	0.209
		4886474, Set2	$\gamma_{max(hs)}$ [b]	0.448	1.66	0.0792	0.193
		4886474, Set3	$\gamma_{max(hs)}$ [b]	0.476	1.66	0.0747	0.182
MK-modified Model [d]							
2.6	150	3888492	$\beta = 1.6$ [e]	1.59	3.99	0.00220	0.0146
2.6	500	4397469	Default	0.710	1.50	0.0552	0.135

[a] Results for MK model (Section 2.6).

[b] Parameter variation: $\gamma_{max(hs)} = 3 \times 10^8$.

[c] 1-D K-S best-fit case of MK, with parameter variations as noted for which the main statistical results are given in Tables A.11, 4.10 and 4.14.

[d] Results for MK-modified model (Section 5.2.2), where a hotspot radius growing with the source age is incorporated.

[e] 1-D K-S best-fit case of MK-modified, for which the main statistical results are given in Tables B.7, 5.11 and 5.12.

The relevant volume fractions (ζ) for these preferred parameter sets (favorable with respect to K-S statistics), are all very low compared to the estimate in GKW01, $\zeta = 53\%$. Still, for certain parameter values (as seen from Tables 7.1, 7.2 and 7.3) this fraction goes as high as 16% for BRW (run with lower a_0, which increases $D(t)$),

55% for KDA (run with lower ρ_0, which increases $D(t)$), and 20% for MK model (run with $x = 3$).

The relevant fraction is greater for higher T_{MaxAge} (for same x), as is evident from the expression for the RG volume, which scales as $t^{9/(5-\beta)}$. For the same T_{MaxAge}, the fraction is higher with $x = 3.0$ than with $x = 2.6$. This might seem counter-intuitive, as with a steeper jet power distribution the volumes occupied should be smaller. The mean RG volume at maximum age, $\langle V(T_{MaxAge})\rangle$ is indeed smaller (by a factor of $1.21/1.44 = 0.84$), as discussed later in Section 7.3.3. But a larger volume fraction at higher x can be explained as follows. Many more sources are needed at the steeper slope ($x = 3$) to yield numbers of sources in the simulations comparable to those in the real surveys. This is clear on inspecting the Tables 7.1, 7.2 and 7.3. To get the same Ratio_{3C}, larger ensemble sizes (by $1.5 - 3.5$ times) are required for $x = 3$ than for $x = 2.6$. Hence with $x = 3$, the increase in ensemble size (by ~ 2) more than offsets the smaller mean volume (by 0.84), which results in the total RG volumes and the final relevant fractions being larger.

The volume fractions were calculated using $x = 3$, $T_{MaxAge} = 500$ Myr and the "1-D K-S best-fit" model parameters (the case which gave the highest total 1-D K-S probability in each model with its favorable x and T_{MaxAge}). This was done to check the validity of the proportionality $\langle V(T_{MaxAge})\rangle \propto T_{MaxAge}^{18/7}$, found in Section 2.3 of GKW01. Assuming, $\zeta \propto \langle V(T_{MaxAge})\rangle$, the following can be noted from the volume fraction results at multiple values of T_{MaxAge} for simulations done using different parameter sets. The $\langle V(T_{MaxAge})\rangle$ scalings with T_{MaxAge} for the "default" and "best-fit" cases of BRW, KDA and MK models lies within,

$$2.0 < \frac{\log(\zeta)}{\log(T_{MaxAge})} = \frac{\log(\langle V(T_{MaxAge})\rangle)}{\log(T_{MaxAge})} < 2.7. \tag{7.20}$$

These results are consistent with the exponent derived by GKW01, $18/7 = 2.57$, taking into consideration the statistical variance.

Figure 7.4 shows plots of the relevant volume fraction, $\Delta\iota(z)$, as a function of redshift, for some of the model simulations. The left hand panels are for the BRW, KDA and MK "1-D K-S best-fit" cases. The right hand panels are for the noted parameter variation (if any) of the models. The quantitative results for all these models can be seen from Tables 7.1, 7.2 and 7.3.

The total relevant volume fraction, ζ, as a function of maximum age, T_{MaxAge}, is

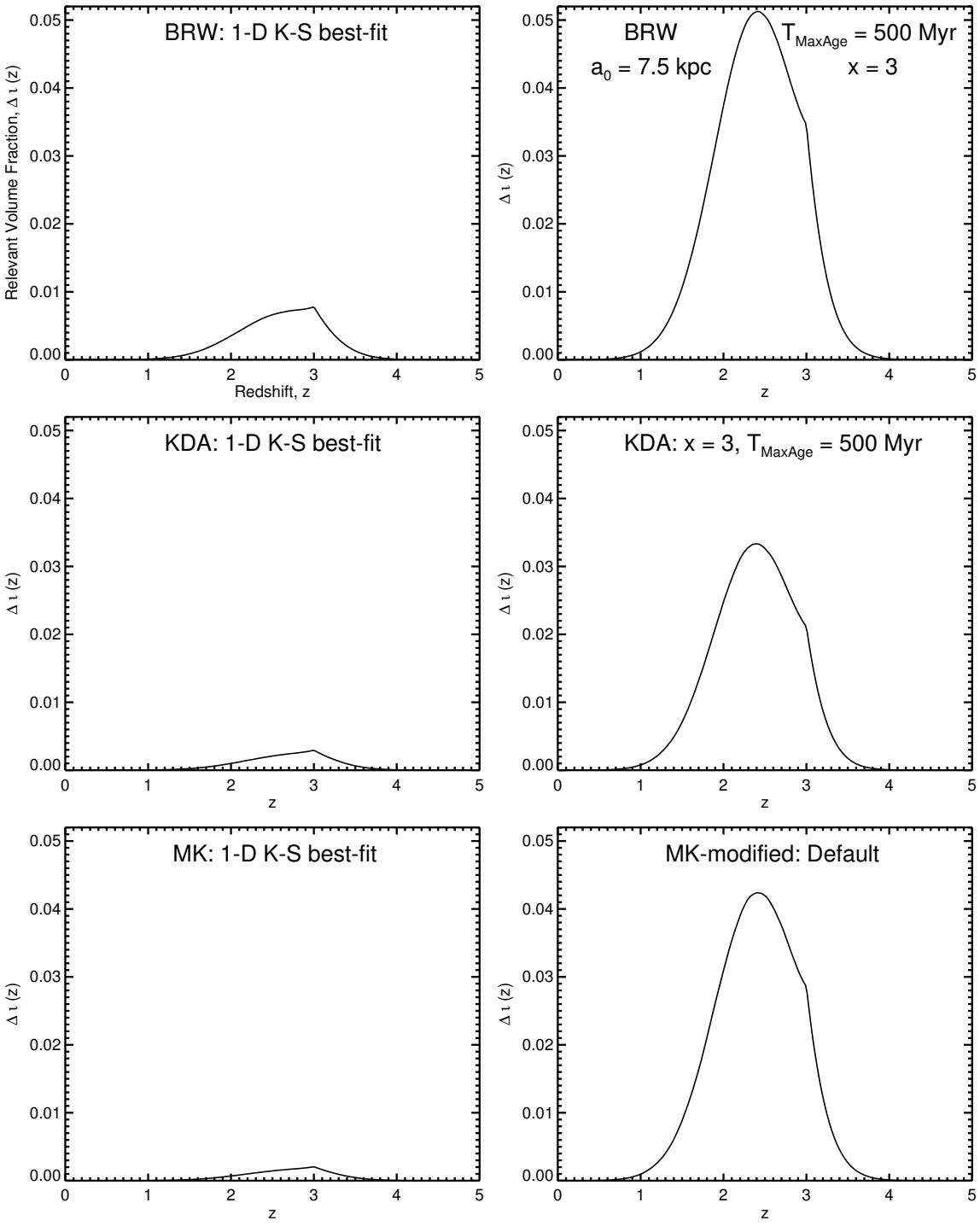

Figure 7.4: Relevant volume fractions of the universe filled by radio galaxies from several model simulations, which are labeled in each panel.

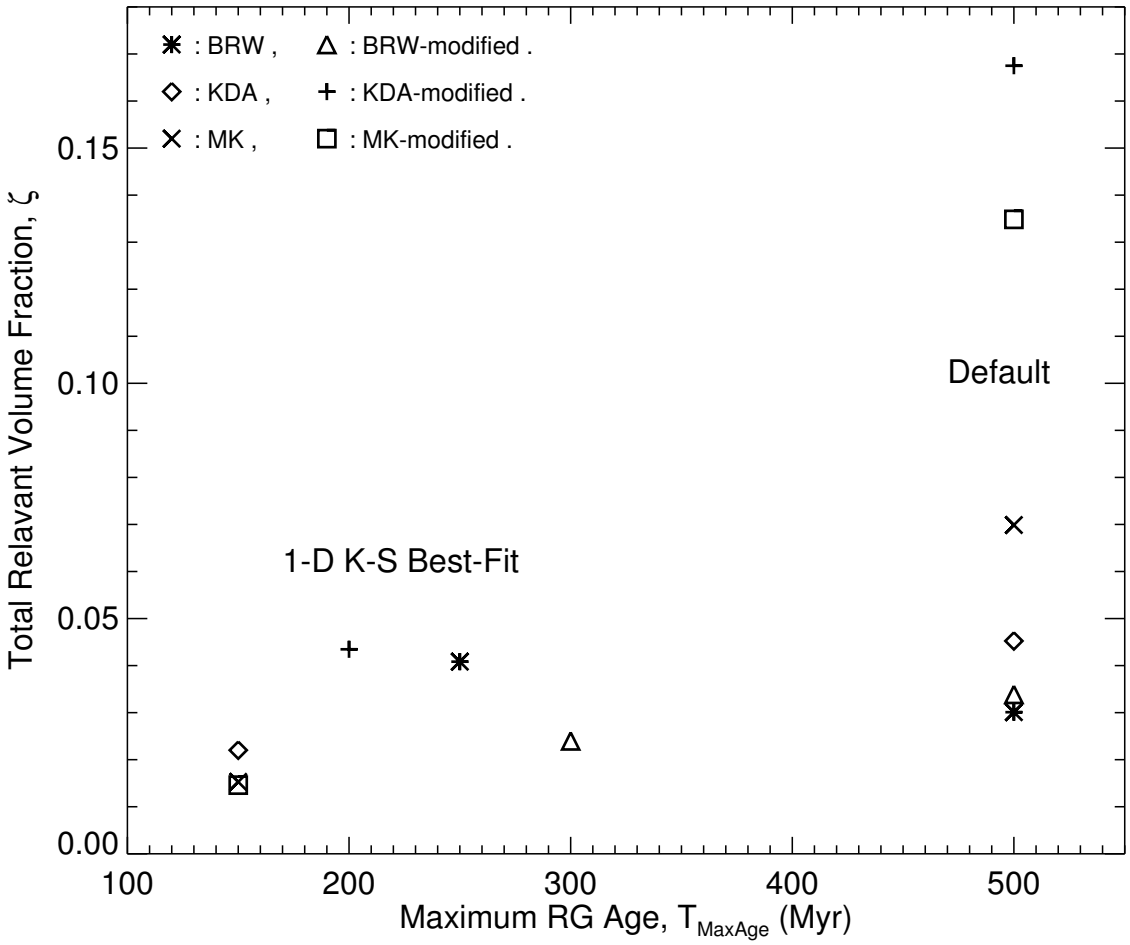

Figure 7.5: Total relevant volume fraction as a function of maximum age, for the "default" and the "1-D K-S best-fit" cases of the six models explored in detail, as distinguished by the plotting symbols.

shown in Figure 7.5 for the "default" and "1-D K-S best-fit" cases of the six models explored in detail. The models are distinguished by the plotting symbols in the figure. The default versions of most of the models give higher ζ values when compared to the corresponding "best-fit" ones, since T_{MaxAge} is higher (the K-S "best-fit"s were obtained with lower T_{MaxAge}). When compared to $\zeta = 0.5$ found in GKW01, most of the values of relevant fractions in Figure 7.5 are significantly smaller; such trends are discussed in detail in Section 7.4.

7.3.3 Mean Volume

In the way the sources are counted to find the average volume (a source counted only at its maximum age), as described in Section 7.2.4, the total number of RGs is preserved. The total count added in all the z-shells is equal to the number of sources in the initial ensemble.

The mean volume computed for two cases of the BRW model are shown in the two panels of Figure 7.6. The top figure plots the average volumes of RGs in the z-shells for the BRW default model: $x = 2.6$, $T_{MaxAge} = 500$ Myr, using an initial ensemble of size 1561417. The bottom plot is for same model but with $x = 3.0$, where the ensemble of size 2930490 is used. The resultant mean volumes are,

$$\begin{aligned} \langle V(T_{MaxAge}) \rangle &= 1.44 \text{ Mpc}^3, \qquad \text{for} \quad x = 2.6, \\ &= 1.21 \text{ Mpc}^3, \qquad \text{for} \quad x = 3.0. \end{aligned} \tag{7.21}$$

Evidently the average volume, $\langle V(T_{MaxAge}) \rangle$, decreases as x increases. With a steeper distribution of jet power (i.e., a higher value of x), Q_0 has a lesser value in a larger portion of sources, thus making the total volume smaller.

In Figure 7.6, the errors (greater deviations from the resultant mean) towards the high ($z > 3$) and low ($z < 1$) redshifts, are due to small number statistics. At such redshifts fewer sources are generated in the initial ensemble, as the redshift birth function, Equation (3.6), peaks at $z_0 = 2.2$ and has a standard deviation of $\sigma_z = 0.6$.

7.4 Comparison of Results with a Previous Estimate

As mentioned in Sections 1.2 and 7.2.3, Gopal-Krishna & Wiita (2001, GKW01) performed a preliminary qualitative calculation to find the relevant volume fraction added over several generations of radio sources during the quasar era. Using default parameter values from BRW, they obtained a cumulative volume filling factor of $\zeta \approx 0.5$. From the results in Section 7.3.2 (Tables 7.1, 7.2 and 7.3, Figure 7.5), we can observe that the relevant fraction obtained in this thesis is considerably smaller than the fraction estimated by GKW01. For the BRW default model (simulation done with initial ensemble of size 1561417 generated using $x = 2.6$, $T_{MaxAge} = 500$ Myr) we obtained $\zeta \approx 0.03$ (2nd entry of Table 7.1), whereas using published graphs

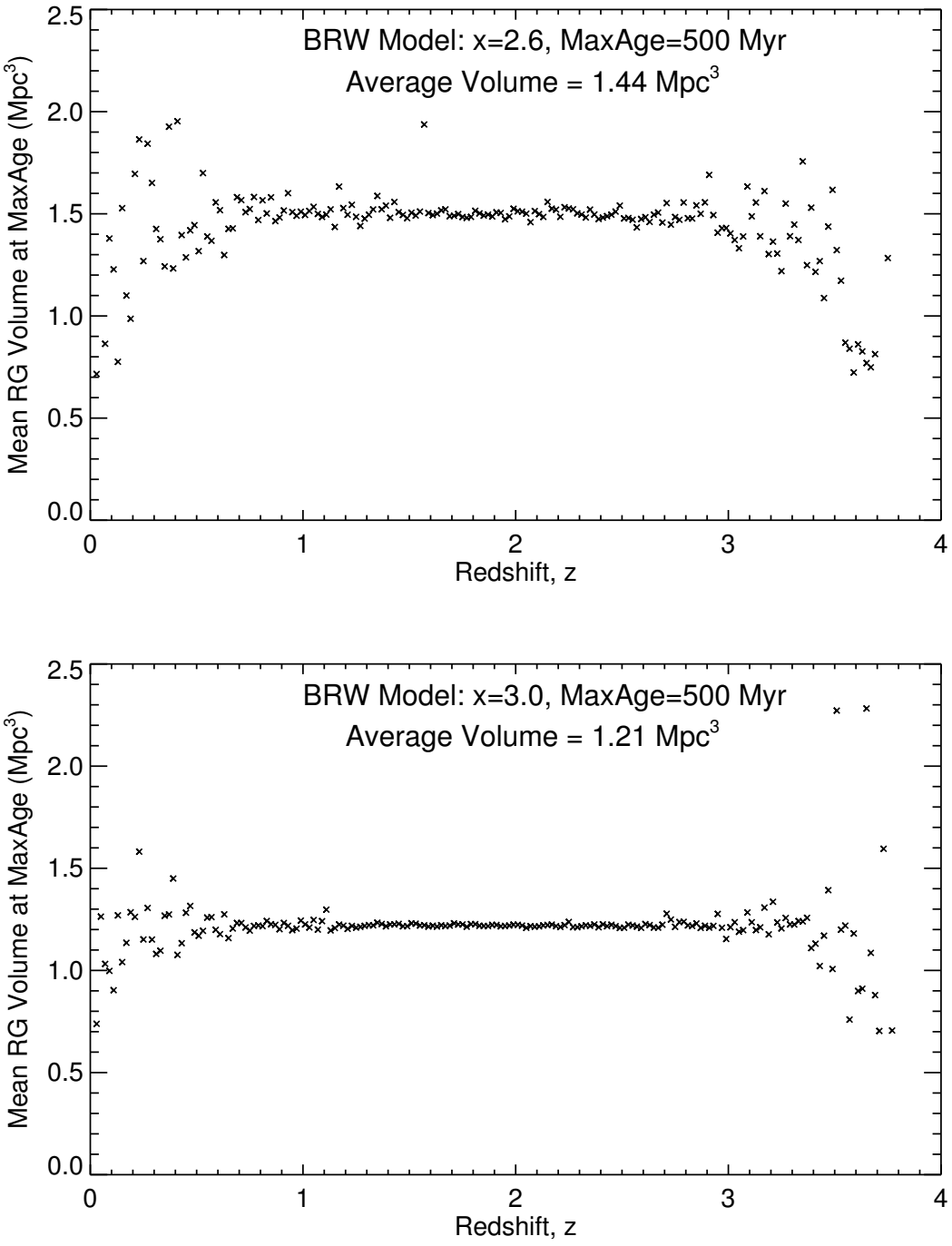

Figure 7.6: Average radio galaxy volume at maximum age for different x, the beam power distribution index.

in BRW for the same model GKW01 obtained $\zeta \approx 0.5$.

Here we discuss some differences between the calculations which can account for much of the discrepancy between the two calculations.

(1) Different cosmology:

We adopted the new consensus cosmology, which is increasingly supported by new data (e.g, WMAP3, Spergel et al. (2006)). This is a flat dark-energy dominated universe with the values of cosmological parameters noted in Section 7.2.1: $H_0 = 71$ km s^{-1} Mpc^{-1}, $\Omega_M = 0.3$, and $\Omega_\Lambda = 0.7$. GKW01 used cosmologies with $H_0 = 50$ km s^{-1} Mpc^{-1}, and with either $\Omega_M = 0$ or 1, but with $\Omega_\Lambda = 0$, an empty or matter dominated flat universe, respectively.

(2) Different lower limit of jet power, Q_0:

In the model simulations performed in this thesis we used $Q_{min} = 5 \times 10^{37}$ W as the minimum jet power, following BRW (as described in Section 3.1.4). GKW01 took the effective lower limit of Q_0 as $Q_m \equiv 7.5 \times 10^{37}$ W (their Section 2.2), which they inferred (by observing the BRW [P–D] tracks in their Figures 13 and 14) to be the minimum power a source must have in order to appear in the BRW data set, where it will have $\log P_{151} = 27.0$ at an early evolutionary stage (at age ≈ 1 Myr).

In the simulations, the minimum Q_0 value comes into effect when the sources in the initial ensemble are alloted their jet power. A higher minimum Q_0 in GKW01 means that the RG jets will be, on average, more powerful, thus making the total RG-volume and the relevant fraction (calculated by them) higher. This leads to a change in the factor f_d used by GKW01 (their Section 2.2). This difference also comes in through its effect on the mean RG volume (next point).

(3) Different $\langle V(T_{MaxAge})\rangle$:

We obtained the average radio galaxy volume at maximum age $T_{MaxAge} = 500$ Myr to be 1.44 Mpc^3, whereas GKW01 obtained a value of 2.1 Mpc^3 (their Section 2.3), using the same BRW default model parameters (except for the different Q_{min}, previous point).

It is easy to show that $\langle V(T_{MaxAge})\rangle$ should scale as $Q_{min}^{3/(5-\beta)}$, since $Q_{max} \gg Q_{min}$. So GKW01's $\langle V(T_{MaxAge})\rangle$ should be higher than ours by

$$\left(\frac{7.5}{5}\right)^{3/(5-\beta)} = 1.42. \tag{7.22}$$

This effect immediately causes the GKW01 relevant volume fraction ζ to be higher

than ours by the same factor of $1.42 = 2.1/1.44$.

(4) Adding multiple generations:

To get the total proper density of RGs, GKW01 multiplied the peak of the corrected RLF by $(t_{QE}/T_{MaxAge}) = 4$ generations of RGs in their Section 2.2. We consider the contribution from multiple generations of RGs by adding the volume fractions as described in Section 7.2.3. We add the values of $\Delta\iota(z)$ in intervals of T_{MaxAge} over the entire QE, so we more precisely take into account the distribution of $\Delta\iota(z)$ vs. z. As can be inferred from Figure 7.3, simply multiplying the peak fraction (highest $\Delta\iota(z)$ in Figure 7.3) by 4, which was done in GKW01, gives an overestimate of ζ by a factor of $0.038/0.030 = 1.27$.

(5) WHIM volume fraction:

As described in Section 7.2.1 and shown in Figure 7.1 (top-right panel), we interpolated the fractional WHIM volume in the universe, which varies with z, from the calculations of Cen & Ostriker (1999). This WHIM volume fraction decreases with increasing redshift, starting from $\simeq 0.095$ at the present epoch, to reach $\simeq 0.01$ at $z \simeq 3$. GKW01 considered a contant WHIM volume fraction of 0.03 at all redshifts of the quasar era. For our computation, the higher WHIM fraction at low-z dominates over the lower WHIM fraction at high-z. This increases the effective WHIM volume of the universe thus reducing the RG relevant fraction.

(6) Average value of z:

In converting from comoving to proper volumes GKW01 used a value of $z = 2.5$. We integrated over each value of z and had an effective average value of $z \sim 2.2$. This value is basically the peak, z_0, of the Gaussian redshift distribution (Equation 3.6) of the radio sources. This explains why the GKW01 result for ζ would exceed ours by another factor of $\sim (1 + 2.5)^3/(1 + 2.2)^3 = 1.31$.

Taken together, the above factors work so as to increase the relevant volume fraction in the estimate of GKW01 in comparison with the more accurate results found from our Monte-Carlo simulations.

– 8 –

Discussion, Caveats and Conclusions

We have performed comprehensive quantitative tests of three detailed models for RG evolution (KDA, BRW and MK), and have extensively explored some modifications in them by allowing the sources' hotspot size or axial ratio to grow with age. This is the first attempt to perform such statistical tests involving four radio source observables (source power, linear size, redshift and spectral index), over three flux-limited complete radio surveys (3CRR, 6CE and 7CRS, which are actually subsamples of the 3C, 6C and 7C radio catalogs where the redshifts of essentially all the sources in the subsamples have been found spectroscopically).

The key result of my thesis work is that no existing model of cosmological evolution of radio galaxy power and dynamics can give acceptable fits to all of the properties of all the surveys considered. Adequate fits to each of the [P–D–z] distributions could often be found for each model for each of the Cambridge catalog subsamples. A few cases (parameter variations) of the KDA, MK, KDA-modified and MK-modified models also gave barely acceptable fits (i.e., 1-D K-S test probability $\mathcal{P} \geq 0.01$) to all of the three source properties [P–D–z] of all three surveys. For the BRW-modified model, 6–7 individual $\mathcal{P}$'s (among total 9 probabilities of P, D, z in the 3 surveys) were acceptable at the best; this was true for only 3–4 $\mathcal{P}$'s (among P, D, z) for the "best" cases of the original BRW model.

But we cannot locate any parameter sets which provide good simultaneous fits to all three catalogs and to all four of these observables, [P–D–z–α]. Of particular concern are the spectral indices, where none of the models provides adequate fit. This is true using either the default parameters suggested by each of these three leading models and their modifications, or when considering extensive variations upon them involving changing one or more of the model parameters to plausible different values.

Actually, the default values of the parameters used in the BRW model gives quite poor fits according to the K-S statistical tests performed, while the default values of the KDA model are marginally the best. We find that the KDA model gives better overall results than do the MK or BRW models. However, the BRW model performs better than MK in reproducing the correlation coefficients of the data.

Our analyses used the redshift birth function of radio sources from Willott et al.

(2001)'s radio luminosity function. We conclude that, using Willott et al. (2001)'s RLF, the KDA and MK models perform better than BRW in fitting the 3CRR, 6CE and 7CRS survey data when compared with respect to K-S based statistical tests, and the KDA model provides the best fits to the correlation coefficients.

8.1 Significance and Shortcomings of Our Simulations

We have compared the leading models of radio lobe power evolution for FR II RGs, namely the KDA, BRW and MK models (Chapter 2), using a simulated radio survey prescription, following BRW (Section 3.3). Each of the hundreds of simulated radio surveys we computed required the generation and analysis of a few 10^6 to $> 10^7$ radio sources and hence, substantial amounts of computing power and time. The total number of Monte Carlo simulations done (including all the models) exceeded 450 and over two billion individual RGs were evolved; this was necessary to narrow down the set of parameters for each model to the "best-fit" ranges as described in this thesis. The 1-D K-S tests were done to narrow down the parameters of the different models to locate the more desirable ones (i.e., cases which gave more favorable statistical results). These "preferred" parameter sets of the models were then compared with the data by using 2-D K-S tests, and correlation coefficient analyses. Finally, the performances of the different models are discussed.

Hydrodynamical modeling of classical double radio sources (e.g., Hooda, Mangalam, & Wiita 1994; Carvalho & O'Dea 2002) shows that the pressure in the nearly self-similarly growing lobes falls with time, while the hotspot pressure does not vary much. The Kaiser, Dennett-Thorpe, & Alexander (1997, KDA) model examined here assumed that the head pressure falls with time (and is proportional to that of the cocoon), so this is a weakness of that model. Blundell, Rawlings, & Willott (1999, BRW) adopted a constant hotspot pressure (implying more adiabatic losses for particles in the hotspot of older sources) while considering the adiabatic expansion of particles out of the hotspots to the lobes. They showed a rough qualitative agreement between their simulated and real 3C and 7C data in the $[P$–D–$z]$ space. Manolakou & Kirk (2002, MK) modified the BRW picture by proposing an acceleration mechanism occuring throughout the head region; they obtained $[P$–$D]$ tracks in somewhat better accord with the 3CRR data, but did not consider $[P$–D–z–$\alpha]$ distributions.

Our much more extensive simulations and statistical analyses, based on K-S tests and correlation coefficients, provides a quantitative way to directly compare the three main models and their modifications. We note that despite the hundreds of simulations we computed which did employ substantial variations on the default parameters for each RG model from Chapter 2 and the modifications done to them in Chapter 5 (results of a large subset of which are displayed in this thesis), we could not completely cover the entire plausible parameter space. We also note that other figures of merit could have been devised to distinguish between the goodness of fits of the data to the various simulation results, since no really suitable multi-parameter statistic is available for samples of this size. Keeping these caveats in mind, we believe both that we have covered the vast majority of the sensible parameter ranges and that our choice of combined 1-D K-S probabilities is a good way for a preliminary comparison between the different simulations. In this spirit, we presented our results and conclusions comparing the consistency of the models with respect to different aspects of the data.

As mentioned in Section 1.4, a quantitative comparison of cosmological radio source evolution model predictions with an observational data sample (the 3C data from Laing et al. 1983) has been done by Kaiser & Alexander (1999a). They considered a progenitor FR II source population being born over cosmic epochs, and evolving according to assumed distribution functions of the model parameters of the KDA and KA models. Constructing simulated samples, they then compared the model's predictions with observations. They used χ^2 statistics in the [P–D] and [P–z] planes to constrain the models. However the binning they used was somewhat arbitrary and the bins appear to be based on the concentration of sources in the observed [P–D–z] planes.

Our approach (based on 1- and 2-dimensional K-S statistics and correlation coefficients) may be as good as can be done since we are dealing with source characteristics in four dimensions (P, D, z, α) and over three observational surveys (3CRR, 6CE and 7CRS) with only a few hundred sources in total. We tried to perform multi-dimensional K-S like tests (discussed in Section 3.4.4) but the limited sizes of the observational samples precluded any useful results from being obtained.

8.2 Model Performances and Comparisons

8.2.1 [P–D] Tracks

The following conclusions can be drawn by comparing the power vs. linear-size (P–D) tracks of the KDA, BRW, MK, KDA-modified, BRW-modified and MK-modified models in Figures 4.1, 5.4, 5.2 and 5.3.

An important feature present in all the [P–D] tracks is the "youth–redshift degeneracy" (described in Section 4.1). A high-power, high-redshift model source has a steeper decrease in its specific 151 MHz luminosity with time, and often falls below the flux-limit of a radio survey at a younger age, as compared to a low-power, low-redshift model source.

All the model tracks have varying steepness, implying different rates of decrease of radio power as a source grows with age, in the different models. The BRW [P–D] tracks are the steepest among all (except one in the MK-modified case for the model source with highest redshift and power). The very steep tracks of the BRW model might be related to the fact that BRW gives the worst fit to the data, when compared with respect to 1-D and 2-D K-S statistical tests (Sections 8.2.4 and 8.2.5).

The BRW-modified tracks are less steep than those of the original BRW. This causes the most significant change that is brought in the model performances (judged by statistical tests) after modification, which is evident from the [P–D] tracks. The BRW-modified model gives substantially better K-S statistical fits to the data when compared to the BRW model, as will be discussed further in Section 8.2.4.

8.2.2 Detection Number Ratio

The ratio of the number of sources detected in a 6C (or 7C) simulation to the number in the real survey, as proportionate to the corresponding 3C ratio, shows the following trends, which are similar in the original and modified models.

The MK simulations produce the best detection number ratios, which are in the range $(0.7, 1.2)$, and their variation from 1 can be reasonably ascribed to statistical (sample) variance. The detection number ratios for KDA simulations are worse than MK, as they almost always gave under-detection in 6C (but by a factor which was acceptable) but often too many 7C sources were detected as compared to the number in the catalog. The detection ratios were all poor for the BRW models, which over detected sources in both 6C and 7C, and the over detection factor in 7C was very

high (~ 2). So, comparing the models by their detection number ratios (Ratio_{6C} and Ratio_{7C}), the MK model gives the best fit, followed by KDA, with BRW giving the worst fits.

However, since large changes in the RLF, which we did not consider, could probably substantially alter these ratios, we do not consider them to be an important discriminant between models.

8.2.3 1-D K-S "Best-Fit" Parameters and Physical Implications

8.2.3.1 Jet Power Distribution and Maximum Age:

Among the 6 RG evolution models which have been extensively compared in this thesis (KDA, BRW, MK and their corresponding modifications), the following conclusions can be drawn about the "best-fit" trends of beam power and maximum age of a typical model RG. These are the two main parameters which govern the volume attained by a radio source.

Nearly all the models produced better statistical fits with the slope of the jet power distribution set to $x = 3$. The default value used in the BRW model is $x = 2.6$. The MK-modified model is the only model which gave better 1-D K-S fits with the beam power index set to that default value. So our statistical fits prefer that RGs have jet powers distributed more steeply between Q_{min} and Q_{max} (Section 3.1.4), i.e., there is a larger number of sources with smaller powers.

Considering the active lifetime of the AGN for which the jets feed the lobes, all the models gave better fits with T_{MaxAge} between 150 – 300 Myr. The default value used in BRW is $T_{MaxAge} = 500$ Myr (Section 3.1.1). Our results favor a maximum age of activity that is 1.7 – 3.3 times smaller than that estimated, i.e., the AGN is switched off at an earlier age than believed. This preferred lower maximum age has the highest impact on the "relevant volume fraction" of RGs, by lowering the fraction (Section 8.3) compared to earlier estimates.

Now we mention some of the power evolution and dynamical parameters which give the 1-D K-S "best-fit"s for each of the original models (KDA, BRW and MK). We discuss what are the implications of those preferred parameter values (when compared to the default values in the models), in terms of the physical conditions prevailing in FR II RGs and their environments.

8.2.3.2 KDA:

Table 4.7 lists the 1-D K-S statistic means and standard deviations for the various parameter sets of KDA model. Considering all test changes, the cases giving the best fits involve the following parameter variations (others same as default value), either applied singly or as double (or even triple) changes. These preferred parameter values are $\rho_0 = 3.6 \times 10^{-22}$ kg m^{-3}, $p = 2.12$ and $a_0 = 1.5$ kpc. Hence, a better fit to the observational data is obtained by having the ambient medium around a typical RG with a lower central density (ρ_0) at a smaller scale length (a_0), i.e., a somewhat less dense environment than deduced by more direct observational methods on a limited sample of relatively nearby galaxies. Such a confining medium allows large enough sources to be found despite the smaller value of T_{MaxAge} and higher value of x than in the default case. A more efficient acceleration mechanism during injection of electrons to the lobe may be implied by the lower energy distribution exponent (p). This value of the exponent was also found to maximize the lobe power emitted.

8.2.3.3 BRW:

The means and standard deviations of 1-D K-S statistics for the BRW simulations are shown in Table 4.8. The preferred parameters which give the best fits to the data samples are: $p = 2.001$, $t_{bs} = 10^3$ yr and $r_{hs} = 1$ kpc. The preferred small injection index (p) makes the model "very leaky". The slow break time (t_{bs}) is smaller, implying the radiating particles leave the hotspot at a faster rate. Both these preferred trends support a more efficient acceleration mechanism of the particles at the hotspot. A smaller hotspot size (r_{hs}) would also allow the particles to leave the hotspot faster. These changes compensate for the smaller value of T_{MaxAge} and higher value of x.

8.2.3.4 MK:

The MK model's relevant 1-D K-S combined probability's means and standard deviations are given in Table 4.9. The best fits to the data samples are obtained by the parameter variations $\gamma_{max(hs)} = 3 \times 10^8$, $\beta = 1.6$ and $\gamma_{min(hs)} = 7$. The preferred maximum Lorentz factor of radiating particles at the hotspots ($\gamma_{max(hs)}$) is higher, and the minimum Lorentz factor ($\gamma_{min(hs)}$) is lower. This indicates that the powerful radiating particles are accelerated to even higher energies by some energetic process in the hotspots, while at the same time particles with lower Lorentz factors also con-

tribute to the total emitted power. The higher ambient medium density power law index of (β), implies that the external environment density falls slightly more steeply. Again, these parameter variations compensate for having more low power sources (higher x) and shorter maximum lifetimes.

8.2.4 1-D K-S Statistic Trends

Our key conclusion is somewhat disappointing. Despite investigating a wide range of parameters (of the original and modified models) we find that no existing model, nor any of the modifications investigated, give excellent fits to all the data simultaneously. However, from the statistical test results, the KDA model appears to give better fits than do the BRW or MK models.

Explicitly judging the original models from the 1-D K-S test results, the MK model frequently produces acceptable statistics for P, z and D. The KDA simulations also often give adequate 1-D K-S statistics. The BRW simulations do not give as good K-S statistics as do the MK and KDA models. After incorporating the 10 kpc linear size cut-off the 1-D K-S statistics for some BRW models improve, but are still not as good as those given by the other two models.

We note the following trends by comparing all the 6 models (the 3 original and the 3 modified) with respect to the 1-D K-S test results they produce. The KDA, MK, BRW-modified and MK-modified models all perform comparably in terms of producing high values of total 1-D K-S probabilities, $\mathcal{P}_{[P,D,z,\alpha]}$ and $\mathcal{P}_{[P,2D,z,\alpha]}$. Considering the "acceptable" parameter variations from Tables 4.7, 4.9, 5.9 and 5.10 the following conclusions can be drawn. Most of the mean $\mathcal{P}_{[P,D,z,\alpha]}$ values are in the range 1.5 – 2.0. The mean $\mathcal{P}_{[P,2D,z,\alpha]}$ values are generally within 2.0 – 2.5, but they have greater standard deviations, and in some cases go to 1.7 or 3.0.

The KDA-modified model is slightly behind the models discussed in the previous paragraph in terms of total $\mathcal{P}_{[P,D,z,\alpha]}$ and $\mathcal{P}_{[P,2D,z,\alpha]}$. From Table 5.8, the four random runs of the "default" KDA-modified model produce

$$\text{Mean}\left(\mathcal{P}_{[P,D,z,\alpha]}\right) = 1.77, \qquad \text{Mean}\left(\mathcal{P}_{[P,2D,z,\alpha]}\right) = 2.21. \tag{8.1}$$

The original BRW model gives the least acceptable 1-D K-S combined probabilities (from Table 4.8), when compared to BRW-modified and the other models. Its mean $\mathcal{P}_{[P,D,z,\alpha]}$ ranges between 0.5 – 1.0, and the mean $\mathcal{P}_{[P,2D,z,\alpha]}$ within 0.7 – 1.2.

The primary modification done to the models, the incorporation of a growing hotspot size or axial ratio in them, produced the following major changes. The preliminary statistical results are substantially better for the BRW-modified model than for the original BRW; the total 1-D K-S probability is better by $\sim 4\sigma$ in the default case, and by $\sim 2.5\sigma$ in the "best-fit" case, of BRW-modified when compared to BRW. Also in BRW-modified, the 1-D K-S probabilities for spectral indices are sometimes better (especially for 7C) and in few cases $\rightarrow 0.01$, for which the fit is not firmly rejected. The MK-modified and KDA-modified models produced 1-D K-S fitting statistics which were slightly better than or comparable to the original MK and KDA model results.

8.2.5 Additional Statistical Tests

The 2-D K-S test results indicate that the "varied" cases of most of the original and modified models (Section 4.9.2 and 5.5.2) can produce adequate fits (as determined by higher values of the K-S probabilities) to the [P–z], [P–D] and [z–D] planes. All (or a good majority) of the non-α 2-D $\mathcal{P}$'s of the "varied" cases are higher than those of the default versions of all the models. As both the 1-D and 2-D K-S statistics point to the same direction, we can be somewhat confident that the "varied" models based on 1-D K-S tests are indeed better fits. Any of the 2-D planes involving α cannot be fit by any of the original or modified models (similar to the worse 1-D fits for α). The α-related 2-D K-S probabilities are ≤ 0.01 for all the models.

Sorting the models in order of the number of non-α 2-D $\mathcal{P}$'s greater than any other model (with the best one first) we find: KDA, MK, MK-modified, KDA-modified, BRW-modified, BRW.

From the 3- and 4-variable Spearman partial rank correlation coefficient analyses on the combined data of the 3 surveys, we see that the KDA models (both original and modified) can match the survey data correlations very closely (at least for P, D and z). Some matches to the real data correlations are acceptable for the original and modified BRW models; they are less good for the MK and MK-modified models. Some models (especially MK) sometimes produce correlations with opposite signature than are observed in the data.

We conclude that the KDA models fit the bulk of the data correlations most closely, followed by BRW, and finally MK. The BRW-modified model provides the best fit to the 4-variable P–D correlation, $r_{PD,z\alpha}$. This indicates that the BRW

model with a growing hotspot is able to reproduce the P–D evolution (seen most prominently in 3C survey data) better than any other model.

8.2.6 Common trends in the $[P–D–z]$ Planes

We now discuss some overall general trends in the slices of the $[P–D–z]$ planes which are present both in the real observational data and in the simulation results for more or less all the surveys.

In the $[P–z]$ plane, the sources lie above a curve determined by the limiting flux of a survey. This happens due to trivial cosmological arguments since sources selected in a survey must have their luminosities above the flux-limit, i.e., must have their monochromatic powers larger than a minimum limiting value. The higher the redshift of a source, the farther back in cosmic time we are looking into, and further away the source is from Earth. The same limiting flux corresponds to increasingly higher specific powers at higher redshifts, because of the cosmological flux-luminosity relation (Equations 3.10 and 3.14). Considering a constant observed flux ($S_\nu(\nu_0)$ in Equation 3.10), the higher the redshift of a source, the larger the cosmological distance factor $\left[(R_0 r)^2 (1+z)\right]$ becomes, which increases the specific power $P_\nu([1+z]\nu_0)$ corresponding to it. So to be above the same flux-limit, the sources at higher redshifts must be more powerful. This brings in the strong P–z correlation.

In addition to the cosmological P–z correlation, another factor makes some contribution to the plane. The high redshift sources undergo more severe energy losses as detailed in the next two paragraphs, which cause the emitted power of high-z sources to fall at a faster rate. Hence in order to be detected at the same flux limit the higher redshift sources must be more and more powerful.

The trends in the $[P–D]$ and $[D–z]$ planes described next are most prominent in the 3C survey (data and simulations). These trends are manifestations of the P–z correlation and the "youth-redshift degeneracy" (discussed in Sections 4.1 and 4.9.3).

There is a D–z evolution, an anti-correlation actually, where D decreases as z of the sources increase. As evident from the $[P–D]$ tracks, the high-z sources show a very steeper decline of their specific powers with age than the low-z sources. The higher the redshift of a source, the more severe energy loss it undergoes (by IC scatering off the CMB and adiabatic expansion losses in the lobes), and thus its output falls below the limiting survey flux at an earlier age, when it was smaller in size. We can only detect these high-z sources at younger ages, for as long as they are still above

the limiting survey flux. So the high-z sources we detect in a flux-limited survey are actually younger and hence smaller, yielding the "linear size evolution" seen in the [D–z] plane.

In the [P–D] plane there is an anti-correlation whereby P decreases as D gets higher. This can be explained due to a combination of the P–z and D–z trends, discussed before, which is a manifestation of the P–z correlation and the "youth -redshift degeneracy". Low-power sources are actually more easily seen at lower redshifts, which allows us to see larger sources.

The sources in the model simulations almost always possessed too steep spectra. Any of the planes involving spectral index presented a very sharp cut-off in α. The α's were always > 0.6 for KDA and BRW models, and > 0.9 for MK models. A majority number of simulated sources in most of the models pile up near the lower limit of the α range; however, in the observational data a majority of sources are concentrated in the middle of the α range which they span.

Sources with $\alpha < 0.5$ in the real 3CRR, 6CE and 7CRS surveys probably include significant contributions from relativistically Doppler boosted core and inner jet components. Such flat-spectrum quasars have central components which arise from superpositions of synchrotron self-absorbed emission from different parts of the inner relativistic jet (e.g., Jarvis & McLure 2006, and references therein). As these models do not take into account the beamed core/jet emission, they cannot reproduce the flat spectra of such sources.

8.3 Relevant Volume Fraction

A major goal of my thesis work has been to calculate what fraction of the "relevant universe" or the large-scale filament-structured WHIM volume does the radio galaxies born over the quasar era cumulatively occupy. From our simulations we found that quite a wide range of relevant volume filling factors can be produced by the allowed range in the model parameters.

For the default and 1-D K-S "best-fit" cases of the models the cumulative volume filling fraction of several generations of radio galaxies varied within $\sim 2 - 7\%$. These filling factors are significantly smaller values than the preliminary qualitative estimate of Gopal-Krishna & Wiita (2001). Using the default parameters of the BRW model, GKW01 claimed the relevant fraction to be $\sim 50\%$. We discussed some of the possible

sources of discrepancy between these two investigations in Section 7.4.

For certain choices of parameter variations of some models, our simulations also produced relevant volume filling factor values as high as $\sim$ 20% and 50%. Recall that Equation (7.10) used $R_T = 5$, which is a conservative high value; if $R_T \simeq 1.3$, then the RG volumes and hence these relevant volume fractions are multiplied by $(5/1.3)^2 = 14.8$.

Hence, on our way to test the robustness of the preliminary exciting idea of substantial cosmological impact of RGs on large scale structures in the universe, we conclude the following. The expanding radio galaxies born during the quasar era play modest to significant roles in the cosmological history of the universe. We could not confidently verify the overwhelming impact of RGs as was claimed in Gopal-Krishna & Wiita (2001), since we obtained smaller volume filling factors as compared to GKW01 for our favored parameter sets.

8.4 Limitations of the Models

There are several observational features (including trends in the [P–D–z–α] planes of the data samples) that cannot be explained by any models considered so far. The [P–D] diagram for the 3CRR data (Figure 3.1a) shows a clear anti-correlation with large scatter. Another interesting feature is the clump of sources in the 6CE (Figure 3.1b) [P–D] diagram near $D \sim 100$ kpc, $P_{151} \sim 27.5$ W Hz^{-1} sr^{-1} (Neeser et al. 1995). Neither of these features involving P–D trends is reproduced in the models. The KDA and MK model simulations (e.g., Figures 4.2, 4.4, 4.5 and 4.7) predict too many very large $D > 1$ Mpc and powerful sources (more in 3C, some in 7C), which are not present in the data. Such limiting features of the models had been discussed in Kaiser & Alexander (1999a).

The BRW 1-D $\mathcal{P}(D)$ were very low for many cases, especially for 3C (from Tables 4.2, 4.5 and 4.8). Also, the BRW [P–D] diagrams for all 3 simulated surveys showed too strong a P–D anti-correlation (e.g., Figures 4.3 and 4.6). This arises because the BRW model simulations produce too many small but powerful sources. A possible explanation of this problem could be the presence of synchrotron self-absorption of the radiation emitted by such small powerful sources, which is not included in the BRW model. Such small sources should fall below the survey flux limit and hence not be detected at a survey frequency of 151 MHz. Including this

effect could improve the relative performance of the BRW model.

An important point to remember is that all the three main models of radio lobe power evolution considered here (KDA, BRW and MK, Chapter 2) are incomplete. They do not yet incorporate enough physics to predict the complete physical conditions prevailing in FR II radio sources, their environments and evolution.

Consideration of additional factors involving extra physics may be necessary in these models. Some of the possible conditions that could be present in the radio sources and their surroundings, and needs to be accounted in the models, are as follows. First, the environmental density (ρ, Section 2.2) could vary with redshift and it must eventually deviate from its power law behavior (Equation 2.1) with distance. The beam power (Q_0) distribution (Equation 3.9) might vary with redshift and the maximum lifetime of AGN activity T_{MaxAge} (Section 3.1.1), could vary with redshift and jet power. Also, the birth function of radio sources with redshift (Equation 3.6) could have a greater variation with luminosity. This RLF should be computed more accurately for a more efficient investigation of such models.

8.5 Suggestions for Future Work

8.5.1 Theoretical

The primary aim of my thesis work was to compare the performances of the radio lobe dynamical and power evolution models and eventually to develop a model, which is a good fit to all the observational data. We have proceeded somewhat toward our goal, whereby we have quantitatively compared the model performances, found reasonable fits for $[P, D, z]$ of the observational data, and have modified the models to find improved fits. But modeling the spectral index behavior has remained elusive. Suitably modifying the models to also get an acceptable α fit will be a very important step forward for such RG evolution studies.

Some possibilities of more future explorations are given in the following. The work can be extended by allowing redshift variations in the environmental density profile (in particular, allow for variations of ρ_0, a_0 and β with cosmic epoch). It should be checked to see if such modified models perform substantially better in fitting the observations.

We can explore more sophisticated models where the jets first propagate through ambient media halos with evolving central densities, and at radial distance scales

~ 100 kpc eventually enter the IGM whose constant density (in space) is also evolving with redshift (Gopal-Krishna & Wiita 1987, 1991). If we compare the resulting distributions of RG sizes, powers and redshifts against observational surveys, then we can simultaneously constrain the range of evolutionary models for both the IGM and the radio source population. Barai et al. (2004) gives preliminary work on the implications of the volumes attained by radio sources considering cosmological evolution of the environmental gas density.

Recently Blundell et al. (2006) provided observational evidence for the discovery of low-energy cutoff of particle acceleration in the lobe of a giant FR II RG. They obtained a value of $\gamma_{min(hs)} \sim 10^4$ as the minimum Lorentz factor of particles in the hotspot. This is substantially higher than the default value in the three main models where $\gamma_{min(hs)} = 1 - 10$. Investigating the models using such tentatively observationally supported higher $\gamma_{min(hs)}$ in them will be a worthwhile venture.

In a recent study Kawakatu & Kino (2006) described the dynamical evolution of the hotspots of radio loud AGN, where the evolution of some properties, namely velocity, pressure, and mass density, were investigated. Their model well reproduced the whole evolution of relativistic jets, when compared with two-dimensional hydrodynamic simulations. Incorporating such dynamically evolving hotspots into the models of radio lobe power evolution analysed in this thesis would be an interesting modification to the models worth exploring.

A potential indicator which can provide an excellent test of whether RGs do really trigger galaxy formation, is the estimation of the 3-point correlation function between radio galaxies in large scale galaxy (redshift) surveys (e.g., Borderia et al. 1991). If our RG impact scenario is robust, then there should be a bias in this correlation function along the direction of radio lobes of the RGs. This will happen because more galaxies are formed along the radio-axis triggered by jet/lobe expansion, as compared to directions perpendicular to the radio-jet.

8.5.2 Observational

The models investigated in this thesis predict the power from the radio lobes only. A natural extension involves the question whether the same models also fit deeper radio catalogs if we take into account the relativistically Doppler boosted core/jet emission. By incorporating the beamed core emission, investigations of simulations of large scale radio surveys containing many thousands of sources, can be done. Some such deep

surveys are Faint Images of the Radio Sky at Twenty-cm, FIRST (Becker et al. 1995), the Westerbork Northern Sky Survey, WENSS (Rengelink et al. 1997) and the NRAO VLA Sky Survey, NVSS (Condon et al. 1998), which can be made adequately complete in redshift through optical identifications (Ivezić et al. 2004) from Sloan Digital Sky Survey, SDSS (York et al. 2000). If simulations can be performed to predict thousands of sources, the possibility of successfully incorporating a multi-dimensional statistical test becomes more viable (as mentioned in Section 3.4.4).

To support or refute our favored picture that RGs do have a substantial impact on global star formation and even the large scale structure of the universe, several potential observational advancements should prove useful. Observation of giant radio galaxies (RGs with projected linear sizes > 1 Mpc) at low frequencies using the Giant Metrewave Radio Telescope (GMRT) (e.g., Konar et al. 2003) is important, in order to explore the structures of RGs and their interactions with the environment in the very large scales.

Still more vital input is expected from upcoming low frequency radio telescope LOFAR (Low Frequency ARray), which holds the potential of observing many high-z RGs and, especially, the fading giant RGs at $z > 1$ (e.g., Röttgering 2003). The Atacama Large Millimeter Array (ALMA) holds substantial promise (e.g., Tarenghi & Wilson 2005). It will bring to millimeter and sub-millimeter astronomy the aperture synthesis techniques of radio astronomy, which enable precision imaging to be done on sub-arcsecond angular scales. It can probe RGs forming billions of years ago when galaxies were very young.

The largest proposed radio telescope, the Square Kilometre Array (SKA), is a big international collaboration, which may revolutionize radio astronomy in the next few decades (e.g., van Driel 2005). SKA will be much larger and more sensitive than the present generation of radio telescopes. It is hoped it will give us crucial information about the formation and evolution of the first radio galaxies in the universe.

References

Achterberg, A., Gallant, Y. A., Kirk, J. G., & Guthmann, A. W. 2001, MNRAS, 328, 393

Adelberger, K. L., Shapley, A. E., Steidel, C. C., Pettini, M., Erb, D. K., & Reddy, N. A. 2005, ApJ, 629, 636

Aguirre, A., Schaye, J., Kim, T.-S., Theuns, T., Rauch, M., & Sargent, W. L. W. 2004, ApJ, 602, 38

Ajiki, M. et al. 2006, PASJ, 58, 499

Anastasiadis, A., & Vlahos, L. 1993, A&A, 275, 427

Antonucci, R. 1993, ARA&A, 31, 473

Antonucci, R. R. J., & Ulvestad, J. S. 1985, ApJ, 294, 158

Aracil, B., Tripp, T. M., Bowen, D. V., Prochaska, J. X., Chen, H.-W., & Frye, B. L. 2006, MNRAS, 367, 139

Archibald, E. N., Dunlop, J. S., Hughes, D. H., Rawlings, S., Eales, S. A., & Ivison, R. J. 2001, MNRAS, 323, 417

Baldwin, J. E. 1982, in IAU Symp. 97: Extragalactic Radio Sources, ed. D. S. Heeschen & C. M. Wade (Dordrecht: D. Reidel Publishing Co.), 21–24

Barai, P., Gopal-Krishna, Osterman, M. A., & Wiita, P. J. 2004, Bull. Astron. Soc. India, 32, 385

Barger, A. J., Cowie, L. L., Bautz, M. W., Brandt, W. N., Garmire, G. P., Hornschemeier, A. E., Ivison, R. J., & Owen, F. N. 2001, AJ, 122, 2177

Barthel, P. D. 1987, in Superluminal Radio Sources, ed. J. A. Zensus & T. J. Pearson (Cambridge: Cambridge University Press), 148–154

Barthel, P. D. 1989, ApJ, 336, 606

Barthel, P. D. 1994, in ASP Conf. Ser. 54: The Physics of Active Galaxies, ed. G. V. Bicknell, M. A. Dopita, & P. J. Quinn (San Francisco: Astronomical Society of the Pacific), 175–186

Baum, S. A., Heckman, T. M., Bridle, A., van Breugel, W. J. M., & Miley, G. K. 1988, ApJS, 68, 643

Becker, R. H., White, R. L., & Helfand, D. J. 1995, ApJ, 450, 559

Begelman, M. C., Blandford, R. D., & Rees, M. J. 1984, Rev. Mod. Phys., 56, 255

Begelman, M. C., & Cioffi, D. F. 1989, ApJ, 345, L21

Begelman, M. C., & Kirk, J. G. 1990, ApJ, 353, 66
Bell, A. R. 1978, MNRAS, 182, 147
Bertone, S., Vogt, C., & Enßlin, T. 2006, MNRAS, 602
Best, P. N., Longair, M. S., & Röttgering, H. J. A. 1996, MNRAS, 280, L9
Bicknell, G. V., Sutherland, R. S., van Breugel, W. J. M., Dopita, M. A., Dey, A., & Miley, G. K. 2000, ApJ, 540, 678
Blain, A. W., Smail, I., Ivison, R. J., & Kneib, J.-P. 1999, MNRAS, 302, 632
Blandford, R. D., & Konigl, A. 1979, ApJ, 232, 34
Blandford, R. D., & Rees, M. J. 1974, MNRAS, 169, 395
Blandford, R. D., & Rees, M. J. 1978, Phys. Scr, 17, 265
Blundell, K. M., Fabian, A. C., Crawford, C. S., Erlund, M. C., & Celotti, A. 2006, ApJ, 644, L13
Blundell, K. M., & Rawlings, S. 1999, Nature, 399, 330
Blundell, K. M., & Rawlings, S. 2000, AJ, 119, 1111
Blundell, K. M., Rawlings, S., & Willott, C. J. 1999, AJ, 117, 677 (BRW)
Borderia, M. J. P., Iovino, A., & Bonometto, S. A. 1991, AJ, 102, 495
Bouwens, R., & Illingworth, G. 2006, New A Rev., 50, 152
Bridle, A. H., & Perley, R. A. 1984, ARA&A, 22, 319
Brown, R. H., & Hazard, C. 1951, MNRAS, 111, 357
Browne, I. W. A. 1983, MNRAS, 204, 23P
Burbidge, G. R. 1956, ApJ, 124, 416
Burns, J. O., Norman, M. L., & Clarke, D. A. 1991, Science, 253, 522
Canizares, C. R., Fabbiano, G., & Trinchieri, G. 1987, ApJ, 312, 503
Carilli, C. L., Perley, R. A., Dreher, J. W., & Leahy, J. P. 1991, ApJ, 383, 554
Carroll, S. M., Press, W. H., & Turner, E. L. 1992, ARA&A, 30, 499
Carvalho, J. C., & O'Dea, C. P. 2002, ApJS, 141, 337
Cen, R., & Ostriker, J. P. 1999, ApJ, 514, 1
Cen, R., & Ostriker, J. P. 2006, preprint: astro-ph/0601008
Cen, R., Tripp, T. M., Ostriker, J. P., & Jenkins, E. B. 2001, ApJ, 559, L5
Chambers, K. C., Miley, G. K., & Joyce, R. R. 1988a, ApJ, 329, L75
Chambers, K. C., Miley, G. K., & van Breugel, W. J. M. 1988b, ApJ, 327, L47
Chokshi, A. 1997, ApJ, 491, 78
Cioffi, D. F., & Blondin, J. M. 1992, ApJ, 392, 458
Condon, J. J., Cotton, W. D., Greisen, E. W., Yin, Q. F., Perley, R. A., Taylor,

G. B., & Broderick, J. J. 1998, AJ, 115, 1693
Connolly, A. J., Szalay, A. S., Dickinson, M., Subbarao, M. U., & Brunner, R. J. 1997, ApJ, 486, L11
Daly, R. A. 1990, ApJ, 355, 416
Davé, R. et al. 2001, ApJ, 552, 473
De Young, D. S. 1989, ApJ, 342, L59
Dey, A., van Breugel, W., Vacca, W. D., & Antonucci, R. 1997, ApJ, 490, 698
Dietrich, M., Hamann, F., Shields, J. C., Constantin, A., Heidt, J., Jäger, K., Vestergaard, M., & Wagner, S. J. 2003, ApJ, 589, 722
Dunlop, J. S., & Peacock, J. A. 1990, MNRAS, 247, 19
Eales, S. A. 1985, MNRAS, 217, 149
Fall, S. M., & Rees, M. J. 1985, ApJ, 298, 18
Falle, S. A. E. G. 1991, MNRAS, 250, 581
Fanaroff, B. L., & Riley, J. M. 1974, MNRAS, 167, 31P
Fanti, C., Fanti, R., Dallacasa, D., Schilizzi, R. T., Spencer, R. E., & Stanghellini, C. 1995, A&A, 302, 317
Fasano, G., & Franceschini, A. 1987, MNRAS, 225, 155
Forman, W., Jones, C., & Tucker, W. 1985, ApJ, 293, 102
Fragile, P. C., Anninos, P., Gustafson, K., & Murray, S. D. 2005, ApJ, 619, 327
Fragile, P. C., Murray, S. D., Anninos, P., & van Breugel, W. 2004, ApJ, 604, 74
Furlanetto, S. R., & Loeb, A. 2001, ApJ, 556, 619
Garrington, S. T., & Conway, R. G. 1991, MNRAS, 250, 198
Gieseler, U. D. J., & Jones, T. W. 2000, A&A, 357, 1133
Goodlet, J.-A. 2006, preprint (PhD Thesis): astro-ph/0602374
Gopal-Krishna, Kulkarni, V. K., & Wiita, P. J. 1996, ApJ, 463, L1
Gopal-Krishna, & Wiita, P. J. 1987, MNRAS, 226, 531
Gopal-Krishna, & Wiita, P. J. 1991, ApJ, 373, 325
Gopal-Krishna, & Wiita, P. J. 2001, ApJ, 560, L115 (GKW01)
Gopal-Krishna, & Wiita, P. J. 2003a, Bull. Astron. Soc. India, 31, 215
Gopal-Krishna, & Wiita, P. J. 2003b, in ASP Conf. Ser. 300: Radio Astronomy at the Fringe, ed. J. A. Zensus, M. H. Cohen, & E. Ros (San Francisco: Astronomical Society of the Pacific), 293–300
Gopal-Krishna, Wiita, P. J., & Barai, P. 2004, J. Korean Astron. Soc., 37, 517
Gopal-Krishna, Wiita, P. J., & Osterman, M. A. 2003, in ASP Conf. Ser. 290: Active

Galactic Nuclei: From Central Engine to Host Galaxy, ed. S. Collin, F. Combes, & I. Shlosman (San Francisco: Astronomical Society of the Pacific), 319–322

Gopal-Krishna, Wiita, P. J., & Saripalli, L. 1989, MNRAS, 239, 173

Greve, T. R., Ivison, R. J., & Stevens, J. A. 2006, Astron. Nachr., 327, 208

Grimes, J. A., Rawlings, S., & Willott, C. J. 2004, MNRAS, 349, 503

Heavens, A. F., & Drury, L. O. 1988, MNRAS, 235, 997

Hogg, D. W. 1999, preprint: astro-ph/9905116

Holmström, L., Sain, S. R., & Miettinen, H. E. 1995, Comput. Phys. Commun., 88, 195

Hooda, J. S., Mangalam, A. V., & Wiita, P. J. 1994, ApJ, 423, 116

Hooda, J. S., & Wiita, P. J. 1998, ApJ, 493, 81

Hopkins, P. F., Richards, G. T., & Hernquist, L. 2006, preprint, submitted to ApJ: astro-ph/0605678

Ivezić, Ž. et al. 2004, in Multiwavelength AGN Surveys, ed. R. Mújica & R. Maiolino (Singapore: World Scientific Publishing Company), 53–56

Jackson, C. A., & Wall, J. V. 1999, MNRAS, 304, 160

Jarvis, M. J., & McLure, R. J. 2006, MNRAS, 369, 182

Jenkins, C. J., Pooley, G. G., & Riley, J. M. 1977, MmRAS, 84, 61

Jennison, R. C., & Das Gupta, M. K. 1953, Nature, 172, 996

Jeyakumar, S., & Saikia, D. J. 2000, MNRAS, 311, 397

Kaiser, C. R. 2000, A&A, 362, 447

Kaiser, C. R., & Alexander, P. 1997, MNRAS, 286, 215 (KA)

Kaiser, C. R., & Alexander, P. 1999a, MNRAS, 302, 515

Kaiser, C. R., & Alexander, P. 1999b, MNRAS, 305, 707

Kaiser, C. R., Dennett-Thorpe, J., & Alexander, P. 1997, MNRAS, 292, 723 (KDA)

Kapahi, V. K. 1975, MNRAS, 172, 513

Kapahi, V. K. 1985, MNRAS, 214, 19P

Kawakatu, N., & Kino, M. 2006, in press in MNRAS: astro-ph/0605482

Kirk, J. G., Guthmann, A. W., Gallant, Y. A., & Achterberg, A. 2000, ApJ, 542, 235

Komissarov, S. S., & Falle, S. A. E. G. 1998, MNRAS, 297, 1087

Konar, C., Saikia, D. J., Ishwara-Chandra, C. H., & Kulkarni, V. K. 2003, Bull. Astron. Soc. India, 31, 437

Kronberg, P. P., Dufton, Q. W., Li, H., & Colgate, S. A. 2001, ApJ, 560, 178

Kronberg, P. P., Lesch, H., & Hopp, U. 1999, ApJ, 511, 56

Kundt, W. 2002, New A Rev., 46, 257

Lacy, M., Rawlings, S., Hill, G. J., Bunker, A. J., Ridgway, S. E., & Stern, D. 1999, MNRAS, 308, 1096

Laing, R. A., Riley, J. M., & Longair, M. S. 1983, MNRAS, 204, 151

Leahy, J. P. 1991, Beams and Jets in Astrophysics, ed. P. A. Hughes, Cambridge Astrophysics Series, No. 19 (Cambridge: Cambridge University Press), 119

Leahy, J. P., Muxlow, T. W. B., & Stephens, P. W. 1989, MNRAS, 239, 401

Ledlow, M. J., & Owen, F. N. 1996, AJ, 112, 9

Legg, T. H. 1970, Nature, 226, 65

Levine, R., & Gnedin, N. Y. 2005, ApJ, 632, 727

Lilly, S. J., Le Fevre, O., Hammer, F., & Crampton, D. 1996, ApJ, 460, L1

Lind, K. R., Payne, D. G., Meier, D. L., & Blandford, R. D. 1989, ApJ, 344, 89

Longair, M. S., Ryle, M., & Scheuer, P. A. G. 1973, MNRAS, 164, 243

Loudin, J. 2003, in PHYSTAT 2003: Statistical Problems in Particle Physics, Astrophysics, and Cosmology, ed. L. Lyons, R. Mount, & R. Reitmeyer (Stanford: SLAC-R-703, eConf C030908), 207–210

Machalski, J., Chyzy, K. T., & Jamrozy, M. 2004a, Acta Astronomica, 54, 249

Machalski, J., Chyzy, K. T., & Jamrozy, M. 2004b, Acta Astronomica, 54, 391

Macklin, J. T. 1982, MNRAS, 199, 1119

Madau, P., Pozzetti, L., & Dickinson, M. 1998, ApJ, 498, 106

Manolakou, K., Anastasiadis, A., & Vlahos, L. 1999, A&A, 345, 653

Manolakou, K., & Kirk, J. G. 2002, A&A, 391, 127 (MK)

Marconi, A., Risaliti, G., Gilli, R., Hunt, L. K., Maiolino, R., & Salvati, M. 2004, MNRAS, 351, 169

Marcowith, A., & Kirk, J. G. 1999, A&A, 347, 391

McCarthy, P. J., van Breugel, W. J. M., Spinrad, H., & Djorgovski, S. 1987, ApJ, 321, L29

McGilchrist, M. M., Baldwin, J. E., Riley, J. M., Titterington, D. J., Waldram, E. M., & Warner, P. J. 1990, MNRAS, 246, 110

McLure, R. J., & Dunlop, J. S. 2004, MNRAS, 352, 1390

Mellema, G., Kurk, J. D., & Röttgering, H. J. A. 2002, A&A, 395, L13

Miley, G. K. 1971, MNRAS, 152, 477

Miley, G. K., Chambers, K. C., van Breugel, W. J. M., & Macchetto, F. 1992, ApJ, 401, L69

Miley, G. K. et al. 2004, Nature, 427, 47

Miller, C. J., Nichol, R. C., Gómez, P. L., Hopkins, A. M., & Bernardi, M. 2003, ApJ, 597, 142

Mukhopadhyay, B., & Chakrabarti, S. K. 2000, A&A, 353, 1029

Mulchaey, J. S., & Zabludoff, A. I. 1998, ApJ, 496, 73

Neeser, M. J., Eales, S. A., Law-Green, J. D., Leahy, J. P., & Rawlings, S. 1995, ApJ, 451, 76

Nesvadba, N. P. H., Lehnert, M. D., Eisenhauer, F., Gilbert, A., Tecza, M., & Abuter, R. 2006, in press in ApJ: astro-ph/0606530

Norman, M. L., Winkler, K.-H. A., Smarr, L., & Smith, M. D. 1982, A&A, 113, 285

Oort, M. J. A., Katgert, P., & Windhorst, R. A. 1987, Nature, 328, 500

Orr, M. J. L., & Browne, I. W. A. 1982, MNRAS, 200, 1067

Overzier, R. A. et al. 2006, ApJ, 637, 58

Owen, F. N., & White, R. A. 1991, MNRAS, 249, 164

Padovani, P., & Urry, C. M. 1991, ApJ, 368, 373

Padovani, P., & Urry, C. M. 1992, ApJ, 387, 449

Peacock, J. A. 1983, MNRAS, 202, 615

Peacock, J. A. 1987, in NATO ASIC Proc. 208: Astrophysical Jets and their Engines, ed. W. Kundt (Dordrecht: D. Reidel Publishing Co.), 185–196

Peacock, J. A. 1999, Cosmological Physics (Cambridge: Cambridge University Press)

Pérez-González, P. G. et al. 2005, ApJ, 630, 82

Perley, R. A., Dreher, J. W., & Cowan, J. J. 1984, ApJ, 285, L35

Peterson, B. M. 1997, An Introduction to Active Galactic Nuclei (Cambridge: Cambridge University Press)

Pieri, M., Martel, H., & Grenon, C. 2006a, preprint, submitted to ApJ: astro-ph/0606423

Pieri, M. M., Schaye, J., & Aguirre, A. 2006b, ApJ, 638, 45

Porciani, C., & Madau, P. 2005, ApJ, 625, L43

Press, W. H., Teukolsky, S. A., Vetterling, W. T., & Flannery, B. P. 1992, Numerical Recipes in C, 2nd Ed. (Cambridge: Cambridge University Press), 645

Prochaska, J. X., Weiner, B. J., Chen, H.-W., & Mulchaey, J. S. 2006, ApJ, 643, 680

Rawlings, S., Eales, S. A., & Lacy, M. 2001, MNRAS, 322, 523

Rawlings, S., & Jarvis, M. J. 2004, MNRAS, 355, L9

Rawlings, S., Willott, C. J., Hill, G. J., Archibald, E. N., Dunlop, J. S., & Hughes,

D. H. 2004, MNRAS, 351, 676
Rees, M. J. 1971, Nature, 229, 312
Rees, M. J. 1989, MNRAS, 239, 1P
Rees, M. J., & Setti, G. 1968, Nature, 219, 127
Rengelink, R. B., Tang, Y., de Bruyn, A. G., Miley, G. K., Bremer, M. N., Röttgering, H. J. A., & Bremer, M. A. R. 1997, A&AS, 124, 259
Rosen, A., & Wiita, P. J. 1988, ApJ, 330, 16
Röttgering, H. 2003, New A Rev., 47, 405
Ryu, D., Kang, H., & Biermann, P. L. 1998, A&A, 335, 19
Sarazin, C. L. 1988, X-ray emission from Clusters of Galaxies (Cambridge: Cambridge University Press)
Sawicki, M., & Thompson, D. 2006a, ApJ, 642, 653
Sawicki, M., & Thompson, D. 2006b, in press in ApJ: astro-ph/0605406
Saxton, C. J., Bicknell, G. V., Sutherland, R. S., & Midgley, S. 2005, MNRAS, 359, 781
Schaye, J., & Aguirre, A. 2005, in IAU Symposium 228, ed. V. Hill, P. François, & F. Primas (Cambridge: Cambridge University Press), 557–568
Schaye, J., Aguirre, A., Kim, T.-S., Theuns, T., Rauch, M., & Sargent, W. L. W. 2003, ApJ, 596, 768
Scheuer, P. A. G. 1974, MNRAS, 166, 513
Scheuer, P. A. G. 1982, in IAU Symp. 97: Extragalactic Radio Sources, ed. D. S. Heeschen & C. M. Wade (Dordrecht: D. Reidel Publishing Co.), 163–165
Scheuer, P. A. G. 1987, in Superluminal Radio Sources, ed. J. A. Zensus & T. J. Pearson (Cambridge: Cambridge University Press), 104–113
Scheuer, P. A. G., & Readhead, A. C. S. 1979, Nature, 277, 182
Scheuer, P. A. G., & Williams, P. J. S. 1968, ARA&A, 6, 321
Shapley, A. E., Erb, D. K., Pettini, M., Steidel, C. C., & Adelberger, K. L. 2004, ApJ, 612, 108
Shklovskii, I. S. 1963, Soviet Ast., 6, 465
Silk, J. 2005, MNRAS, 364, 1337
Soltan, A. M. 2006, preprint: astro-ph/0604465
Spergel, D. N. et al. 2006, preprint, submitted to ApJ: astro-ph/0603449
Spergel, D. N. et al. 2003, ApJS, 148, 175
Spruit, H. C. 1988, A&A, 194, 319

Steidel, C. C., Adelberger, K. L., Giavalisco, M., Dickinson, M., & Pettini, M. 1999, ApJ, 519, 1

Tarenghi, M., & Wilson, T. L. 2005, in EAS Publications Series 15: Radio Astronomy from Karl Jansky to Microjansky, ed. L. I. Gurvits, S. Frey, & S. Rawlings (Les Ulis Cedex A: EdP-Sciences), 423–430

Tripp, T. M., Aracil, B., Bowen, D. V., & Jenkins, E. B. 2006, ApJ, 643, L77

Tumlinson, J., Shull, J. M., Giroux, M. L., & Stocke, J. T. 2005, ApJ, 620, 95

Ueda, Y., Akiyama, M., Ohta, K., & Miyaji, T. 2003, ApJ, 598, 886

Urry, C. M., & Padovani, P. 1995, PASP, 107, 803

van Driel, W. 2005, in SF2A-2005: Semaine de l'Astrophysique Francaise, ed. F. Casoli, T. Contini, J. M. Hameury, & L. Pagani (Les Ulis Cedex A: EdP-Sciences), 53

Venemans, B. P. et al. 2002, ApJ, 569, L11

Venemans, B. P. et al. 2005, A&A, 431, 793

Venemans, B. P. et al. 2004, A&A, 424, L17

Vernaleo, J. C., & Reynolds, C. S. 2006, ApJ, 645, 83

Viel, M., Branchini, E., Cen, R., Matarrese, S., Mazzotta, P., & Ostriker, J. P. 2003, MNRAS, 341, 792

Wardle, J. F. C., & Aaron, S. E. 1997, MNRAS, 286, 425

Wardle, J. F. C., & Miley, G. K. 1974, A&A, 30, 305

Weinberg, S. 1989, Rev. Mod. Phys., 61, 1

Wiita, P. J., & Norman, M. L. 1992, ApJ, 385, 478

Wiita, P. J., Rosen, A., Gopal-Krishna, & Saripalli, L. 1989, in Hot spots in extragalactic radio sources: Lecture Notes in Physics, ed. K. Meisenheimer & H. J. Roser, Vol. 327 (Berlin: Springer Verlag), 173–178

Willott, C. J., Rawlings, S., Blundell, K. M., Lacy, M., & Eales, S. A. 2001, MNRAS, 322, 536

Willott, C. J., Rawlings, S., Jarvis, M. J., & Blundell, K. M. 2003, MNRAS, 339, 173

York, D. G. et al. 2000, AJ, 120, 1579

Zheng, W. et al. 2006, ApJ, 640, 574

Zirm, A. W. et al. 2005, ApJ, 630, 68

Appendices

– A –

Detailed Original (Previously Published) Model Result Tables

A.1 Original KDA Model

Table A.1: KDA Model Results for Run 1: 1-D K-S Statistics for Parameter Variations [a]

Varied Model Parameter	Survey	Ratio_{3C} Ratio_{6C} Ratio_{7C}	$\mathcal{P}(K\text{–}S)$				$\mathcal{P}_{[P,D,z,\alpha]}$ $\mathcal{P}_{[P,2D,z,\alpha]}$
			$\mathcal{P}(P)$	$\mathcal{P}(D)$	$\mathcal{P}(z)$	$\mathcal{P}(\alpha)$	
Default [b]	3C	1 (2.06) [c]	0.171	0.0183	0.474	3.22e-09	1.77
	6C	0.920	0.583	0.509	0.577	3.66e-10	2.15
	7C	1.38	0.00541	0.0645	0.0121	6.24e-04	
$\beta = 2.02$	3C	1 (1.32)	0.286	3.90e-04	0.312	1.31e-10	1.85
	6C	1.11	0.583	0.173	0.716	1.29e-09	2.25
	7C	1.59	0.00761	0.476	0.0267	0.00525	
$a_0 = 1.5$ kpc	3C	1 (1.22)	0.133	0.0938	0.387	2.04e-18	1.89
	6C	1.06	0.879	0.0432	0.561	1.29e-09	2.29
	7C	1.50	0.0271	0.451	0.0385	4.69e-05	
$\rho_0 = \rho_1$ [d]	3C	1 (1.02)	0.334	0.0373	0.668	1.96e-18	2.09
	6C	1.22	0.879	0.107	0.293	1.29e-09	2.29
	7C	1.55	0.105	0.152	0.0544	3.37e-07	
$\Gamma_B = 5/3$	3C	1 (1.77)	0.161	0.0508	0.387	2.02e-18	2.28
	6C	1.05	0.740	0.501	0.737	1.29e-09	3.06
	7C	1.45	0.00828	0.668	0.0180	4.54e-05	
$\gamma_{min(hs)} = 10$	3C	1 (3.0)	0.197	0.0940	0.192	5.85e-11	1.33
	6C	0.891	0.212	0.509	0.585	3.66e-10	1.75
	7C	1.30	8.11e-04	0.0193	0.00317	6.24e-04	
$\gamma_{max(hs)} = 10^7$	3C	1 (2.63)	0.0938	0.0129	0.192	6.48e-10	2.01
	6C	0.833	0.310	0.915	0.585	3.66e-10	3.17
	7C	1.30	0.00133	0.922	0.00517	0.00134	
$p = 2.12$	3C	1 (2.01)	0.319	0.0178	0.474	2.99e-10	2.01
	6C	0.942	0.583	0.629	0.432	3.66e-10	2.56

Continued on next page ...

Table A.1: continued from previous page ...

Varied Model Parameter	Survey	Ratio_{3C} Ratio_{6C} Ratio_{7C}	$\mathcal{P}(K\text{–}S)$ $\mathcal{P}(P)$	$\mathcal{P}(D)$	$\mathcal{P}(z)$	$\mathcal{P}(\alpha)$	$\mathcal{P}_{[P,D,z,\alpha]}$ $\mathcal{P}_{[P,2D,z,\alpha]}$
	7C	1.40	0.00541	0.232	0.0121	1.87e-05	
$\Gamma_B = 5/3$	3C	1 (2.22)	0.0357	0.0128	0.247	2.89e-15	1.27
$\gamma_{max(hs)} = 10^7$	6C	0.916	0.434	0.371	0.583	1.29e-09	1.61
	7C	1.38	0.00134	0.152	0.00794	4.85e-05	
$\Gamma_B = 5/3$	3C	1 (1.73)	0.209	2.37e-04	0.474	1.37e-16	2.02
$p = 2.12$	6C	1.07	0.740	0.509	0.580	1.29e-09	2.49
	7C	1.46	0.00828	0.251	0.0180	2.92e-09	
$\Gamma_B = 5/3$	3C	1 (0.821)	0.266	0.00248	0.668	7.04e-22	1.86
$\rho_0 = \rho_1$ [d]	6C	1.22	0.583	0.107	0.413	1.29e-09	1.95
	7C	1.68	0.139	0.0343	0.0758	2.25e-10	
$\gamma_{max(hs)} = 10^7$	3C	1 (2.79)	0.0930	0.274	0.192	7.35e-15	1.39
$p = 2.12$	6C	0.870	0.317	0.259	0.583	3.66e-10	1.92
	7C	1.33	8.21e-04	0.152	0.00495	0.00127	
$\gamma_{max(hs)} = 10^7$	3C	1 (1.32)	0.174	0.0253	0.312	2.02e-18	1.71
$\rho_0 = \rho_1$ [d]	6C	1.05	0.740	0.174	0.716	1.29e-09	1.94
	7C	1.47	0.0389	0.153	0.0385	1.81e-05	
$\rho_0 = \rho_1$ [d]	3C	1 (0.993)	0.413	0.0502	0.766	7.42e-21	2.33
$p = 2.12$	6C	1.23	0.879	0.113	0.293	1.29e-09	2.60
	7C	1.58	0.105	0.232	0.0544	3.24e-07	
$\rho_0 = \rho_1$ [d]	3C	1 (0.6)	0.698	0.00734	0.669	5.81e-15	1.98
$a_0 = 1.5$ kpc	6C	0.977	0.876	0.117	0.538	3.16e-07	2.06
	7C	1.63	0.115	0.0329	0.0457	3.11e-07	
$p = 2.12$	3C	1 (1.17)	0.265	0.00572	0.474	2.40e-20	2.21
$a_0 = 1.5$ kpc	6C	1.10	0.879	0.352	0.416	1.29e-09	2.79
	7C	1.55	0.0271	0.589	0.0385	7.19e-06	
$\rho_0 = \rho_1$ [d]	3C	1 (0.586)	0.782	5.42e-04	0.768	2.32e-17	2.21
$p = 2.12$	6C	0.971	0.769	0.00916	0.592	2.43e-06	2.42
$a_0 = 1.5$ kpc	7C	1.65	0.118	0.346	0.0477	3.05e-09	

[a] Each run (with one or more parameter variations) is done with the same initial ensemble (Set 1) of size 4861474, which is generated using $x = 3.0$ and $T_{MaxAge} = 150$ Myr. The 1-D K-S statistics are calculated by excluding sources with total linear size $D < 1$ kpc.

[b] Parameter values for dynamical and power evolution of radio sources set equal to those given in the first KDA model (Kaiser et al. 1997). See Table 2.1.

[c] Always, $\text{Ratio}_{3C} = 1$, because of the way it is defined. The number in parentheses gives the ratio of the number of sources detected in 3C simulation (with given ensemble size) as compared to the real 3C survey.

[d] $\rho_1 = \rho_{0\ (\text{Default})}/2 = 3.6 \times 10^{-22}$ kg m^{-3}.

Table A.2: KDA Model Results for Run 2: 1-D K-S Statistics for Parameter Variations [a]

Varied Model Parameter	Survey	Ratio_{3C} Ratio_{6C} Ratio_{7C}	$\mathcal{P}(K\text{–}S)$ $\mathcal{P}(P)$	$\mathcal{P}(D)$	$\mathcal{P}(z)$	$\mathcal{P}(\alpha)$	$\mathcal{P}_{[P,D,z,\alpha]}$ $\mathcal{P}_{[P,2D,z,\alpha]}$
Default [b]	3C	1 (2.12)	0.122	0.00569	0.474	1.40e-16	1.23
	6C	0.869	0.212	0.362	0.308	3.66e-10	1.52
	7C	1.44	0.00213	0.0965	0.00761	0.00551	
$\beta = 2.02$	3C	1 (1.36)	0.0677	0.208	0.581	1.66e-17	1.35
	6C	1.02	0.218	0.174	0.308	1.29e-09	1.69
	7C	1.56	0.0183	0.0329	0.0116	2.76e-04	
$a_0 = 1.5$ kpc	3C	1 (1.24)	0.0674	0.00371	0.596	1.72e-24	1.44
	6C	0.806	0.218	0.259	0.317	1.29e-09	1.82
	7C	1.51	0.0271	0.342	0.0375	2.56e-06	
$\rho_0 = \rho_1$ [c]	3C	1 (1.04)	0.160	0.0124	0.524	5.67e-24	1.58
	6C	0.977	0.583	0.259	0.317	1.29e-09	1.86
	7C	1.55	0.0125	0.167	0.0366	1.00e-06	
$\Gamma_B = 5/3$	3C	1 (1.81)	0.0354	0.0356	0.387	7.51e-22	1.24
	6C	0.906	0.434	0.174	0.558	1.29e-09	1.41
	7C	1.48	0.00815	0.0383	0.0116	9.10e-07	
$\gamma_{max(hs)} = 10^7$	3C	1 (2.61)	0.0488	0.164	0.312	6.00e-18	1.38
	6C	0.963	0.583	0.174	0.437	3.66e-10	1.76
	7C	1.41	4.60e-04	0.166	0.00200	0.00277	
$p = 2.12$	3C	1 (2.09)	0.0674	6.30e-04	0.474	1.76e-17	1.60
	6C	0.866	0.310	0.352	0.413	3.66e-10	2.20
	7C	1.45	0.00216	0.610	0.00768	4.93e-05	
$\rho_0 = \rho_1$ [c]	3C	1 (1.03)	0.161	6.26e-04	0.524	7.16e-28	1.49
$p = 2.12$	6C	0.967	0.583	0.113	0.317	1.29e-09	1.66
	7C	1.54	0.0185	0.158	0.0517	1.00e-06	
$\rho_0 = \rho_1$ [c]	3C	1 (0.545)	0.495	3.72e-04	0.779	8.52e-20	2.30
$a_0 = 1.5$ kpc	6C	1.33	0.648	0.0269	0.914	4.03e-08	2.51
	7C	1.66	0.153	0.333	0.180	8.65e-10	
$p = 2.12$	3C	1 (1.21)	0.0674	3.89e-04	0.593	1.00e-26	1.25
$a_0 = 1.5$ kpc	6C	0.857	0.218	0.241	0.317	1.29e-09	1.43
	7C	1.55	0.0271	0.0564	0.0379	9.10e-07	

Continued on next page ...

Table A.2: continued from previous page ...

Varied Model Parameter	Survey	Ratio_{3C} Ratio_{6C} Ratio_{7C}	$\mathcal{P}(K$–$S)$				$\mathcal{P}_{[P,D,z,\alpha]}$ $\mathcal{P}_{[P,2D,z,\alpha]}$
			$\mathcal{P}(P)$	$\mathcal{P}(D)$	$\mathcal{P}(z)$	$\mathcal{P}(\alpha)$	
$\rho_0 = \rho_1$ [c]	3C	1 (0.531)	0.665	0.00139	0.599	5.97e-23	2.49
$p = 2.12$	6C	1.36	0.841	0.0269	0.914	3.04e-07	2.80
$a_0 = 1.5$ kpc	7C	1.69	0.163	0.487	0.184	8.25e-10	

[a] Each run (with one or more parameter variations) is done with the same initial ensemble (Set 2) of size 4861474, which is generated using $x = 3.0$ and $T_{MaxAge} = 150$ Myr. The 1-D K-S statistics are calculated by excluding sources with total linear size $D < 1$ kpc.

[b] Parameter values for dynamical and power evolution of radio sources set equal to those given in the first KDA model (Kaiser et al. 1997). See Table 2.1.

[c] $\rho_1 = \rho_{0\ (\text{Default})}/2 = 3.6 \times 10^{-22}$ kg m^{-3}.

Table A.3: KDA Model Results for Run 3: 1-D K-S Statistics for Parameter Variations [a]

Varied Model Parameter	Survey	Ratio_{3C} Ratio_{6C} Ratio_{7C}	$\mathcal{P}(K\text{–}S)$ $\mathcal{P}(P)$	$\mathcal{P}(D)$	$\mathcal{P}(z)$	$\mathcal{P}(\alpha)$	$\mathcal{P}_{[P,D,z,\alpha]}$ $\mathcal{P}_{[P,2D,z,\alpha]}$
Default [b]	3C	1 (1.99)	0.122	0.0941	0.581	1.08e-11	1.95
	6C	0.934	0.444	0.176	0.558	3.66e-10	2.54
	7C	1.56	0.00828	0.638	0.0120	5.63e-05	
$\beta = 2.02$	3C	1 (1.29)	0.0906	0.0361	0.421	3.19e-13	1.28
	6C	1.04	0.434	0.164	0.442	1.29e-09	1.46
	7C	1.70	0.0271	0.0603	0.0171	0.00304	
$a_0 = 1.5$ kpc	3C	1 (1.17)	0.0911	0.0366	0.511	1.72e-17	1.92
	6C	1.03	0.434	0.0250	0.591	1.29e-09	2.52
	7C	1.63	0.0271	0.905	0.0385	2.56e-06	
$\rho_0 = \rho_1$ [c]	3C	1 (1.04)	0.122	0.00378	0.778	2.04e-18	2.12
	6C	0.977	0.593	0.0428	0.591	1.29e-09	2.52
	7C	1.58	0.0185	0.607	0.0544	3.25e-08	
$\Gamma_B = 5/3$	3C	1 (1.71)	0.0355	0.164	0.511	1.72e-17	1.82
	6C	0.958	0.317	0.371	0.442	1.29e-09	2.59
	7C	1.60	0.0185	0.607	0.0121	7.19e-06	
$\gamma_{max(hs)} = 10^7$	3C	1 (2.52)	0.123	0.0364	0.387	5.78e-11	1.25
	6C	0.973	0.310	0.174	0.585	3.66e-10	1.42
	7C	1.50	0.00216	0.0343	0.00495	0.00624	
$p = 2.12$	3C	1 (1.96)	0.0911	0.0685	0.581	1.08e-11	2.01
	6C	0.960	0.444	0.164	0.413	3.66e-10	2.79
	7C	1.57	0.00815	0.992	0.0120	2.63e-04	
$\Gamma_B = 5/3$	3C	1 (1.66)	0.0678	0.0502	0.421	1.66e-17	1.34
$p = 2.12$	6C	0.9375	0.317	0.0428	0.413	1.29e-09	1.69
	7C	1.63	0.0183	0.451	0.0178	0.00127	
$\Gamma_B = 5/3$	3C	1 (0.848)	0.0674	0.0175	0.597	5.53e-24	2.14
$\rho_0 = \rho_1$ [c]	6C	1.12	0.664	0.00740	0.897	1.39e-08	2.55
	7C	1.68	0.0186	0.644	0.0544	8.25e-10	
$\rho_0 = \rho_1$ [c]	3C	1 (1.01)	0.122	0.00572	0.778	2.42e-21	2.30
$p = 2.12$	6C	1.01	0.593	0.0428	0.593	1.29e-09	2.88
	7C	1.61	0.0271	0.892	0.0546	3.11e-07	

Continued on next page ...

Table A.3: continued from previous page ...

Varied Model Parameter	Survey	Ratio_{3C} Ratio_{6C} Ratio_{7C}	$\mathcal{P}(K\text{–}S)$				$\mathcal{P}_{[P,D,z,\alpha]}$ $\mathcal{P}_{[P,2D,z,\alpha]}$
			$\mathcal{P}(P)$	$\mathcal{P}(D)$	$\mathcal{P}(z)$	$\mathcal{P}(\alpha)$	
$\rho_0 = \rho_1$ [c]	3C	1 (0.621)	0.0486	0.0269	0.662	5.02e-19	1.40
$a_0 = 1.5$ kpc	6C	1.0	0.738	0.0936	0.317	1.83e-07	1.56
	7C	1.51	0.0509	0.144	0.129	5.89e-11	
$p = 2.12$	3C	1 (1.15)	0.160	0.00101	0.608	2.44e-20	1.85
$a_0 = 1.5$ kpc	6C	1.05	0.583	0.00383	0.591	1.29e-09	2.15
	7C	1.62	0.0125	0.476	0.0385	1.02e-06	
$\rho_0 = \rho_1$ [c]	3C	1 (0.6)	0.0992	0.0220	0.611	1.02e-20	1.58
$p = 2.12$	6C	1.06	0.729	0.394	0.252	9.19e-07	1.94
$a_0 = 1.5$ kpc	7C	1.52	0.0558	0.233	0.137	1.49e-11	

[a] Each run (with one or more parameter variations) is done with the same initial ensemble (Set 3) of size 4861474, which is generated using $x = 3.0$ and $T_{MaxAge} = 150$ Myr. The 1-D K-S statistics are calculated by excluding sources with total linear size $D < 1$ kpc.

[b] Parameter values for dynamical and power evolution of radio sources set equal to those given in the first KDA model (Kaiser et al. 1997). See Table 2.1.

[c] $\rho_1 = \rho_{0\ \text{(Default)}}/2 = 3.6 \times 10^{-22}$ kg m^{-3}.

Table A.4: KDA Model Results for Run 4: 1-D K-S Statistics for Parameter Variations [a]

Varied Model Parameter	Survey	Ratio_{3C} Ratio_{6C} Ratio_{7C}	$\mathcal{P}(K\text{–}S)$ $\mathcal{P}(P)$	$\mathcal{P}(D)$	$\mathcal{P}(z)$	$\mathcal{P}(\alpha)$	$\mathcal{P}_{[P,D,z,\alpha]}$ $\mathcal{P}_{[P,2D,z,\alpha]}$
Default [b]	3C	1 (2.0)	0.161	0.00858	0.423	2.99e-10	1.62
	6C	0.905	0.761	0.244	0.532	3.66e-10	1.82
	7C	1.45	0.00541	0.0657	0.0123	5.45e-05	
$\beta = 2.02$	3C	1 (1.19)	0.207	0.0129	0.610	1.08e-11	1.95
	6C	0.939	0.794	0.248	0.689	1.29e-09	2.13
	7C	1.80	0.0125	0.00273	0.0183	2.76e-04	
$a_0 = 1.5$ kpc	3C	1 (1.13)	0.264	0.0125	0.423	1.03e-15	1.92
	6C	0.945	0.634	0.178	0.689	1.29e-09	2.26
	7C	1.53	0.0125	0.360	0.0385	3.37e-07	
$\rho_0 = \rho_1$ [c]	3C	1 (0.952)	0.265	0.0186	0.515	4.89e-17	2.16
	6C	1.07	0.879	0.244	0.308	1.29e-09	2.72
	7C	1.67	0.0271	0.626	0.0544	3.39e-08	
$\Gamma_B = 5/3$	3C	1 (1.68)	0.0681	0.00378	0.127	4.75e-17	1.36
	6C	0.891	0.751	0.371	0.532	1.29e-09	1.69
	7C	1.58	0.00541	0.154	0.0123	3.24e-07	
$\gamma_{max(hs)} = 10^7$	3C	1 (2.45)	0.0122	0.0678	0.579	7.92e-13	1.68
	6C	1.0	0.317	0.509	0.444	3.66e-10	2.28
	7C	1.44	7.86e-04	0.346	0.00761	0.00148	
$p = 2.12$	3C	1 (1.94)	0.0921	0.0260	0.344	1.08e-15	1.82
	6C	0.925	0.751	0.784	0.532	1.29e-09	2.38
	7C	1.48	0.00500	0.0609	0.0123	5.89e-04	
$\rho_0 = \rho_1$ [c]	3C	1 (0.931)	0.266	0.0502	0.524	5.75e-18	1.75
$p = 2.12$	6C	1.02	0.879	0.174	0.211	1.29e-09	1.95
	7C	1.67	0.0271	0.0581	0.0544	1.04e-08	
$\rho_0 = \rho_1$ [c]	3C	1 (0.524)	0.212	0.00375	0.339	2.46e-15	1.64
$a_0 = 1.5$ kpc	6C	0.888	0.749	0.505	0.211	2.65e-06	2.23
	7C	1.76	0.123	0.607	0.138	9.92e-09	
$p = 2.12$	3C	1 (1.12)	0.160	0.00100	0.342	4.96e-17	1.62
$a_0 = 1.5$ kpc	6C	0.988	0.789	0.0229	0.532	1.29e-09	1.86
	7C	1.53	0.0125	0.365	0.0385	3.39e-08	

Continued on next page ...

Table A.4: continued from previous page ...

Varied Model Parameter	Survey	Ratio_{3C} Ratio_{6C} Ratio_{7C}	$\mathcal{P}(K\text{–}S)$				$\mathcal{P}_{[P,D,z,\alpha]}$ $\mathcal{P}_{[P,2D,z,\alpha]}$
			$\mathcal{P}(P)$	$\mathcal{P}(D)$	$\mathcal{P}(z)$	$\mathcal{P}(\alpha)$	
$\rho_0 = \rho_1$ [c]	3C	1 (0.483)	0.199	0.00123	0.196	1.62e-16	1.27
$p = 2.12$	6C	0.964	0.749	0.196	0.211	5.80e-06	1.63
$a_0 = 1.5$ kpc	7C	1.93	0.0818	0.443	0.171	2.99e-07	

[a] Each run (with one or more parameter variations) is done with the same initial ensemble (Set 4) of size 4861474, which is generated using $x = 3.0$ and $T_{MaxAge} = 150$ Myr. The 1-D K-S statistics are calculated by excluding sources with total linear size $D < 1$ kpc.

[b] Parameter values for dynamical and power evolution of radio sources set equal to those given in the first KDA model (Kaiser et al. 1997). See Table 2.1.

[c] $\rho_1 = \rho_{0\ (\text{Default})}/2 = 3.6 \times 10^{-22}$ kg m^{-3}.

Table A.5: KDA Model: Performance Ranks for Best-Fit Parameter Variations [a]

Model	$\mathcal{P}(K$–$S)$	Run 1	Run 2	Run 3	Run 4	Average [b]
Default [c]	$\mathcal{P}_{[P,D,z]}$	11	11	4	9	8.75
	$\mathcal{P}_{[P,2D,z]}$	10	9	4	9	8
$\beta = 2.02$	$\mathcal{P}_{[P,D,z]}$	10	8	10	2	7.5
	$\mathcal{P}_{[P,2D,z]}$	9	7	10	6	8
$a_0 = 1.5$ kpc	$\mathcal{P}_{[P,D,z]}$	9	6	5	3	5.75
	$\mathcal{P}_{[P,2D,z]}$	8	5	5	4	5.5
$\rho_0 = \rho_1$ [d]	$\mathcal{P}_{[P,D,z]}$	5	4	2	1	3
	$\mathcal{P}_{[P,2D,z]}$	7	4	6	1	4.5
$\Gamma_B = 5/3$	$\mathcal{P}_{[P,D,z]}$	2	10	7	10	7.25
	$\mathcal{P}_{[P,2D,z]}$	2	11	3	10	6.5
$\gamma_{max(hs)} = 10^7$	$\mathcal{P}_{[P,D,z]}$	6	7	11	6	7.5
	$\mathcal{P}_{[P,2D,z]}$	1	6	11	3	5.25
$p = 2.12$	$\mathcal{P}_{[P,D,z]}$	7	3	3	4	4.25
	$\mathcal{P}_{[P,2D,z]}$	5	3	2	2	3
$\rho_0 = \rho_1$ [d]	$\mathcal{P}_{[P,D,z]}$	1	5	1	5	3
$p = 2.12$	$\mathcal{P}_{[P,2D,z]}$	4	8	1	7	5
$\rho_0 = \rho_1$ [d]	$\mathcal{P}_{[P,D,z]}$	8	2	9	7	6.5
$a_0 = 1.5$ kpc	$\mathcal{P}_{[P,2D,z]}$	11	2	9	5	6.75
$p = 2.12$	$\mathcal{P}_{[P,D,z]}$	3	9	6	8	6.5
$a_0 = 1.5$ kpc	$\mathcal{P}_{[P,2D,z]}$	3	10	7	8	7
ρ_0, p, a_0 [e]	$\mathcal{P}_{[P,D,z]}$	4	1	8	11	6
	$\mathcal{P}_{[P,2D,z]}$	6	1	8	11	6.5

[a] Each run is done using $x = 3.0$ and $T_{MaxAge} = 150$ Myr for the initial population of size 4861474; the 4 runs, whose ranks are displayed, differ in the initial random seeds. The ranks are according to the combined 1-D K-S statistic results of the 4 runs tabulated in detail in Tables A.1, A.2, A.3 and A.4, which are also summarised in Table 4.7.

[b] Overall rank score (obtained by averaging separate ranks from the four runs) of each of the 11 KDA cases shown here; two values indicate a tie.

[c] Parameter values for dynamical and power evolution of radio sources set equal to those given in the first KDA model (Kaiser et al. 1997). See Table 2.1.

[d] $\rho_1 = \rho_{0\ (\mathrm{Default})}/2 = 3.6 \times 10^{-22}$ kg m^{-3}.

[e] Values of 3 parameters changed in the runs to $\rho_0 = \rho_1$, $p = 2.12$, $a_0 = 1.5$ kpc.

A.2 Original BRW Model

Table A.6: BRW Model Results for Run 1: 1-D K-S Statistics for Parameter Variations [a]

Varied Model Parameter	Survey	Ratio_{3C} Ratio_{6C} Ratio_{7C}	$\mathcal{P}(K\text{–}S)$ $\mathcal{P}(P)$	$\mathcal{P}(D)$	$\mathcal{P}(z)$	$\mathcal{P}(\alpha)$	$\mathcal{P}_{[P,D,z,\alpha]}$ $\mathcal{P}_{[P,2D,z,\alpha]}$
Default [b]	3C	1 (1.68) [c]	0.0809	5.13e-08	0.244	0.00208	0.655
	6C	1.13	0.0468	0.0141	0.140	3.66e-10	0.867
	7C	1.46	2.80e-05	0.333	1.41e-05	0.00316	
$\beta = 1$	3C	1 (4.01)	0.0325	0.0508	0.0616	1.44e-07	0.420
	6C	1.12	0.0549	0.106	0.140	2.94e-17	0.623
	7C	1.36	1.60e-05	0.140	5.04e-05	3.15e-06	
$a_0 = 7.5$ kpc	3C	1 (1.11)	0.0595	6.14e-10	0.308	6.75e-06	0.632
	6C	1.10	0.0160	0.0428	0.302	1.29e-09	0.694
	7C	1.48	2.71e-04	0.0581	2.62e-05	1.41e-04	
$a_0 = 20$ kpc	3C	1 (3.8)	0.0306	4.11e-07	0.0447	0.00210	0.415
	6C	1.31	0.0456	0.253	0.140	3.73e-13	0.638
	7C	1.38	2.21e-06	0.103	1.42e-05	3.15e-06	
$\rho_0 = \rho_1$ [d]	3C	1 (0.834)	0.108	1.03e-11	0.247	7.08e-08	0.540
	6C	1.22	0.0816	0.0141	0.140	1.29e-09	0.583
	7C	1.56	7.44e-04	0.0569	7.73e-06	1.41e-04	
$\rho_0 = \rho_2$ [e]	3C	1 (2.88)	0.0103	5.30e-08	0.0819	0.00737	0.277
	6C	1.24	0.00465	0.00401	0.140	3.83e-13	0.370
	7C	1.45	1.50e-05	0.148	1.44e-05	2.26e-05	
$\gamma_{max(hs)} = 10^{10}$	3C	1 (1.68)	0.0809	5.87e-09	0.244	0.00208	0.613
	6C	1.13	0.0885	0.00401	0.140	3.66e-10	0.757
	7C	1.48	2.64e-04	0.232	1.41e-05	0.00332	
$p = 2.001$	3C	1 (0.910)	0.464	2.90e-09	0.568	0.00486	1.37
	6C	1.19	0.0796	0.0428	0.310	3.66e-10	1.46
	7C	1.60	0.00187	0.100	1.54e-04	0.00332	
$p = 2.999$	3C	1 (2.68)	0.0103	2.61e-08	0.0582	0.00729	0.415
	6C	1.21	0.00879	0.174	0.141	1.24e-09	0.667
	7C	1.38	8.33e-06	0.232	1.41e-05	0.00663	

Continued on next page ...

Table A.6: continued from previous page ...

Varied Model Parameter	Survey	Ratio$_{3C}$ Ratio$_{6C}$ Ratio$_{7C}$	$\mathcal{P}(K$–$S)$				$\mathcal{P}_{[P,D,z,\alpha]}$ $\mathcal{P}_{[P,2D,z,\alpha]}$
			$\mathcal{P}(P)$	$\mathcal{P}(D)$	$\mathcal{P}(z)$	$\mathcal{P}(\alpha)$	
	3C	1 (0.655)	0.383	1.28e-16	0.474	3.68e-06	1.21
$r_{hs} = 1$ kpc	6C	1.24	0.204	0.00205	0.212	1.29e-09	1.30
	7C	1.72	2.67e-04	0.148	4.69e-05	1.41e-04	
	3C	1 (3.09)	0.00464	1.06e-07	0.0582	0.0456	0.701
$r_{hs} = 5$ kpc	6C	1.20	0.0277	0.0428	0.140	1.59e-12	1.23
	7C	1.24	8.04e-06	0.828	7.58e-06	8.76e-06	
	3C	1 (1.17)	0.240	1.10e-07	0.474	0.00487	1.42
$t_{bs} = 10^3$ yr	6C	1.15	0.0481	0.509	0.310	3.66e-10	1.89
	7C	1.52	7.53e-04	0.251	1.46e-04	0.00332	
	3C	1 (1.68)	0.0807	2.37e-11	0.375	5.10e-04	0.682
$t_{bs} = 10^7$ yr	6C	1.28	0.0460	0.0141	0.206	3.83e-13	0.748
	7C	1.51	4.25e-06	0.0940	7.58e-06	8.76e-06	
	3C	1 (1.54)	0.108	2.44e-08	0.384	0.00487	1.02
$t_{bf} = 0.01$ yr	6C	1.15	0.0473	0.0709	0.140	3.66e-10	1.42
	7C	1.48	1.50e-05	0.589	7.62e-06	0.00332	
	3C	1 (1.88)	0.0594	3.83e-07	0.237	0.00485	0.830
$t_{bf} = 100$ yr	6C	1.19	0.0473	0.491	0.212	3.66e-10	1.20
	7C	1.45	8.16e-06	0.0957	7.58e-06	0.00324	
$p = 2.001$	3C	1 (0.910)	0.464	1.29e-08	0.568	0.00486	1.48
$t_{bs} = 10^3$ yr	6C	1.21	0.0796	0.259	0.310	3.66e-10	1.68
	7C	1.60	0.00187	0.0586	1.54e-04	0.00332	
$p = 2.001$	3C	1 (0.338)	0.218	2.36e-08	0.0826	0.00166	0.517 [g]
$r_{hs} = 1$ kpc	6C	1.48	0.251	9.37e-04	0.448	1.39e-06	0.519 [g]
	7C	1.80	0.0240	0.00270	0.0130	1.41e-04	
$t_{bs} = 10^3$ yr	3C	1 (0.455)	0.459	4.35e-08	0.607	3.62e-04	1.02 [g]
$r_{hs} = 1$ kpc	6C	1.44	0.253	0.00307	0.253	4.69e-07	1.03 [g]
	7C	1.73	0.0286	0.0191	0.00259	1.41e-04	
$p = 2.001$	3C	1 (0.628)	0.596	6.57e-07	0.545	9.91e-05	1.09 [g]
$a_0 = 7.5$ kpc	6C	1.26	0.163	0.0105	0.163	1.62e-08	1.10 [g]
	7C	1.49	0.00136	6.15e-04	2.37e-04	7.21e-04	

Continued on next page ...

Table A.6: continued from previous page ...

Varied Model Parameter	Survey	Ratio_{3C} Ratio_{6C} Ratio_{7C}	$\mathcal{P}(K\text{–}S)$				$\mathcal{P}_{[P,D,z,\alpha]}$ $\mathcal{P}_{[P,2D,z,\alpha]}$
			$\mathcal{P}(P)$	$\mathcal{P}(D)$	$\mathcal{P}(z)$	$\mathcal{P}(\alpha)$	
$t_{bs} = 10^3$ yr	3C	1 (0.786)	0.304	1.32e-09	0.312	6.78e-06	0.866
$a_0 = 7.5$ kpc	6C	1.25	0.129	0.0428	0.212	1.27e-09	0.900
	7C	1.60	7.44e-04	0.0111	4.73e-05	7.21e-04	

[a] Each run (with one or two parameter variations) is done with the same initial ensemble (Set 1) of size 3355926, which is generated using $x = 3.0$ and $T_{MaxAge} = 250$ Myr. The 1-D K-S statistics are calculated by excluding sources with total linear size $D < 10$ kpc.

[b] Parameter values for dynamical and power evolution of radio sources set equal to those given in the BRW model (Blundell et al. 1999). See Table 2.1.

[c] Always, $\text{Ratio}_{3C} = 1$, because of the way it is defined. The number in parentheses gives the ratio of the number of sources detected in 3C simulation (with given ensemble size) as compared to the real 3C survey.

[d] $\rho_1 = \rho_{0\ (\text{Default})}/2 = 8.35 \times 10^{-24}$ kg m^{-3}.

[e] $\rho_2 = 2 \times \rho_{0\ (\text{Default})} = 3.34 \times 10^{-23}$ kg m^{-3}.

[g] Numbers of sources detected in some of the simulated surveys are considerably smaller than in the real surveys, so the 1-D K-S statistic does not hold much significance.

Table A.7: BRW Model Results for Run 2: 1-D K-S Statistics for Parameter Variations [a]

Varied Model Parameter	Survey	Ratio_{3C} Ratio_{6C} Ratio_{7C}	$\mathcal{P}(K\text{–}S)$ $\mathcal{P}(P)$	$\mathcal{P}(D)$	$\mathcal{P}(z)$	$\mathcal{P}(\alpha)$	$\mathcal{P}_{[P,D,z,\alpha]}$ $\mathcal{P}_{[P,2D,z,\alpha]}$
Default [b]	3C	1 (1.58)	0.143	1.61e-06	0.301	1.13e-04	0.806
	6C	1.44	0.134	0.174	0.206	3.66-10	0.952
	7C	1.61	4.25e-06	0.0586	4.25e-06	0.00316	
$a_0 = 7.5$ kpc	3C	1 (1.08)	0.144	1.27e-08	0.459	1.33e-07	0.736
	6C	1.53	0.0149	0.0250	0.136	1.29e-09	0.773
	7C	1.66	4.95e-05	0.0343	1.13e-06	0.00158	
$\gamma_{max(hs)} = 10^{10}$	3C	1 (1.59)	0.143	5.30e-08	0.375	0.00131	0.691
	6C	1.46	0.0460	4.68e-04	0.206	3.66e-10	0.703
	7C	1.63	8.04e-06	0.0199	4.25e-06	0.00663	
$p = 2.001$	3C	1 (0.876)	0.264	5.03e-06	0.680	2.87e-04	1.39
	6C	1.44	0.0473	0.511	0.141	3.66e-10	1.72
	7C	1.81	9.07e-05	0.00538	8.04e-06	0.00332	
$r_{hs} = 1$ kpc	3C	1 (0.6)	0.554	4.41e-08	0.783	9.92e-08	1.39 [c]
	6C	1.58	0.159	0.0265	0.366	2.65e-09	1.41 [c]
	7C	2.04	2.03e-04	0.0191	6.95e-06	1.41e-04	
$r_{hs} = 5$ kpc	3C	1 (3.03)	0.00418	6.14e-09	0.0423	0.00492	0.387
	6C	1.36	0.00879	0.0685	0.134	1.59e-12	0.638
	7C	1.39	2.83e-08	0.339	2.08e-06	3.11e-04	
$t_{bs} = 10^3$ yr	3C	1 (1.10)	0.264	2.29e-07	0.568	1.88e-04	0.964
	6C	1.58	0.0262	0.0141	0.136	3.66e-10	0.993
	7C	1.78	1.53e-05	0.0329	8.04e-06	0.00154	
$t_{bs} = 10^7$ yr	3C	1 (1.59)	0.239	2.96e-09	0.386	1.89e-04	0.813
	6C	1.54	0.0270	0.00764	0.206	3.73e-13	0.853
	7C	1.65	2.83e-07	0.0581	2.21e-06	8.76e-06	
$t_{bf} = 0.01$ yr	3C	1 (1.48)	0.187	1.35e-09	0.386	5.08e-04	0.924
	6C	1.48	0.0160	0.174	0.141	3.66e-10	1.18
	7C	1.63	4.25e-06	0.232	4.25e-06	0.00332	
$t_{bf} = 100$ yr	3C	1 (1.79)	0.0978	1.07e-07	0.185	6.61e-05	0.563
	6C	1.35	0.0745	0.0709	0.206	3.66e-10	0.665
	7C	1.61	5.70e-07	0.0940	2.21e-06	0.00154	

Continued on next page ...

Table A.7: continued from previous page ...

Varied Model Parameter	Survey	Ratio_{3C} Ratio_{6C} Ratio_{7C}	$\mathcal{P}(K\text{–}S)$				$\mathcal{P}_{[P,D,z,\alpha]}$ $\mathcal{P}_{[P,2D,z,\alpha]}$
			$\mathcal{P}(P)$	$\mathcal{P}(D)$	$\mathcal{P}(z)$	$\mathcal{P}(\alpha)$	
$p = 2.001$	3C	1 (0.876)	0.264	2.18e-07	0.680	2.87e-04	1.20
$t_{bs} = 10^3$ yr	6C	1.46	0.0758	0.174	0.141	3.66e-10	1.31
	7C	1.81	9.07e-05	0.00538	8.04e-06	0.00332	
$p = 2.001$	3C	1 (0.297)	0.391	1.68e-07	0.456	4.48e-05	0.936 [c]
$r_{hs} = 1$ kpc	6C	1.16	0.623	0.0910	0.377	6.18e-05	1.01 [c]
	7C	2.13	0.0312	0.0586	0.0145	1.41e-04	
$t_{bs} = 10^3$ yr	3C	1 (0.434)	0.404	2.60e-07	0.640	4.89e-06	1.33 [c]
$r_{hs} = 1$ kpc	6C	1.43	0.463	0.215	0.463	4.67e-07	1.49 [c]
	7C	1.85	0.0118	0.0931	0.00226	1.41e-04	
$p = 2.001$	3C	1 (0.579)	0.358	1.23e-06	0.595	1.75e-05	1.11 [c]
$a_0 = 7.5$ kpc	6C	1.40	0.249	0.0333	0.353	1.30e-08	1.15 [c]
	7C	1.79	1.66e-04	0.0339	5.07e-05	3.26e-04	
$t_{bs} = 10^3$ yr	3C	1 (0.731)	0.122	4.23e-07	0.472	1.32e-07	0.825
$a_0 = 7.5$ kpc	6C	1.37	0.0468	0.0727	0.212	1.29e-09	0.892
	7C	1.82	8.79e-05	0.0339	8.04e-06	1.41e-04	

[a] Each run (with one or two parameter variations) is done with the same initial ensemble (Set 2) of size 3355926, which is generated using $x = 3.0$ and $T_{MaxAge} = 250$ Myr. The 1-D K-S statistics are calculated by excluding sources with total linear size $D < 10$ kpc.

[b] Parameter values for dynamical and power evolution of radio sources set equal to those given in the BRW model (Blundell et al. 1999). See Table 2.1.

[c] Numbers of sources detected in some of the simulated surveys are considerably smaller than in the real surveys, so the 1-D K-S statistic does not hold much significance.

Table A.8: BRW Model Results for Run 3: 1-D K-S Statistics for Parameter Variations [a]

Varied Model Parameter	Survey	Ratio_{3C} Ratio_{6C} Ratio_{7C}	$\mathcal{P}(K\text{–}S)$				$\mathcal{P}_{[P,D,z,\alpha]}$ $\mathcal{P}_{[P,2D,z,\alpha]}$
			$\mathcal{P}(P)$	$\mathcal{P}(D)$	$\mathcal{P}(z)$	$\mathcal{P}(\alpha)$	
Default [b]	3C	1 (1.33)	0.111	6.14e-10	0.247	5.08e-04	0.601
	6C	1.42	0.0285	0.114	0.140	3.66e-10	0.738
	7C	1.85	4.25e-06	0.105	2.64e-05	7.42e-04	
$a_0 = 7.5$ kpc	3C	1 (0.869)	0.330	2.90e-09	0.668	9.34e-07	1.63
	6C	1.77	0.268	0.00764	0.583	1.29e-09	1.73
	7C	1.94	1.55e-05	0.148	5.04e-05	7.21e-04	
$\gamma_{max(hs)} = 10^{10}$	3C	1 (1.34)	0.110	2.37e-11	0.247	5.20e-04	0.761
	6C	1.42	0.0283	0.00772	0.140	3.66e-10	1.06
	7C	1.85	2.21e-06	0.479	2.61e-05	7.21e-04	
$p = 2.001$	3C	1 (0.614)	0.0287	5.08e-06	0.0275	6.58e-05	0.807
	6C	2.05	0.434	0.0250	0.580	3.66e-10	0.915
	7C	2.47	1.58e-04	0.152	4.54e-04	0.00332	
$r_{hs} = 1$ kpc	3C	1 (0.421)	0.0327	4.88e-05	0.0154	1.91e-05	0.825 [c]
	6C	2.34	0.911	1.90e-04	0.348	1.84e-09	0.828 [c]
	7C	2.77	1.26e-04	0.00545	7.63e-05	1.41e-04	
$r_{hs} = 5$ kpc	3C	1 (2.92)	0.0150	6.38e-10	0.0583	0.00737	0.358
	6C	1.04	0.00860	0.0141	0.0893	3.83e-13	0.581
	7C	1.31	2.66e-07	0.351	2.08e-06	2.26e-05	
$t_{bs} = 10^3$ yr	3C	1 (0.897)	0.121	6.08e-09	0.593	1.88e-04	1.01
	6C	1.62	0.116	0.0141	0.310	3.66e-10	1.04
	7C	2.05	1.52e-05	0.0343	8.79e-05	0.00332	
$t_{bs} = 10^7$ yr	3C	1 (1.37)	0.0824	1.21e-13	0.247	1.01e-04	0.440
	6C	1.37	0.0283	9.92e-04	0.0893	3.83e-13	0.477
	7C	1.83	1.16e-06	0.0592	1.42e-05	3.26e-06	
$t_{bf} = 0.01$ yr	3C	1 (1.24)	0.146	1.06e-11	0.312	3.11e-04	0.670
	6C	1.46	0.0777	0.0252	0.141	3.66e-10	0.745
	7C	1.92	2.75e-05	0.0957	2.61e-05	0.00332	
$t_{bf} = 100$ yr	3C	1 (1.63)	0.0611	2.91e-10	0.112	5.08e-04	0.360
	6C	1.24	0.0283	0.0252	0.0893	3.66e-10	0.472
	7C	1.66	8.20e-06	0.158	1.42e-05	0.00332	

Continued on next page ...

Table A.8: continued from previous page ...

Varied Model Parameter	Survey	Ratio$_{3C}$ Ratio$_{6C}$ Ratio$_{7C}$	$\mathcal{P}(K$–$S)$				$\mathcal{P}_{[P,D,z,\alpha]}$ $\mathcal{P}_{[P,2D,z,\alpha]}$
			$\mathcal{P}(P)$	$\mathcal{P}(D)$	$\mathcal{P}(z)$	$\mathcal{P}(\alpha)$	
$p = 2.001$	3C	1 (0.614)	0.0202	8.62e-07	0.0275	6.58e-05	0.760
$t_{bs} = 10^3$ yr	6C	2.02	0.434	0.0252	0.572	3.66e-10	0.834
	7C	2.47	1.58e-04	0.0965	4.54e-04	0.00332	
$t_{bs} = 10^3$ yr	3C	1 (0.317)	0.0985	3.29e-05	0.0592	1.87e-05	0.472 [c]
$r_{hs} = 1$ kpc	6C	2.01	0.334	0.00361	0.382	1.40e-07	0.486 [c]
	7C	2.56	0.00791	0.0199	0.00147	1.41e-04	
$p = 2.001$	3C	1 (0.407)	0.108	1.14e-04	0.0578	0.00215	0.669 [c]
$a_0 = 7.5$ kpc	6C	2.12	0.648	0.00423	0.272	6.97e-09	0.691 [c]
	7C	2.63	1.97e-04	0.0329	1.77e-04	7.42e-04	
$t_{bs} = 10^3$ yr	3C	1 (0.552)	0.0140	1.66e-06	0.0387	2.52e-07	0.713
$a_0 = 7.5$ kpc	6C	1.97	0.583	0.00205	0.425	1.29e-09	0.736
	7C	2.29	2.78e-05	0.0353	8.95e-05	3.26e-04	

[a] Each run (with one or two parameter variations) is done with the same initial ensemble (Set 3) of size 3355926, which is generated using $x = 3.0$ and $T_{MaxAge} = 250$ Myr. The 1-D K-S statistics are calculated by excluding sources with total linear size $D < 10$ kpc.

[b] Parameter values for dynamical and power evolution of radio sources set equal to those given in the BRW model (Blundell et al. 1999). See Table 2.1.

[c] Numbers of sources detected in some of the simulated surveys are considerably smaller than in the real surveys, so the 1-D K-S statistic does not hold much significance.

Table A.9: BRW Model Results for Run 4: 1-D K-S Statistics for Parameter Variations [a]

Varied Model Parameter	Survey	Ratio_{3C} Ratio_{6C} Ratio_{7C}	$\mathcal{P}(K\text{–}S)$				$\mathcal{P}_{[P,D,z,\alpha]}$ $\mathcal{P}_{[P,2D,z,\alpha]}$
			$\mathcal{P}(P)$	$\mathcal{P}(D)$	$\mathcal{P}(z)$	$\mathcal{P}(\alpha)$	
Default [b]	3C	1 (1.50)	0.147	2.92e-10	0.0836	8.18e-04	0.661
	6C	1.14	0.0739	0.116	0.137	1.27e-09	0.959
	7C	1.81	4.40e-06	0.367	8.95e-05	0.00332	
$a_0 = 7.5$ kpc	3C	1 (0.972)	0.290	5.46e-11	0.148	5.04e-07	1.01
	6C	1.17	0.277	0.0440	0.580	1.29e-09	1.05
	7C	2.02	8.79e-05	0.0104	2.64e-04	1.41e-04	
$\gamma_{max(hs)} = 10^{10}$	3C	1 (1.51)	0.111	1.06e-07	0.0836	1.12e-04	0.553
	6C	1.15	0.0739	0.0252	0.137	1.27e-09	0.777
	7C	1.81	4.40e-06	0.342	8.95e-05	0.00332	
$p = 2.001$	3C	1 (0.779)	0.0202	1.27e-08	0.104	1.88e-04	0.730
	6C	1.26	0.537	0.113	0.304	3.66e-10	0.802
	7C	2.26	4.60e-04	0.00130	7.56e-04	0.00332	
$r_{hs} = 1$ kpc	3C	1 (0.490)	0.0400	5.46e-11	0.0775	3.68e-10	0.666 [c]
	6C	1.58	0.395	0.0250	0.430	1.29e-09	0.683 [c]
	7C	2.82	0.00495	0.00273	0.00495	1.41e-04	
$r_{hs} = 5$ kpc	3C	1 (3.09)	0.0430	7.89e-07	0.0319	0.0159	0.367
	6C	1.15	0.0157	0.00405	0.0900	3.83e-13	0.592
	7C	1.41	1.16e-06	0.365	8.00e-06	8.76e-06	
$t_{bs} = 10^3$ yr	3C	1 (1.01)	0.227	4.08e-07	0.192	8.18e-04	0.871
	6C	1.07	0.204	0.0142	0.434	3.66e-10	0.919
	7C	2.07	5.11e-05	0.0639	2.69e-04	0.00332	
$t_{bs} = 10^7$ yr	3C	1 (1.49)	0.245	5.72e-11	0.0836	3.12e-04	0.518
	6C	1.22	0.0521	0.00764	0.208	3.83e-13	0.543
	7C	1.88	5.70e-07	0.0332	8.95e-05	3.26e-06	
$t_{bf} = 0.01$ yr	3C	1 (1.37)	0.191	1.03e-07	0.112	8.31e-04	0.640
	6C	1.19	0.189	0.00764	0.304	1.27e-09	0.666
	7C	1.93	2.80e-05	0.0343	1.56e-04	0.00158	
$t_{bf} = 100$ yr	3C	1 (1.79)	0.110	2.13e-07	0.0613	5.20e-04	0.360
	6C	1.15	0.0160	0.174	0.0864	1.29e-09	0.483
	7C	1.69	2.25e-06	0.0208	4.95e-05	0.00154	

Continued on next page ...

Table A.9: continued from previous page ...

Varied Model Parameter	Survey	Ratio$_{3C}$ Ratio$_{6C}$ Ratio$_{7C}$	$\mathcal{P}(K$–$S)$				$\mathcal{P}_{[P,D,z,\alpha]}$ $\mathcal{P}_{[P,2D,z,\alpha]}$
			$\mathcal{P}(P)$	$\mathcal{P}(D)$	$\mathcal{P}(z)$	$\mathcal{P}(\alpha)$	
$p = 2.001$	3C	1 (0.752)	0.0202	2.10e-07	0.0775	1.89e-04	0.753
$t_{bs} = 10^3$ yr	6C	1.31	0.537	0.174	0.304	3.66e-10	0.875
	7C	2.33	2.72e-04	0.0191	7.56e-04	0.00332	
$t_{bs} = 10^3$ yr	3C	1 (0.345)	0.296	3.84e-04	0.724	5.47e-05	1.40 [c]
$r_{hs} = 1$ kpc	6C	1.2	0.901	0.320	0.400	7.36e-06	1.59 [c]
	7C	2.99	0.0500	0.0931	0.0378	3.26e-04	
$p = 2.001$	3C	1 (0.455)	0.0580	2.34e-04	0.125	3.46e-05	0.520 [c]
$a_0 = 7.5$ kpc	6C	1.36	0.402	0.0499	0.250	1.83e-07	0.580 [c]
	7C	2.73	0.00676	0.0564	0.00518	1.41e-04	
$t_{bs} = 10^3$ yr	3C	1 (0.607)	0.135	6.08e-09	0.176	5.02e-07	0.531
$a_0 = 7.5$ kpc	6C	1.39	0.126	0.00203	0.209	1.29e-09	0.536
	7C	2.54	0.00202	0.00538	0.00198	7.21e-04	

[a] Each run (with one or two parameter variations) is done with the same initial ensemble (Set 4) of size 3355926, which is generated using $x = 3.0$ and $T_{MaxAge} = 250$ Myr. The 1-D K-S statistics are calculated by excluding sources with total linear size $D < 10$ kpc.

[b] Parameter values for dynamical and power evolution of radio sources set equal to those given in the BRW model (Blundell et al. 1999). See Table 2.1.

[c] Numbers of sources detected in some of the simulated surveys are considerably smaller than in the real surveys, so the 1-D K-S statistic does not hold much significance.

Table A.10: BRW Model: Performance Ranks for Best-Fit Parameter Variations [a]

Model	$\mathcal{P}(K\text{–}S)$	Run 1	Run 2	Run 3	Run 4	Average [b]
Default [c]	$\mathcal{P}_{[P,D,z]}$	12	10	10	7	9.75
	$\mathcal{P}_{[P,2D,z]}$	11	8	8	3	7.5
$a_0 = 7.5$ kpc	$\mathcal{P}_{[P,D,z]}$	13	11	1	2	6.75
	$\mathcal{P}_{[P,2D,z]}$	14	11	1	2	7
$\gamma_{max(hs)} = 10^{10}$	$\mathcal{P}_{[P,D,z]}$	14	12	5	9	10
	$\mathcal{P}_{[P,2D,z]}$	12	12	2	7	8.25
$p = 2.001$	$\mathcal{P}_{[P,D,z]}$	3	1	4	5	3.25
	$\mathcal{P}_{[P,2D,z]}$	3	1	4	6	3.5
$r_{hs} = 1$ kpc	$\mathcal{P}_{[P,D,z]}$	4	2	3	6	3.75
	$\mathcal{P}_{[P,2D,z]}$	5	3	6	8	5.5
$r_{hs} = 5$ kpc	$\mathcal{P}_{[P,D,z]}$	10	14	14	13	12.75
	$\mathcal{P}_{[P,2D,z]}$	6	14	11	10	10.25
$t_{bs} = 10^3$ yr	$\mathcal{P}_{[P,D,z]}$	2	6	2	3	3.25
	$\mathcal{P}_{[P,2D,z]}$	1	7	3	4	3.75
$t_{bs} = 10^7$ yr	$\mathcal{P}_{[P,D,z]}$	11	9	12	12	11
	$\mathcal{P}_{[P,2D,z]}$	13	10	13	12	12
$t_{bf} = 0.01$ yr	$\mathcal{P}_{[P,D,z]}$	7	7	8	8	7.5
	$\mathcal{P}_{[P,2D,z]}$	4	5	7	9	6.25
$t_{bf} = 100$ yr	$\mathcal{P}_{[P,D,z]}$	9	13	13	14	12.25
	$\mathcal{P}_{[P,2D,z]}$	7	13	14	14	12
$p = 2.001$	$\mathcal{P}_{[P,D,z]}$	1	4	6	4	3.75
$t_{bs} = 10^3$ yr	$\mathcal{P}_{[P,2D,z]}$	2	4	5	5	4
$t_{bs} = 10^3$ yr	$\mathcal{P}_{[P,D,z]}$	6	3	11	1	5.25
$r_{hs} = 1$ kpc	$\mathcal{P}_{[P,2D,z]}$	9	2	12	1	6
$p = 2.001$	$\mathcal{P}_{[P,D,z]}$	5	5	9	11	7.5
$a_0 = 7.5$ kpc	$\mathcal{P}_{[P,2D,z]}$	8	6	10	11	8.75
$t_{bs} = 10^3$ yr	$\mathcal{P}_{[P,D,z]}$	8	8	7	10	8.25
$a_0 = 7.5$ kpc	$\mathcal{P}_{[P,2D,z]}$	10	9	9	13	10.25

[a] Each run is done using $x = 3.0$ and $T_{MaxAge} = 250$ Myr for the initial population of size 3355926; the 4 runs, whose ranks are displayed, differ in the initial random seeds. The ranks are according to the combined 1-D K-S statistic results of the 4 runs tabulated in detail in Tables A.6, A.7, A.8 and A.9, which are also summarised in Table 4.8.

[b] Overall rank score (obtained by averaging separate ranks from the four runs) of each of the 14 BRW cases shown here; two values indicate a tie.

[c] Parameter values for dynamical and power evolution of radio sources set equal to those given in the BRW model (Blundell et al. 1999). See Table 2.1.

A.3 Original MK Model

Table A.11: MK Model Results for Run 1: 1-D K-S Statistics for Parameter Variations [a]

Varied Model Parameter	Survey	Ratio$_{3C}$ Ratio$_{6C}$ Ratio$_{7C}$	$\mathcal{P}(K\text{–}S)$ $\mathcal{P}(P)$	$\mathcal{P}(D)$	$\mathcal{P}(z)$	$\mathcal{P}(\alpha)$	$\mathcal{P}_{[P,D,z,\alpha]}$ $\mathcal{P}_{[P,2D,z,\alpha]}$
Default [b]	3C	1 (1.16) [c]	0.0678	0.0354	0.668	0	1.76
	6C	0.938	0.740	0.0709	0.131	1.80e-24	2.20
	7C	1.10	0.00815	0.589	0.0267	1.58e-15	
$\beta = 1.0$	3C	1 (2.93)	0.00830	2.74e-06	0.387	0	1.16
	6C	0.624	0.218	0.0685	0.529	1.80e-24	1.44
	7C	0.826	4.88e-04	0.384	0.0183	7.23e-15	
$\beta = 1.6$	3C	1 (0.986)	0.334	0.0265	0.474	0	1.83
	6C	1.05	0.583	0.364	0.275	1.80e-24	2.30
	7C	1.14	0.00125	0.339	0.0183	1.58e-15	
$a_0 = 7.5$ kpc	3C	1 (0.8)	0.203	0.0520	0.796	2.02e-43	1.56
	6C	0.862	0.896	0.0337	0.170	5.14e-20	1.65
	7C	1.17	0.00548	0.0343	0.0181	8.46e-13	
$a_0 = 20$ kpc	3C	1 (2.48)	0.0488	0.0681	0.387	0	1.74
	6C	0.764	0.241	0.277	0.529	2.36e-25	2.53
	7C	0.991	5.11e-05	0.905	0.0180	2.37e-19	
$\rho_0 = \rho_1$ [d]	3C	1 (0.814)	0.161	0.0186	0.766	0	1.97
	6C	0.869	0.879	0.0135	0.0790	1.80e-24	2.39
	7C	1.18	0.00807	0.638	0.0183	1.91e-13	
$\rho_0 = \rho_2$ [e]	3C	1 (2)	0.0177	0.125	0.474	0	1.69
	6C	0.733	0.317	0.109	0.416	2.36e-25	2.39
	7C	0.984	0.00197	0.825	0.0385	5.01e-17	
$\gamma_{min(hs)} = 7$	3C	1 (0.690)	0.305	0.0697	0.869	7.29e-44	1.82
	6C	0.825	0.860	0.156	0.218	6.69e-18	2.11
	7C	1.11	0.00999	0.251	0.0510	5.33e-17	
$\gamma_{max(hs)} = 3 \times 10^8$	3C	1 (1.11)	0.0678	0.0361	0.668	0	2.47
	6C	0.963	0.740	0.809	0.199	1.80e-24	3.58
	7C	1.10	0.00815	0.917	0.0267	1.54e-15	

Continued on next page ...

Table A.11: continued from previous page ...

Varied Model Parameter	Survey	Ratio_{3C} Ratio_{6C} Ratio_{7C}	$\mathcal{P}(K\text{–}S)$				$\mathcal{P}_{[P,D,z,\alpha]}$ $\mathcal{P}_{[P,2D,z,\alpha]}$
			$\mathcal{P}(P)$	$\mathcal{P}(D)$	$\mathcal{P}(z)$	$\mathcal{P}(\alpha)$	
	3C	1 (1.13)	0.00605	0.00163	0.192	0	0.787
$\epsilon = 1.5$	6C	0.915	0.434	0.174	0.131	1.80e-24	1.00
	7C	1.01	1.52e-05	0.167	0.0183	1.91e-13	
$\gamma_{max(hs)} = 3 \times 10^8$	3C	1 (0.931)	0.423	0.0331	0.451	0	1.53
$\beta = 1.6$	6C	1	0.543	0.0645	0.201	1.91e-23	1.74
	7C	1.17	0.00103	0.237	0.0117	1.58e-15	
$\gamma_{max(hs)} = 3 \times 10^8$	3C	1 (0.662)	0.501	0.0704	0.653	7.76e-43	2.12
$\gamma_{min(hs)} = 7$	6C	0.807	0.892	0.0661	0.338	3.10e-17	2.68
	7C	1.10	0.00683	0.778	0.0503	5.33e-17	
$\beta = 1.6$	3C	1 (0.6)	0.251	0.00359	0.809	2.13e-40	1.78
$\gamma_{min(hs)} = 7$	6C	0.718	0.853	0.564	0.246	4.83e-15	2.22
	7C	1.03	0.00186	0.333	0.0888	5.33e-17	

[a] Each run (with one or two parameter variations) is done with the same initial ensemble (Set 1) of size 4861474, which is generated using $x = 3.0$ and $T_{MaxAge} = 150$ Myr. The 1-D K-S statistics are calculated by excluding sources with total linear size $D < 1$ kpc.

[b] Parameter values for dynamical and power evolution of radio sources set equal to those given in the MK model (Manolakou & Kirk 2002). See Table 2.1.

[c] Always, $\text{Ratio}_{3C} = 1$, because of the way it is defined. The number in parentheses gives the ratio of the number of sources detected in 3C simulation (with given ensemble size) as compared to the real 3C survey.

[d] $\rho_1 = \rho_{0\ (\text{Default})}/1.5 = 1.133 \times 10^{-23}$ kg m^{-3}.

[e] $\rho_2 = 2 \times \rho_{0\ (\text{Default})} = 3.4 \times 10^{-23}$ kg m^{-3}.

Table A.12: MK Model Results for Run 2: 1-D K-S Statistics for Parameter Variations [a]

Varied Model Parameter	Survey	Ratio_{3C} Ratio_{6C} Ratio_{7C}	$\mathcal{P}(K\text{–}S)$ $\mathcal{P}(P)$	$\mathcal{P}(D)$	$\mathcal{P}(z)$	$\mathcal{P}(\alpha)$	$\mathcal{P}_{[P,D,z,\alpha]}$ $\mathcal{P}_{[P,2D,z,\alpha]}$
Default [b]	3C	1 (1.17)	0.0494	0.00379	0.220	0	1.05
	6C	0.799	0.218	0.352	0.444	1.80e-24	1.31
	7C	0.975	0.00123	0.0639	0.0995	1.58e-15	
$\beta = 1.6$	3C	1 (0.938)	0.102	0.00357	0.174	0	1.48
	6C	0.864	0.113	0.571	0.593	7.60e-22	2.20
	7C	1.10	0.00124	0.635	0.106	1.58e-15	
$a_0 = 7.5$ kpc	3C	1 (0.821)	0.0734	3.69e-04	0.151	5.04e-44	1.50
	6C	0.819	0.119	0.128	0.858	9.86e-20	2.11
	7C	1.06	0.0329	0.897	0.164	7.79e-13	
$a_0 = 20$ kpc	3C	1 (2.52)	0.00824	0.0125	0.387	0	1.20
	6C	0.678	0.212	0.362	0.199	2.36e-25	1.73
	7C	1.02	4.52e-04	0.476	0.0120	1.54e-18	
$\rho_0 = \rho_1$ [c]	3C	1 (0.848)	0.0698	4.04e-05	0.175	8.41e-45	1.32
	6C	0.793	0.119	0.151	0.912	9.86e-20	1.79
	7C	1.03	0.0302	0.638	0.160	7.79e-13	
$\rho_0 = \rho_2$ [d]	3C	1 (2.03)	0.0249	0.0508	0.485	0	1.21
	6C	0.686	0.0893	0.501	0.308	2.36e-25	1.63
	7C	1.02	4.60e-04	0.0931	0.0261	5.17e-17	
$\gamma_{min} = 7$	3C	1 (0.579)	0.110	0.0266	0.473	1.61e-38	1.77
	6C	1.10	0.288	0.788	0.729	3.79e-19	2.29
	7C	1.21	0.0715	0.177	0.295	9.86e-20	
$\gamma_{max} = 3 \times 10^8$	3C	1 (1.11)	0.0674	0.0508	0.280	0	1.49
	6C	0.823	0.218	0.509	0.444	1.80e-24	2.07
	7C	0.971	0.00312	0.349	0.140	1.58e-15	
$\gamma_{max(hs)} = 3 \times 10^8$ $\beta = 1.6$	3C	1 (0.917)	0.0874	0.00874	0.238	0	1.87
	6C	0.846	0.0864	0.841	0.625	2.39e-21	2.92
	7C	1.09	0.00356	0.942	0.108	1.58e-15	
$\gamma_{max(hs)} = 3 \times 10^8$ $\gamma_{min(hs)} = 7$	3C	1 (0.566)	0.143	0.0344	0.325	5.84e-39	1.69
	6C	1.19	0.410	0.0820	0.632	9.86e-20	2.17
	7C	1.20	0.0943	0.671	0.323	1.49e-15	

Continued on next page ...

Table A.12: continued from previous page ...

Varied Model Parameter	Survey	Ratio_{3C} Ratio_{6C} Ratio_{7C}	$\mathcal{P}(K\text{–}S)$				$\mathcal{P}_{[P,D,z,\alpha]}$ $\mathcal{P}_{[P,2D,z,\alpha]}$
			$\mathcal{P}(P)$	$\mathcal{P}(D)$	$\mathcal{P}(z)$	$\mathcal{P}(\alpha)$	
$\beta = 1.6$	3C	1 (0.503)	0.132	0.108	0.703	4.05e-35	1.57
$\gamma_{min(hs)} = 7$	6C	1.16	0.708	0.0707	0.462	3.19e-18	1.72
	7C	1.19	0.0708	0.0581	0.295	1.49e-15	

[a] Each run (with one or two parameter variations) is done with the same initial ensemble (Set 2) of size 4861474, which is generated using $x = 3.0$ and $T_{MaxAge} = 150$ Myr. The 1-D K-S statistics are calculated by excluding sources with total linear size $D < 1$ kpc.

[b] Parameter values for dynamical and power evolution of radio sources set equal to those given in the MK model (Manolakou & Kirk 2002). See Table 2.1.

[c] $\rho_1 = \rho_{0\ \text{(Default)}}/1.5 = 1.133 \times 10^{-23}$ kg m^{-3}.

[d] $\rho_2 = 2 \times \rho_{0\ \text{(Default)}} = 3.4 \times 10^{-23}$ kg m^{-3}.

Table A.13: MK Model Results for Run 3: 1-D K-S Statistics for Parameter Variations [a]

Varied Model Parameter	Survey	Ratio_{3C} Ratio_{6C} Ratio_{7C}	$\mathcal{P}(K\text{–}S)$ $\mathcal{P}(P)$	$\mathcal{P}(D)$	$\mathcal{P}(z)$	$\mathcal{P}(\alpha)$	$\mathcal{P}_{[P,D,z,\alpha]}$ $\mathcal{P}_{[P,2D,z,\alpha]}$
Default [b]	3C	1 (1.14)	0.0353	0.0508	0.778	0	1.87
	6C	0.758	0.0395	0.386	0.591	1.80e-24	2.44
	7C	1.12	0.0123	0.454	0.0758	1.58e-15	
$\beta = 1.6$	3C	1 (0.966)	0.0473	0.0406	0.808	0	2.37
	6C	0.732	0.351	0.780	0.394	2.71e-20	3.40
	7C	1.15	0.0238	0.942	0.0795	1.58e-15	
$a_0 = 7.5$ kpc	3C	1 (0.807)	0.0167	0.00357	0.743	1.26e-43	1.73
	6C	0.769	0.684	0.463	0.323	7.59e-19	2.15
	7C	1.08	0.00329	0.306	0.137	8.69e-13	
$a_0 = 20$ kpc	3C	1 (2.41)	0.0350	0.0260	0.474	0	1.36
	6C	0.764	0.0893	0.0409	0.199	2.28e-25	2.01
	7C	1.09	2.78e-05	0.978	0.0178	2.45e-19	
$\rho_0 = \rho_1$ [c]	3C	1 (0.828)	0.0143	0.00893	0.671	3.08e-44	1.61
	6C	0.771	0.649	0.166	0.309	3.79e-19	1.99
	7C	1.08	0.00294	0.479	0.127	1.91e-13	
$\rho_0 = \rho_2$ [d]	3C	1 (1.89)	0.0665	0.414	0.581	0	2.33
	6C	0.812	0.0893	0.509	0.437	2.36e-25	3.65
	7C	1.07	2.87e-04	0.965	0.0267	9.23e-18	
$\gamma_{min} = 7$	3C	1 (0.683)	0.0236	0.222	0.666	1.20e-42	1.61
	6C	0.732	0.925	0.127	0.181	1.54e-16	2.00
	7C	1.01	0.0125	0.233	0.201	5.33e-17	
$\gamma_{max} = 3 \times 10^8$	3C	1 (1.10)	0.0250	0.0940	0.778	0	2.12
	6C	0.719	0.0388	0.371	0.591	1.80e-24	2.92
	7C	1.10	0.0185	0.778	0.104	1.58e-15	
$\epsilon = 1.5$	3C	1 (1.12)	0.0175	0.0502	0.568	0	1.14
	6C	0.710	0.212	0.264	0.0885	1.80e-24	1.46
	7C	1.01	8.91e-05	0.166	0.0513	1.91e-13	
$\gamma_{max(hs)} = 3 \times 10^8$ $\beta = 1.6$	3C	1 (0.917)	0.0342	0.102	0.837	0	1.91
	6C	0.714	0.418	0.210	0.302	1.92e-19	2.51
	7C	1.17	0.0237	0.647	0.0866	1.58e-15	

Continued on next page ...

Table A.13: continued from previous page ...

Varied Model Parameter	Survey	Ratio_{3C} Ratio_{6C} Ratio_{7C}	$\mathcal{P}(K\text{–}S)$				$\mathcal{P}_{[P,D,z,\alpha]}$ $\mathcal{P}_{[P,2D,z,\alpha]}$
			$\mathcal{P}(P)$	$\mathcal{P}(D)$	$\mathcal{P}(z)$	$\mathcal{P}(\alpha)$	
$\gamma_{max(hs)} = 3 \times 10^8$	3C	1 (0.662)	0.0215	0.220	0.620	7.29e-42	1.88
$\gamma_{min(hs)} = 7$	6C	0.755	0.925	0.127	0.0866	1.54e-16	2.60
	7C	0.979	0.0141	0.798	0.231	5.33e-17	
$\beta = 1.6$	3C	1 (0.566)	0.00434	0.156	0.389	5.84e-39	1.27
$\gamma_{min(hs)} = 7$	6C	0.762	0.993	0.416	0.141	4.83e-15	1.63
	7C	1.01	0.00916	0.0991	0.212	5.33e-17	

[a] Each run (with one or two parameter variations) is done with the same initial ensemble (Set 2) of size 4861474, which is generated using $x = 3.0$ and $T_{MaxAge} = 150$ Myr. The 1-D K-S statistics are calculated by excluding sources with total linear size $D < 1$ kpc.

[b] Parameter values for dynamical and power evolution of radio sources set equal to those given in the MK model (Manolakou & Kirk 2002). See Table 2.1.

[c] $\rho_1 = \rho_{0\ (\text{Default})}/1.5 = 1.133 \times 10^{-23}$ kg m^{-3}.

[d] $\rho_2 = 2 \times \rho_{0\ (\text{Default})} = 3.4 \times 10^{-23}$ kg m^{-3}.

Table A.14: MK Model Results for Run 4: 1-D K-S Statistics for Parameter Variations [a]

Varied Model Parameter	Survey	Ratio_{3C} Ratio_{6C} Ratio_{7C}	$\mathcal{P}(K\text{–}S)$ $\mathcal{P}(P)$	$\mathcal{P}(D)$	$\mathcal{P}(z)$	$\mathcal{P}(\alpha)$	$\mathcal{P}_{[P,D,z,\alpha]}$ $\mathcal{P}_{[P,2D,z,\alpha]}$
Default [b]	3C	1 (1.07)	0.0177	0.00842	0.710	0	1.67
	6C	0.871	0.583	0.476	0.139	1.80e-24	2.08
	7C	1.15	0.00341	0.166	0.0758	1.54e-15	
$\beta = 1.6$	3C	1 (0.890)	0.0408	0.0563	0.700	0	1.59
	6C	0.795	0.264	0.400	0.247	2.71e-20	2.15
	7C	1.26	0.00394	0.479	0.0586	1.58e-15	
$a_0 = 7.5$ kpc	3C	1 (0.738)	0.0548	0.0700	0.260	1.55e-41	1.29
	6C	0.748	0.361	0.725	0.270	1.43e-17	1.92
	7C	1.21	0.0105	0.365	0.106	8.69e-13	
$a_0 = 20$ kpc	3C	1 (2.38)	0.0176	0.0508	0.579	0	1.67
	6C	0.681	0.317	0.371	0.186	2.36e-25	2.42
	7C	1.04	2.72e-04	0.752	0.0123	1.49e-18	
$\rho_0 = \rho_1$ [c]	3C	1 (0.752)	0.0497	0.259	0.326	5.75e-42	1.81
	6C	0.711	0.459	0.892	0.155	3.10e-17	2.92
	7C	1.21	0.0115	0.772	0.0964	8.46e-13	
$\rho_0 = \rho_2$ [d]	3C	1 (1.85)	0.0253	0.0940	0.581	0	1.50
	6C	0.746	0.434	0.0709	0.121	2.36e-25	2.01
	7C	1.06	1.63e-04	0.614	0.0267	9.23e-18	
$\gamma_{min} = 7$	3C	1 (0.628)	0.0962	0.420	0.324	1.66e-41	1.65
	6C	0.769	0.149	0.257	0.368	3.54e-16	2.58
	7C	1.10	0.0152	0.795	0.188	5.33e-17	
$\gamma_{max} = 3 \times 10^8$	3C	1 (1.05)	0.0253	0.0125	0.721	0	1.85
	6C	0.855	0.583	0.174	0.0885	1.80e-24	2.46
	7C	1.13	0.00337	0.795	0.0758	1.58e-15	
$\gamma_{max(hs)} = 3 \times 10^8$ $\beta = 1.6$	3C	1 (0.855)	0.0574	0.169	0.498	0	1.43
	6C	0.766	0.317	0.351	0.302	1.92e-19	1.97
	7C	1.24	0.00236	0.339	0.0566	1.58e-15	
$\gamma_{max(hs)} = 3 \times 10^8$ $\gamma_{min(hs)} = 7$	3C	1 (0.6)	0.138	0.420	0.188	2.13e-40	1.20
	6C	0.833	0.0866	0.251	0.340	1.54e-16	1.78
	7C	1.12	0.0283	0.232	0.205	5.33e-17	

Continued on next page ...

Table A.14: continued from previous page ...

Varied Model Parameter	Survey	Ratio_{3C} Ratio_{6C} Ratio_{7C}	$\mathcal{P}(K\text{–}S)$				$\mathcal{P}_{[P,D,z,\alpha]}$ $\mathcal{P}_{[P,2D,z,\alpha]}$
			$\mathcal{P}(P)$	$\mathcal{P}(D)$	$\mathcal{P}(z)$	$\mathcal{P}(\alpha)$	
$\beta = 1.6$	3C	1 (0.545)	0.0327	0.254	0.643	4.57e-38	1.38
$\gamma_{min(hs)} = 7$	6C	0.759	0.291	0.374	0.510	1.21e-14	1.78
	7C	1.16	0.0187	0.0991	0.189	5.33e-17	

[a] Each run (with one or two parameter variations) is done with the same initial ensemble (Set 4) of size 4861474, which is generated using $x = 3.0$ and $T_{MaxAge} = 150$ Myr. The 1-D K-S statistics are calculated by excluding sources with total linear size $D < 1$ kpc.

[b] Parameter values for dynamical and power evolution of radio sources set equal to those given in the MK model (Manolakou & Kirk 2002). See Table 2.1.

[c] $\rho_1 = \rho_{0\ \text{(Default)}}/1.5 = 1.133 \times 10^{-23}$ kg m^{-3}.

[d] $\rho_2 = 2 \times \rho_{0\ \text{(Default)}} = 3.4 \times 10^{-23}$ kg m^{-3}.

Table A.15: MK Model: Performance Ranks for Best-Fit Parameter Variations [a]

Model	$\mathcal{P}(K$–$S)$	Run 1	Run 2	Run 3	Run 4	Average [b]
Default [c]	$\mathcal{P}_{[P,D,z]}$	7	11	6	4	7
	$\mathcal{P}_{[P,2D,z]}$	8	11	6	6	7.75
$\beta = 1.6$	$\mathcal{P}_{[P,D,z]}$	4	7	1	6	4.5
	$\mathcal{P}_{[P,2D,z]}$	6	3	2	5	4
$a_0 = 7.5$ kpc	$\mathcal{P}_{[P,D,z]}$	10	5	7	10	8
	$\mathcal{P}_{[P,2D,z]}$	11	5	7	9	8
$a_0 = 20$ kpc	$\mathcal{P}_{[P,D,z]}$	8	10	10	3	7.75
	$\mathcal{P}_{[P,2D,z]}$	3	8	8	4	5.75
$\rho_0 = \rho_1$ [d]	$\mathcal{P}_{[P,D,z]}$	3	8	9	2	5.5
	$\mathcal{P}_{[P,2D,z]}$	4	7	10	1	5.5
$\rho_0 = \rho_2$ [e]	$\mathcal{P}_{[P,D,z]}$	9	9	2	7	6.75
	$\mathcal{P}_{[P,2D,z]}$	5	10	1	7	5.75
$\gamma_{min} = 7$	$\mathcal{P}_{[P,D,z]}$	5	2	8	5	5
	$\mathcal{P}_{[P,2D,z]}$	9	2	9	2	5.5
$\gamma_{max} = 3 \times 10^8$	$\mathcal{P}_{[P,D,z]}$	1	6	3	1	2.75
	$\mathcal{P}_{[P,2D,z]}$	1	6	3	3	3.25
$\gamma_{max(hs)} = 3 \times 10^8$	$\mathcal{P}_{[P,D,z]}$	11	1	4	8	6
$\beta = 1.6$	$\mathcal{P}_{[P,2D,z]}$	10	1	5	8	6
$\gamma_{max(hs)} = 3 \times 10^8$	$\mathcal{P}_{[P,D,z]}$	2	3	5	11	5.25
$\gamma_{min(hs)} = 7$	$\mathcal{P}_{[P,2D,z]}$	2	4	4	10	5
$\beta = 1.6$	$\mathcal{P}_{[P,D,z]}$	6	4	11	9	7.5
$\gamma_{min(hs)} = 7$	$\mathcal{P}_{[P,2D,z]}$	7	9	11	11	9.5

[a] Each run is done using $x = 3.0$ and $T_{MaxAge} = 150$ Myr for the initial population of size 4861474; the 4 runs, whose ranks are displayed, differ in the initial random seeds. The ranks are according to the combined 1-D K-S statistic results of the 4 runs tabulated in detail in Tables A.11, A.12, A.13 and A.14, which are also summarised in Table 4.9.

[b] Overall rank score (average of separate ranks from the four runs) of each of the 11 MK cases.

[c] Parameter values set equal to those given in the MK model (Manolakou & Kirk 2002). See Table 2.1.

[d] $\rho_1 = \rho_{0\ (\text{Default})}/1.5 = 1.133 \times 10^{-23}$ kg m^{-3}.

[e] $\rho_2 = 2 \times \rho_{0\ (\text{Default})} = 3.4 \times 10^{-23}$ kg m^{-3}.

– B –

Detailed Modified Model Result Tables

B.1 Modified BRW Model

Table B.1: Modified BRW Model Results for Run 1: 1-D K-S Statistics [a]

Varied Model Parameter	Survey	Ratio_{3C} Ratio_{6C} Ratio_{7C}	$\mathcal{P}(K\text{–}S)$ $\mathcal{P}(P)$	$\mathcal{P}(D)$	$\mathcal{P}(z)$	$\mathcal{P}(\alpha)$	$\mathcal{P}_{[P,D,z,\alpha]}$ $\mathcal{P}_{[P,2D,z,\alpha]}$
	3C	1 (1.99) [c]	0.227	2.35e-04	0.220	5.35e-14	1.34
BRW-modified [b]	6C	0.964	0.887	0.0136	0.298	9.98e-11	1.48
	7C	1.38	4.60e-04	0.218	0.00126	0.00154	
	3C	1 (1.61)	0.385	9.79e-08	0.247	0.0632	1.83
KDA Env. [d]	6C	1.26	0.963	0.641	0.287	6.89e-07	2.23
β, a_0, ρ_0	7C	1.62	3.45e-06	0.00105	1.27e-05	0.0198	
	3C	1 (7.08)	0.0110	2.76e-10	0.0616	3.54e-08	0.511
$\beta = 1.0$	6C	0.925	0.416	1.81e-07	0.183	2.11e-09	0.571
	7C	0.967	6.84e-06	0.0978	2.36e-04	0.00112	
	3C	1 (0.662)	0.134	1.02e-15	0.358	0.256	0.638 [h]
$\beta = 2.0$	6C	1.21	0.0908	7.07e-06	0.335	2.72e-04	0.639 [h]
	7C	1.82	1.60e-04	9.49e-04	1.54e-05	0.0554	
	3C	1 (1.21)	0.0530	1.01e-07	0.0532	1.44e-16	0.791
$a_0 = 7.5$ kpc	6C	1.15	0.362	0.0626	0.0754	1.96e-06	1.18
	7C	1.46	0.0169	0.572	0.00458	0.00861	
	3C	1 (3.36)	0.197	2.25e-04	0.477	3.01e-08	2.07
$a_0 = 15$ kpc	6C	1.00	0.932	0.00148	0.408	7.24e-09	2.62
	7C	1.39	1.32e-04	0.893	3.99e-04	0.00122	
	3C	1 (4.90)	0.0629	8.88e-06	0.148	1.76e-06	0.865
$a_0 = 20$ kpc	6C	1.16	0.564	6.91e-04	0.287	2.11e-09	0.982
	7C	1.32	3.58e-06	0.190	4.28e-05	5.45e-06	
	3C	1 (0.848)	0.136	2.50e-06	0.171	1.08e-15	0.790
$\rho_0 = \rho_1$ [e]	6C	1.20	0.107	0.0212	0.0126	5.35e-06	1.15

Continued on next page ...

Table B.1: continued from previous page ...

Varied Model Parameter	Survey	Ratio_{3C} Ratio_{6C} Ratio_{7C}	$\mathcal{P}(K\text{–}S)$				$\mathcal{P}_{[P,D,z,\alpha]}$ $\mathcal{P}_{[P,2D,z,\alpha]}$
			$\mathcal{P}(P)$	$\mathcal{P}(D)$	$\mathcal{P}(z)$	$\mathcal{P}(\alpha)$	
	7C	1.51	0.0367	0.565	0.0161	3.15e-05	
$\rho_0 = \rho_2$ [f]	3C	1 (3.66)	0.152	1.42e-04	0.388	6.40e-08	1.51
	6C	0.982	0.963	0.0357	0.408	2.11e-09	1.61
	7C	1.37	2.30e-05	0.129	2.34e-04	3.76e-05	
$\rho_0 = \rho_3$ [g]	3C	1 (6.58)	0.0229	0.0365	0.0616	3.22e-11	0.656
	6C	1.12	0.416	0.0202	0.287	5.79e-13	0.783
	7C	1.28	4.48e-07	0.128	2.35e-05	6.46e-07	
$\Gamma_C = 5/3$	3C	1 (0.159)	0.00283	0.00201	0.0105	0.0361	1.13 [h]
	6C	1.35	0.987	0.00293	0.764	0.0261	1.14 [h]
	7C	1.75	0.698	0.00197	0.569	0.00528	
$\gamma_{min(hs)} = 10$	3C	1 (2.62)	0.319	4.87e-06	0.485	2.07e-12	2.03
	6C	0.954	0.950	0.0212	0.408	7.62e-08	2.39
	7C	1.34	6.97e-04	0.575	0.00111	0.00917	
$\gamma_{max(hs)} = 10^{10}$	3C	1 (1.99)	0.221	2.62e-06	0.221	1.05e-15	1.14
	6C	0.995	0.533	0.00601	0.272	7.62e-08	1.33
	7C	1.40	0.00455	0.301	0.00287	0.00468	
$\gamma_{max(hs)} = 10^{16}$	3C	1 (1.99)	0.227	8.37e-05	0.220	5.35e-14	1.09
	6C	0.998	0.533	0.00158	0.272	7.62e-08	1.21
	7C	1.41	0.00455	0.199	0.00287	0.00468	
$p = 2.001$	3C	1 (1.12)	0.00898	1.59e-05	0.0191	3.98e-16	0.315
	6C	1.06	0.0661	0.00158	0.00675	2.33e-07	0.490
	7C	1.35	0.0353	0.286	0.0344	0.0198	
$p = 2.5$	3C	1 (2.90)	0.252	6.14e-04	0.485	1.47e-08	1.73
	6C	1.02	0.869	0.0344	0.556	7.24e-09	1.83
	7C	1.44	6.84e-06	0.121	2.34e-04	0.0104	
$p = 2.999$	3C	1 (3.03)	0.198	1.41e-04	0.371	5.09e-12	1.79
	6C	1.11	0.869	0.0206	0.194	7.24e-09	2.34
	7C	1.52	8.02e-05	0.879	1.35e-04	0.00468	
$t_{bs} = 10^3$ yr	3C	1 (1.39)	0.130	2.70e-05	0.0532	2.83e-15	0.743
	6C	1.12	0.509	0.00622	0.109	7.62e-08	0.863

Continued on next page ...

Table B.1: continued from previous page ...

Varied Model Parameter	Survey	Ratio_{3C} Ratio_{6C} Ratio_{7C}	$\mathcal{P}(K$–$S)$				$\mathcal{P}_{[P,D,z,\alpha]}$ $\mathcal{P}_{[P,2D,z,\alpha]}$
			$\mathcal{P}(P)$	$\mathcal{P}(D)$	$\mathcal{P}(z)$	$\mathcal{P}(\alpha)$	
	7C	1.46	0.0371	0.190	0.0161	0.0192	
	3C	1 (1.70)	7.23e-04	1.90e-07	6.75e-04	1.28e-07	0.397
$t_{bs} = 10^7$ yr	6C	1.04	0.389	0.0110	0.0667	2.11e-09	0.477
	7C	1.49	0.0113	0.121	0.0166	1.46e-05	
	3C	1 (1.8)	0.0978	1.02e-07	0.130	2.79e-15	0.809
$t_{bf} = 0.01$ yr	6C	0.992	0.641	0.00150	0.188	7.62e-08	0.857
	7C	1.46	0.00481	0.0770	0.00458	0.00500	
	3C	1 (2.10)	0.320	2.79e-05	0.351	5.88e-11	1.22
$t_{bf} = 10$ yr	6C	0.962	0.542	0.0111	0.188	7.62e-08	1.31
	7C	1.38	0.00181	0.131	0.00287	0.0103	
	3C	1 (2.28)	0.320	0.00100	0.524	4.91e-12	2.31
$t_{bf} = 100$ yr	6C	0.947	0.953	0.349	0.283	7.62e-08	3.00
	7C	1.35	0.00180	0.760	0.00182	0.00230	
	3C	1 (2.51)	0.254	2.77e-05	0.485	2.05e-12	1.84
$t_{bf} = 10^3$ yr	6C	0.939	0.730	0.0626	0.404	7.62e-08	2.23
	7C	1.37	2.32e-04	0.565	0.00111	0.00861	
$t_{bf} = 100$ yr	3C	1 (3.03)	0.254	0.00101	0.485	1.65e-09	2.24
$\gamma_{min(hs)} = 10$	6C	0.977	0.998	0.0231	0.556	7.62e-08	2.75
	7C	1.32	2.29e-04	0.819	3.99e-04	0.00237	
$t_{bf} = 100$ yr	3C	1 (1.86)	0.147	1.07e-07	0.192	0.0385	1.17
KDA Env. [d]	6C	1.22	0.684	0.0626	0.556	6.89e-07	1.22
β, a_0, ρ_0	7C	1.62	3.45e-06	0.0163	1.27e-05	0.0103	
$t_{bf} = 100$ yr	3C	1 (3.86)	0.152	1.42e-04	0.312	1.73e-06	1.45
$a_0 = 15$ kpc	6C	0.994	0.564	0.0371	0.408	7.24e-09	1.83
	7C	1.35	1.36e-04	0.575	1.35e-04	9.32e-05	
$\gamma_{min(hs)} = 10$	3C	1 (2.23)	0.0978	7.58e-07	0.148	0.0200	0.849
KDA Env. [d]	6C	1.22	0.177	0.0371	0.724	2.33e-07	0.882
β, a_0, ρ_0	7C	1.59	7.63e-05	0.0155	6.77e-06	0.0198	
$\gamma_{min(hs)} = 10$	3C	1 (4.54)	0.115	3.97e-07	0.192	3.54e-09	1.17
$a_0 = 15$ kpc	6C	1.05	0.564	2.50e-05	0.408	7.24e-09	1.42

Continued on next page ...

Table B.1: continued from previous page ...

Varied Model Parameter	Survey	Ratio_{3C} Ratio_{6C} Ratio_{7C}	$\mathcal{P}(K\text{–}S)$				$\mathcal{P}_{[P,D,z,\alpha]}$ $\mathcal{P}_{[P,2D,z,\alpha]}$
			$\mathcal{P}(P)$	$\mathcal{P}(D)$	$\mathcal{P}(z)$	$\mathcal{P}(\alpha)$	
	7C	1.30	6.84e-06	0.412	7.67e-05	3.76e-05	

[a] Each run (with one or more parameter variations) is done with the same initial ensemble (Set 1) of size 4963343, which is generated using $x = 3.0$ and $T_{MaxAge} = 300$ Myr.

[b] Parameter values for dynamical and power evolution of radio sources are set equal to those given in the BRW model (Blundell et al. 1999) (Table 2.1), except for assuming that the hotspot size grows with source age according to Jeyakumar & Saikia (2000).

[c] Always, $\text{Ratio}_{3C} = 1$, because of the way it is defined. The number in parentheses gives the ratio of the number of sources detected in 3C simulation (with given ensemble size) as compared to the real 3C survey.

[d] Parameters defining the external environment density profile are set to those of the KDA model, namely, $\beta = 1.9, a_0 = 2$ kpc, $\rho_0 = 7.2 \times 10^{-22}$ kg m^{-3}.

[e] $\rho_1 = \rho_{0\ \text{(Default)}}/2 = 8.35 \times 10^{-24}$ kg m^{-3}.

[f] $\rho_2 = 2 \times \rho_{0\ \text{(Default)}} = 3.34 \times 10^{-23}$ kg m^{-3}.

[g] $\rho_3 = 4 \times \rho_{0\ \text{(Default)}} = 6.68 \times 10^{-23}$ kg m^{-3}.

[h] Numbers of sources detected in some of the simulated surveys are considerably smaller than in the real surveys, so the 1-D K-S statistic does not hold much significance.

Table B.2: Modified BRW Model Results for Run 2: 1-D K-S Statistics [a]

Varied Model Parameter	Survey	Ratio_{3C} Ratio_{6C} Ratio_{7C}	$\mathcal{P}(K\text{–}S)$ $\mathcal{P}(P)$	$\mathcal{P}(D)$	$\mathcal{P}(z)$	$\mathcal{P}(\alpha)$	$\mathcal{P}_{[P,D,z,\alpha]}$ $\mathcal{P}_{[P,2D,z,\alpha]}$
BRW-modified [b]	3C	1 (1.85)	0.320	9.70e-04	0.581	2.69e-11	1.75
	6C	1.12	0.897	0.0709	0.131	9.98e-11	1.95
	7C	1.47	2.80e-04	0.248	7.56e-04	0.00148	
KDA Env. [c]	3C	1 (1.72)	0.302	7.35e-07	0.474	0.00616	2.28
β, a_0, ρ_0	6C	1.34	0.951	0.0212	0.960	2.33e-07	2.57
	7C	1.54	1.27e-05	0.454	2.32e-05	0.0104	
$a_0 = 15$ kpc	3C	1 (3.36)	0.150	8.88e-06	0.474	3.18e-08	1.55
	6C	1.02	0.864	0.0117	0.287	7.24e-09	1.76
	7C	1.42	2.36e-04	0.319	2.34e-04	5.49e-04	
$a_0 = 20$ kpc	3C	1 (4.99)	0.0621	0.00159	0.148	1.97e-06	1.29
	6C	1.12	0.724	0.0371	0.550	2.11e-09	1.57
	7C	1.35	6.84e-06	0.412	4.28e-05	5.45e-06	
$\rho_0 = \rho_2$ [d]	3C	1 (3.66)	0.196	2.36e-04	0.387	6.34e-08	1.52
	6C	1.02	0.724	0.0111	0.404	2.11e-09	1.75
	7C	1.42	3.96e-04	0.360	1.35e-04	1.46e-05	
$\gamma_{min(hs)} = 10$	3C	1 (2.43)	0.197	0.0179	0.485	1.38e-08	1.61
	6C	1.15	0.701	0.0685	0.389	7.62e-08	1.84
	7C	1.43	0.00111	0.286	3.99e-04	0.0104	
$\gamma_{max(hs)} = 10^{10}$	3C	1 (1.86)	0.320	0.00159	0.581	1.11e-11	1.57
	6C	1.16	0.389	0.0354	0.0735	7.62e-08	1.94
	7C	1.50	0.0106	0.565	0.00180	0.00468	
$p = 2.5$	3C	1 (2.83)	0.152	2.68e-05	0.485	1.46e-09	1.41
	6C	1.10	0.416	0.0626	0.194	7.24e-09	1.80
	7C	1.48	7.63e-05	0.572	7.67e-05	5.32e-04	
$p = 2.999$	3C	1 (2.94)	0.197	0.00153	0.144	1.42e-08	1.53
	6C	1.15	0.564	0.474	0.126	7.24e-09	2.28
	7C	1.57	4.32e-05	0.738	7.67e-05	0.00247	
$t_{bf} = 10$ yr	3C	1 (1.95)	0.320	6.06e-04	0.581	5.78e-11	1.33
	6C	1.09	0.389	0.0126	0.0735	7.62e-08	1.45
	7C	1.48	0.00723	0.190	0.00180	0.00247	

Continued on next page ...

Table B.2: continued from previous page ...

Varied Model Parameter	Survey	Ratio$_{3C}$ Ratio$_{6C}$ Ratio$_{7C}$	$\mathcal{P}(K$–$S)$				$\mathcal{P}_{[P,D,z,\alpha]}$ $\mathcal{P}_{[P,2D,z,\alpha]}$
			$\mathcal{P}(P)$	$\mathcal{P}(D)$	$\mathcal{P}(z)$	$\mathcal{P}(\alpha)$	
	3C	1 (2.09)	0.253	6.30e-04	0.485	3.26e-10	1.27
$t_{bf} = 100$ yr	6C	1.07	0.362	0.0968	0.183	7.62e-08	1.46
	7C	1.50	0.00298	0.204	6.70e-04	0.00247	
	3C	1 (2.32)	0.198	2.28e-04	0.485	4.97e-12	1.72
$t_{bf} = 10^3$ yr	6C	1.09	0.713	0.0626	0.283	7.62e-08	2.13
	7C	1.46	1.27e-05	0.603	3.99e-04	0.00481	
$t_{bf} = 100$ yr	3C	1 (3.01)	0.122	0.0252	0.387	2.40e-07	1.49
$\gamma_{min(hs)} = 10$	6C	1.10	0.564	0.0582	0.556	7.62e-08	1.76
	7C	1.34	4.03e-04	0.343	1.35e-04	1.98e-04	
$t_{bf} = 100$ yr	3C	1 (3.92)	0.150	0.00366	0.312	1.76e-06	1.47
$a_0 = 15$ kpc	6C	0.992	0.416	0.00622	0.408	7.24e-09	1.96
	7C	1.37	1.27e-05	0.784	7.67e-05	5.49e-04	

[a] Each run (with one or more parameter variations) is done with the same initial ensemble (Set 2) of size 4963343, which is generated using $x = 3.0$ and $T_{MaxAge} = 300$ Myr.

[b] Parameter values for dynamical and power evolution of radio sources are set equal to those given in the BRW model (Blundell et al. 1999) (Table 2.1), except for assuming that the hotspot size grows with source age according to Jeyakumar & Saikia (2000).

[c] Parameters defining the external environment density profile are set to those of the KDA model, namely, $\beta = 1.9, a_0 = 2$ kpc, $\rho_0 = 7.2 \times 10^{-22}$ kg m^{-3}.

[d] $\rho_2 = 2 \times \rho_{0\ \text{(Default)}} = 3.34 \times 10^{-23}$ kg m^{-3}.

Table B.3: Modified BRW Model Results for Run 3: 1-D K-S Statistics [a]

Varied Model Parameter	Survey	Ratio_{3C} Ratio_{6C} Ratio_{7C}	$\mathcal{P}(K\text{–}S)$ $\mathcal{P}(P)$	$\mathcal{P}(D)$	$\mathcal{P}(z)$	$\mathcal{P}(\alpha)$	$\mathcal{P}_{[P,D,z,\alpha]}$ $\mathcal{P}_{[P,2D,z,\alpha]}$
BRW-modified [b]	3C	1 (1.78)	0.290	1.02e-07	0.354	1.31e-13	1.61
	6C	1.18	0.583	0.509	0.295	9.98e-11	2.02
	7C	1.55	0.00207	0.142	0.00200	0.00316	
KDA Env. [c]	3C	1 (1.48)	0.574	2.87e-09	0.474	0.0632	1.62
β, a_0, ρ_0	6C	1.59	0.564	0.00587	0.287	6.76e-07	1.66
	7C	1.80	7.49e-05	0.0510	7.43e-05	0.0104	
$a_0 = 15$ kpc	3C	1 (3.30)	0.114	4.89e-06	0.474	1.55e-08	2.32
	6C	1.12	0.954	0.482	0.533	7.24e-09	3.10
	7C	1.29	4.32e-05	0.790	0.00111	0.00120	
$a_0 = 20$ kpc	3C	1 (5.08)	0.0850	4.89e-06	0.148	4.86e-07	0.862
	6C	1.16	0.293	0.232	0.287	2.11e-09	1.12
	7C	1.22	1.32e-04	0.190	1.35e-04	5.45e-06	
$\rho_0 = \rho_2$ [d]	3C	1 (3.61)	0.115	0.0181	0.312	1.28e-07	1.39
	6C	1.09	0.564	0.0357	0.404	2.11e-09	1.74
	7C	1.25	7.74e-05	0.504	6.70e-04	9.32e-05	
$\gamma_{min(hs)} = 10$	3C	1 (2.46)	0.320	1.57e-05	0.484	1.65e-09	1.89
	6C	1.21	0.710	0.323	0.408	7.62e-08	2.27
	7C	1.39	0.00111	0.286	0.00111	0.00534	
$\gamma_{max(hs)} = 10^{10}$	3C	1 (1.79)	0.177	1.51e-05	0.353	7.92e-13	1.88
	6C	1.25	0.811	0.327	0.272	7.62e-08	2.53
	7C	1.57	0.00286	0.732	0.00451	0.00214	
$p = 2.5$	3C	1 (2.76)	0.197	2.66e-06	0.484	5.88e-11	1.47
	6C	1.29	0.724	0.0344	0.408	7.24e-09	1.54
	7C	1.43	1.36e-04	0.0763	6.70e-04	0.00534	
$p = 2.999$	3C	1 (3.0)	0.253	2.63e-06	0.385	8.37e-13	1.59
	6C	1.32	0.564	0.0951	0.408	7.24e-09	1.93
	7C	1.39	7.49e-05	0.454	6.59e-04	0.00237	
$t_{bf} = 10$ yr	3C	1 (1.89)	0.320	3.87e-04	0.526	2.13e-12	1.30
	6C	1.24	0.276	0.0935	0.272	7.62e-08	1.41
	7C	1.53	0.00178	0.0741	0.00451	0.00500	

Continued on next page ...

Table B.3: continued from previous page ...

Varied Model Parameter	Survey	Ratio_{3C} Ratio_{6C} Ratio_{7C}	$\mathcal{P}(K\text{–}S)$				$\mathcal{P}_{[P,D,z,\alpha]}$ $\mathcal{P}_{[P,2D,z,\alpha]}$
			$\mathcal{P}(P)$	$\mathcal{P}(D)$	$\mathcal{P}(z)$	$\mathcal{P}(\alpha)$	
	3C	1 (2.10)	0.253	1.21e-08	0.580	5.04e-14	1.80
$t_{bf} = 100$ yr	6C	1.18	0.542	0.0212	0.389	7.62e-08	2.17
	7C	1.47	0.00187	0.584	0.00180	0.00917	
	3C	1 (2.37)	0.320	8.84e-06	0.484	1.43e-09	2.09
$t_{bf} = 10^3$ yr	6C	1.16	0.960	0.0572	0.408	7.62e-08	2.50
	7C	1.41	0.00450	0.619	0.00180	0.00109	
$t_{bf} = 100$ yr	3C	1 (2.99)	0.197	6.30e-04	0.474	1.31e-13	1.61
$\gamma_{min(hs)} = 10$	6C	1.19	0.724	0.154	0.408	7.62e-08	1.82
	7C	1.27	1.34e-04	0.194	6.70e-04	0.00534	
$t_{bf} = 100$ yr	3C	1 (3.79)	0.151	0.00247	0.312	3.03e-08	1.50
$a_0 = 15$ kpc	6C	1.12	0.867	0.234	0.408	7.24e-09	1.73
	7C	1.25	2.33e-05	0.130	3.99e-04	5.49e-04	

[a] Each run (with one or more parameter variations) is done with the same initial ensemble (Set 3) of size 4963343, which is generated using $x = 3.0$ and $T_{MaxAge} = 300$ Myr.

[b] Parameter values for dynamical and power evolution of radio sources are set equal to those given in the BRW model (Blundell et al. 1999) (Table 2.1), except for assuming that the hotspot size grows with source age according to (Jeyakumar & Saikia 2000).

[c] Parameters defining the external environment density profile are set to those of the KDA model, namely, $\beta = 1.9, a_0 = 2$ kpc, $\rho_0 = 7.2 \times 10^{-22}$ kg m^{-3}.

[d] $\rho_2 = 2 \times \rho_{0\ \text{(Default)}} = 3.34 \times 10^{-23}$ kg m^{-3}.

Table B.4: Modified BRW Model Results for Run 4: 1-D K-S Statistics [a]

Varied Model Parameter	Survey	Ratio_{3C} Ratio_{6C} Ratio_{7C}	$\mathcal{P}(K\text{–}S)$ $\mathcal{P}(P)$	$\mathcal{P}(D)$	$\mathcal{P}(z)$	$\mathcal{P}(\alpha)$	$\mathcal{P}_{[P,D,z,\alpha]}$ $\mathcal{P}_{[P,2D,z,\alpha]}$
BRW-modified [b]	3C	1 (1.68)	0.177	8.37e-05	0.171	3.29e-13	1.73
	6C	1.15	0.481	0.0402	0.897	3.58e-10	2.23
	7C	1.58	0.00202	0.787	4.54e-04	0.00296	
KDA Env. [c]	3C	1 (1.61)	0.194	2.37e-08	0.680	0.0632	1.810
	6C	1.40	0.520	7.50e-04	0.956	2.33e-07	1.812
β, a_0, ρ_0	7C	1.63	7.74e-05	0.00214	4.28e-05	0.0104	
$a_0 = 15$ kpc	3C	1 (3.21)	0.198	2.63e-06	0.474	6.10e-08	1.54
	6C	1.11	0.416	0.00158	0.556	7.24e-09	1.80
	7C	1.49	6.77e-06	0.420	7.67e-05	0.00120	
$a_0 = 20$ kpc	3C	1 (4.79)	0.0621	1.42e-04	0.112	9.34e-07	0.901
	6C	1.15	0.564	0.153	0.408	2.11e-09	1.01
	7C	1.37	9.35e-07	0.0247	4.28e-05	5.45e-06	
$\rho_0 = \rho_2$ [d]	3C	1 (3.50)	0.0852	4.89e-06	0.387	3.26e-10	1.77
	6C	1.13	0.724	0.0582	0.556	2.11e-09	2.26
	7C	1.45	2.36e-04	0.741	1.35e-04	1.46e-05	
$\gamma_{min(hs)} = 10$	3C	1 (2.37)	0.253	1.36e-04	0.579	6.02e-11	2.31
	6C	1.19	0.831	0.227	0.716	7.62e-08	2.81
	7C	1.48	7.70e-05	0.584	1.35e-04	0.00117	
$\gamma_{max(hs)} = 10^{10}$	3C	1 (1.68)	0.177	2.79e-05	0.171	3.29e-13	2.29
	6C	1.19	0.943	0.234	0.994	7.62e-08	3.01
	7C	1.61	0.00115	0.932	0.00111	4.56e-04	
$p = 2.5$	3C	1 (2.69)	0.253	2.36e-04	0.451	1.20e-11	1.79
	6C	1.27	0.724	0.0361	0.556	7.24e-09	2.06
	7C	1.53	2.34e-05	0.412	7.56e-05	0.00534	
$p = 2.999$	3C	1 (2.91)	0.177	3.89e-04	0.297	8.34e-15	1.22
	6C	1.25	0.564	0.0354	0.287	7.24e-09	1.43
	7C	1.56	2.34e-05	0.305	4.28e-05	0.00481	
$t_{bf} = 10$ yr	3C	1 (1.76)	0.290	8.81e-06	0.280	2.91e-15	2.06
	6C	1.19	0.771	0.0609	0.945	7.62e-08	2.47
	7C	1.59	4.03e-04	0.603	6.70e-04	0.00976	

Continued on next page ...

Table B.4: continued from previous page ...

Varied Model Parameter	Survey	Ratio$_{3C}$ Ratio$_{6C}$ Ratio$_{7C}$	$\mathcal{P}(K$–$S)$				$\mathcal{P}_{[P,D,z,\alpha]}$ $\mathcal{P}_{[P,2D,z,\alpha]}$
			$\mathcal{P}(P)$	$\mathcal{P}(D)$	$\mathcal{P}(z)$	$\mathcal{P}(\alpha)$	
	3C	1 (1.94)	0.253	8.37e-05	0.622	8.34e-15	2.66
$t_{bf} = 100$ yr	6C	1.20	0.869	0.234	0.862	7.62e-08	3.34
	7C	1.55	6.75e-04	0.879	3.99e-04	0.00481	
	3C	1 (2.23)	0.198	2.36e-04	0.579	6.44e-11	2.05
$t_{bf} = 10^3$ yr	6C	1.17	0.878	0.00300	0.862	7.62e-08	2.23
	7C	1.52	3.96e-04	0.286	1.35e-04	0.00500	
$t_{bf} = 100$ yr	3C	1 (2.86)	0.113	0.00379	0.483	2.80e-11	2.11
$\gamma_{min(hs)} = 10$	6C	1.16	0.869	0.159	0.716	7.62e-08	2.62
	7C	1.38	3.52e-06	0.668	4.28e-05	0.00917	
$t_{bf} = 100$ yr	3C	1 (3.71)	0.0624	2.66e-06	0.247	1.76e-06	1.58
$a_0 = 15$ kpc	6C	1.16	0.416	0.0992	0.556	2.11e-09	2.23
	7C	1.41	0.00115	0.971	7.67e-05	5.49e-04	

[a] Each run (with one or more parameter variations) is done with the same initial ensemble (Set 4) of size 4963343, which is generated using $x = 3.0$ and $T_{MaxAge} = 300$ Myr.

[b] Parameter values for dynamical and power evolution of radio sources are set equal to those given in the BRW model (Blundell et al. 1999) (Table 2.1), except for assuming that the hotspot size grows with source age according to Jeyakumar & Saikia (2000).

[c] Parameters defining the external environment density profile are set to those of the KDA model, namely, $\beta = 1.9, a_0 = 2$ kpc, $\rho_0 = 7.2 \times 10^{-22}$ kg m^{-3}.

[d] $\rho_2 = 2 \times \rho_{0\ \text{(Default)}} = 3.34 \times 10^{-23}$ kg m^{-3}.

Table B.5: Modified BRW Model Results: Performance Ranks [a]

Model	$\mathcal{P}(K\text{–}S)$	Run 1	Run 2	Run 3	Run 4	Average [b]
Modified [c]	$\mathcal{P}_{[P,D,z,\alpha]}$	11	2	7	10	7.5
	$\mathcal{P}_{[P,2D,z,\alpha]}$	11	5	6	8	7.5
KDA Env. [d]	$\mathcal{P}_{[P,D,z,\alpha]}$	6	1	6	7	5
β, a_0, ρ_0	$\mathcal{P}_{[P,2D,z,\alpha]}$	6	1	11	11	7.25
$a_0 = 15$ kpc	$\mathcal{P}_{[P,D,z,\alpha]}$	3	6	1	12	5.5
	$\mathcal{P}_{[P,2D,z,\alpha]}$	3	10	1	12	6.5
$a_0 = 20$ kpc	$\mathcal{P}_{[P,D,z,\alpha]}$	14	13	14	14	13.75
	$\mathcal{P}_{[P,2D,z,\alpha]}$	14	12	14	14	13.5
$\rho_0 = \rho_2$ [e]	$\mathcal{P}_{[P,D,z,\alpha]}$	9	8	12	9	9.5
	$\mathcal{P}_{[P,2D,z,\alpha]}$	10	11	9	6	9
$\gamma_{min(hs)} = 10$	$\mathcal{P}_{[P,D,z,\alpha]}$	4	4	3	2	3.25
	$\mathcal{P}_{[P,2D,z,\alpha]}$	4	7	4	3	4.5
$\gamma_{max(hs)} = 10^{10}$	$\mathcal{P}_{[P,D,z,\alpha]}$	13	5	4	3	6.25
	$\mathcal{P}_{[P,2D,z,\alpha]}$	12	6	2	2	5.5
$p = 2.5$	$\mathcal{P}_{[P,D,z,\alpha]}$	8	11	11	8	9.5
	$\mathcal{P}_{[P,2D,z,\alpha]}$	8	8	12	10	9.5
$p = 2.999$	$\mathcal{P}_{[P,D,z,\alpha]}$	7	7	9	13	9
	$\mathcal{P}_{[P,2D,z,\alpha]}$	5	2	7	13	6.75
$t_{bf} = 10$ yr	$\mathcal{P}_{[P,D,z,\alpha]}$	12	12	13	5	10.5
	$\mathcal{P}_{[P,2D,z,\alpha]}$	13	14	13	5	11.25
$t_{bf} = 100$ yr	$\mathcal{P}_{[P,D,z,\alpha]}$	1	14	5	1	5.25
	$\mathcal{P}_{[P,2D,z,\alpha]}$	1	13	5	1	5
$t_{bf} = 10^3$ yr	$\mathcal{P}_{[P,D,z,\alpha]}$	5	3	2	6	4
	$\mathcal{P}_{[P,2D,z,\alpha]}$	7	3	3	9	5.5
$t_{bf} = 100$ yr	$\mathcal{P}_{[P,D,z,\alpha]}$	2	9	8	4	5.75
$\gamma_{min(hs)} = 10$	$\mathcal{P}_{[P,2D,z,\alpha]}$	2	9	8	4	5.75
$t_{bf} = 100$ yr	$\mathcal{P}_{[P,D,z,\alpha]}$	10	10	10	11	10.25
$a_0 = 15$ kpc	$\mathcal{P}_{[P,2D,z,\alpha]}$	9	4	10	7	7.5

[a] Each run is done using $x = 3.0$ and $T_{MaxAge} = 300$ Myr for the initial population of size 4963343; the 4 runs, whose ranks are displayed, differ in the initial random seeds. The ranks are according to the combined 1-D K-S statistic results of the 4 runs tabulated in detail in Tables B.1, B.2, B.3 and B.4, which are also summarised in Table 5.9.

[b] Overall rank score (obtained by averaging separate ranks from the four runs) of each of the 14 BRW-modified cases shown here.

[c] Parameter values for dynamical and power evolution of radio sources are set equal to those given in the BRW model (Blundell et al. 1999) (Table 2.1), except for assuming that the hotspot size grows with source age according to Jeyakumar & Saikia (2000).

[d] Parameters defining the external environment density profile are set to those of the KDA model, namely, $\beta = 1.9, a_0 = 2$ kpc, $\rho_0 = 7.2 \times 10^{-22}$ kg m^{-3}.

[e] $\rho_2 = 2 \times \rho_{0\ \text{(Default)}} = 3.34 \times 10^{-23}$ kg m^{-3}.

B.2 Modified MK Model

Table B.6: Modified MK Model Results for Run 1: 1-D K-S Statistics [a]

Varied Model Parameter	Survey	Ratio_{3C} Ratio_{6C} Ratio_{7C}	$\mathcal{P}(K\text{–}S)$ $\mathcal{P}(P)$	$\mathcal{P}(D)$	$\mathcal{P}(z)$	$\mathcal{P}(\alpha)$	$\mathcal{P}_{[P,D,z,\alpha]}$ $\mathcal{P}_{[P,2D,z,\alpha]}$
MK-modified	3C	1 (1.66) [b]	0.0122	0.420	0.360	0	1.91
	6C	1.02	0.564	0.0643	0.556	1.83e-24	2.73
	7C	1.34	1.34e-04	0.584	0.0161	4.15e-20	
KDA Env. [c] β, a_0, ρ_0	3C	1 (1.81)	0.00553	0.00253	0.485	0	1.55
	6C	0.866	0.157	0.485	0.556	1.83e-24	2.15
	7C	1.30	1.24e-05	0.483	0.00180	2.79e-19	
$\beta = 1.0$	3C	1 (2.34)	0.00368	8.37e-05	0.474	0	1.27
	6C	0.886	0.331	7.50e-04	0.498	1.83e-24	1.54
	7C	1.21	4.26e-05	0.434	0.00710	8.39e-22	
$\beta = 1.6$	3C	1 (1.58)	0.0253	0.425	0.227	0	2.07
	6C	0.961	0.464	0.234	0.556	1.83e-24	3.22
	7C	1.31	2.29e-04	0.959	0.0108	2.79e-19	
$a_0 = 7.5$ kpc	3C	1 (1.33)	0.0681	0.420	0.0399	0	1.52
	6C	0.966	0.229	0.0609	0.716	1.83e-24	2.32
	7C	1.40	4.03e-04	0.565	0.0108	4.30e-20	
$a_0 = 20$ kpc	3C	1 (2.84)	0.00359	0.718	0.312	0	1.74
	6C	0.999	0.416	3.44e-04	0.408	1.83e-24	2.64
	7C	1.26	4.18e-05	0.301	0.00182	8.39e-22	
$\rho_0 = \rho_1$ [d]	3C	1 (1.35)	0.0921	0.0260	0.0399	0	0.987
	6C	0.964	0.229	0.0117	0.655	1.83e-24	1.27
	7C	1.39	6.56e-04	0.412	0.0108	4.30e-20	
$\rho_0 = \rho_2$ [e]	3C	1 (2.37)	0.00826	0.425	0.483	0	1.58
	6C	0.959	0.293	7.50e-04	0.556	1.83e-24	2.13
	7C	1.30	7.74e-05	0.204	0.00291	6.13e-21	
$\gamma_{min(hs)} = 7$	3C	1 (1.08)	0.0921	0.0697	0.101	0	1.31
	6C	1.01	0.224	0.102	0.556	1.83e-24	1.93
	7C	1.33	2.33e-05	0.790	0.0108	8.39e-22	

Continued on next page ...

Table B.6: continued from previous page ...

Varied Model Parameter	Survey	Ratio_{3C} Ratio_{6C} Ratio_{7C}	$\mathcal{P}(K\text{–}S)$ $\mathcal{P}(P)$	$\mathcal{P}(D)$	$\mathcal{P}(z)$	$\mathcal{P}(\alpha)$	$\mathcal{P}_{[P,D,z,\alpha]}$ $\mathcal{P}_{[P,2D,z,\alpha]}$
$\gamma_{min(hs)} = 100$	3C	1 (10.8)	8.29e-04	2.01e-07	0.00485	0	0.199
	6C	0.840	0.0809	4.05e-06	0.199	6.76e-22	0.216
	7C	1.02	9.50e-10	0.0267	9.25e-07	1.74e-18	
$\gamma_{max(hs)} = 3 \times 10^8$	3C	1 (1.61)	0.00826	0.419	0.288	0	1.66
	6C	0.989	0.724	0.0626	0.408	1.83e-24	2.29
	7C	1.34	2.29e-04	0.286	0.0161	4.15e-20	
$p = 2.001$	3C	1 (2.35)	0.0629	0.00159	0.483	2.45e-39	1.22
	6C	1.01	0.575	2.55e-05	0.362	4.45e-21	1.31
	7C	1.40	1.36e-04	0.131	0.00458	6.90e-17	
$p = 2.3$	3C	1 (1.26)	0.0356	0.510	0.135	0	2.02
	6C	0.934	0.293	0.102	0.716	1.83e-24	3.20
	7C	1.36	0.00108	0.999	0.0238	3.72e-20	
$\epsilon = 0.675$	3C	1 (1.64)	0.0911	0.00159	0.227	0	1.07
	6C	1.10	0.564	0.00158	0.408	1.83e-24	1.19
	7C	1.42	6.64e-04	0.190	0.0161	6.13e-21	
$\epsilon = 1.4$	3C	1 (1.81)	0.0177	0.275	0.485	0	1.98
	6C	0.870	0.229	0.234	0.556	1.35e-23	2.96
	7C	1.28	2.30e-05	0.913	0.00458	2.89e-19	
$\eta = 0.2$	3C	1 (0.545)	0.00922	0.0365	7.11e-04	0	1.01 [f]
	6C	1.05	0.333	7.50e-04	0.533	1.83e-24	1.17 [f]
	7C	1.27	0.0173	0.204	0.293	4.30e-20	
$\eta = 0.6$	3C	1 (3.23)	0.0175	0.532	0.192	0	1.44
	6C	1.00	0.416	0.00152	0.556	1.83e-24	2.05
	7C	1.21	1.10e-07	0.128	6.81e-04	4.15e-20	
$\tau = 2 \times 10^{-4}$	3C	1 (4.06)	0.0253	4.88e-05	0.112	0	0.680
	6C	0.994	0.564	1.65e-07	0.267	1.40e-23	0.696
	7C	1.25	3.58e-06	0.0273	4.06e-04	1.74e-18	
$\tau = 3 \times 10^{-3}$	3C	1 (1.19)	0.0497	0.167	0.135	0	1.37
	6C	0.933	0.0959	0.240	0.564	1.83e-24	2.14
	7C	1.34	1.34e-04	0.732	0.00708	5.91e-21	

Continued on next page ...

Table B.6: continued from previous page ...

Varied Model Parameter	Survey	Ratio_{3C} Ratio_{6C} Ratio_{7C}	$\mathcal{P}(K\text{–}S)$				$\mathcal{P}_{[P,D,z,\alpha]}$ $\mathcal{P}_{[P,2D,z,\alpha]}$
			$\mathcal{P}(P)$	$\mathcal{P}(D)$	$\mathcal{P}(z)$	$\mathcal{P}(\alpha)$	
$\epsilon = 1.4$	3C	1 (1.63)	0.00154	0.217	0.485	0	1.64
$\beta = 1.6$	6C	0.885	0.0709	0.0626	0.408	1.40e-23	2.49
	7C	1.30	2.30e-05	0.971	0.00183	2.79e-19	
$\epsilon = 1.4$	3C	1 (1.34)	0.0176	0.178	0.176	0	1.18
$a_0 = 7.5$ kpc	6C	0.943	0.293	0.158	0.416	1.40e-23	1.70
	7C	1.36	4.26e-05	0.412	0.00459	2.89e-19	
$\beta = 1.6$	3C	1 (1.22)	0.0670	0.0518	0.101	0	1.27
$a_0 = 7.5$ kpc	6C	0.995	0.293	0.0626	0.408	1.40e-23	1.92
	7C	1.38	2.36e-04	0.915	0.00710	4.30e-20	

[a] Each run (with one or more parameter variations) is done with the same initial ensemble (Set 1) of size 3888492, which is generated using $x = 2.6$ and $T_{MaxAge} = 150$ Myr. In these MK-modified model simulations, the hotspot size grows (Jeyakumar & Saikia 2000) with source age according to Case 2 (quadratic fit) from Section 5.1, and a fixed $r_{hs(t_0)} = 0.02$ kpc, is used.

[b] Always, $\text{Ratio}_{3C} = 1$, because of the way it is defined. The number in parentheses gives the ratio of the number of sources detected in 3C simulation (with given ensemble size) as compared to the real 3C survey.

[c] Parameters defining the external environment density profile are set to those of the KDA model, namely, $\beta = 1.9, a_0 = 2$ kpc, $\rho_0 = 7.2 \times 10^{-22}$ kg m^{-3}.

[d] $\rho_1 = \rho_{0\ \text{(Default)}}/1.5 = 1.133 \times 10^{-23}$ kg m^{-3}.

[e] $\rho_2 = 2 \times \rho_{0\ \text{(Default)}} = 3.4 \times 10^{-23}$ kg m^{-3}.

[f] Numbers of sources detected in some of the simulated surveys are considerably smaller than in the real surveys, so the 1-D K-S statistic does not hold much significance.

Table B.7: Modified MK Model Results for Run 2: 1-D K-S Statistics [a]

Varied Model Parameter	Survey	Ratio$_{3C}$ Ratio$_{6C}$ Ratio$_{7C}$	$\mathcal{P}(K$–$S)$				$\mathcal{P}_{[P,D,z,\alpha]}$ $\mathcal{P}_{[P,2D,z,\alpha]}$
			$\mathcal{P}(P)$	$\mathcal{P}(D)$	$\mathcal{P}(z)$	$\mathcal{P}(\alpha)$	
MK-modified	3C	1 (1.77)	0.0491	0.521	0.535	0	2.12
	6C	1.08	0.624	0.102	0.506	1.83e-24	2.88
	7C	1.06	0.00187	0.301	0.0491	6.13e-21	
KDA Env. [b] β, a_0, ρ_0	3C	1 (1.84)	0.0122	0.00898	0.474	0	1.43
	6C	1.02	0.416	0.240	0.408	1.83e-24	1.84
	7C	1.10	3.99e-04	0.417	0.00458	4.30e-20	
$\beta = 1.6$	3C	1 (1.59)	0.121	0.709	0.535	0	2.73
	6C	1.09	0.724	0.103	0.408	1.83e-24	4.04
	7C	1.07	0.00479	0.879	0.0491	4.15e-20	
$a_0 = 7.5$ kpc	3C	1 (1.37)	0.0913	0.615	0.360	0	1.98
	6C	1.03	0.707	0.102	0.125	1.83e-24	2.91
	7C	1.05	0.00703	0.412	0.0689	6.13e-21	
$a_0 = 20$ kpc	3C	1 (2.94)	0.0253	0.802	0.192	0	2.28
	6C	1.02	0.564	0.0212	0.533	1.83e-24	3.64
	7C	1.07	1.34e-04	0.893	0.00708	8.39e-22	
$\rho_0 = \rho_2$ [c]	3C	1 (2.46)	0.0177	0.0508	0.387	0	1.11
	6C	1.04	0.416	0.0113	0.556	1.83e-24	1.18
	7C	1.10	0.00181	0.0264	0.0108	5.91e-21	
$\gamma_{max(hs)} = 3 \times 10^8$	3C	1 (1.70)	0.0674	0.212	0.360	0	1.69
	6C	1.03	0.869	0.159	0.503	1.83e-24	2.03
	7C	1.07	0.00307	0.0465	0.0491	6.13e-21	
$p = 2.3$	3C	1 (1.28)	0.122	0.0957	0.360	0	1.50
	6C	1.11	0.635	0.259	0.192	1.83e-24	1.89
	7C	1.08	0.0157	0.218	0.0951	1.06e-22	
$\epsilon = 1.4$	3C	1 (1.82)	0.122	0.619	0.568	0	2.22
	6C	0.981	0.479	0.349	0.408	1.35e-23	3.18
	7C	1.06	2.44e-04	0.199	0.0108	4.30e-20	
$\epsilon = 1.4$ $\beta = 1.6$	3C	1 (1.70)	0.0906	0.178	0.580	0	1.98
	6C	1.02	0.416	0.242	0.408	1.40e-23	2.76
	7C	1.06	0.00110	0.732	0.0108	2.79e-19	

Continued on next page ...

Table B.7: continued from previous page ...

Varied Model Parameter	Survey	Ratio_{3C} Ratio_{6C} Ratio_{7C}	$\mathcal{P}(K\text{–}S)$				$\mathcal{P}_{[P,D,z,\alpha]}$ $\mathcal{P}_{[P,2D,z,\alpha]}$
			$\mathcal{P}(P)$	$\mathcal{P}(D)$	$\mathcal{P}(z)$	$\mathcal{P}(\alpha)$	
$\epsilon = 1.4$	3C	1 (1.47)	0.0910	0.216	0.581	0	2.04
$a_0 = 7.5$ kpc	6C	1.02	0.340	0.485	0.408	1.40e-23	2.90
	7C	0.967	0.00108	0.565	0.0238	1.74e-18	
$\beta = 1.6$	3C	1 (1.23)	0.207	0.216	0.535	0	2.26
$a_0 = 7.5$ kpc	6C	1.08	0.724	0.340	0.194	1.35e-23	3.13
	7C	1.05	0.0106	0.732	0.0491	4.30e-20	

[a] Each run (with one or more parameter variations) is done with the same initial ensemble (Set 2) of size 3888492, which is generated using $x = 2.6$ and $T_{MaxAge} = 150$ Myr. In these MK-modified model simulations, the hotspot size grows (Jeyakumar & Saikia 2000) with source age according to Case 2 (quadratic fit) from Section 5.1, and a fixed $r_{hs(t_0)} = 0.02$ kpc, is used.

[b] Parameters defining the external environment density profile are set to those of the KDA model, namely, $\beta = 1.9, a_0 = 2$ kpc, $\rho_0 = 7.2 \times 10^{-22}$ kg m^{-3}.

[c] $\rho_2 = 2 \times \rho_{0\ \text{(Default)}} = 3.4 \times 10^{-23}$ kg m^{-3}.

Table B.8: Modified MK Model Results for Run 3: 1-D K-S Statistics [a]

Varied Model Parameter	Survey	Ratio_{3C} Ratio_{6C} Ratio_{7C}	$\mathcal{P}(K\text{–}S)$ $\mathcal{P}(P)$	$\mathcal{P}(D)$	$\mathcal{P}(z)$	$\mathcal{P}(\alpha)$	$\mathcal{P}_{[P,D,z,\alpha]}$ $\mathcal{P}_{[P,2D,z,\alpha]}$
MK-modified	3C	1 (1.54)	0.0913	0.340	0.280	0	1.39
	6C	0.913	0.469	0.0350	0.408	1.83e-24	1.78
	7C	1.21	0.00763	0.0465	0.0713	4.15e-20	
KDA Env. [b] β, a_0, ρ_0	3C	1 (1.66)	0.00238	0.00260	0.568	0	1.91
	6C	0.956	0.329	0.331	0.716	1.83e-24	2.58
	7C	1.14	6.75e-04	0.750	0.0108	4.30e-20	
$\beta = 1.6$	3C	1 (1.4)	0.00826	0.515	0.351	0	1.58
	6C	0.931	0.333	0.0599	0.556	1.83e-24	2.18
	7C	1.23	0.00750	0.0801	0.0491	4.30e-20	
$a_0 = 7.5$ kpc	3C	1 (1.22)	0.0176	0.334	0.280	0	1.61
	6C	0.907	0.464	0.0984	0.716	1.83e-24	2.09
	7C	1.15	0.00687	0.129	0.0951	4.15e-20	
$a_0 = 20$ kpc	3C	1 (2.97)	0.00153	0.0260	0.247	0	1.07
	6C	0.883	0.327	0.0113	0.716	1.83e-24	1.22
	7C	1.06	1.34e-04	0.193	0.00708	8.39e-22	
$\rho_0 = \rho_2$ [c]	3C	1 (2.49)	0.0119	0.164	0.483	0	1.57
	6C	0.810	0.564	0.0626	0.716	1.83e-24	1.82
	7C	1.08	7.20e-04	0.0741	0.0161	5.91e-21	
$\gamma_{max(hs)} = 3 \times 10^8$	3C	1 (1.50)	0.0488	0.0940	0.351	0	1.23
	6C	0.871	0.469	0.0984	0.408	1.83e-24	1.44
	7C	1.22	0.00763	0.0801	0.0689	4.15e-20	
$p = 2.3$	3C	1 (1.2)	0.0176	0.348	0.351	0	1.99
	6C	0.863	0.227	0.230	0.716	1.83e-24	2.84
	7C	1.10	0.0116	0.584	0.173	8.08e-22	
$\epsilon = 1.4$	3C	1 (1.59)	0.00819	0.607	0.581	0	2.39
	6C	0.957	0.327	0.102	0.556	1.83e-24	3.61
	7C	1.16	0.00190	0.896	0.0238	2.89e-19	
$\epsilon = 1.4$ $\beta = 1.6$	3C	1 (1.48)	0.00153	0.0373	0.581	0	2.04
	6C	0.963	0.331	0.471	0.556	1.35e-23	2.91
	7C	1.15	0.00181	0.879	0.0238	1.74e-18	

Continued on next page ...

Table B.8: continued from previous page ...

Varied Model Parameter	Survey	Ratio_{3C} Ratio_{6C} Ratio_{7C}	$\mathcal{P}(K\text{–}S)$				$\mathcal{P}_{[P,D,z,\alpha]}$ $\mathcal{P}_{[P,2D,z,\alpha]}$
			$\mathcal{P}(P)$	$\mathcal{P}(D)$	$\mathcal{P}(z)$	$\mathcal{P}(\alpha)$	
$\epsilon = 1.4$	3C	1 (1.2)	0.00824	0.638	0.351	0	2.41
$a_0 = 7.5$ kpc	6C	1.03	0.612	0.150	0.506	1.40e-23	3.70
	7C	1.19	0.00687	0.917	0.0491	2.79e-19	
$\beta = 1.6$	3C	1 (1.10)	0.00826	0.552	0.524	0	2.32
$a_0 = 7.5$ kpc	6C	0.977	0.331	0.331	0.716	1.83e-24	3.28
	7C	1.19	0.0105	0.319	0.173	4.30e-20	

[a] Each run (with one or more parameter variations) is done with the same initial ensemble (Set 3) of size 3888492, which is generated using $x = 2.6$ and $T_{MaxAge} = 150$ Myr. In these MK-modified model simulations, the hotspot size grows (Jeyakumar & Saikia 2000) with source age according to Case 2 (quadratic fit) from Section 5.1, and a fixed $r_{hs(t_0)} = 0.02$ kpc, is used.

[b] Parameters defining the external environment density profile are set to those of the KDA model, namely, $\beta = 1.9, a_0 = 2$ kpc, $\rho_0 = 7.2 \times 10^{-22}$ kg m^{-3}.

[c] $\rho_2 = 2 \times \rho_{0\ \text{(Default)}} = 3.4 \times 10^{-23}$ kg m^{-3}.

Table B.9: Modified MK Model Results for Run 4: 1-D K-S Statistics [a]

Varied Model Parameter	Survey	Ratio$_{3C}$ Ratio$_{6C}$ Ratio$_{7C}$	$\mathcal{P}(K\text{–}S)$ $\mathcal{P}(P)$	$\mathcal{P}(D)$	$\mathcal{P}(z)$	$\mathcal{P}(\alpha)$	$\mathcal{P}_{[P,D,z,\alpha]}$ $\mathcal{P}_{[P,2D,z,\alpha]}$
	3C	1 (2.0)	0.00557	0.0373	0.474	0	1.46
MK-modified	6C	0.621	0.0460	0.241	0.580	2.99e-26	2.02
	7C	0.992	2.69e-04	0.610	0.0251	5.38e-21	
	3C	1 (2.13)	0.00826	1.65e-05	0.312	0	1.16
KDA Env. [b]	6C	0.721	0.113	0.349	0.727	1.35e-23	1.46
β, a_0, ρ_0	7C	1.02	1.27e-05	0.138	0.00271	4.15e-20	
	3C	1 (1.86)	0.00824	0.0972	0.474	0	1.58
$\beta = 1.6$	6C	0.693	0.371	0.240	0.556	1.83e-24	2.08
	7C	1.06	4.28e-05	0.412	0.0106	4.15e-20	
	3C	1 (1.59)	0.00553	0.420	0.580	0	2.12
$a_0 = 7.5$ kpc	6C	0.720	0.724	0.0582	0.533	1.35e-23	2.84
	7C	1.06	0.00111	0.428	0.0238	4.30e-20	
	3C	1 (3.10)	2.28e-05	0.425	0.192	0	1.30
$a_0 = 20$ kpc	6C	0.719	0.575	0.0200	0.401	1.83e-24	1.78
	7C	1.09	7.49e-05	0.0755	0.00456	8.39e-22	
	3C	1 (2.72)	2.27e-04	0.272	0.214	0	1.08
$\rho_0 = \rho_2$ [c]	6C	0.662	0.176	0.00319	0.707	1.83e-24	1.39
	7C	1.06	4.32e-05	0.0465	0.0108	5.91e-21	
	3C	1 (1.92)	0.0176	0.127	0.484	0	1.62
$\gamma_{max(hs)} = 3 \times 10^8$	6C	0.652	0.514	0.00319	0.547	1.83e-24	2.01
	7C	1.02	0.00451	0.431	0.0486	6.13e-21	
	3C	1 (1.53)	0.0122	0.0709	0.580	0	1.60
$p = 2.3$	6C	0.711	0.612	0.0626	0.556	1.83e-24	1.83
	7C	1.04	0.00111	0.201	0.0325	1.06e-22	
	3C	1 (2.05)	0.00366	0.0561	0.423	0	1.58
$\epsilon = 1.4$	6C	0.663	0.371	0.0626	0.716	1.40e-23	2.04
	7C	1.01	4.26e-05	0.594	0.0108	2.69e-19	
$\epsilon = 1.4$	3C	1 (1.94)	0.00549	0.0128	0.474	0	1.61
$\beta = 1.6$	6C	0.698	0.258	0.240	0.556	1.40e-23	2.22
	7C	0.992	2.35e-05	0.732	0.00287	2.79e-19	

Continued on next page ...

Table B.9: continued from previous page ...

Varied Model Parameter	Survey	Ratio_{3C} Ratio_{6C} Ratio_{7C}	$\mathcal{P}(K$–$S)$				$\mathcal{P}_{[P,D,z,\alpha]}$ $\mathcal{P}_{[P,2D,z,\alpha]}$
			$\mathcal{P}(P)$	$\mathcal{P}(D)$	$\mathcal{P}(z)$	$\mathcal{P}(\alpha)$	
$\epsilon = 1.4$	3C	1 (1.69)	0.0494	0.0195	0.484	0	1.43
$a_0 = 7.5$ kpc	6C	0.698	0.0238	0.101	0.556	1.40e-23	1.96
	7C	0.991	2.38e-05	0.732	0.00287	2.79e-19	
$\beta = 1.6$	3C	1 (1.49)	0.0249	0.00874	0.580	0	1.34
$a_0 = 7.5$ kpc	6C	0.719	0.520	0.0371	0.387	1.35e-23	1.49
	7C	1.01	1.36e-04	0.190	0.0159	4.30e-20	

[a] Each run (with one or more parameter variations) is done with the same initial ensemble (Set 4) of size 3888492, which is generated using $x = 2.6$ and $T_{MaxAge} = 150$ Myr. In these MK-modified model simulations, the hotspot size grows (Jeyakumar & Saikia 2000) with source age according to Case 2 (quadratic fit) from Section 5.1, and a fixed $r_{hs(t_0)} = 0.02$ kpc, is used.

[b] Parameters defining the external environment density profile are set to those of the KDA model, namely, $\beta = 1.9, a_0 = 2$ kpc, $\rho_0 = 7.2 \times 10^{-22}$ kg m^{-3}.

[c] $\rho_2 = 2 \times \rho_{0\ \text{(Default)}} = 3.4 \times 10^{-23}$ kg m^{-3}.

Table B.10: Modified MK Model Results: Performance Ranks [a]

Model	$\mathcal{P}(K\text{–}S)$	Run 1	Run 2	Run 3	Run 4	Average [b]
MK-modified	$\mathcal{P}_{[P,D,z,\alpha]}$	4	5	10	7	6.5
	$\mathcal{P}_{[P,2D,z,\alpha]}$	4	7	10	5	6.5
KDA Env. [c]	$\mathcal{P}_{[P,D,z,\alpha]}$	9	11	6	11	9.25
β, a_0, ρ_0	$\mathcal{P}_{[P,2D,z,\alpha]}$	9	11	6	11	9.25
$\beta = 1.6$	$\mathcal{P}_{[P,D,z,\alpha]}$	1	1	8	6	4
	$\mathcal{P}_{[P,2D,z,\alpha]}$	1	1	7	3	3
$a_0 = 7.5$ kpc	$\mathcal{P}_{[P,D,z,\alpha]}$	10	8	7	1	6.5
	$\mathcal{P}_{[P,2D,z,\alpha]}$	7	5	8	1	5.25
$a_0 = 20$ kpc	$\mathcal{P}_{[P,D,z,\alpha]}$	5	2	12	10	7.25
	$\mathcal{P}_{[P,2D,z,\alpha]}$	5	2	12	9	7
$\rho_0 = \rho_2$ [d]	$\mathcal{P}_{[P,D,z,\alpha]}$	8	12	9	12	10.25
	$\mathcal{P}_{[P,2D,z,\alpha]}$	10	12	9	12	10.75
$\gamma_{max(hs)} = 3 \times 10^8$	$\mathcal{P}_{[P,D,z,\alpha]}$	6	9	11	2	7
	$\mathcal{P}_{[P,2D,z,\alpha]}$	8	9	11	6	8.5
$p = 2.3$	$\mathcal{P}_{[P,D,z,\alpha]}$	2	10	5	4	5.25
	$\mathcal{P}_{[P,2D,z,\alpha]}$	2	10	5	8	6.25
$\epsilon = 1.4$	$\mathcal{P}_{[P,D,z,\alpha]}$	3	4	2	5	3.5
	$\mathcal{P}_{[P,2D,z,\alpha]}$	3	3	2	4	3
$\epsilon = 1.4$	$\mathcal{P}_{[P,D,z,\alpha]}$	7	7	4	3	5.25
$\beta = 1.6$	$\mathcal{P}_{[P,2D,z,\alpha]}$	6	8	4	2	5
$\epsilon = 1.4$	$\mathcal{P}_{[P,D,z,\alpha]}$	12	6	1	8	6.75
$a_0 = 7.5$ kpc	$\mathcal{P}_{[P,2D,z,\alpha]}$	12	6	1	7	6.5
$\beta = 1.6$	$\mathcal{P}_{[P,D,z,\alpha]}$	11	3	3	9	6.5
$a_0 = 7.5$ kpc	$\mathcal{P}_{[P,2D,z,\alpha]}$	11	4	3	10	7

[a] Each run is done using $x = 2.6$ and $T_{MaxAge} = 150$ Myr for the initial population of size 3888492; the 4 runs, whose ranks are displayed, differ in the initial random seeds. The ranks are according to the combined 1-D K-S statistic results of the 4 runs tabulated in detail in Tables B.6, B.7, B.8 and B.9, which are also summarised in Table 5.10.

[b] Overall rank score (obtained by averaging separate ranks from the four runs) of each of the 12 MK-modified cases shown here.

[c] Parameters defining the external environment density profile are set to those of the KDA model, namely, $\beta = 1.9, a_0 = 2$ kpc, $\rho_0 = 7.2 \times 10^{-22}$ kg m^{-3}.

[d] $\rho_2 = 2 \times \rho_{0\ \text{(Default)}} = 3.4 \times 10^{-23}$ kg m^{-3}.